A search for flavour changing neutral currents involving a top quark and a Z boson, using the data collected by the CMS experiment at a centre-of-mass energy of 13 TeV

Isis Van Parijs

Proefschrift ingediend met het oog op het behalen van de academische graad Doctor in de Wetenschappen

Published in Faculteit Wetenschappen & Bio-ingenieurswetenschappen
Vrije Universiteit Brussel
At 26 January 2018

Responsible Contact: Isis Van Parijs
Interuniversity Institute for High Energies
Supervisor: Prof. Jorgen D'Hondt

Doctoral examination commission:

Chair:		Prof. Dr. B. Craps	Vrije Universiteit Brussel
Secretary:		Prof. Dr. S. Buitink	Vrije Universiteit Brussel
Supervisor:		Prof. Dr. J. D'Hondt	Vrije Universiteit Brussel
Other:			
	DNTK:	Prof. Dr. P. Van Mulders	Vrije Universiteit Brussel
	DSCH:	Prof. Dr. S. Ballet	Vrije Universiteit Brussel
	External	Prof. Dr. B. Fuks	Sorbonne Université
	External:	Prof. Dr. A. Onofre	LIP and University do Minho

Date of Hand-in:	7 December 2017
Date of Private Defense:	17 January 2018
Date of Public Defense:	26 January 2018

ISBN 9789492312655
NUR 924, 926

The figures used between the sections are taken from Ref. [1].
The cover figure is taken from Ref. [2].

Contents

Introduction

The Standard Model (SM) of particle physics is the theory of fundamental particles and their interactions. This theory has been experimentally confirmed and all its predicted particles have been found. Despite its many successes, the Standard Model has its shortcomings and can not explain phenomena such as neutrino masses, dark matter, dark energy or gravity. The heaviest particle in the Standard Model is the top quark and physicists believe that it has an enhanced sensitivity to various new particles and interactions suggested by beyond the Standard Model theories. Its lifetime is so short that it does not form bound states, making it possible to study the bare quark. Furthermore, the top quark has a distinct signature since it almost exclusively decays to a W boson and a bottom quark. This makes the top quark the ideal candidate to directly study quark properties. On top of this, many beyond the Standard Model physics phenomena are investigated by measuring the production rate of top quarks by studying the Wtb vertex and interactions that are heavily suppressed in the Standard Model are researched. The Large Hadron Collider (LHC) is a top quark factory, producing a large number of events containing top quarks. At the proton collision points, experiments are placed to study these collisions. The work presented in the thesis uses the data collected by one of such an experiment, the Compact Muon Solenoid (CMS), and investigates flavour changing neutral currents (FCNC).

In the 1960s, the charged current process occurring when a charged kaon decays to a muon ($K^+ \rightarrow \mu^+\nu_\mu$) was a well known process. The neutral current process $K^0_L \rightarrow \mu^+\mu^-$ was however not observed. This suppression of neutral currents with respect to charged currents was baffling the physicists. At that time, only three different quarks were known and although the existence of a fourth quark was proposed, there was no evidence for it yet. The GIM mechanism [3, 4], proposed in 1970, was the theory providing a satisfying explanation for the suppression of neutral current processes compared to charged current processes, via a fourth quark with specific couplings to the other quarks. This brought a revolution in physics, and the GIM mechanism combined with then already existing measurements provided indirect indications of the charm quark before it was directly observed in J/Ψ meson decays [5]. This confirmed that flavour changing neutral currents, which change the flavour of a fermion without altering its electric charge, are highly suppressed in the Standard Model.

The first evidence for flavour changing neutral currents was provided in 2005 by the CDF experiment [6], by looking at $B^0_s \rightarrow \phi\phi$ decays. However, it was the large production rate of b hadrons at the LHC that made it possible for the LHCb and CMS collaboration to measure the FCNC decays of b hadrons [7]. Their combined data provided the first discovery of FCNC decays with the $B_s^0 \rightarrow \mu^-\mu^+$ decay. This observation agreed with the Standard Model prediction and has put stringent limits on many beyond the Standard Model theories. Recent interpretations for bottom to strange quark transitions have even found strong hints for new physics [8]. These interpretations are based on the discrepancy from the Standard Model prediction, measured in 2013 by the LHCb collaboration for $B \rightarrow K^*\mu^-\mu^+$ [9–12], and confirmed in 2015 [13]. Additionally, a deficit for the branching ratios of several decays such as $B_s \rightarrow \phi\mu^-\mu^+$ with respect to the Standard Model predictions has been found in 2013 [14] and 2015 [15] by the LHCb collaboration. The Belle experiment confirmed these measurements in 2016 [16, 17]. Another remarkably observation was made by the LHCb collaboration in 2014 [18], where it was observed that the deviations from the Standard Model were stronger for the $B \rightarrow K^*\mu^-\mu^+$ decays than for $B \rightarrow K^*e^-e^+$. This hints for a violation of lepton flavour universality. The Belle experiment has confirmed these hints by measuring the lepton flavour universality violating terms in 2016 [17] and also the update with more data of LHCb in 2016 [19, 20] still points towards this direction. The CMS and ATLAS collaborations have also measured $B_s^0 \rightarrow \phi\phi$ decays [21, 22], confirming the LHCb results. In Ref. [8], several beyond the Standard Model theories have been identified as possible candidates for a new comprehending theory and time will point out which ones will prevail.

The search presented in this thesis is performed on data collected by the Compact Muon Solenoid (CMS) experiment at a centre-of-mass energy of 13 TeV, resulting in 35.9 fb^{-1} of integrated luminosity. The anomalous couplings of a Z boson to a top quark and an up or charm quark are being investigated for three-lepton signatures in the final state of proton collisions. In the Standard Model, the branching fraction for a top quark decaying into a charm or up quark and a Z boson is of the order of 10^{-14} [3, 23]. Several extensions of the Standard Model however enhance the FCNC branching fractions and can be probed at the LHC [23]. Additional to the potential signals in top quark pair events, these interactions may result in flavour changing single top quark production through a top-Z-quark vertex. Up to this moment, the searches performed on top quark related flavour changing neutral currents are done at the Tevatron, a proton-antiproton collider, by the CDF [24] and D0 [25] collaborations, as well as at the LHC by the ATLAS [26, 27] and CMS [28–30] collaborations. Their limits are still far from the sensitivity required to reach the Standard Model predictions, leaving a large phase space to reveal or exclude new physics phenomena.

The first chapter of this thesis introduces the Standard Model of particle physics as well as a brief introduction into effective field theories. The end of this chapter focuses on flavour changing neutral currents involving top-Z-quark interactions and overviews the current experimental limits. The second chapter gives a description of the Large Hadron Collider (LHC) at CERN, as well as the CMS experiment. Its coordinate system, hardware, and data acquisition are discussed. The analysis techniques used for the search presented in this thesis are discussed in the third chapter. Here, the simulation of proton collisions is explained, and an introduction is given to Boosted Decision Trees as well as the statistical methodology used for the search. In the fourth chapter, the reconstruction and identification of particles within CMS is explained. At the end, an overview is given of the corrections that one needs to apply for making the simulation agree with data. The event selection and categorisation used for the search are explained in the fifth chapter. Here, the analysis strategy is set and the statistically independent data sets are defined. The templates of variable distributions used for the limits on the FCNC top-Z-quark coupling are discussed in the sixth chapter, and the results are presented. The final chapter concludes the search and an outlook to the future is given.

There is a place, like no place on earth. A land full of wonder mystery, and danger! Some say, to survive it, you need to be as mad as a hatter. Which, luckily, I am.

- Lewis Caroll, Alice in Wonderland

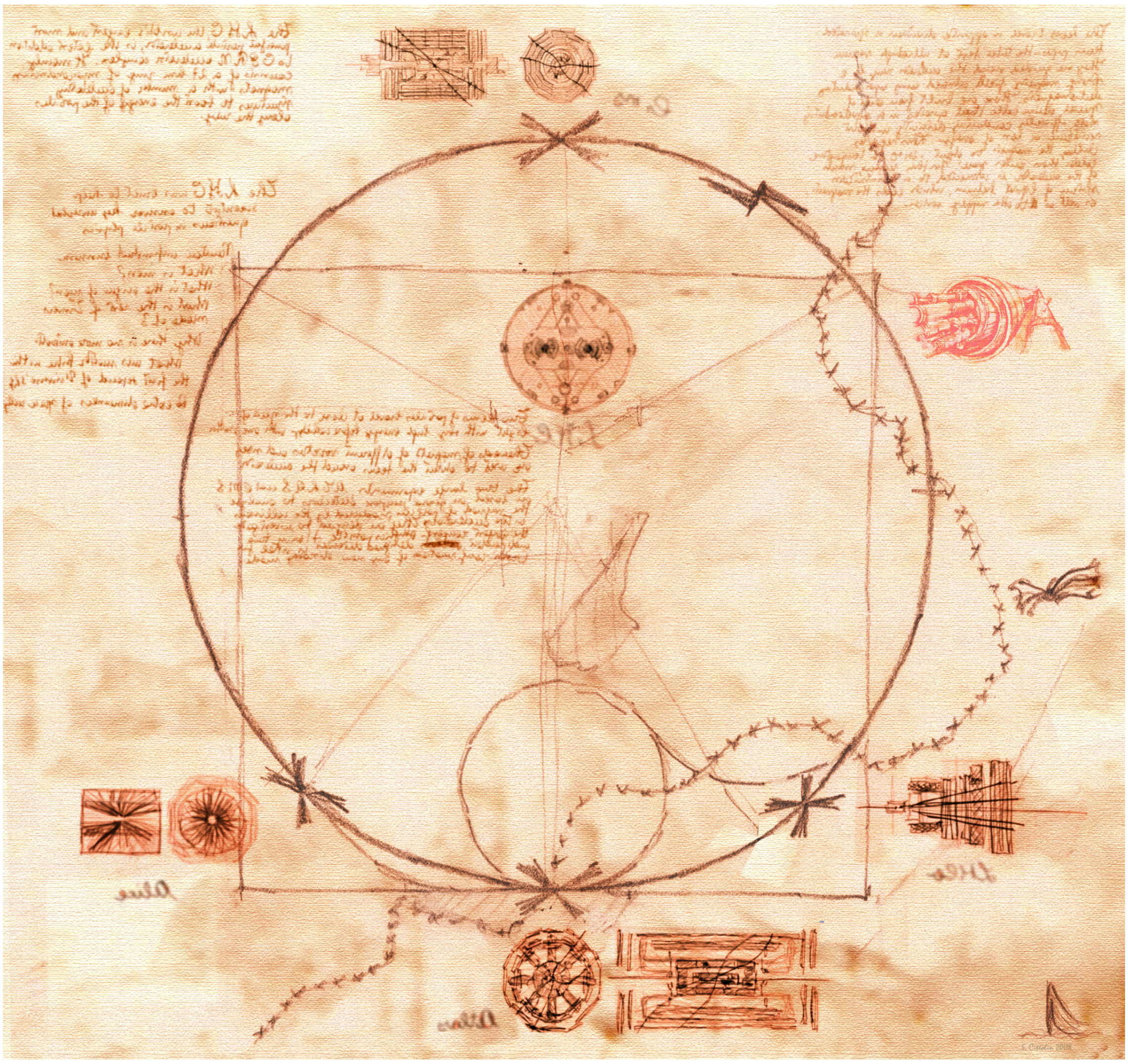

Theoretical basis 1

The Standard Model (SM) [31] is a name given in the 1970s to a theory describing the fundamental particles and their interactions. This quantum field theory describes the particles and their interactions as fields and has successfully incorporated three of the four fundamental forces in the universe. In Section 1.1, the particle content of the SM is summarised, while Section 1.2 describes the SM Lagrangian and its symmetries. In Section 1.3, the flavour content of the SM is highlighted, and Section 1.4 focuses on the top quark in the SM.

The successful theory of the SM has some shortcomings which are discussed in Section 1.5 and lead to searches for a more general theory. One of the approaches is using an effective field theory (EFT) [32] to search for new physics in a model independent way. In Section 1.6, a short introduction to the effective field theory approach is given and an EFT model focussing on flavour changing neutral currents (FCNC) involving a top quark is presented. Its current experimental constraints are given in Section 1.7.

1.1 Elementary particles and forces

The interactions in nature can be described by four forces, the strong force, the electromagnetic (EM) force, the weak force and the gravitational force. These interactions happen via particles with an integer spin known as bosons. The strong interaction is mediated by eight gluons g, while the electromagnetic force is mediated by photons γ, and the weak force by Z and $W^{\pm}$ bosons. In Table 1.1, the forces and their characteristics are summarised. The gravitational force is the only force not included in the SM and can be neglected for energies lower than the Planck scale (1.22×10^{19} GeV).

Table 1.1: The four forces of nature and their characteristics.

	Range	Mediator
Strong force	10^{-15} m	8 gluons
Electromagnetic force	∞	photon
Weak force	10^{-18} m	$W^{\pm}$, Z bosons
Gravitational force	∞	unknown

The fermions are the particles that make up the visible matter in the universe. They carry half integer spin and can be subdivided into leptons and quarks, where leptons do not interact strongly. Each fermion has a corresponding anti-fermion which has the same mass and is oppositely charged. The electron e is the first elementary particle discovered [33] and belongs to the first generation of leptons together with the electron neutrino ν_e. The second generation comprises the muon μ and muon neutrino ν_μ, whereas the third generation consists of the tau τ and tau neutrino ν_τ. The neutrinos are neutral particles, while the other leptons have charge $\pm q_e$ with q_e representing the elementary charge of 1.602×10^{-19} C. The masses of charged leptons differ by four orders of magnitude between the first and third generations. In the SM the neutrinos are assumed to be massless, nonetheless it is experimentally established that neutrinos do have a tiny non-zero mass [34, 35]. In Table 1.2, the leptons and their properties in the SM are summarised.

Table 1.2: The properties of the leptons in the three generations of the SM [36], where q_e represents the elementary charge.

Generation	Particle	Mass	Charge
First	e^-	0.511 MeV	$-q_e$
	ν_e	≈ 0	0
Second	μ^-	106 MeV	$-q_e$
	ν_μ	≈ 0	0
Third	τ^-	1777 MeV	$-q_e$
	ν_τ	≈ 0	0

The quarks are also divided into three generations. Unlike the leptons, they carry colour charge and can interact via the strong interaction. The top quark, discovered in 1995 at the Tevatron [37, 38], is the heaviest SM particle with a mass[1] measured to be $173.34 \pm 0.27(\text{stat}) \pm 0.71(\text{syst})$ GeV [39]. The quarks and their properties are summarised in Table 1.3. In nature, only colour neutral objects can exist. This has as consequence that quarks are bound through gluons into mesons (quark+anti-quark) and baryons (three quarks). These mesons and baryons are mostly short-lived and unstable particles that rapidly decay through $W^\pm$ and Z bosons. The only known stable baryon is the proton, made up of two up quarks and one down quark.

The scalar boson, commonly known as the Higgs boson, is the last piece of the SM discovered in 2012 [40, 41]. It is responsible for the masses of the $W^\pm$ and Z boson, and that of the fermions.

[1] In this thesis all masses and energies are expressed in natural units, where the speed of light and $\hbar$ are taken to be equal to one.

Table 1.3: The properties of the quarks in the three generations of the SM [36], where q_e represents the elementary charge.

Generation	Particle	Mass	Charge
First	up u	$2.2^{+0.6}_{-0.4}$ MeV	$\frac{2}{3}\,q_e$
	down d	$4.7^{+0.5}_{-0.4}$ MeV	$-\frac{1}{3}\,q_e$
Second	charm c	1.28 ± 0.03 GeV	$\frac{2}{3}\,q_e$
	strange s	96^{+8}_{-4} MeV	$-\frac{1}{3}\,q_e$
Third	top t	$173.34 \pm 0.27(\text{stat}) \pm 0.71(\text{syst})$ GeV	$\frac{2}{3}\,q_e$
	bottom b	$4.18^{+0.04}_{-0.03}$ GeV	$-\frac{1}{3}\,q_e$

1.2 Standard Model Lagrangian, connecting fields with particles

The SM is a quantum field theory and thus describes the dynamics and kinematics of particles and forces by a Lagrangian $\mathscr{L}$. The theory is based on the $SU(3)_C \times SU(2)_L \times U(1)_Y$ gauge symmetry, where $SU(2)_L \times U(1)_Y$ describes the electroweak interaction and $SU(3)_C$ the strong interaction. The indices refer to colour C, the left chiral nature of the $SU(2)_L$ coupling L, and the weak hypercharge Y. Its Lagrangian is constructed in a way that the symmetries representing physics conservation laws such as conservation of energy, momentum and angular momentum are represented. The symmetries under local gauge transformations are sustained by demanding gauge invariance[2].

The $U(1)_Y$ group has one generator Y with an associated gauge field B_μ. The three gauge fields W^1_μ, W^2_μ, and W^3_μ, are associated to $SU(2)_L$ with three generators that can be written as half the Pauli matrices:

$$T_1 = \frac{1}{2}\begin{pmatrix} 0 & 1 \\ 1 & 0 \end{pmatrix},\ T_2 = \frac{1}{2}\begin{pmatrix} 0 & -i \\ i & 0 \end{pmatrix},\ \text{and}\ T_3 = \frac{1}{2}\begin{pmatrix} 1 & 0 \\ 0 & -1 \end{pmatrix}. \tag{1.1}$$

The generators T^a satisfy the Lie algebra:

$$\left[T_a, T_b\right] = i\epsilon_{abc}T^c \text{ and} \left[T_a, Y\right] = 0, \tag{1.2}$$

where ϵ_{abc} is an antisymmetric tensor. The gauge fields of $SU(2)_L$ only couple to left-handed fermions as required by the observed parity violating nature of the weak force. The $SU(3)_C$ group represents quantum chromodynamics (QCD). It has eight generators corresponding to eight gluon fields $G^{1...8}_\mu$. Unlike $SU(2)_L \times U(1)_Y$, $SU(3)_C$ is not chiral.

Under $SU(3)_C$, quarks are colour triplets while leptons are colour singlets. This implies that the quarks carry a colour index ranging between one and three, whereas leptons do not take part

[2]Different field configurations of unobservable fields can result in identical quantities. Transformations between such configurations are called gauge transformations and the absence of change in the measurable quantities is a characteristic called gauge invariance.

in strong interactions. Based on the chirality, the quarks and leptons are organized in doublets or singlets. Each generation i of fermions consists of left-handed doublets and right-handed singlets:

$$\mathrm{l_{L,i}} = \begin{pmatrix} \mathrm{e_{L,i}} \\ \nu_{\mathrm{L,i}} \end{pmatrix},\ \mathrm{e_{R,i}},\ \mathrm{q_{L,i}} = \begin{pmatrix} \mathrm{u_{L,i}} \\ \mathrm{d_{L,i}} \end{pmatrix},\ \mathrm{u_{R,i}},\ \text{and}\ \mathrm{d_{R,i}} \tag{1.3}$$

The SM Lagrangian can be decomposed as a sum of four terms

$$\mathscr{L}_{\mathrm{SM}} = \mathscr{L}_{\mathrm{gauge}} + \mathscr{L}_{\mathrm{f}} + \mathscr{L}_{\mathrm{Yuk}} + \mathscr{L}_{\phi}, \tag{1.4}$$

that are related to the gauge, fermion, Yukawa and scalar sectors. The gauge Lagrangian regroups the gauge fields of all three symmetry groups, and the fermionic part consists of kinetic energy terms for quarks and leptons. The interaction between fermions and the scalar doublet ϕ gives rise to fermion masses and is described by the Yukawa Lagrangian. The scalar part of the Lagrangian is composed of a kinetic and potential component related to the scalar boson, described in more detail below.

For the electroweak theory, two coupling constants are introduced, namely g' for $\mathrm{U(1)_Y}$ and g for $\mathrm{SU(2)_L}$. The physically observable gauge bosons of this theory are the photon field A_μ, the Z boson field Z^0_μ, and the W boson fields $\mathrm{W}^\pm_\mu$. These are a superposition of the four gauge fields of $\mathrm{SU(2)_L} \times \mathrm{U(1)_Y}$:

$$\begin{aligned} \mathrm{A}_\mu &= \sin\theta_\mathrm{W} \mathrm{W}^3_\mu + \cos\theta_\mathrm{W} \mathrm{B}_\mu, \\ \mathrm{Z}^0_\mu &= \cos\theta_\mathrm{W} \mathrm{W}^3_\mu - \sin\theta_\mathrm{W} \mathrm{B}_\mu,\ \text{and} \\ \mathrm{W}^\pm_\mu &= \sqrt{\frac{1}{2}}\left(\mathrm{W}^1_\mu \mp i\mathrm{W}^2_\mu\right), \end{aligned} \tag{1.5}$$

where θ_W represents the weak mixing angle defined as $\tan\theta_\mathrm{W} = \frac{g'}{g}$.

The coupling constant representing the strength of the QCD interactions is denoted as g_s. In QCD there is asymptotic freedom whereby the strong coupling constant becomes weaker as the energy with which the interaction between strongly interacting particles is probed increases, and stronger as the distance between the particles increases. A consequence of this is known as colour confinement, the quarks and gluons can not exist on their own and are not observed individually. Through hadronisation, they are bound in colour neutral states called hadrons.

Electroweak symmetry breaking

In $\mathscr{L}_{\mathrm{gauge}}$ and $\mathscr{L}_{\mathrm{f}}$ no mass terms for fermions are present because only singlets under $\mathrm{SU(3)_C} \times \mathrm{SU(2)_L} \times \mathrm{U(1)_Y}$ can acquire a mass with an interaction of the type $m^2\phi^\dagger\phi$ without breaking the gauge invariance. In order to accommodate mass terms for fermions and gauge fields, electroweak symmetry breaking leading to $\mathscr{L}_\phi$ is introduced.

The scalar doublet is introduced in the SM as

$$\phi = \frac{1}{\sqrt{2}}\begin{pmatrix} \varphi_1 + i\varphi_2 \\ \varphi_3 + i\varphi_4 \end{pmatrix}. \tag{1.6}$$

Its field potential is of the form

$$V(\phi) = \mu^2\phi^\dagger\phi + \lambda(\phi^\dagger\phi)^2, \tag{1.7}$$

with $\mu^2 < 0$ and λ a positive number. This choice of parameters gives the potential a "Mexican hat" shape. It has an infinite set of minima (ground states) and by expanding the field around an arbitrary choice of ground state, the electroweak symmetry is broken ($\not{EW}$):

$$\phi = \begin{pmatrix} 0 \\ \frac{v}{\sqrt{2}} \end{pmatrix} + \hat{\phi}, \tag{1.8}$$

where v is the vacuum expectation value (vev), measured to be around 246 GeV [36] and corresponds to $\sqrt{\frac{-\mu}{\lambda}}$. The scalar doublet's four degrees of freedom are reduced to three degrees of freedom that couple to the gauge fields and fix the mass of the W^+, W^- and Z bosons:

$$m_\mathrm{W} = \frac{1}{2}v|g| \quad \text{and} \quad m_\mathrm{Z} = \frac{1}{2}v\sqrt{g'^2 + g^2}. \tag{1.9}$$

The remaining fourth degree of freedom gives rise to a physically observable particle, called the Brout-Englert-Higgs (BEH), SM scalar or Higgs boson, denoted as H. This spontaneous symmetry breaking leaves the gauge invariance intact. The Higgs field couples universally to fermions with a strength proportional to their masses, and to gauge bosons with a strength proportional to the square of their masses.

1.3 Flavours in the SM

Flavour changing charged currents are introduced in 1963 by Nicola Cabibbo [42]. Via interactions with a W boson the flavour of the quarks is changed. At the time of the postulation only up, down, and strange quarks were known and the charged weak current was described as a coupling between the up quark and $\mathrm{d_{weak}}$, where $\mathrm{d_{weak}}$ is a linear combination of the down and strange quarks, $\mathrm{d_{weak}} = \cos\theta_c\,\mathrm{d} + \sin\theta_c\,\mathrm{s}$. This linear combination is a direct consequence of the chosen rotation

$$\begin{pmatrix} \mathrm{d_{weak}} \\ \mathrm{s_{weak}} \end{pmatrix} = \begin{pmatrix} \cos\theta_c & \sin\theta_c \\ -\sin\theta_c & \cos\theta_c \end{pmatrix} \begin{pmatrix} \mathrm{d} \\ \mathrm{s} \end{pmatrix} = \mathscr{R}\begin{pmatrix} \mathrm{d} \\ \mathrm{s} \end{pmatrix}, \tag{1.10}$$

where the rotation angle θ_c is known as the Cabibbo angle. This provides a definition for the charged weak current between u and d quarks,

$$J_\mu = \bar{\mathrm{u}}\gamma_\mu\left(1 + \gamma_5\right)\mathrm{d_{weak}}, \tag{1.11}$$

with the Dirac matrices[3] denoted as γ_μ, and the γ_5 matrix is defined as $\gamma^5 = i\gamma^0\gamma^1\gamma^2\gamma^3$. A consequence of Cabibbo's approach is that the $\mathrm{s_{weak}}$ is left uncoupled, leading Glashow, Iliopoulos and Maiani (GIM) [3, 4, 43] to require the existence of a fourth quark with charge $\frac{2}{3}\mathrm{q_e}$. This

[3] The Dirac matrices [31] are a set of matrices that are defined by the anti commutator relation $\{\gamma^\mu, \gamma^\nu\} = 2g^{\mu\nu}$, with $g^{\mu\nu}$ the Minkowski metric on space-time.

quark, known as the charm quark, couples to $\mathrm{s}_{\mathrm{weak}}$ and the new definition of the charged weak current is

$$J_\mu = \begin{pmatrix} \bar{\mathrm{u}} & \bar{\mathrm{c}} \end{pmatrix} \gamma_\mu \left(1+\gamma_5\right) \mathscr{R} \begin{pmatrix} d \\ s \end{pmatrix} \equiv \bar{U} \gamma_\mu \left(1+\gamma_5\right) \mathscr{R} D. \tag{1.12}$$

The neutral weak current is defined as

$$J_3 = \bar{D} \gamma_\mu \left(1+\gamma_5\right) \left(\mathscr{R}^\dagger \mathscr{R}\right) D, \tag{1.13}$$

and is diagonal in flavour space. This has as consequence that no flavour changing neutral currents occur at tree-level interactions [31] in the SM.

Kobayashi and Maskawa generalised the Cabibbo rotation matrix to accommodate a third generation of quarks. The result is a 3×3 unitary matrix known as the CKM matrix $\mathscr{V}_{\mathrm{CKM}}$, responsible for the mixing of weak interaction states of down-type quarks:

$$\begin{pmatrix} \mathrm{d}_{\mathrm{weak}} \\ \mathrm{s}_{\mathrm{weak}} \\ \mathrm{b}_{\mathrm{weak}} \end{pmatrix} = \begin{pmatrix} V_{\mathrm{ud}} & V_{\mathrm{us}} & V_{\mathrm{ub}} \\ V_{\mathrm{cd}} & V_{\mathrm{cs}} & V_{\mathrm{cb}} \\ V_{\mathrm{td}} & V_{\mathrm{ts}} & V_{\mathrm{tb}} \end{pmatrix} \begin{pmatrix} \mathrm{d} \\ \mathrm{s} \\ \mathrm{b} \end{pmatrix} \equiv \mathscr{V}_{\mathrm{CKM}} \begin{pmatrix} \mathrm{d} \\ \mathrm{s} \\ \mathrm{b} \end{pmatrix}, \tag{1.14}$$

where $\mathscr{V}_{\mathrm{CKM}}$ is unitary $\left(\mathscr{V}^\dagger_{\mathrm{CKM}} \mathscr{V}_{\mathrm{CKM}} = \mathbb{1}\right)$. A general 3×3 unitary matrix depends on three real angles and six phases. For the CKM matrix, the freedom to redefine the phases of the quark eigenstates can remove five of the phases, leaving a single physical phase known as the Kobayashi-Maskawa phase. This phase is responsible for the charge parity violation in the SM [44]. Each element $|V_{\mathrm{ij}}|$ of $\mathscr{V}_{\mathrm{CKM}}$ squared represents the transition probability of a quark i going to a quark j, and is experimentally determined to be [36]

$$\mathscr{V}_{\mathrm{CKM}} = \begin{pmatrix} 0.97425 \pm 0.00022 & 0.2253 \pm 0.0008 & (4.13 \pm 0.49) \times 10^{-3} \\ 0.225 \pm 0.008 & 0.986 \pm 0.016 & (41.1 \pm 1.3) \times 10^{-3} \\ (8.4 \pm 0.6) \times 10^{-3} & (40.0 \pm 2.7) \times 10^{-3} & 1.021 \pm 0.032 \end{pmatrix}. \tag{1.15}$$

From Equation 1.15 follows that top quarks predominantly decay via charged weak currents to bottom quarks, with a probability consistent with unity. In the SM, FCNC can only occur via higher loop interactions which are highly suppressed. The expected transition probabilities for a top quark decaying via a FCNC interaction in the SM are given in Table 1.4. The FCNC top quark interactions of the SM are still beyond the reach of the sensitivity of current experiments.

Table 1.4: The predicted branching fractions $\mathscr{B}$ for FCNC decays involving the top quark in the SM [23].

Process	$\mathscr{B}$ in the SM	Process	$\mathscr{B}$ in the SM
$t \to uZ$	8×10^{-17}	$t \to cZ$	1×10^{-14}
$t \to u\gamma$	4×10^{-16}	$t \to c\gamma$	5×10^{-14}
$t \to ug$	4×10^{-14}	$t \to cg$	5×10^{-12}
$t \to uH$	2×10^{-17}	$t \to cH$	3×10^{-15}

1.4 The top quark in the SM

Discovered in 1995 by the CDF and D0 collaborations at the Tevatron with proton-antiproton data [45, 46], the top quark plays an important role in high energy physics. Its Yukawa interaction is given by

$$\mathscr{L}_{\text{top}-\text{Yukawa}} = -\frac{\lambda_t v}{\sqrt{2}} \bar{t}_L t_R - \frac{\lambda_t}{\sqrt{2}} H \, \bar{t}_L t_R + \text{h.c.}, \tag{1.16}$$

yielding a Yukawa coupling of [36]

$$\lambda_t = \frac{\sqrt{2} m_t}{v} = 0.991 \pm 0.003. \tag{1.17}$$

This Yukawa coupling is very large compared to the other Yukawa couplings in the SM ($\mathcal{O}(10^{-2})$), leading to the belief that the top quark may have an important role in understanding the mechanism of electroweak symmetry breaking. On top of this, the very short lifetime of the top quark makes it an excellent candidate to study the properties of a bare quark. Its high mass, almost 40 times higher than the mass of the closest fermion in mass, leads to a large coupling with the Higgs boson and makes the top quark an interesting candidate to investigate how particles acquire mass.

The CKM matrix element V_{tb}, given in Equation 1.15, is experimentally found to be much larger than V_{ts}, V_{td}, and close to unity. The top quark decays through electroweak interactions since the W boson mass is smaller than the top quark mass and the W boson can be on shell. A consequence of this is that the top quark has a very short lifetime of only $1/\Gamma_t \approx 5 \times 10^{-25}$ s [36] leading to the fact that the formation of bound states involving top quarks is not allowed. This lifetime is even shorter than the typical hadronisation timescale of $1/\Lambda_{QCD} \approx 10^{-23}$ s, prohibiting gluons to radiate from the top quark and keeping its spin coherent. Since the weak interactions have a vector-axial vector (V-A) coupling structure[4] , the top quark spin orientation can be derived from the angular distributions of its decay products. This makes it possible to study the polarisation of top quarks from the angular distributions in various processes.

The massiveness of the top quark leads to the fact that a large amount of energy is needed to create one. This is only the case for high energy collisions such as those happening in the Earth's upper atmosphere when cosmic rays collide with particles in air, or at particle

[4]In the SM a vector - axial vector coupling structure $\left(\gamma^\mu - \gamma^\mu\gamma^5\right)$ is predicted that only permits left-handed fermions or right-handed anti fermions to interact with a spin-1 particle.

accelerators. The production of top quarks happens in two ways: single via the electroweak interaction or in pairs via the strong interaction. At hadron colliders, pair production of top quarks dominates via gluon (gg→t$\bar{t}$) or quark fusion (q$\bar{q}$→ t$\bar{t}$). In Figure 1.1, the different top quark pair production mechanisms are shown. At the LHC, the production channel of gluon fusion is the main contributor to the top quark pair cross section compared to quark fusion at the Tevatron. The gg→t$\bar{t}$ process contributes 80-90% to the total top quark pair production cross section in the LHC centre-of-mass energy regime of 7-14 TeV [36]. In Table 1.5 the predicted top quark pair production cross sections are given for the LHC and the Tevatron, while in Figure **??**, a summary plot of the LHC and Tevatron top quark pair production cross section measurements as a function of the centre-of-mass energy can be found. These measurements are found to be in agreement with their SM predictions.

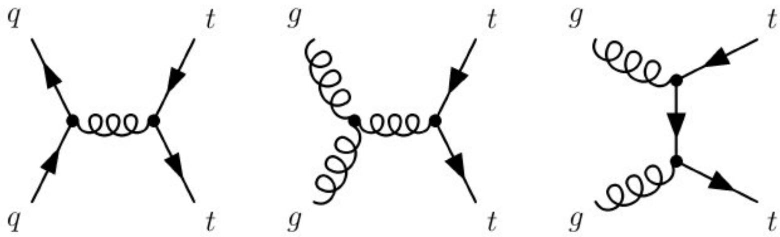

Figure 1.1: Leading order diagrams of the top quark pair production. Gluon fusion (right and middle) are the dominant processes at the LHC, while quark fusion (left) is the dominant one at the Tevatron.

Table 1.5: Predictions on the top quark pair production cross sections at next-to-next-to-leading order per centre-of-mass energy [36]. The first uncertainty is from scale dependence, while the second uncertainty originates from parton density functions.

Experiment	Top quark mass	Centre-of-mass energy	Cross section (pb)
Tevatron	$m_t = 173.3$ GeV	$\sqrt{s} = 1.96$ TeV	$\sigma_{t\bar{t}} = 7.16^{+0.11+0.17}_{-0.20-0.12}$
LHC	$m_t = 173.2$ GeV	$\sqrt{s} = 7$ TeV	$\sigma_{t\bar{t}} = 173.6^{+4.5+8.9}_{-5.9-8.9}$
LHC	$m_t = 173.2$ GeV	$\sqrt{s} = 8$ TeV	$\sigma_{t\bar{t}} = 247.7^{+6.3+11.5}_{-8.5-11.5}$
LHC	$m_t = 173.2$ GeV	$\sqrt{s} = 13$ TeV	$\sigma_{t\bar{t}} = 816.0^{+19.4+34.4}_{-28.6-34.4}$

The singly produced top quarks are produced via the electroweak interaction. These production mechanisms are subdivided at leading order into three main channels based on the virtuality ($Q^2 = -p_\mu p^\mu$) of the exchanged W boson. In Figure 1.3, the corresponding Feynman diagrams are shown. The single top quark production cross sections, given in Table 1.6, are smaller than the top quark pair production cross sections since the electroweak coupling strength is smaller than the strong coupling strength. In addition, for the single top quark production, there is the need of sea quarks (b, $\bar{q}$) in the initial states for which the parton density functions increase less steeply at low momentum fractions compared to the gluon parton density functions.

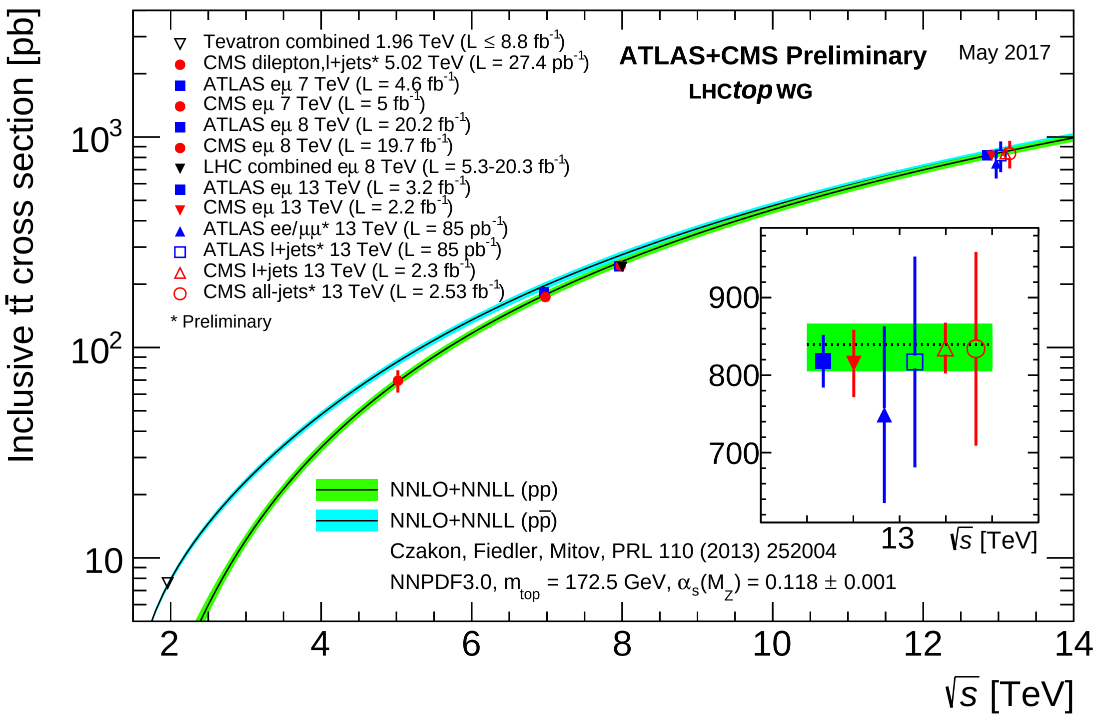

Figure 1.2: Summary of the LHC and the Tevatron measurements of the top quark pair production cross section as function of the centre-of-mass energy compared with the next-to-next-to-leading order QCD calculation. The theory bands are the uncertainties due to renormalization and factorisation scales, parton density functions and the strong coupling. The mass of the top quark is assumed to be 172.5 GeV. Measurements for the same centre-of-mass energy are slightly off-set for clarity. Figure taken from [47].

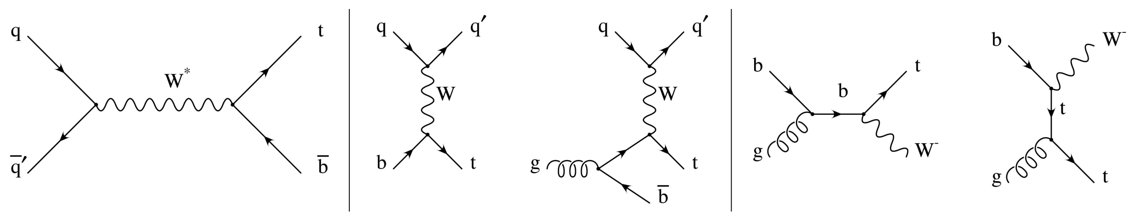

Figure 1.3: Leading order Feynman diagrams of the electroweak production of single top quarks in the *s*-channel (left), *t*-channel (middle), and for the tW associated production. Figure taken from [48].

The production via the t-channel has a virtuality of the W boson $Q^2 > 0$, making it space-like. It is produced via the scattering of the W boson of a bottom quark coming from a proton or from gluon splitting ($g \rightarrow b\bar{b}$). It has the highest single top quark cross section in proton collisions and the top quark production is roughly twice as large than the antitop quark. This is a consequence of the up-down valence quark composition of the proton. This feature makes the t-channel sensitive to the parton density functions of the proton. The s-channel is the production mechanism with the smallest cross section. Here the W boson is time-like ($Q^2 < 0$) which requires the W boson to have a large virtuality to produce the heavier top quark. It is produced from two quarks belonging to the same isodoublet (e.g. $u\bar{d}$) and subsequently decays to $t\bar{b}$. This process gets enhanced by many beyond the Standard Model scenarios via the addition of new heavy particles such as W'. The tW-channel has a top quark produced in association with a W boson produced on shell, $Q^2 = -m_W^2$. This mode is negligible at the Tevatron, but of relevant size at the LHC. The tW-channel is sensitive to new physics affecting the Wtb vertex. The single top quark production cross section measurements by the CMS collaboration can be found in Figure 1.4 and are not showing any significant deviations from their SM predictions.

Table 1.6: Predictions on the single top quark production cross sections at next-to-leading order per centre-of-mass energy [36]. The uncertainties from scale dependence and from parton density functions are combined in quadrature or given separately (scale + PDF). For the t-channel production at the LHC, the relative proportions to t and $\bar{t}$ are 65% and 35%. For the s-channel this is respectively 69% and 31%. At the Tevatron, the t-and s-channel cross sections are identical. The tW-channel has an equal proportion of top and antitop quarks at the LHC. For Tevatron, the top quark mass is assumed to be 173.3 GeV, while the LHC predictions use $m_t = 172.5$ GeV [36, 49].

Collider	Centre-of-mass energy	Cross section $\sigma_{t+\bar{t}}$ (pb)		
		t-channel	s-channel	tW-channel
Tevatron	$\sqrt{s} = 1.96$ TeV	$2.06^{+0.13}_{-0.13}$	$1.03^{+0.05}_{-0.05}$	–
LHC	$\sqrt{s} = 7$ TeV	$63.89^{+2.91}_{-2.52}$	$4.29^{+0.19}_{-0.17}$	$15.74^{+0.40+1.10}_{-0.40-1.14}$
LHC	$\sqrt{s} = 8$ TeV	$84.69^{+3.76}_{-3.23}$	$5.24^{+0.22}_{-0.20}$	$22.37^{+0.60+1.40}_{-0.60-1.40}$
LHC	$\sqrt{s} = 13$ TeV	$216.99^{+9.04}_{-7.71}$	$10.32^{+0.40}_{-0.36}$	$71.7^{+1.80+3.40}_{-1.80-3.40}$

1.5 Motivation for new physics

Many high energy experiments confirm the success of the SM. In particular the scalar boson, the cornerstone of the SM, has consecrated the theory. Unfortunately there are also strong indications that the SM ought to be a lower energy expression of a more global theory. The existence of physics beyond the SM (BSM) [51] is strongly motivated. These motivations are based on direct evidence from observation such as the existence of neutrino masses, the existence of dark matter and dark energy, or the matter-antimatter asymmetry, and also from theoretical problems such as the hierarchy problem, the coupling unification or the large numbers of free parameters in the SM.

In the SM, the neutrinos are assumed to be massless, while experiments with solar, atmospheric, reactor and accelerator neutrinos have established that neutrinos can oscillate and change flavour

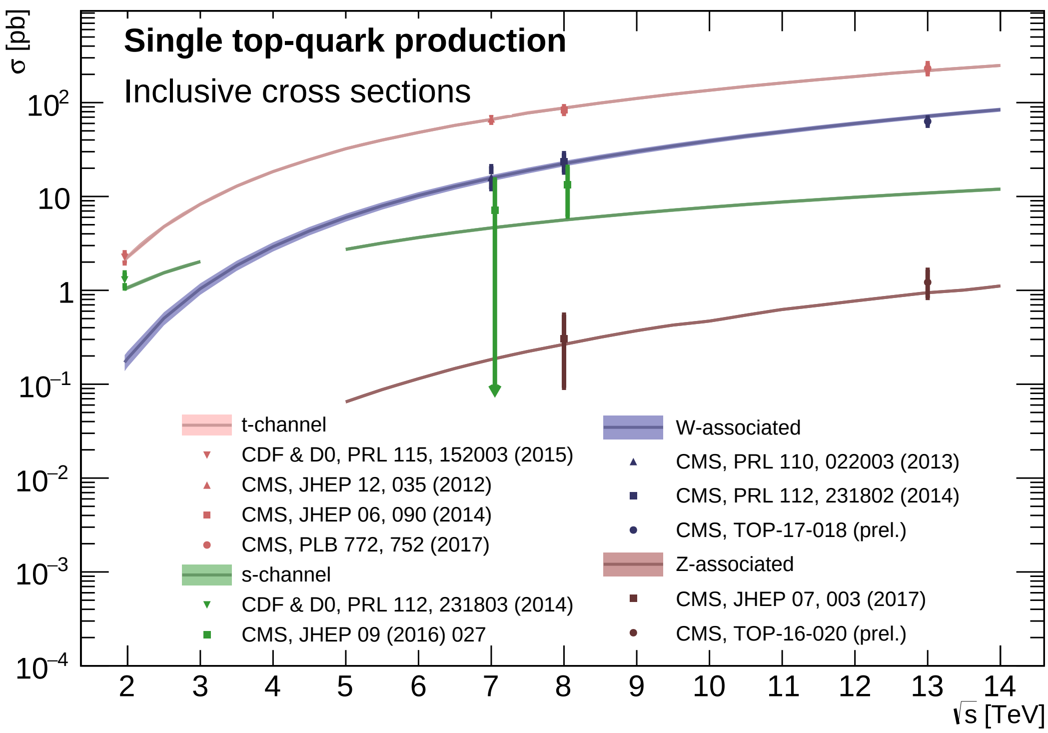

Figure 1.4: Summary of the measurements of the single top quark production cross section as function of the centre-of-mass energy. Figure taken from [50].

during flight [34, 35]. These oscillations are only possible when neutrinos have masses. The flavour neutrinos (ν_e, ν_μ, ν_τ) are then linear expressions of the fields of at least three mass eigenstate neutrinos ν_1, ν_2, and ν_3.

The ordinary or baryonic matter described by the SM describes only 5% of the mass and energy content of the universe. Astrophysical evidence indicated that dark matter is contributing to approximately 27% and dark energy to 68% of the content of the universe. From the measurements of the temperature and polarization anisotropies of the cosmic microwave background by the Planck experiment [52], the density of cold non baryonic matter is determined. Cold dark matter is assumed to be only sensitive to the weak and gravitational force, leading to only one possible SM candidate: the neutrino. However, the neutrinos are too light to account for the vast amount of dark matter and other models are needed. Dark energy is assumed to be responsible for the acceleration in the expansion of the universe [53].

At the Big Bang, matter and antimatter are assumed to be produced in equal quantities. However, it is clear that we are solely surrounded by matter. In 1967, Sakharov identified three mechanisms that are necessary to obtain a global matter antimatter asymmetry [54]. These mechanisms are those of baryon and lepton number violation, that at a given moment in time there was a thermal imbalance for the interactions in the universe, and there is charge C and charge parity CP violation[5].

The large number of free parameters in the SM comes from the nine fermion masses, three CKM mixing angles and one CP violating phase, one EM coupling constant g', one weak coupling constant g, one strong coupling constant g_s, one QCD vacuum angle, one vacuum expectation value, and one mass of the scalar boson. This large number of free parameters leads to the expectation of a more elegant and profound theory beyond the SM.

The hierarchy problem [55] is related to the huge difference in energy between the weak scale and the Planck scale. The vev of the Brout-Englert-Higgs field determines the weak scale that is approximately 246 GeV. The radiative corrections to the scalar boson squared mass m_{H}^2, coming from its self couplings and couplings to fermions and gauge bosons, are quadratically proportional to the ultraviolet momentum cut-off Λ_{UV}. This cut-off is at least equal to the energy to which the SM is valid without the need of new physics. For the SM to be valid up to the Planck mass, the correction to m_{H}^2 becomes thirty orders of magnitude larger than m_{H}^2. This implies that an extraordinary cancellation of terms should happen. This is also known as the naturalness problem of the H boson mass.

The correction to the squared mass of the scalar boson coming from a fermion f, coupling to the scalar field ϕ with a coupling λ_{f} is given by

$$\Delta m_{\mathrm{H}}^2 = -\frac{|\lambda_{\mathrm{f}}|^2}{8\pi^2}\Lambda_{\mathrm{UV}}^2, \tag{1.18}$$

while the correction to the mass from a scalar particle S with a mass m_{S}, coupling to the scalar field with a Lagrangian term $-\lambda_{\mathrm{S}}|\phi|^2|\mathrm{S}|^2$ is

$$\Delta m_{\mathrm{H}}^2 = \frac{|\lambda_{\mathrm{S}}|^2}{16\pi^2}\left(\Lambda_{\mathrm{UV}}^2 - 2m_{\mathrm{S}}^2 \ln\left(\frac{\Lambda_{\mathrm{UV}}}{m_{\mathrm{S}}}\right) + ...\right). \tag{1.19}$$

As one can see the correction term to m_{H}^2 is in both cases much larger than m_{H}^2 itself. By introducing BSM physics models that introduce new scalar particles at the TeV scale that couple to the scalar boson, one can cancel the Λ_{UV}^2 divergence and avoid this fine-tuning.

The choice of the $\mathrm{SU(3)_C \times SU(2)_L \times U(1)_Y}$ symmetry group itself as well as the separate treatment of the three forces included in the SM raises concern. The intensity of the forces shows a large disparity around the electroweak scale, but have comparable strengths at higher energies. The electromagnetic and weak forces are unified in a electroweak interaction, but the strong coupling constant does not encounter the other coupling constants at high energies. In order to reach a grand unification, the running of couplings can be modified by the addition of new particles in BSM models.

[5] The rate of a process $i \to f$ can be different from the CP-conjugate process: $\tilde{i} \to \tilde{f}$. The SM includes sources of CP-violation through the residual phase of the CKM matrix. However, these could not account for the magnitude of the asymmetry observed.

1.6 An effective approach beyond the SM: FCNC involving a top quark

The closeness of the top quark mass to the electroweak scale led physicists to believe that the top quark is a sensitive probe for new physics. Studying its properties is therefore an important topic of the experimental program at the LHC. Several extensions of the SM enhance the top quark FCNC branching fractions and can be probed at the LHC [23], for which a selection is shown in Table 1.7. Previous searches have been performed at the Tevatron by the CDF [24] and D0 [25] collaborations, and at the LHC by the ATLAS [26, 27, 56–58] and CMS [28–30, 59, 60] collaborations.

Table 1.7: The predicted branching fractions $\mathscr{B}$ for FCNC interactions involving the top quark in some BSM models [23]: quark singlet (QS), generic two Higgs doublet model (2HDM) and the minimal supersymmetric extensions to the SM (MSSM).

Process	QS	2HDM	MSSM
$t \to uZ$	$\leq 1.1 \times 10^{-4}$	–	$\leq 2 \times 10^{-6}$
$t \to u\gamma$	$\leq 7.5 \times 10^{-9}$	–	$\leq 2 \times 10^{-6}$
$t \to ug$	$\leq 1.5 \times 10^{-7}$	–	$\leq 8 \times 10^{-5}$
$t \to uH$	$\leq 4.1 \times 10^{-5}$	$\leq 5.5\ 10^{-6}$	$\leq 10^{-5}$
$t \to cZ$	$\leq 1.1 \times 10^{-4}$	$\leq 10^{-7}$	$\leq 2 \times 10^{-6}$
$t \to c\gamma$	$\leq 7.5 \times 10^{-9}$	$\leq 10^{-6}$	$\leq 2 \times 10^{-6}$
$t \to cg$	$\leq 1.5 \times 10^{-7}$	$\leq 10^{-4}$	$\leq 8 \times 10^{-5}$
$t \to cH$	$\leq 4.1 \times 10^{-5}$	$\leq 10^{-3}$	$\leq 10^{-5}$

The impact of BSM models can be written in a model independent way by means of an effective field theory valid up to an energy scale Λ. The basis of such theories is that problems can be simplified if one looks at the relevant scale of the process that one wants to investigate. For example, the chemical properties of a hydrogen atom can be described without any knowledge of quark interactions inside the proton. In this case, the proton can be considered the elementary object (indivisible) due to the fact that the binding energy of the constituents is much bigger than the energy of the electron in orbit around the proton. Effective field theories are based on this kind of separation of different energy scales in a system [61]. These theories can be used for theories where the perturbative expansion cannot be trusted, e.g. QCD at low energy, or as bottom up approach to look for new physics in a model independent way. The latter is the way effective field theory will be used throughout this thesis.

The SM can be seen as an effective theory applicable up to energies not exceeding a scale Λ. Therefore, remnants should still be valid and the theory above that scale should have a gauge group containing $SU(3)_C \times SU(2)_L \times U(1)_Y$ and all the SM degrees of freedom, as well as reduce to the SM at lower energies. The general SM Lagrangian becomes then

$$\mathscr{L}_{SM+EFT} = \mathscr{L}_{SM}^{(4)} + \sum_i \frac{\bar{c}_i^{(5)}}{\Lambda} Q_i^{(5)} + \sum_i \frac{\bar{c}_i^{(6)}}{\Lambda^2} Q_i^{(6)} + \mathscr{O}\left(\frac{1}{\Lambda^3}\right), \tag{1.20}$$

where $Q_i^{(n)}$ are dimension-n operators (currents) and $\bar{c}_i^{(n)}$ the corresponding dimensionless coupling constants, so-called Wilson coefficients. The Wilson coefficients are determined by the underlying high energy theory.

In the Warsaw basis [62], a set of independent operators of dimension 5 and 6 are built out of the SM fields and are consistent with the SM gauge symmetries and is fully derived in Ref. [62]. In general the various measurements show a good agreement with the SM predictions and by lack of deviations from the SM, limits on the anomalous couplings can be derived. The estimated coupling strengths per operator contributing to single top quark production obtained from various measurements at the LHC and Tevatron are shown in Figure 1.5 for which the conventions are discussed in Ref. [63]. These results are consistent with the SM expectation for which those operators vanish.

For simplicity, the assumption is made that new physics effects are exclusively described by dimension-6 operators, thus neglecting neutrino physics which are described by dimension-5 operators. In the fully gauge symmetric case, the EFT Lagrangian is then given by

$$\mathscr{L}_{\mathrm{SM+EFT}} = \mathscr{L}_{\mathrm{SM}} + \sum_i \frac{\bar{c}_i}{\Lambda^2} O_i + \mathscr{O}\left(\frac{1}{\Lambda^3}\right), \tag{1.21}$$

where the Wilson coefficients $\bar{c}_i$ depend on the considered theory and on the way that new physics couples to the SM particles. Taking into account that Λ is large, contributions suppressed by powers of Λ greater than two are neglected. Additionally, all four fermion operators are omitted for the rest of this thesis. The Warsaw basis is adopted for the independent effective operators [62], parametrising the new physics effects relevant for the flavour changing neutral current interactions of the top quark as,

$$\begin{aligned}\mathscr{L}^{\mathrm{t}}_{\mathrm{EFT}} = &\frac{\bar{c}_{uG}}{\Lambda^2}\Phi^\dagger\cdot\left[\bar{Q}_{\mathrm{L}}\sigma^{\mu\nu}\mathscr{T}_a u_{\mathrm{R}}\right]G^a_{\mu\nu} + \frac{\bar{c}_{uB}}{\Lambda^2}\Phi^\dagger\cdot\left[\bar{Q}_{\mathrm{L}}\sigma^{\mu\nu}u_{\mathrm{R}}\right]B_{\mu\nu} + \frac{2\bar{c}_{uW}}{\Lambda^2}\Phi^\dagger T_i\cdot\left[\bar{Q}_{\mathrm{L}}\sigma^{\mu\nu}u_{\mathrm{R}}\right]W^i_{\mu\nu}\\ &+ i\frac{\bar{c}_{hu}}{\Lambda^2}\left[\Phi^\dagger \overleftrightarrow{D}_\mu \Phi\right]\left[\bar{u}_{\mathrm{R}}\gamma^\mu u_{\mathrm{R}}\right] + i\frac{\bar{c}^{(1)}_{hq}}{\Lambda^2}\left[\Phi^\dagger \overleftrightarrow{D}_\mu \Phi\right]\left[\bar{Q}_{\mathrm{L}}\gamma^\mu Q_{\mathrm{L}}\right]\\ &+ i\frac{4\bar{c}^{(3)}_{hq}}{\Lambda^2}\left[\Phi^\dagger T_i \overleftrightarrow{D}_\mu \Phi\right]\left[\bar{Q}_{\mathrm{L}}\gamma^\mu T^i Q_{\mathrm{L}}\right] + \frac{\bar{c}_{uh}}{\Lambda^2}\Phi^\dagger\Phi\,\Phi^\dagger\cdot\left[\bar{Q}_{\mathrm{L}}u_{\mathrm{R}}\right] + \mathrm{h.c.}\,,\end{aligned} \tag{1.22}$$

with all flavour indices implied and $\sigma^{\mu\nu}$ is equal to $\frac{i}{2}\left[\gamma^\mu,\gamma^\nu\right]$. The left handed $\mathrm{SU(2)_L}$ doublet of the quark fields is denoted by Q_{L}, the up-type right handed fields by u_{R}, the $\mathrm{SU(2)_L}$ doublet of the Higgs field by Φ, the field strength tensors as

$$\begin{aligned}B_{\mu\nu} &= \partial_\mu B_\nu - \partial_\nu B_\mu,\\ W^k_{\mu\nu} &= \partial_\mu W^k_\nu - \partial_\nu W^k_\mu + g\epsilon^k_{ij}W^i_\mu W^j_\nu,\\ G^a_{\mu\nu} &= \partial_\mu G^a_\nu - \partial_\nu G^a_\mu + g_s f^a_{bc}G^b_\mu G^c_\nu,\end{aligned} \tag{1.23}$$

denoting the structure constant of the $\mathrm{SU(3)_C}$ group as f^a_{bc} and the structure constant of the $\mathrm{SU(2)_L}$ group as ϵ^k_{ij}. The gauge covariant derivatives are defined as

$$D_\mu\Phi = \partial_\mu\Phi - \frac{1}{2}ig'B_\mu\Phi - igT_k W^k_\mu\Phi \tag{1.24}$$

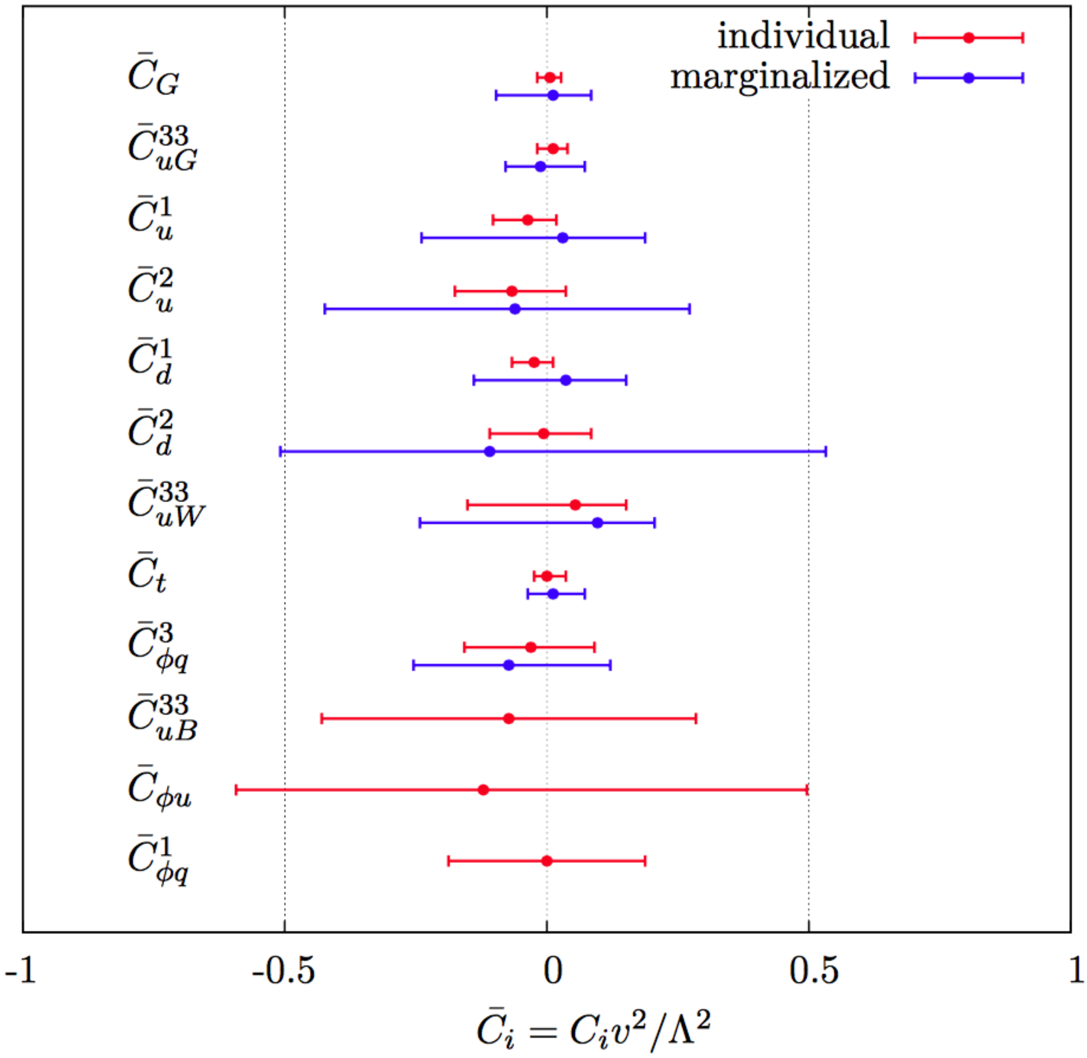

Figure 1.5: Global fit results of top quark effective field theory to experimental data including all constrained operators at dimension six. For the operators, the Warsaw basis of [62] is used. The bounds are set on the coefficients described in [64] of various operators contributing to top quark production and decay in two cases (red) all other coefficients set to zero, or (blue) all other coefficients are marginalised over. Figure taken from [64].

with the conventions of Section 1.2. The representation matrices T of $SU(2)_L$ are defined in Equation 1.1 and are half the Pauli matrices, while the representation matrices $\mathscr{T}$ of $SU(3)_C$ are the Gell-Mann matrices [31]. The hermitian derivative operator is defined as

$$\Phi^\dagger \overleftrightarrow{D} \Phi = \Phi^\dagger D^\mu \Phi - D_\mu \Phi^\dagger \Phi. \tag{1.25}$$

After electroweak symmetry breaking, the operators induce [23, 65] both corrections to the SM couplings and new interactions at tree level such as FCNC interactions. The Lagrangian of Equation 1.22 can then equivalently be written as

$$\begin{aligned}\mathscr{L}^{\mathrm{t}}_{\mathrm{EFT}} = \frac{\sqrt{2}}{2} \sum_{\mathrm{q=u,c}} \Big[& g' \frac{\kappa_{\mathrm{t\gamma q}}}{\Lambda} \mathrm{A}_{\mu\nu} \bar{\mathrm{t}} \sigma^{\mu\nu} \left(f^{\mathrm{L}}_{\mathrm{\gamma q}} P_{\mathrm{L}} + f^{\mathrm{R}}_{\mathrm{\gamma q}} P_{\mathrm{R}} \right) \mathrm{q} \\ & + \frac{g}{2\cos\theta_{\mathrm{W}}} \frac{\kappa_{\mathrm{tZq}}}{\Lambda} \mathrm{Z}_{\mu\nu} \bar{\mathrm{t}} \sigma^{\mu\nu} \left(f^{\mathrm{L}}_{\mathrm{Zq}} P_{\mathrm{L}} + f^{\mathrm{R}}_{\mathrm{Zq}} P_{\mathrm{R}} \right) \mathrm{q} \\ & + \frac{\sqrt{2} g}{4\cos\theta_{\mathrm{W}}} \zeta_{\mathrm{tZq}} \bar{\mathrm{t}} \gamma^{\mu} \left(\tilde{f}^{\mathrm{L}}_{\mathrm{q}} P_{\mathrm{L}} + \tilde{f}^{\mathrm{R}}_{\mathrm{q}} P_{\mathrm{R}} \right) \mathrm{q} \mathrm{Z}_{\mu} \\ & + g_{\mathrm{s}} \frac{\kappa_{\mathrm{tgq}}}{\Lambda} \bar{\mathrm{t}} \sigma^{\mu\nu} \mathscr{T}_{\mathrm{a}} \left(f^{\mathrm{L}}_{\mathrm{gq}} P_{\mathrm{L}} + f^{\mathrm{R}}_{\mathrm{gq}} P_{\mathrm{R}} \right) \mathrm{q} \mathrm{G}^{\mathrm{a}}_{\mu\nu} \\ & + \eta_{\mathrm{Hqt}} \bar{\mathrm{t}} \left(\hat{f}^{\mathrm{L}}_{\mathrm{q}} P_{\mathrm{L}} + \hat{f}^{\mathrm{R}}_{\mathrm{q}} P_{\mathrm{R}} \right) \mathrm{q} \mathrm{H} + \mathrm{h.c.} \Big],\end{aligned} \tag{1.26}$$

which gives the FCNC interactions of the top quark that are not present in the SM. The value of the FCNC couplings at scale Λ are represented by κ_{tZq}, κ_{tgq}, $\kappa_{\mathrm{t\gamma q}}$, ζ_{tZq}, and η_{Hqt}. These are assumed to be real and positive, with the unit of GeV^{-1} for $\kappa_{\mathrm{tXq}}/\Lambda$ and no unit for ζ_{xqt} and η_{xqt}. In the equation, the left- and right-handed chirality projector operators are denoted by P_{L} and P_{R}. The complex chiral parameters are normalized according to $|f^{\mathrm{L}}_{\mathrm{xq}}|^2 + |f^{\mathrm{R}}_{\mathrm{xq}}|^2 = 1$, $|\tilde{f}^{\mathrm{L}}_{\mathrm{q}}|^2 + |\tilde{f}^{\mathrm{R}}_{\mathrm{q}}|^2 = 1$, and $|\hat{f}^{\mathrm{L}}_{\mathrm{q}}|^2 + |\hat{f}^{\mathrm{R}}_{\mathrm{q}}|^2 = 1$. In the expression for $\mathscr{L}^{\mathrm{t}}_{\mathrm{EFT}}$, the unitary gauge is adopted and the scalar field is expanded around its vacuum expectation value v with H being the SM Higgs boson. The field strength tensors of the photon A_μ, the gluon field $\mathrm{G}^{1\ldots8}_\mu$, and the Z boson Z^0_μ are defined as

$$\begin{aligned}\mathrm{A}_{\mu\nu} &= \partial_\mu \mathrm{A}_\nu - \partial_\nu \mathrm{A}_\mu, \\ \mathrm{Z}_{\mu\nu} &= \partial_\mu \mathrm{Z}_\nu - \partial_\nu \mathrm{Z}_\mu, \text{ and} \\ \mathrm{G}^{\mathrm{a}}_{\mu\nu} &= \partial_\mu \mathrm{G}^{\mathrm{a}}_\nu - \partial_\nu \mathrm{G}^{\mathrm{a}}_\mu + g_{\mathrm{s}} f^{\mathrm{a}}_{\mathrm{bc}} \mathrm{G}^{\mathrm{b}}_\mu \mathrm{G}^{\mathrm{c}}_\nu.\end{aligned} \tag{1.27}$$

The relations between the Wilson coefficients in Equation 1.22 and the coupling strengths of the interactions in Equation 1.26 can be derived. The 14 effective operators are mapped onto 10 free parameters providing a more minimal parametrisation of the anomalous interactions of the top quark:

$$\begin{aligned}
\kappa_{\mathrm{tgq}} f^{\mathrm{L}}_{\mathrm{gq}} &= \tfrac{v}{g_{\mathrm{s}}\Lambda} \left[\bar{c}_{uG}\right]^*_{i3}, & \kappa_{\mathrm{tgq}} f^{\mathrm{R}}_{\mathrm{gq}} &= \tfrac{v}{g_{\mathrm{s}}\Lambda} \left[\bar{c}_{uG}\right]_{3i}, \\
\kappa_{\mathrm{t\gamma q}} f^{\mathrm{L}}_{\mathrm{\gamma q}} &= \tfrac{v}{g'\Lambda} \left[\cos\theta_{\mathrm{W}} \bar{c}_{uB} - \sin\theta_{\mathrm{W}} \bar{c}_{uW}\right]^*_{i3}, & \kappa_{\mathrm{t\gamma q}} f^{\mathrm{R}}_{\mathrm{\gamma q}} &= \tfrac{v}{g'\Lambda} \left[\sin\theta_{\mathrm{W}} \bar{c}_{uB} - \cos\theta_{\mathrm{W}} \bar{c}_{uW}\right]_{3i}, \\
\kappa_{\mathrm{tZq}} f^{\mathrm{L}}_{\mathrm{Zq}} &= -\tfrac{2\cos\theta_{\mathrm{W}} v}{g\Lambda} \left[\sin\theta_{\mathrm{W}} \bar{c}_{uB} + \cos\theta_{\mathrm{W}} \bar{c}_{uW}\right]^*_{i3}, & \kappa_{\mathrm{tZq}} f^{\mathrm{R}}_{\mathrm{Zq}} &= -\tfrac{2\cos\theta_{\mathrm{W}} v}{g\Lambda} \left[\cos\theta_{\mathrm{W}} \bar{c}_{uB} + \sin\theta_{\mathrm{W}} \bar{c}_{uW}\right]_{3i}, \\
\zeta_{\mathrm{tZq}} \tilde{f}^{\mathrm{L}}_{\mathrm{Zq}} &= -\tfrac{2v^2}{\Lambda^2} \left[\left(\bar{c}^{(1)}_{hq} - \bar{c}^{(3)}_{hq}\right)_{i3} + \left(\bar{c}^{(1)}_{hq} - \bar{c}^{(3)}_{hq}\right)^*_{3i}\right], & \zeta_{\mathrm{tZq}} \tilde{f}^{\mathrm{R}}_{\mathrm{Zq}} &= -\tfrac{2v^2}{\Lambda^2} \left[(\bar{c}_{hu})_{i3} + (\bar{c}_{hu})^*_{3i}\right], \\
\eta_{\mathrm{tHq}} \hat{f}^{\mathrm{L}}_{\mathrm{Hq}} &= \tfrac{3v^2}{2\Lambda^2} \left[\bar{c}_{uh}\right]^*_{3i}, & \eta_{\mathrm{tHq}} \hat{f}^{\mathrm{R}}_{\mathrm{Hq}} &= \tfrac{3v^2}{2\Lambda^2} \left[\bar{c}_{uh}\right]_{i3}.
\end{aligned}$$

(1.28)

1.7 Experimental constraints on top-FCNC

Experimental particle physicists commonly put limits on the branching fractions which allow an easier interpretation across different EFT models. The branching fraction takes a value between zero and one and is defined as

$$\mathscr{B}(\mathrm{t} \to \mathrm{qX}) = \frac{\delta^2_{\mathrm{tXq}} \Gamma_{\mathrm{t}\to\mathrm{qX}}}{\Gamma_{\mathrm{t}}}, \tag{1.29}$$

where $\Gamma_{\mathrm{t}\to\mathrm{qX}}$ represents the FCNC decay width[6] for a coupling strength $\delta^2_{\mathrm{tXq}} = 1$, and Γ_{t} the full decay width of the top quark. In the SM, supposing a top quark mass of 172.5 GeV, the full width becomes $\Gamma^{\mathrm{SM}}_{\mathrm{t}} = 1.32$ GeV [66].

Searches for top-FCNC usually adopt a search strategy depending on the experimental set-up and the FCNC interaction of interest, looking either for FCNC interactions in the production of a single top quark or in its decay for top quark pair interactions. In Figure 1.6, these two cases are shown for the tZq vertex.

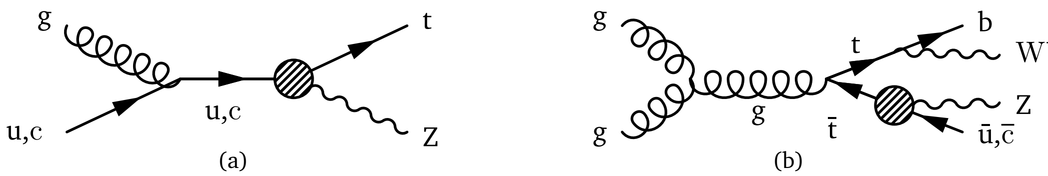

Figure 1.6: Feynman diagrams for the processes with a tZq FCNC interaction, where the FCNC interaction is indicated with the shaded dot. (a) Single top quark production through an FCNC interaction. (b) Top quark pair production with an FCNC induced decay.

The observation of top-FCNC interactions has yet to come and experiments have so far only been able to put upper bounds on the branching fractions. An overview of the best current limits is given in Table 1.8. In Figure 1.7 a comparison is shown between the current best limits set by ATLAS and CMS with respect to several BSM model benchmark predictions. From there one can see that FCNC searches involving a Z or H boson are close to excluding or confirming several BSM theories. In Figure 1.8, the searches performed by CMS are summarised. For the tZq vertex, the current most stringent limit is set by the ATLAS collaboration at a centre-of-mass energy of 13 TeV [58]. The observed (expected) limits at 95% CL are $\mathscr{B}(\mathrm{t} \to \mathrm{uZ}) < 1.7 \times 10^{-4}$ (2.4×10^{-4}) and $\mathscr{B}(\mathrm{t} \to \mathrm{cZ}) < 2.3 \times 10^{-4}$ (3.2×10^{-4}). The most stringent limit from the CMS collaboration comes from Ref. [28] where both single top quark and top quark pair processes are studied. The observed (expected) limits at 95% CL for a centre-of-mass energy of 8 TeV for the FCNC tZq interaction by CMS are $\mathscr{B}(\mathrm{t} \to \mathrm{uZ}) < 2.2 \times 10^{-4}$ (2.7×10^{-4}) and $\mathscr{B}(\mathrm{t} \to \mathrm{cZ}) < 4.9 \times 10^{-4}$ (12×10^{-4}). In Figure 1.9, the summary of the 95% confidence

[6] The decay width of a certain process represents the probability per unit time that a particle will decay. The total decay width, defined as the sum of all possible decay widths of a particle, is inversely proportional to its lifetime.

level observed limits on the branching fractions of the top quark decays to a charm or up quark and a neutral boson is given, considering the results from the HERA, the LEP, the Tevatron, and the LHC.

Table 1.8: Overview of the most stringent observed and expected experimental limits on top-FCNC branching fractions $\mathscr{B}$ at 95% confidence level.

Process	Search mode	Observed $\mathscr{B}$	Expected $\mathscr{B}$	Experiment	
$t \rightarrow uZ$	top quark pair decay	1.7×10^{-4}	2.4×10^{-4}	ATLAS	[58]
$t \rightarrow u\gamma$	single top quark production	1.3×10^{-4}	1.9×10^{-4}	CMS	[30]
$t \rightarrow ug$	single top quark production	2.0×10^{-5}	2.8×10^{-5}	CMS	[67]
$t \rightarrow uH$	top quark pair decay	2.4×10^{-3}	1.7×10^{-3}	ATLAS	[57]
$t \rightarrow cZ$	top quark pair decay	2.3×10^{-4}	3.2×10^{-4}	ATLAS	[58]
$t \rightarrow c\gamma$	single top quark production	2.0×10^{-3}	1.7×10^{-3}	CMS	[30]
$t \rightarrow cg$	single top quark production	2.0×10^{-4}	1.8×10^{-4}	ATLAS	[27]
$t \rightarrow cH$	top quark pair decay	2.2×10^{-3}	1.6×10^{-3}	ATLAS	[57]

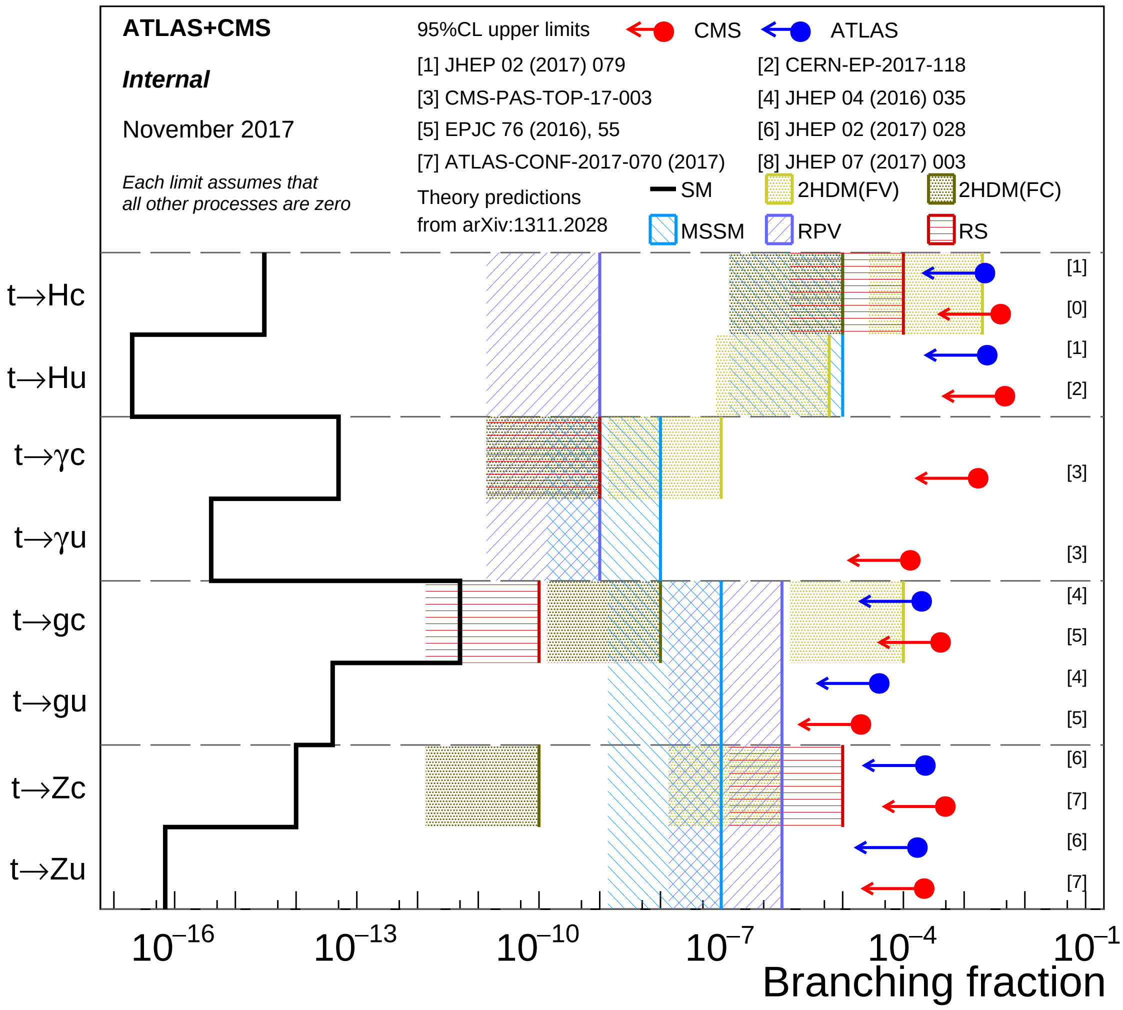

Figure 1.7: Current best limits at 95% confidence level on the branching fractions set by CMS and ATLAS for top-FCNC interactions. Figure adapted from [50].

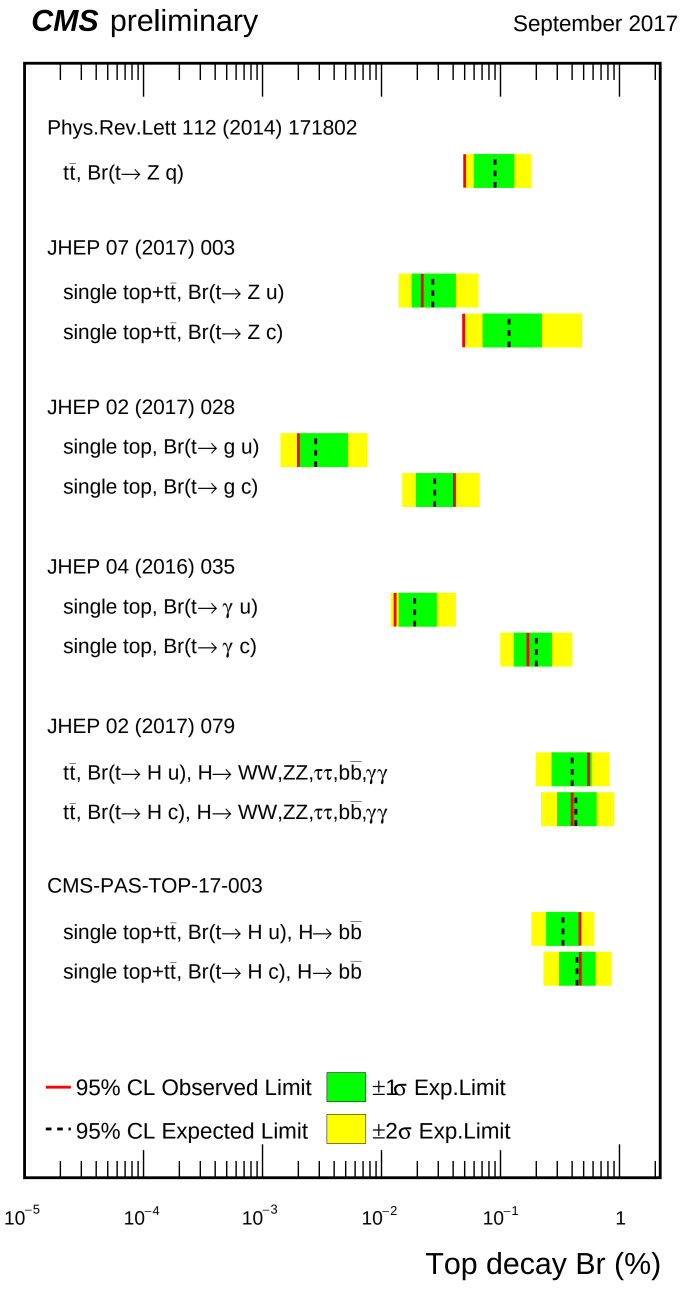

Figure 1.8: Summary of the FCNC branching fractions from CMS searches at a centre-of-mass energy of 8 TeV. Figure taken from [50].

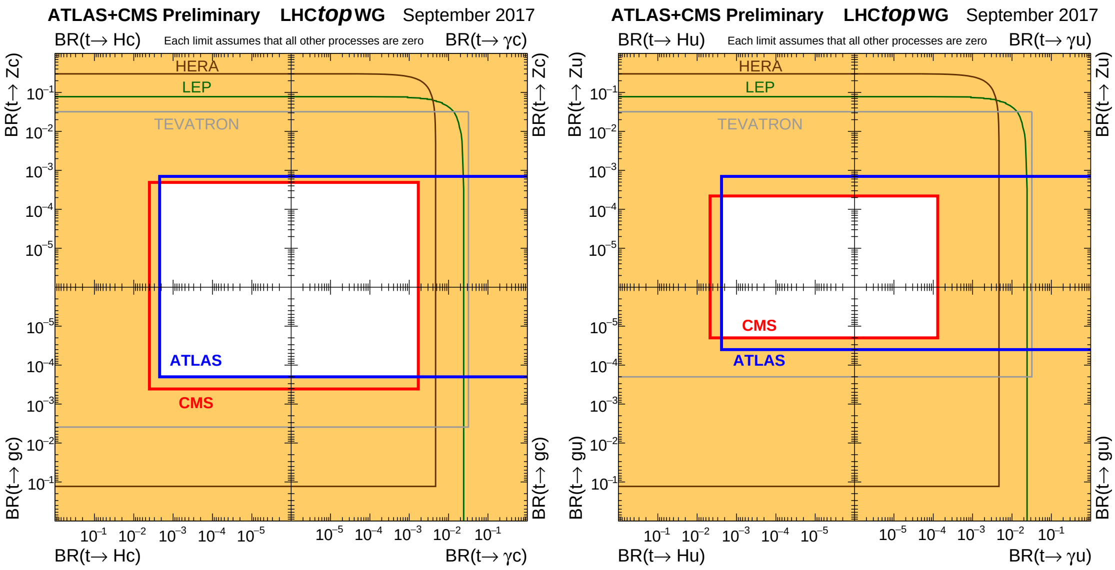

Figure 1.9: Summary of the current 95% confidence level observed limits on the branching fractions of the top quark decays via flavour changing neutral currents to a charm (left) or up (right) quark and a neutral boson. The coloured lines represent the results from HERA (the most stringent limits between the ones obtained by the H1 and ZEUS collaborations, in brown), LEP (combined ALEPH, DELPHI, L3 and OPAL collaborations result, in green), TEVATRON (the most stringent limits between the ones obtained by the CDF and D0 collaborations, in grey). The yellow area represents the region excluded by the ATLAS and the CMS Collaborations. Figure taken from [47].

Experimental set-up 2

A key objective of the Large Hadron Collider (LHC) was the search for the Brout-Englert-Higgs boson. The Large Electron Positron (LEP) [68] and Tevatron [69] experiments established that the mass of the scalar boson had to be larger than 114 GeV [70, 71], and smaller than approximate 1 TeV due to unitarity and perturbativity constraints [72]. On top of this, the search for new physics such as supersymmetry or the understanding of dark matter were part of the motivation for building the LHC. Since the start of its operation, the LHC is pushing the boundaries of the Standard Model, putting the most stringent limits on physics beyond the Standard Model as well as precision measurements of the parameters of the Standard Model. A milestone of the LHC is the discovery of the scalar boson in 2012 by the two largest experiments at the LHC [40, 41].

This chapter is dedicated to the experimental set-up of the LHC and the Compact Muon Solenoid (CMS) experiment. Section 2.1 describes the LHC and its acceleration process for protons to reach their design energies. The CMS experiment and its components are presented in Section 2.2. The upgrades performed during the long shutdown in 2013 are discussed in Section 2.2.4. The data acquisition of CMS is presented in Section 2.2.3, while the CMS computing model is shown in Section 2.2.5.

2.1 The Large Hadron Collider

The LHC has started its era of cutting edge science on 10 September 2008 [73] after approval by the European Organisation of Nuclear Research (CERN) in 1995 [74]. Installed in the previous LEP tunnel, the LHC consists of a 26.7 km quasi ring, that is installed between 45 and 170 m under the French-Swiss border amidst Cessy (France) and Meyrin (Switzerland). Built to study rare physics phenomena at high energies, the LHC can accelerate mainly two types of particles, protons and lead ions Pb^{45+}, and provides collisions at four interaction points, where the particle bunches are crossing. Experiments for studying the collisions are installed at each interaction point.

As can be seen in Figure 2.1, the LHC is the last element in a chain that creates, injects and accelerates protons. The starting point is the ionisation of hydrogen, creating protons that are injected in a linear accelerator (LINAC 2). Here, the protons obtain an energy of 50 MeV. They continue to the Proton Synchrotron Booster (PSB or Booster), where the packs of protons are accelerated to 1.4 GeV and each pack is split up in twelve bunches with 25 or 50 ns spacing. The Proton Synchrotron (PS) then increases their energy to 25 GeV before the Super Proton Synchrotron (SPS) increases the proton energy up to 450 GeV. Each accelerator ring expands in radius in order to reduce the energy loss of the protons by synchrotron radiation[1]. Furthermore, the magnets responsible for the bending of the proton trajectories have to be strong enough to sustain the higher proton energy. Ultimately, the proton bunches are injected into opposite directions into the LHC, where they are accelerated to 3.5 TeV (in 2010 and 2011), 4 TeV (in 2012 and 2013) or 6.5 TeV (in 2015-2017) [75].

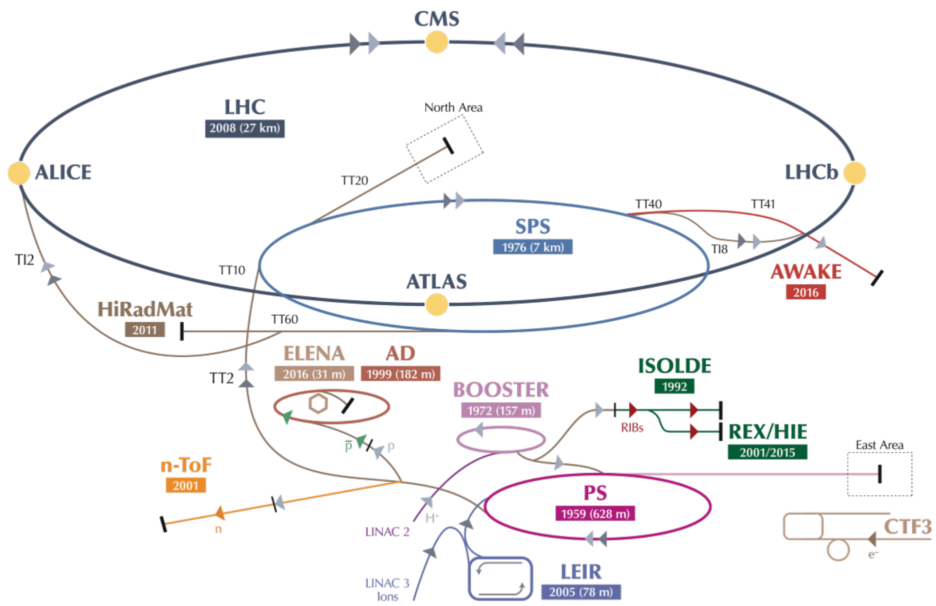

Figure 2.1: Schematic representation of the accelerator complex at CERN [76]. The LHC (dark blue) is the last element in chain of accelerators. Protons are successively accelerated by LINAC 2, the Booster, the Proton Synchrotron (PS) and the Super Proton Synchrotron (SPS) before entering the LHC.

In Figure 2.2 the LHC programme is shown. the first data collisions, so-called Run 1 period, lasted from 2008 until 16 February 2013 after which the CERN accelerator complex shut down for two years of planned maintenance and consolidation during so-called long shutdown 1 (LS1). On 23 March 2015, the new data taking period known as Run 2 started. There was a brief end of the year extended technical stop (EYETS) at the end of 2016. The main activities carried out during the EYETS were the maintenance of systems such as the cryogenics, the cooling, electrical systems, as well as a de-cabling and cabling campaign on the SPS [77]. Run 2 will last until July 2018 when the long shutdown 2 (LS2) will begin for 2 years. The main goal of this shutdown is the LHC injectors upgrade (LIU), but also maintenance and consolidation will be performed. Furthermore, preparations for the High Luminosity LHC (HL-LHC), which

[1]This energy loss is proportional to the fourth power of the proton energy and inversely proportional to the bending radius.

will start in 2024, will be done. More information about phase 1 upgrades during the LS1 and the EYETS in 2016 for CMS is given in Section 2.2.4.
Before the start of the LHC in 2010, the previous energy record was held by the Tevatron collider at Fermilab, colliding protons with antiprotons at $\sqrt{s}$ = 1.96 TeV. When completely filled, the LHC nominally contains 2220 bunches in Run 2, compared to 1380 in Run 1.

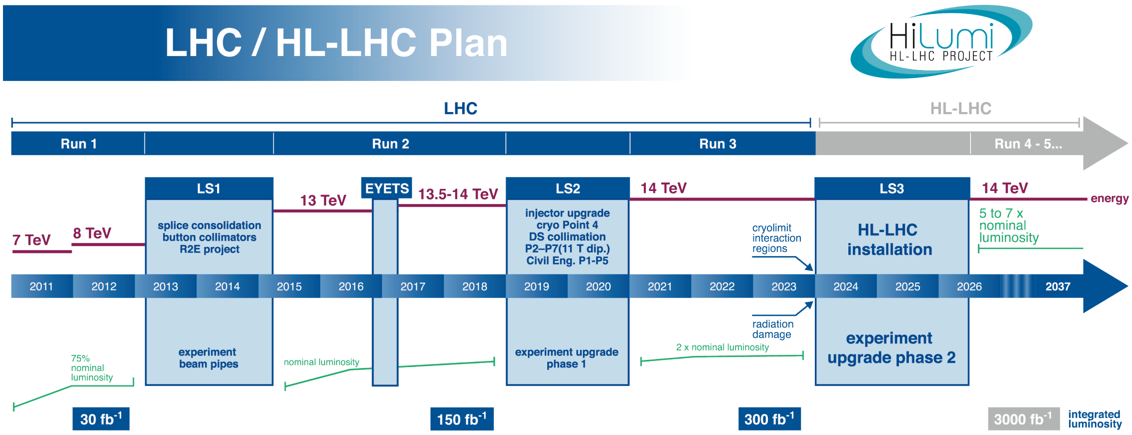

Figure 2.2: The HL-LHC timeline. Figure taken from [78].

Inside the LHC ring [79], the protons are accelerated by means of radio frequency cavities, while 1232 dipole magnets of approximately 15 m long, each weighing 35 t ensure the deflection of the beams. The two proton beams circulate in opposite direction in separate pipes inside of the magnet. Through the use of a strong electric current in the coils of the magnet, magnetic fields are generated and cause the protons to bend in the required orbits. In order for the coil to become superconducting and able to produce a strong magnetic field of 8.3 T, the magnet structure is surrounded by a vessel. This vessel is filled with liquid Helium making it possible to cool down the magnet to 1.9 K. In order to get more focussed and stabilised proton beams, additional higher-order multipole and corrector magnets are placed along the LHC beam line.

The LHC is home to seven experiments, each located at an interaction point:

- A Toroidal LHC ApparatuS (ATLAS) [80] and the Compact Muon Solenoid (CMS) [81] experiments are the two general purpose detectors at the LHC. They both have a hermetic, cylindrical structure and were designed to search for new physics phenomena along with precision measurements of the Standard Model. The existence of two distinct experiments allows cross-confirmation of any discovery.
- A Large Ion Collider Experiment (ALICE) [82] and the LHC Beauty (LHCb) [83] experiments are focusing on specific phenomena. ALICE studies strongly interacting matter at extreme energy densities where a quark-gluon plasma forms in heavy ion collisions (Pb-Pb or p-Pb). LHCb searches for differences between matter and antimatter with the focus on b quark physics.

- The forward LHC (LHCf) [84] and the TOTal cross section, Elastic scattering and diffraction dissociation Measurement (TOTEM) [85] experiments are two smaller experiments that focus on head-on collisions. LHCf consists of two parts placed before and after ATLAS and studies particles created at very small angles. TOTEM is placed in the same cavern as CMS and measures the total proton-proton cross section and studies elastic and diffractive scattering.
- The Monopoles and Exotics Detector At the LHC (MoEDAL) [86] experiment is situated near LHCb and tries to find magnetic monopoles.

For the enhancement of the exploration of rare events and thus enhancing the number of collisions, high beam energies as well as high beam intensities are required. The luminosity [87] is a measure of the number of collisions that can be produced in a detector per square meter and per second and is the key role player in the enhancement of the beam intensity. The LHC collisions create a number of events per second given by

$$N_{\mathrm{event}} = L\sigma_{\mathrm{event}}, \tag{2.1}$$

where σ_{event} is the cross section of the process of interest and L the machine instantaneous luminosity. This luminosity depends only on the beam parameters and is for a Gaussian beam expressed as

$$L = \frac{1}{4\pi} N_{\mathrm{b}} n_{\mathrm{b}} f_{rev} \frac{N_{\mathrm{b}}}{\epsilon_n} \left(1 + \left(\frac{\theta_c \sigma_z}{2\sigma^*}\right)^2\right)^{-\frac{1}{2}} \frac{\gamma_{\mathrm{r}}}{\beta^*}. \tag{2.2}$$

The number of particles per bunch is expressed by N_{b}, while n_{b} is the number of bunches per beam, f_{rev} the revolution frequency, γ_{r} the relativistic gamma factor, ϵ_n the normalized transverse beam emittance - a quality for the confinement of the beam , β^* the beta function at the collision point - a measurement for the width of the beam, θ_c the angle between two beams at the interaction point, σ_{z} the mean length of one bunch, and σ^* the mean height of one bunch. In Equation 2.2, the blue part represents the stream of particles, the red part the brilliance, and the green part the geometric reduction factor due to the crossing angle at the interaction point.

The peak design luminosity for the LHC is $10^{34}\,\mathrm{cm}^{-2}\mathrm{s}^{-1}$, which leads to about 1 billion proton interactions per second. In 2016, the LHC was around 10% above this design luminosity [88]. The luminosity is not a constant in time since it diminishes due to collisions between the beams, and the interaction of the protons and the particle gas that is trapped in the centre of the vacuum tubes due to the magnetic field. The diffusion of the beam degrades the emittance and therefore also the luminosity. For this reason, the mean lifetime of a beam inside the LHC is around 15 h. The integrated luminosity - the luminosity provided in a certain time range - recorded by CMS over the year 2016 is given in Figure 2.3. In Run 2, the peak luminosity is 13-17$\times 10^{34}\,\mathrm{cm}^{-2}\mathrm{s}^{-1}$ compared to 7.7$\times 10^{33}\,\mathrm{cm}^{-2}\mathrm{s}^{-1}$ in Run 1. The recorded luminosity is validated for physics analysis keeping 35.9 fb^{-1} during 2016 data taking.

Multiple proton-proton interactions can occur during one bunch crossing, referred to as pileup. On average, the number of pileup events is proportional to the luminosity times the total inelastic proton-proton cross section. In 2016, an average of about 27 of pileup interactions has been observed in 13 TeV proton collisions at the interaction point of CMS. For 2012, this number was about 21 pileup interactions for 8 TeV collisions.

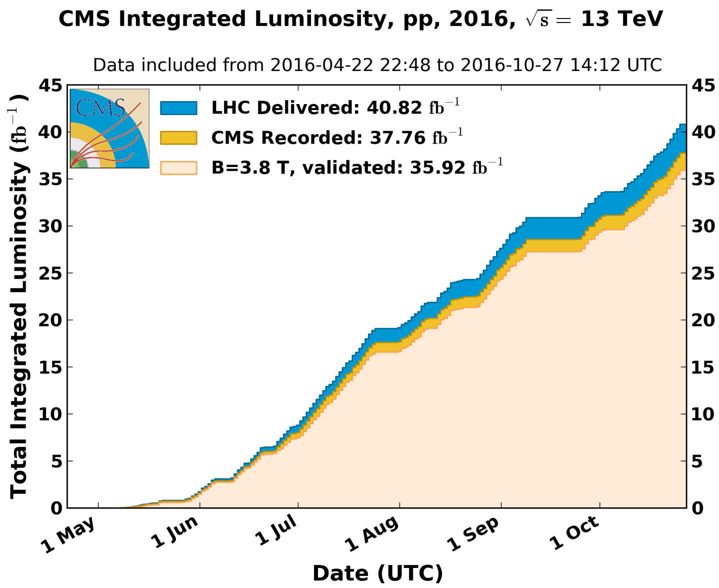

Figure 2.3: Cumulative offline luminosity measured versus day delivered by the LHC (blue), and recorded by CMS (orange), and certified as good for physics analysis during stable beams (light orange) during stable beams and for proton collisions at 13 TeV centre-of-mass energy in 2016. [89].

2.2 The Compact Muon Solenoid

At one of the collision points of the LHC, the CMS detector [90, 91] is placed. Weighing 14 000 t, this cylindrical detector is about 28.7 m long and 15 m in diameter. It has an onion like structure of several specialised detectors and contains a superconducting solenoid with a magnetic field of 3.8 T. Since the LHC produces collisions in a hadronic environment, the main backgrounds of rare physics processes are multi-jet processes produced by the strong interaction. Therefore, good identification, momentum resolution, and charge determination of muons, electrons and photons are one of the main goals of the CMS detector. Additionally, a good charged particle momentum resolution and reconstruction efficiency in the inner tracker provides identification for jets coming from b quarks or tau particles. Also the electromagnetic resolution for an efficient photon and lepton isolation as well as a good hadronic calorimeter for the missing transverse energy[2] were kept into account while designing CMS. In Figure 2.4, an overview of the CMS detector is shown.

[2]The missing transverse energy comes from an imbalance in the transverse plane. This will be discussed in Chapter 4.

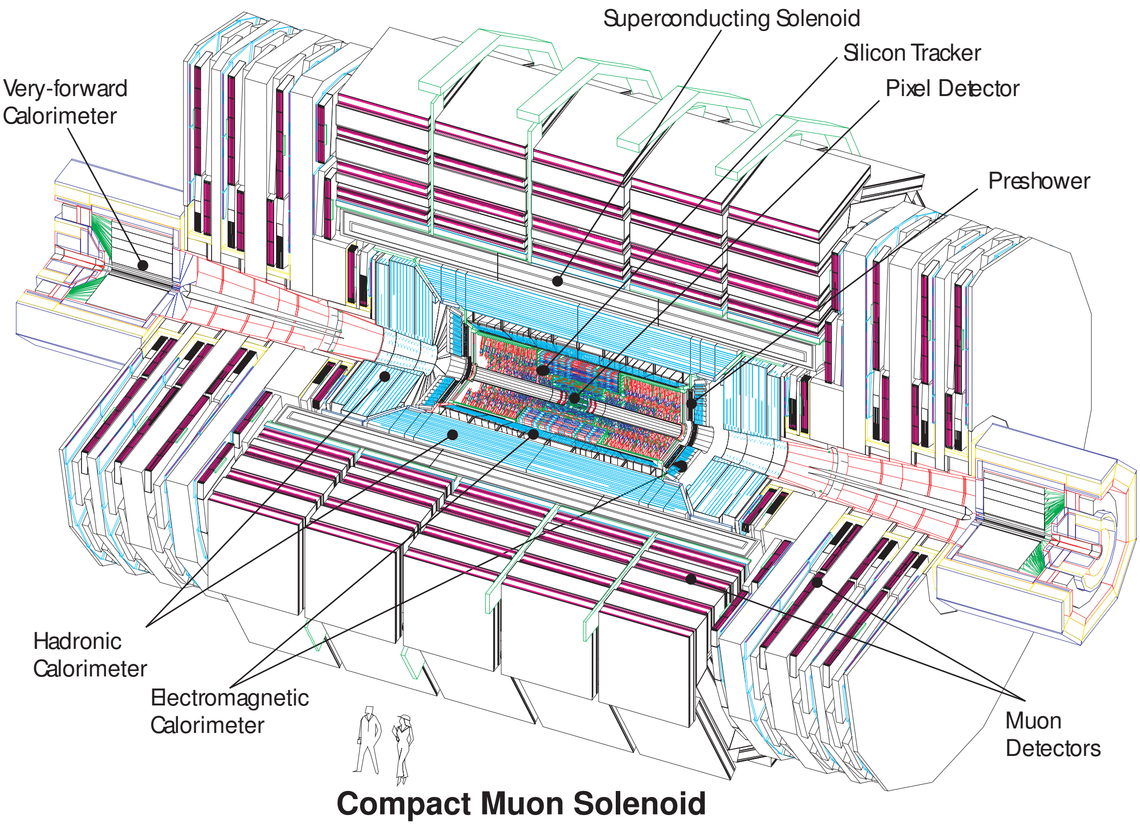

Figure 2.4: Mechanical layout of the CMS detector. Figure taken from [92].

2.2.1 CMS coordinate system

The coordinate system used by CMS can be found in Figure 2.5. The origin of the right handed orthogonal coordinate system is chosen to be the point of collisions. The x-axis points towards the centre of the LHC ring such that the y-axis points towards the sky, and the z-axis lies tangent to the beam axis. Since the experiment has a cylindrical shape, customary coordinates are used to describe the momentum $\vec{p}$: the distance $p = |\vec{p}|$, the azimuthal angle[3] $\phi \in [-\pi, \pi]$, the pseudo-rapidity[4] η :

$$\eta = -\ln\left(\tan\left(\frac{\theta}{2}\right)\right). \tag{2.3}$$

For the energies considered at the LHC, where $E >> m$, the pseudo-rapidity is a good approximation of the rapidity y

$$y = \frac{1}{2}\ln\left(\frac{E+p_z}{E-p_z}\right), \tag{2.4}$$

where the difference of rapidities of two particles is invariant under a Lorentz boost in the z-direction.

[3] The azimuthal angle is the angle between the x-axis and the projection in the transverse plane of the momentum $\vec{p}$, denoted as $\vec{p}_T$.

[4] The pseudorapidity is expressed by the polar angle θ between the direction of $\vec{p}$ and the beam.

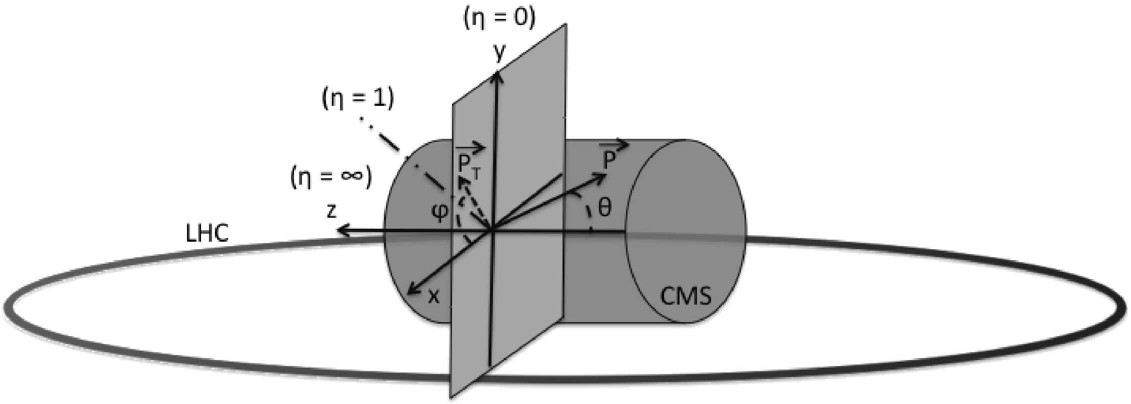

Figure 2.5: Representation of the coordinate system used by CMS. The point of origin is put at the collision point. The x-axis points towards the centre of the LHC ring such that the z-axis lies tangent to the beam axis.

2.2.2 Towards the heart of CMS

The CMS detector can be divided into two parts. A central barrel is placed around the beam pipe $\left(|\eta| < 1.4\right)$, and two plugs (endcaps) ensure the hermeticity of the detector. In Figure 2.4 and Figure 2.6 the onion like structure of the CMS detector is visible. The choice of a solenoid of 12.9 m long and 5.9 m diameter gives the advantage of bending the particle trajectories in the transverse plane. The hadronic calorimeter (Section 2.2.2.3), the electromagnetic calorimeter (Section 2.2.2.4) and the tracker (Section 2.2.2.5) are within the solenoid (Section 2.2.2.2), while the muon chambers (Section 2.2.2.1) are placed outside the solenoid. The data used for the search presented in this thesis is collected after the long shutdown 1. After discussing each part of CMS in their Run 1 configuration, Section 2.2.4 elaborates on their different upgrades for the data collected in Run 2.

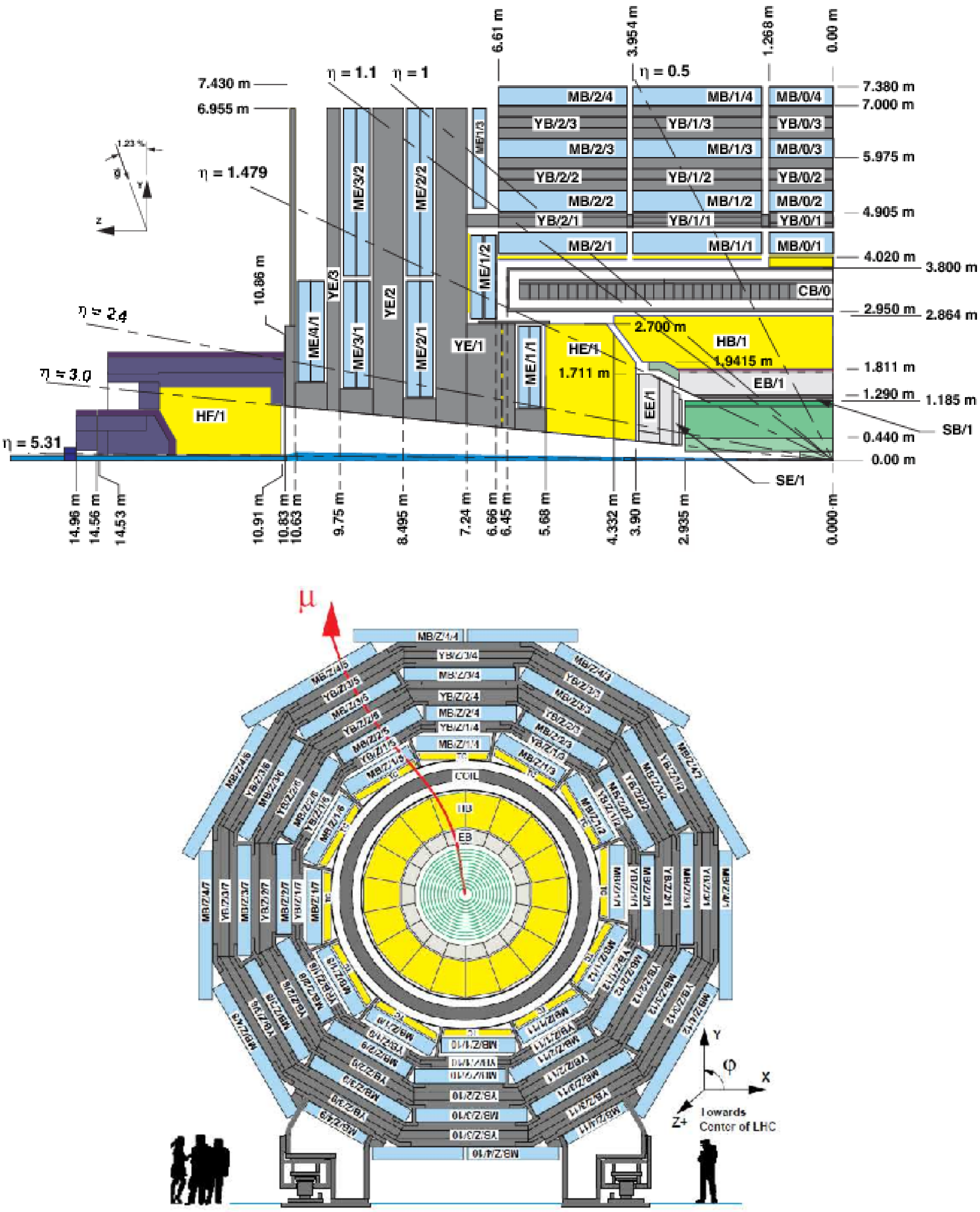

Figure 2.6: Schematic view of the CMS detector in the Run 1 configuration. The longitudinal view of one quarter of the detector is given at the top, while the transversal view is shown at the bottom. The muon system barrel elements are denoted as MBZ/N/S, where Z= −2... + 2 is the barrel wheel number, N= 1...4 the station number and S= 1...12 the sector number. Similary, the steel return yokes are denoted as YBZ/N/S. The solenoid is denoted as CB0, while the hadronic calorimeter is denoted as HE (endcap)/ HB (barrel)/HF (forward) and the electromagnet calorimeter as EE (endcap)/EB (barrel). The green part represents the tracking system (tracker + pixel). Figure taken from [93].

2.2.2.1 Muon system

The outermost part of CMS consists of the muon system. The magnet return yoke is interleaved with gaseous detector chambers for muon identification and momentum measurement. The barrel contains muon stations arranged in five separate iron wheels, while in the endcap four muon stations are mounted onto three independent iron discs on each side. Each barrel wheel has 12 sectors in the azimuthal angle.

The muon system is divided into three parts, shown in Figure 2.7. The muon rate and neutron induced backgrounds are small and the magnetic field is very low for the barrel, thus CMS can use drift tube (DT) chambers. For the endcaps however, the muon and background flux is much higher and there is a need to use cathode strip chambers (CSC) which are able to provide a faster response, higher granularity and have a better resistance against radiation. In order to form a redundant trigger system, resistive plate chambers (RPC) are added. This makes a total of 250 DT, 540 CSC and 610 RPC chambers. In Figure 2.6 the arrangement is shown.

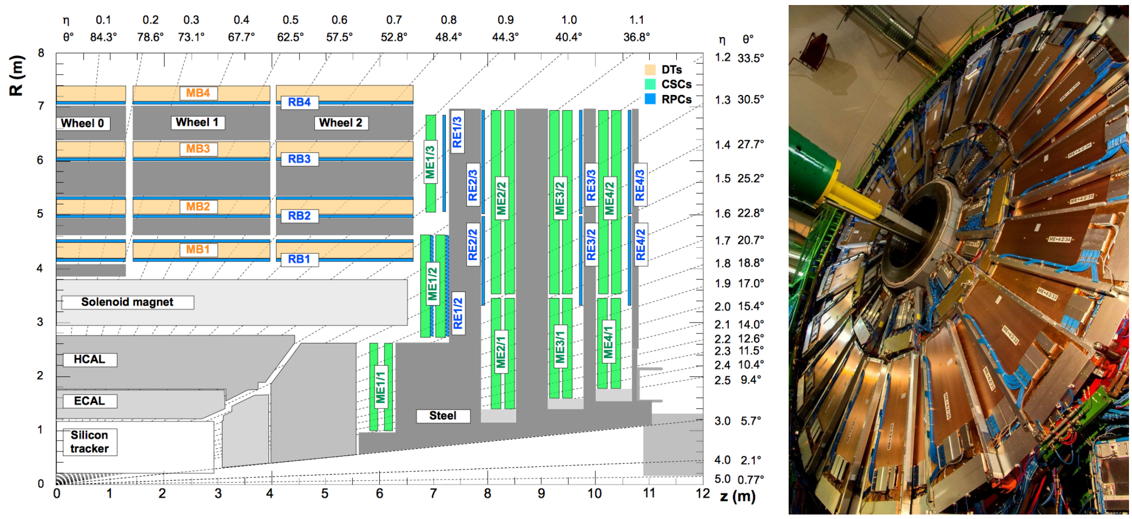

Figure 2.7: (Left) Schematic view of one quarter of the CMS muon system in the Run 1 configuration. The cathode strip chambers (CSC) are shown in green, the drift tubes (DT) are shown in yellow, while the resistive plate chambers (RPC) are shown in blue. Figure taken from [93]. (Right) Cathode strip chambers (ME+4/2 chambers on YE+3). Photo taken from [94].

Providing a measurement for $|\eta| < 1.2$, the DT chambers in the barrel are on average 2×2.5 m^2 in size and consist of 12 layers of DT cells[5] arranged in three groups of four. The $r\phi$ coordinate is provided by the two outside groups, while the middle group measures the z coordinate. For the outer muon station, the DT chambers contain only eight layers of DT cells, providing a muon position in the $r\phi$ plane. There are four CSC stations in each endcap, providing muon measurements for $0.9 < |\eta| < 2.4$. These CSCs are multi-wired proportional chambers that consist of six anode wire planes crossed by seven copper strips cathode panels in a gas volume. The r coordinate is provided by the copper strips, while the ϕ coordinate comes from the anode wires, giving a two dimensional position measurement. There are six

[5] The DT cells are 4 cm wide gas tubes with positively charged stretched wires inside.

layers of RPCs in the barrel muon system and one layer into each of the first three stations of the endcap. They are made from two high resistive plastic plates with an applied voltage and separated by a gas volume. Read-out strips mounted on top of the plastic plates detect the signal generated by a muon passing through the gas volume. The RPCs provide a fast response with a time resolution of 1 ns and cover a range of $|\eta| < 1.8$.

The muon system provides triggering on muons, identifying muons and improves the momentum measurement and charge determination of high p_{T} muons. On top of the muon system, a fraction of the muon energy is deposited in the electromagnetic calorimeter, the hadronic calorimeter, and outer calorimeter. The high magnetic field enables an efficient first level trigger and allows a good momentum resolution of $\Delta p/p \approx 1\%$ for a p_{T} of 100 GeV and $\approx 10\%$ for a p_{T} of 1 TeV. There is an efficient muon measurement up to $|\eta| < 2.4$.

2.2.2.2 Solenoid

Making use of the knowledge of previous experiments like ALEPH and DELPHI at LEP and H1 at HERA, CMS chose for a large super conducting solenoid with a a length of 12.9 m and a inner bore of 5.9 m [91]. With 2168 turns, a current of 18.5 kA resulting in a magnetic field of 3.8 T, and a total energy of 2.7 GJ, a large bending power can be obtained for a modestly-sized solenoid. In order to ensure a good momentum resolution in the forward regions, a favourable length/radius was necessary. In Figure 2.8, a picture of the CMS solenoid is shown.

The solenoid uses a high-purity aluminium stabilised conductor with indirect cooling from liquid helium, together with full epoxy impregnation. A four-layer winding is implemented that can withstand an outward pressure of 64 atm. The NbTi cable is co-extruded by pure aluminium that acts as a thermal stabilizer and has an aluminium alloy for mechanical reinforcement. The magnetic field lines are closed using five iron wheels, noted by YB in Figure 2.6.

2.2.2.3 Hadronic calorimeter

The hadronic calorimeter (HCAL) is dedicated to precisely measure the energy of charged and neutral hadrons via a succession of absorbers and scintillators. This makes it crucial for physics analyses with hadronic jets or missing transverse energy. The HCAL barrel extends between $1.77 < r < 2.95$ m, where r is the radius in the transverse plane with respect to the beam. Due to space limitations, the HCAL needs to be as small as possible and is made from materials with short interaction lengths[6]. On top of this, the HCAL should be as hermetic as possible and extend to large absolute pseudo rapidities such that it can provide a good measurement of the missing transverse energy.

The quality of the energy measurements is dependent on the fraction of the hadronic shower that can be detected. Therefore, the HCAL barrel (HB) inside the solenoid is reinforced by an outer hadronic calorimeter between the solenoid and muon detectors (HO, see Figure 2.9), using the solenoid as extra absorber. This increases the thickness to 12 interaction lengths. The HB

[6] Here the interaction length is the nuclear interaction length and this is the length needed for absorbing 36.7% of the relativistic charged particles. For the electromagnetic calorimeter this is defined in radiation length X_0. The radiation length is the mean distance over which a high energy electron loses all but $1/e$ of its energy by bremsstrahlung.

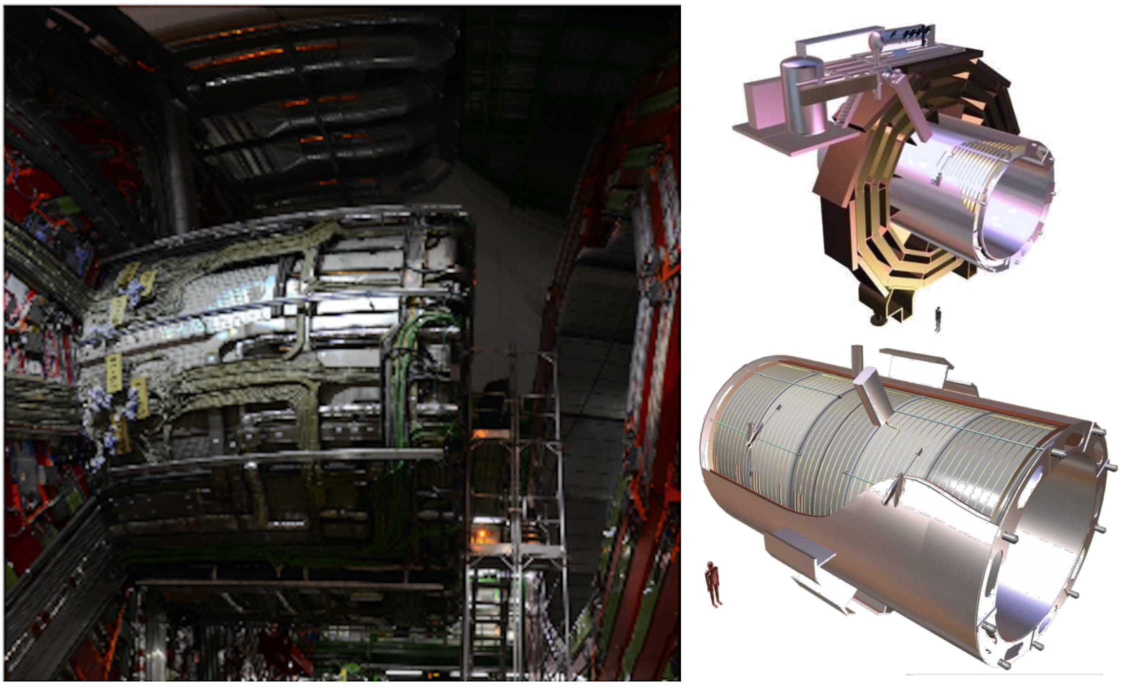

Figure 2.8: (Left) CMS solenoid during the long shutdown in 2013. (Right) An impression of the solenoid magnet taken from [95].

and HO provide measurements for $|\eta| < 1.3$, while an endcap on each side (HE, $1.3 < |\eta| < 3$) and a forward calorimeter (HF, $3.0 < |\eta| < 5.2$) extend the pseudorapidity range.

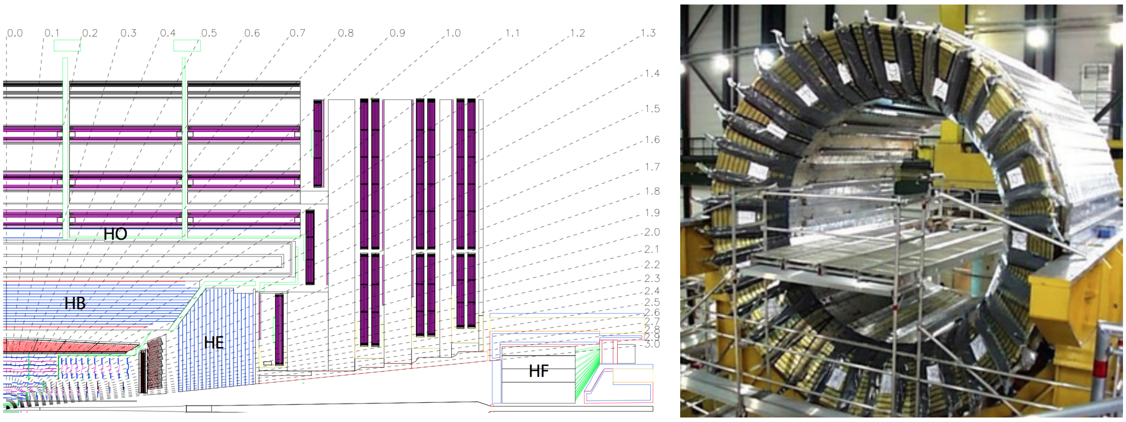

Figure 2.9: (Left) Longitudinal view of the CMS detector showing the locations of the HB, HE, HO, and HF calorimeters. Figure taken from [81]. (Right) CMS barrel calorimeter. Photo taken from [96].

The HB is made of 16 absorber plates where most of them are built from brass and others are made from stainless steal and is about five to ten interaction lengths thick. It is divided in $\eta \times \phi$ towers and contains 2592 read-out channels. The HO complements the HB and extends the reach up to twelve interaction lengths. This subsystem contains 2160 read-out channels. The HE is also composed of brass absorber plates and has a thickness corresponding to approximately ten interaction lengths, with 2592 read-out channels. The HF experiences intense particle fluxes with an expected energy of 760 GeV deposited on average in a proton interaction, compared to 100 GeV in the rest of the detector. Therefore, these are Cherenkov light detectors made of radiation hard quartz fibres. The main causes of such large energy events are high energy muons and charged particles from late showering hadrons. The HF represents 1728 read-out channels.

The HCAL and electromagnetic calorimeter combined, can measure the hadron energy with a resolution $\Delta E/E \approx 100\%\sqrt{E[\mathrm{GeV}]} + 5\%$.

2.2.2.4 Electromagnetic calorimeter

The electromagnetic calorimeter (ECAL) is designed to measure the energy of photons and electrons and covers $|\eta| < 3$. It is an hermetic, homogeneous detector and consists of 75 848 lead tungstate ($PbWO_4$) crystals. These crystals have a fast response time - 80% of the light is emitted within 25 ns- and are radiation hard. The electromagnetic showers produced by passing electrons or photons, ionize the crystal atoms which emit a blue-green scintillation light, that is collected by silicon avalanche photodiodes (APDs) in the barrel and vacuum phototriodes (VPTs) in the endcaps.

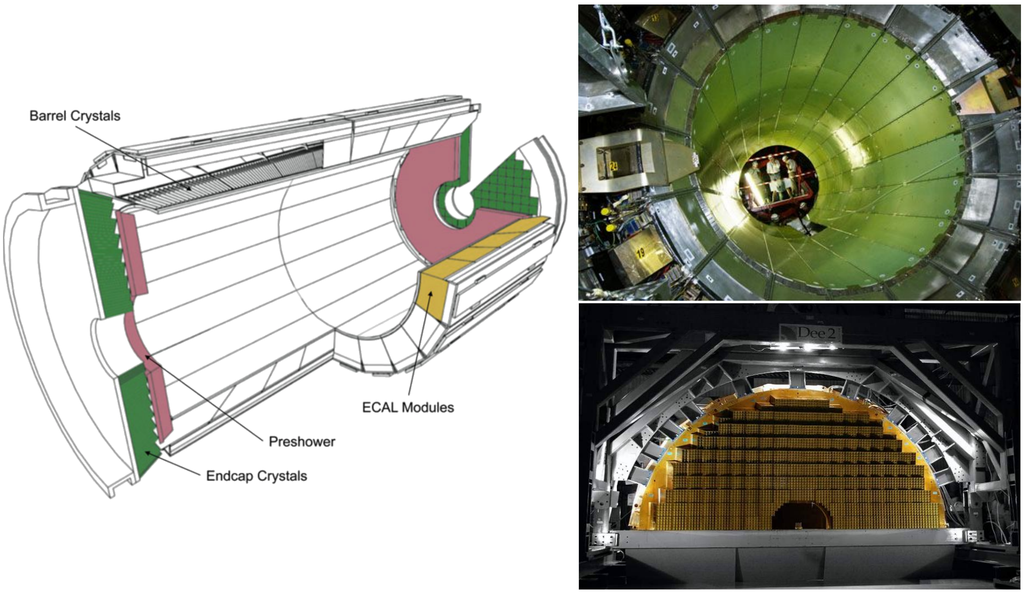

Figure 2.10: (Left) Schematic cross section of the electromagnetic calorimeter taken from [81]. (Right top) The ECAL barrel during construction (photo taken from [97]). (Right bottom) One half of an EE (photo taken from [98]).

There are three parts: a central barrel (EB), an endcap region (EE) and a preshower (ES) (Figure 2.10). The EB has an inner radius of 129 cm and corresponds to a pseudorapidity of $0 < |\eta| < 1.479$. At a distance of 314 cm from the vertex and covering a pseudorapidity of $1.479 < |\eta| < 3.0$, are the EE. They consist of semi-circular aluminium plates from which structural units of 5×5 crystals (supercrystals) are supported. The ES is placed in front of the crystal calorimeter over the endcap pseudorapidity range with two planes of silicon strip detectors as active elements.

The electromagnetic shower will typically involve more than one channel. More than 90% of the energy of a 35 GeV electron or photon is contained in a 5 × 5 matrix of crystals. A clustering algorithm is applied in order to associate the energy deposits to the particles impinging the calorimeter. The achieved position resolution for the barrel is $2{\times}10^{-3}$ rad in ϕ and 10^{-3} in η [99]. For the endcaps this is $5{\times}10^{-3}$ rad in ϕ and $2{\times}10^{-3}$ in η . The energy E is reconstructed by a supercluster algorithm, taking into account energy radiated via bremsstrahlung or conversion [81]. The energy resolution is given by

$$\frac{\sigma(E)}{E} = \frac{2.8\%}{\sqrt{E}} \oplus \frac{0.128}{E(\mathrm{GeV})} \oplus 0.3\%, \tag{2.5}$$

in the absence of a magnetic field, where the contributions come from the stochastic, noise and constant terms respectively. For a typical shower energy of 100 GeV, the dominating term is the constant term indicating that the performance is highly dependent on the quality of calibration and monitoring.

2.2.2.5 Inner tracking system and operations

The tracking system (tracker) [100] is the detecting unit closest to the point of interaction. Used for the reconstruction of trajectories from charged particles with $|\eta| < 2.5$ that are bent by the magnetic field, it provides a measurement of the particles momenta. The tracker is also responsible for the determination of the interaction point or vertex. It should be able to provide high granularity as well as fast read-out, and be able to endure high radiation. For these reasons, the CMS collaboration chose silicon detector technology.

The tracking system consists of a cylinder of 5.8 m long and 2.5 m in diameter. As shown in Figure 2.11, the tracker consists of a large silicon strip tracker with a small silicon pixel tracker inside. The inner pixel region ($4.4 < r < 10.2$ cm), gets the highest flux of particles. Therefore, pixel silicon sensors of 100 × 150 μm^2 are used. The pixel tracker consists of three cylindrical barrels that are complemented by two discs of pixel modules at each side. The silicon strip tracker ($20 < r < 116$ cm) has three subdivisions. The Tracker Inner Barrel and Discs (TIB, TID, see Figure 2.12) are composed of four barrel layers accompanied by three discs at each end. The outer part of the tracker - Tracker Outer Barrel (TOB) - consists of six barrel layers. There are nine outer discs of silicon sensors, referred to as Tracker End Caps (TEC).

The pixel detector, shown in Figure 2.13, has 1440 modules that cover an area of about 1 m^2 and have 6six million pixels. It provides a three-dimensional position measurement of the hits arising from the interaction from charged particles with the sensors. In transverse coordinates ($r\phi$), the hit position resolution is about 10 μm, while 20-40 μm is obtained in the longitudinal coordinate (z). The TIB/TID, shown in Figure 2.12, delivers up to four $r\phi$-measurements using 320 μm thick silicon micro-strip sensors. These sensors are placed with their strips parallel to the beam axis in the barrel and radial in the discs. In the TIB, the first two layers have a strip pitch of 80 μm, while the remaining two have a strip pitch of 120 μm. This leads to a respective single point resolution of 23 μm and 35 μm. For the TID, the pitch varies between 100 μm and 141 μm. The TOB provides six $r\phi$-measurements with a single point resolution of 53 μm in the

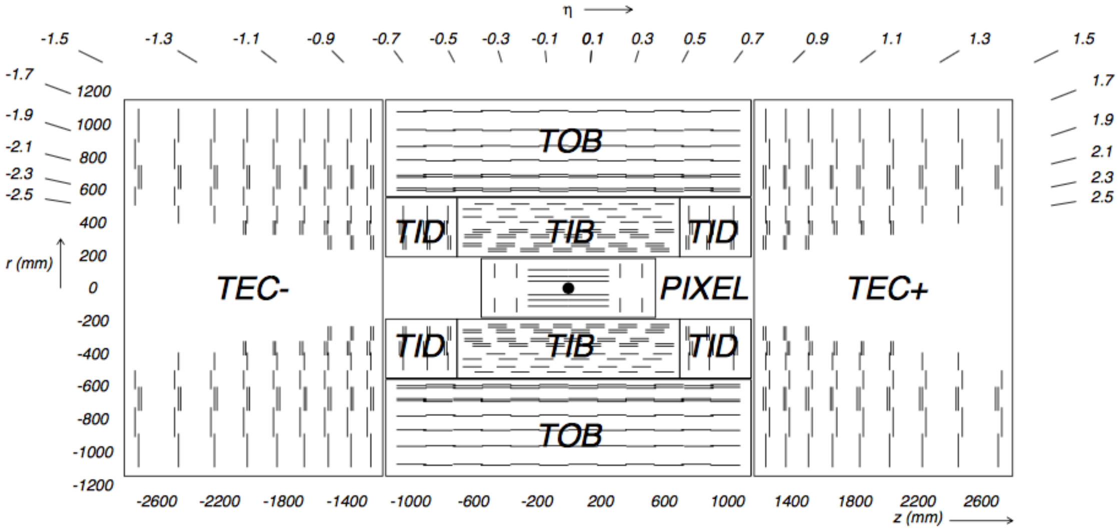

Figure 2.11: Schematic cross section through the CMS tracker. Each line represents a detector module. Double lines indicate back-to-back modules that deliver stereo hits. The tracker inner barrel (TIB) and inner discs (TID) are set around the pixel detector. The tracker outer Barrel (TOB) and endcaps (TEC) form the outer layers. Figure taken from [81].

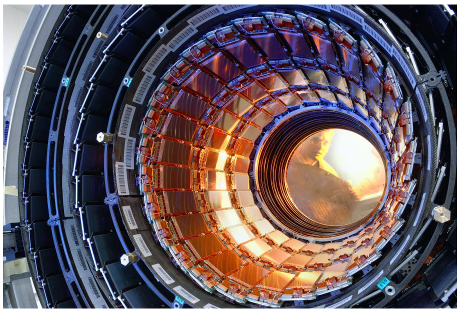

Figure 2.12: First half of the inner tracker barrel, consisting of three layers of silicon modules. Picture taken from [101].

Figure 2.13: The pixel barrel being re-installed after the Long Shutdown in 2015, around the beam pipe at CMS. Picture taken from [102].

first four layers, and 35 μm in the last two layers. It consists of 500 μm thick microstrip sensors with strip pitches of 183 μm (first 4 layers) or 122 μm (last two layers). The TEC provides up to 9 ϕ-measurements via 9 discs consisting of up to 7 rings of silicon microstrip sensors of 97 μm to 184 μm average pitch.

A second coordinate measurement (z in the barrel, r on the discs) is provided through the use of a second micro strip detector module mounted back-to-back with a stereo angle of 100 mrad. This is done on the modules in the first two layers and rings of the TIB, TID, and TOB, as well as rings 1, 2, and 5 of the TECs (double lines in Figure 2.11). The resolution in the z direction is approximately 230 μm in the TIB and 530 μm in the TOB, and is varying with pitch in the TID and TEC. To allow overlay and avoid gaps in acceptance, each module is shifted slightly in r or z with respect to its neighbouring modules within a layer. A third coordinate can then be provided by the sensor plane position. With this detector lay-out, at least nine points per charged particle trajectory can be measured in an $|\eta|$ range up to 2.4, with at least four of them being two dimensional. The CMS silicon tracker has 9.3 million read-out channels and covers an active area of about 198 m^2.

2.2.3 Data acquisition

At a design luminosity of 10^{34} $cm^{-2}s^{-1}$, the proton interaction rate exceeds 1 GHz. Given the large size of an event (about 1 MB) and the high crossing rate, it is impossible for the CMS experiment to store all the data generated. In order to deal with the large amount of data, a two level trigger system has been put in place. The first level (Level-1) is a custom hardware system, while a second high level trigger (HLT) is software based, running on a large farm of computers.

CMS Level-1 Trigger

The Level-1 Trigger has to be a flexible, maintainable system, capable of adapting to the evolving physics programme of CMS [103]. Its output rate is restricted to 100 kHz imposed by the CMS read-out electronics. It is implemented by custom hardware and selects events containing candidate objects - e.g. ionization deposits consistent with a muon, or energy clusters corresponding to an electron / photon / tau lepton / missing transverse energy / jet. Collisions with large momenta can be selected using of the scalar sum of the transverse momenta of the jets.

By buffering the raw data from the CMS subdetectors in front-end drivers, the Level-1 Trigger has a pipeline memory of 3.2 μs to decide whether to keep or reject an event. The trigger primitives from the calorimeters and muon detectors are processed in several steps and combined into a global trigger. This information is then combined with the input from the other subsystems for the HLT. The separate inputs are synchronized to each other and the LHC orbit clock and sent to the global trigger module. Here, Level-1 Trigger algorithms are performed within 1 μs to decide whether to keep the event.

CMS HLT Trigger

The HLT is an array of commercially available computers with a programmable menu that has an event output rate of on average 400 Hz for offline storage. The data processing is based on an HLT path. This is a set of algorithmic steps used to reconstruct objects to define selection criteria. Here, the information of all subdetectors can be combined to reconstruct higher level objects.

2.2.4 Phase 1 upgrades

Before the start of taking collision data for 13 TeV operations on 3 June 2015, CMS had a long shutdown (LS1) [104]. During this shutdown, the section of the beryllium beam pipe within CMS was replaced by a narrower one to make room for future upgrades. This operation required the pixel detector to be removed and reinserted into CMS.

During Run 2, higher particle fluxes with respect to Run 1 are expected. To avoid long-term damage caused by the intense particle flux at the heart of CMS, the tracker has been made ready to operate at much lower temperature than during Run 1.

During the first data taking period of the LHC (2010 to 2013), the tracker operated at +4°C. With the higher LHC beam intensities from 2015 onwards, the tracker needs to be operated at much lower temperatures. The reason for this is that with intense irradiation, the doping concentration changes, the leakage current increases proportional to the fluence and the charge collection efficiency decreases due to charge trapping. Mostly the leakage current (I) is affected by the temperature change:

$$I \propto T^2 e^{-\frac{E_g}{2kT}}, \tag{2.6}$$

where T is the operating temperature, E_g the band gap and k the Boltzmann constant. There is approximately a factor 15 between the leakage currents at room temperatures and at −10 °C.

During the LS1, the CMS cooling plant was refurbished [105] and the fluorocarbon cooling system overhauled. To help suppressing the humidity inside the tracker, new methods for vapour sealing and insulation were applied. Furthermore, several hundred high-precision sensors are used to monitor the humidity and temperature. In order to get as dry air as possible, a new dry-gas plant provides eight times more dry gas (air or nitrogen) than during the first run, and allows regulation of the flow. As a final addition, the cooling bundles outside the tracker are equipped with heater wires and temperature sensors in order to maintain safe operations above the cavern dew point. For the data taking during Run 2, the tracker is operated at −15 °C.

The electromagnetic calorimeter preshower system was damaged during Run 1, therefore the preshower discs were removed, repaired and reinstalled successfully inside CMS in 2014. For the ECAL in Run 1, the energy reconstruction happened via a weighted sum of the digitized samples [106]. For Run 2 however, the reconstruction had to be made more resistant for out-of-time pileup and a multi-fit approach has been set into place. In this approach, the pulse shape is modelled as a sum of one in-time pulse plus the out-of-time pulses [99]. The energy resolution is better than 2% in the central barrel region and 2-5 % elsewhere.

During the LS1, the muon system underwent major upgrades [107, 108]. To help the discrimination between interesting low momentum muons coming from collisions and muons caused by backgrounds, a fourth triggering and measurement station for muons was added in each of the endcaps. In the fourth station of each endcap, the outermost rings of CSC and RPC chambers were completed, providing an angular coverage of $1.2 < |\eta| < 1.8$ for Run 2, increasing the system redundancy, and allowing tighter cuts on the trigger quality. In order to reduce the environmental noise, outer yoke discs have been placed on both sides for the endcaps. At the innermost rings of the first station, the CSCs have been upgraded by refurbishing the read-out electronics to make use of the full detector granularity instead of groups of three as was the case for Run 1.

Other upgrades during the LS1 involved the installation of several new detectors into CMS for measuring the collision rate within the detector and to monitor beam related backgrounds. Also, since the HF experiences intense particle fluxes, it became clear during Run 1 that the glass windows of the PMTs need replacing which was also carried out during the LS1.

In Run 2, with the increase in centre-of-mass energy and a higher luminosity, a larger number of simultaneous inelastic collisions per crossing is expected with respect to Run 1. For this, the CMS Level-1 Trigger has been upgraded [109]. All hardware, software, databases and the timing control system have been replaced for Run 2, where the main changes are that the muon system now uses the redundancy of the muon detector system earlier to make a high resolution muon trigger. Other upgrades are also performed, including providing the global trigger with more Level-1 Trigger algorithms.

After the first half of Run 2, during the EYETS, the innermost part of detection in CMS (pixel detector) was replaced, enhancing the particle tracking capabilities of CMS. The data used in the framework of this thesis however is collected before this upgrade. More information on the pixel upgrade can be found in Refs. [110, 111].

2.2.5 CMS computing model

The selected data is stored, processed and dispersed via the Worldwide Large Hadron Collider Computing Grid (WLCG) [112, 113]. This has a tiered structure that functions as a single, coherent system. The WLCG centres are shown in Figure 2.14.

At CERN and the Wigner Research Centre for physics, a single Tier-0 is located. The raw data collected by the experiments is archived here, and a first reconstruction of the data is done. This data is then already in a file format usable for physics analysis. Furthermore, the Tier-0 is able to reprocess data when new calibrations become available. From the Tier-0 site, the data is distributed to a total of 14 Tier-1 centres. These take care of the data reprocessing and storage. From the Tier-1 sites, the data is distributed further over 150 Tier-2 centres. These make the data accessible for physics analysis and are also being used for the production of simulated data. The data is made accessible for physicists around the world. For CMS, the Tier-0 site at CERN reconstructs the full collision events and the backup of the data is sent to seven Tier-1 computer centres in France, Germany, Italy, Spain, Taiwan, UK, and the US. There are forty Tier-2 centres for specific analysis tasks.

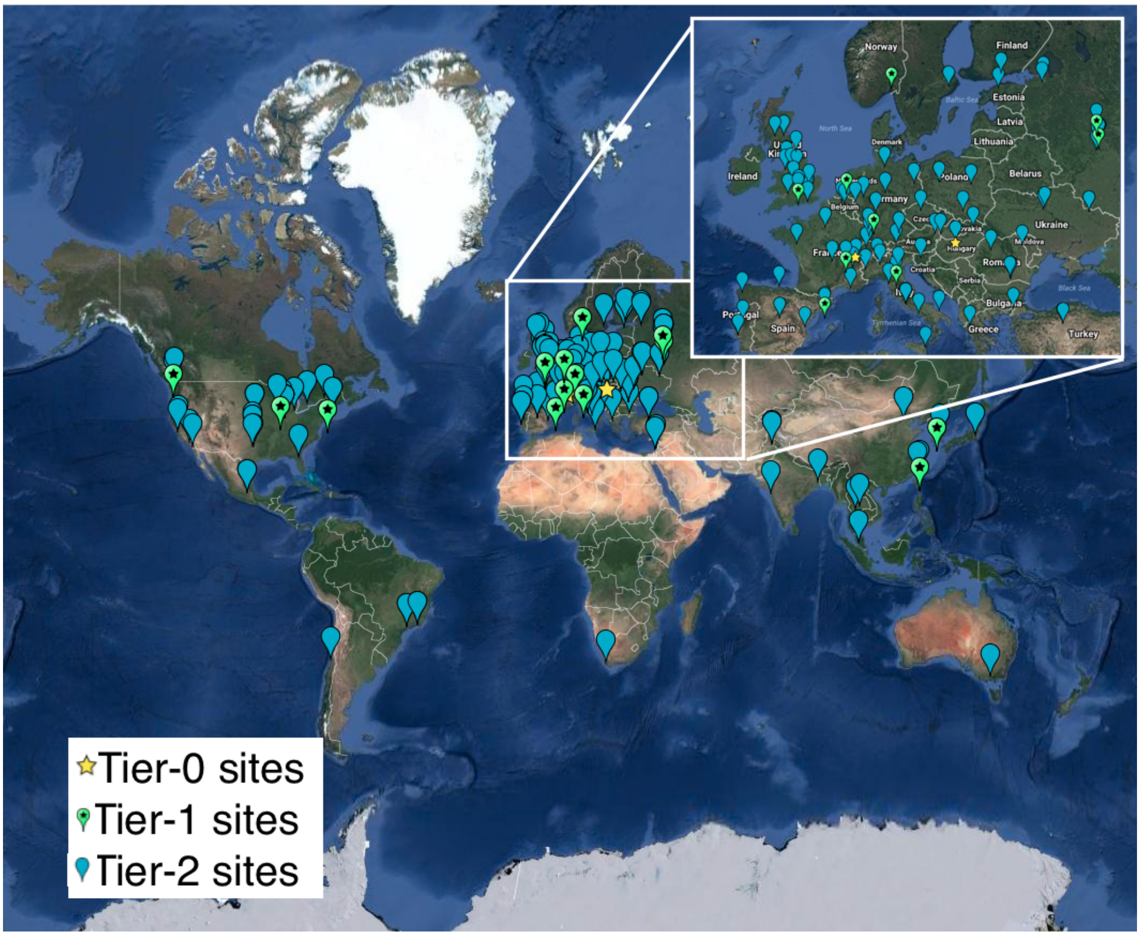

Figure 2.14: Worldwide LHC Computing Grid in 2017. Figure adapted from [114].

3 Analysis techniques

In order to study the collisions coming from high energy experiments, many tools have been developed. In Section 3.1, the physics of hadron collisions at high energies are presented. These insights are used to generate events via Monte Carlo event generators, explained in Section 3.2. Machine learning helps to differentiate between signal- and background-like events. In Section 3.3, the multivariate technique of boosted decision trees is explained. This yields powerful discriminants for separating signal and background events and provides distributions for template-based maximum likelihood fits. The fitting method used in the search presented in this thesis is discussed in Section 3.4.

3.1 Hadron collisions at high energies

All partons can be approximated as free when there is sufficiently high momentum transfer in hadron collisions. This makes it possible to treat a hadron-hadron scattering as a single parton-parton interaction. The momentum of the parton can then be expressed as a fraction of the hadron momentum

$$\vec{p}_{\text{parton}} = x\vec{p}_{\text{hadron}}, \tag{3.1}$$

where x is referred to as the Björken scaling variable. The interaction of two protons A and B, $\mathrm{p_A p_B} \rightarrow \mathrm{X}$, can then be factorised in terms of partonic cross sections $\hat{\sigma}_{\mathrm{ij}\rightarrow\mathrm{X}}$ [115]

$$\sigma_{\mathrm{p_A p_B}\rightarrow\mathrm{X}} = \sum_{\mathrm{ij}} \iint dx_1 dx_2\, f_{\mathrm{i}}^{\mathrm{A}}(x_1, Q^2) f_{\mathrm{j}}^{\mathrm{B}}(x_2, Q^2) d\hat{\sigma}_{\mathrm{ij}\rightarrow\mathrm{X}}, \tag{3.2}$$

where i and j are the partons resolved from $\mathrm{p_A}$ and p_{B}. The parton density functions (PDF) are denoted as $f_{\mathrm{i}}(x_{\mathrm{j}}, Q^2)$, and Q^2 is the factorisation scale more commonly denoted as μ_{F}. This factorisation scale represents the energy at which the hadronic interaction can be expressed as a product of the partonic cross section and the process independent PDF. In Figure 3.1, the kinematic regions in x and μ_{F} are shown for fixed target and collider experiments.

The parton density functions (PDF) [116–118] represent the momentum distribution of the proton amongst its partons at an energy scale μ_{F}. These functions are obtained from global fits to data since they can not be determined from first principles. From measurements on

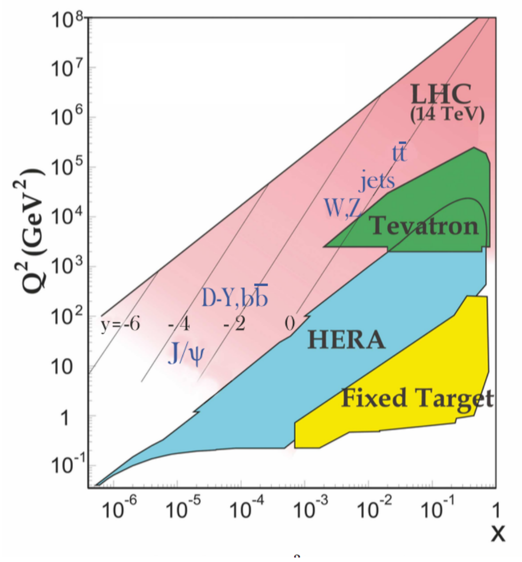

Figure 3.1: Kinematic regions in momentum fraction x and factorisation scale Q^2 probed by fixed-target and collider experiments. Some of the final states accessible at the LHC are indicated in the appropriate regions, where y is the rapidity. In this figure, the incoming partons have $x_{1,2} = (M/14\text{ TeV})e^{\pm y}$ with $Q = M$ where M is the mass of the state shown in blue in the figure. For example, exclusive J/ψ and ϒ production at high $|y|$ at the LHC may probe the gluon PDF down to $x \sim 10^{-5}$. Figure taken from [36].

deep inelastic scattering using lepton-proton collision data from the HERA collider [119], supplemented with proton-antiproton collisions from the Tevatron [120], and proton collision data from the ATLAS, CMS and LHCb collaborations at the LHC (Run 1) [121] the PDFs are determined and included in global PDF sets known as the PDF4LHC recommendation [118]. Their measurement at scale μ_F is extrapolated to higher energies by use of the DGLAP equations [122]. Once these PDFs are known, the cross section of a certain process can be calculated and used as input for the Monte Carlo generators used to make the simulated data samples at the LHC. In the framework of this thesis, the NLO PDF4LHC15_100 set is used. This set is an envelope of three PDF sets: CT14, MMHT14 and NNPDF3.0 [118]. As illustration, the dependency of the PDFs on the momentum fraction x is shown for the NNPDF3.0 for $\mu_F^2 = 10$ GeV^2 and LHC scale $\mu_F^2 = 10^4$ GeV^2 in Figure 3.2. The gluon density dominates for most values of the momentum fraction, implying that it is easier to probe gluons than quarks in the proton. When the Björken scale is set to one, the parton densities of the valence quarks of the proton, up and down quarks, dominate over the gluon density. The sea quarks originating from gluon splitting, the charm, anti-up, and anti-down quarks, have lower densities in general for the proton. The resolution scale μ_F^2 is typically taken to be the energy scale of the collision. For the top quark pair production a scale of $\mu_F^2 = (350\text{ GeV})^2$ is chosen, meaning that the centre-of-mass energy of the hard interaction is about twice the top quark mass. The uncertainty on the parton distributions is evaluated using the Hessian technique [123], where a matrix with a dimension identical to the number of free parameters needs to be diagonalised. In the case of PDF4LHC15_100 set, this translates into 100 orthonormal eigenvectors and 200 variations of the PDF parameters in the plus and minus direction.

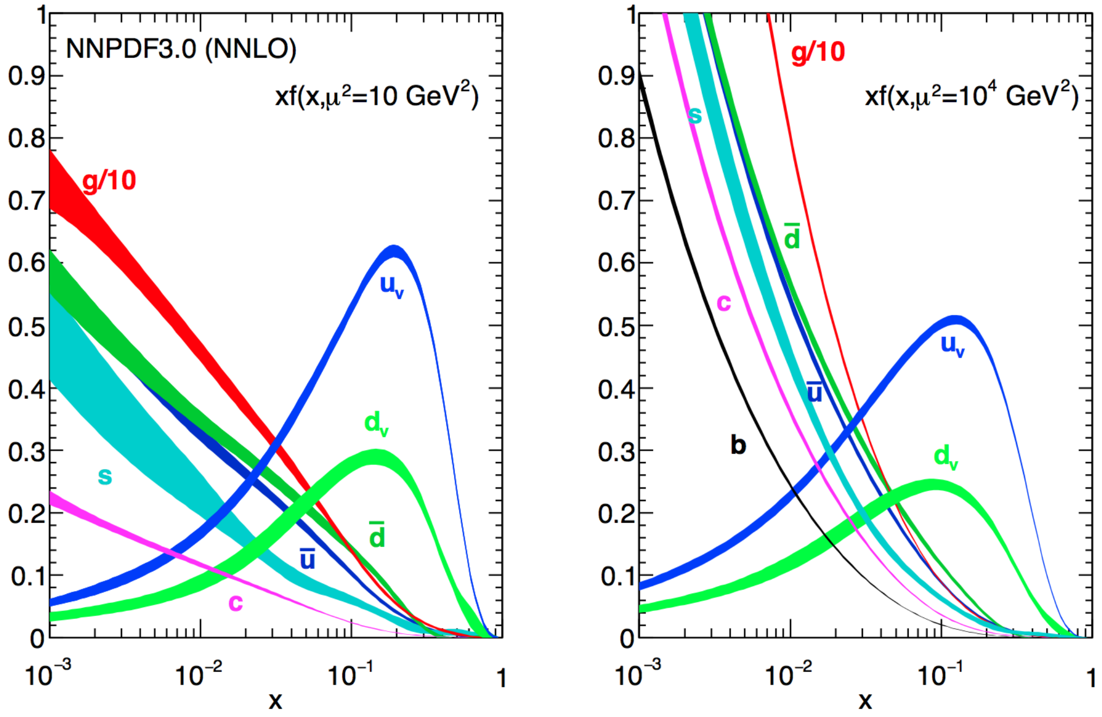

Figure 3.2: The momentum fraction x times the parton distribution functions $f(x)$, where $f = u_v, d_v, \bar{u}, \bar{d}, s, c$, or g as a function of the momentum fraction obtained in the NNLO NNPDF3.0 global analysis at factorisation scales $\mu_F^2 = \mu^2 = 10\,\text{GeV}^2$ (left) and $\mu_F^2 = \mu^2 = 10^4\,\text{GeV}^2$ (right), with $\alpha_S(M_Z^2) = 0.118$. The gluon PDF has been scaled down by a factor of 0.1. Figure taken from [36].

Quantum fluctuations can cause divergences at high energies. This is solved by introducing a renormalisation scale μ_R to redefine physical quantities, making the theory still able to describe the experimental regime. A consequence of this method is that the coupling constants will run as a function of μ_R. Beyond the renormalisation scale, the high energy effects such as the loop corrections to propagators (self energy) are absorbed in the physical quantities through a renormalisation of the fields. In particular, the running behaviour of the strong coupling constant[1] α_S is found to be

$$\alpha_S = \frac{\alpha_S(\mu_0^2)}{1 + \alpha_S(\mu_0^2)\frac{33-2n_f}{12\pi}\ln\left(\frac{|\mu_R^2|}{\mu_0^2}\right)}, \tag{3.3}$$

with n_f the number of quarks and μ_0 the reference scale at which the coupling is known. The current world average of the strong coupling constant at the Z boson mass is $\alpha_S(\mu_R = m_Z) = 0.1181 \pm 0.0011$ [36]. From Equation 3.3 one can see easily that the coupling strength decreases with increasing renormalisation scale, this is known as asymptotic freedom. Additionally, following the behaviour of $\alpha_S(\mu_R^2)$, a limit $\Lambda_{QCD} \approx 200\,\text{MeV}$ is found for which α_S becomes larger than one. Below this limit, the perturbative calculations of observables is no longer valid.

[1]The strong coupling constant is defined as $\alpha_S = \frac{g_S^2}{4\pi}$.

Cross sections can be written in terms of interacting vertices contributing to the matrix element (ME) originating from elements of a perturbative series [124], allowing them to be expanded as a power series of the coupling constant α

$$\sigma = \sigma_{\mathrm{LO}} \left(1 + \left(\frac{\alpha}{2\pi} \right) \sigma_1 + \left(\frac{\alpha}{2\pi} \right)^2 \sigma_2 + ... \right). \tag{3.4}$$

Leading order (LO) accuracy contains the minimal amount of vertices in the process, then depending on where the series is cut-off one speaks of next-to-leading order (NLO), or next-to-next-to-leading order (NNLO) accuracy in α. Predictions including higher order corrections tend to be less affected by theoretical uncertainties originating from a variation of the chosen renormalisation and factorisation scales.

3.2 Event generation

In order to compare reconstructed data with theoretical predictions, collision events are generated and passed through a simulation of the CMS detector and an emulation of its read-out. For the detector simulation, a so-called full simulation package [125, 126] based on the `Geant4` toolkit [127] is employed. This allows detailed simulations of the interactions of the particles with the detector material.

3.2.1 Fundamentals of simulating a proton collision

The generation of $\mathrm{pp} \rightarrow \mathrm{X}$ events is subdivided into sequential steps [128–130], as shown in Figure 3.3.

The interaction of two incoming protons is often soft and elastic leading to events that are not interesting in the framework of this thesis. More intriguing are the hard interactions between two partons from the incoming protons. The event generation starts from the matrix elements of a hard scattering process of interest. The corresponding cross section integral is sampled using Monte Carlo techniques and the resulting sample of events reflects the probability distribution of a process over its final state phase space. A parton shower (PS) program is then used to simulate the hadronisation of final state partons, coming from the sample of events of the hard interaction, into hadrons which then decay further. On top of this, radiation of soft gluons or quarks from initial or final state partons is simulated. These are respectively referred to as initial state radiation (ISR) or final state radiation (FSR). The contributions from soft secondary interactions, the so-called underlying event (UE), and colour reconnection effects are also taken into account. A brief overview of the programs used for the event generation of the signal and main background processes used in the search presented in this thesis, is given in the following section.

3.2.2 Programs for event generation

The `FEYNRULES` package [131] allows for the calculation of the Feynman rules in momentum space for any quantum field theory model. By use of a Lagrangian, the set of Feynman rules associated with this Lagrangian is calculated. Via the `Universal Feynrules Output` (UFO) [132] the results are then passed to matrix element generators.

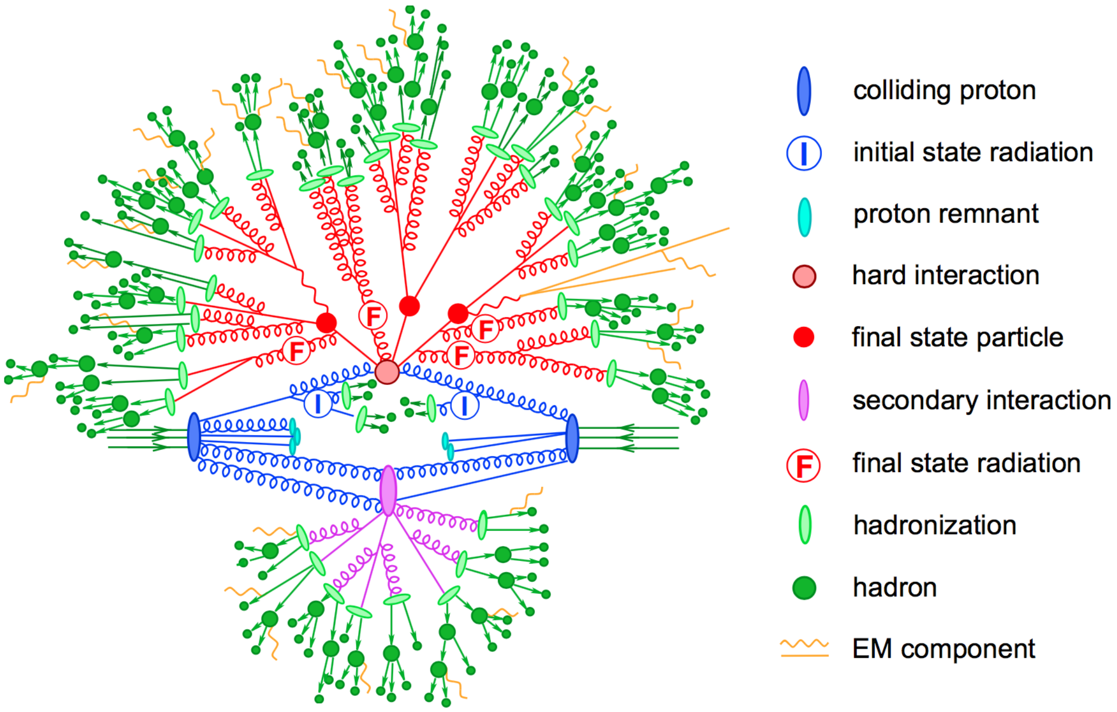

Figure 3.3: Sketch of a hadron collision as simulated by a Monte-Carlo event generator. The light red blob in the centre represents the hard collision, surrounded by a tree-like structure representing Bremsstrahlung simulated by parton showers shwon in red. The purple blob indicates a secondary hard scattering event. Parton-to-hadron transitions are represented by light green blobs, dark green blobs indicate hadron decays, while yellow lines signal soft photon radiation. The blue lines represent radiations from initial partons. Figure taken from [130].

The MadGraph program [133] is used to interpret the physics model and calculate the corresponding Feynman diagrams and matrix elements. After this, MadEvent [134] is used to generate the hard scattering events. These generated events can then be interfaced with Pythia [135, 136] for parton showers using for example the MLM merging scheme [137].

The MadGraph5_aMC@NLO program [138] extends the LO MadGraph [133] so that NLO QCD corrections could be handled as well. This combination supports the generation of samples at LO or NLO together with a dedicated matching to parton showers using the MC@NLO [139] scheme. In the MC@NLO prescription, a certain fraction of events with negative weights are produced originating from the subtraction of amplitudes that contain additional emissions from the NLO matrix element to prevent double-counting.

The POWHEG box (versions 1 and 2) [140–145] contains predefined implementations of various processes at NLO. It applies the POWHEG method for ME- to PS- matching, where the hardest radiation generated from the ME has priority over subsequent PS emission to remove the overlap with the PS simulation.

The JHU generator (version 7.02) [146–149] is used to generate the parton level information including full spin and polarization correlations. It is commonly used for studying the spin and parity properties of new resonances such as $ab \to X \to VV$, where $V = Z, W, \gamma$.

The generation of events from processes involving the production and decay of resonances creates a computational heavy load, especially at NLO. The narrow width approximation assumes that the resonant particle is on-shell. This factorizes the production and decay amplitude, allowing for the simulation of the production and decay of heavy resonances like top quarks or Higgs bosons to be performed in separate steps. The MadSpin program [150] extends this approach and accounts for off-shell effects through a partial reweighting of the events. Additionally, spin correlation effects between production and decay products are taken into account.

The Pythia program (versions 6 and 8) [135, 136] generates events of various processes at LO. However, more commonly it is used for its PS simulation by interfacing it with other LO and NLO event generators to perform parton showering, hadronisation, and simulation of the underlying event. In this thesis the underlying event tunes [151] are the CUETP8M2T4, CUETP8M1 and CUETP8M2 tunes.

The detector response is simulated via the Geant4 [127] program. This program tracks the particles through the detector material via a detailed description of the detector and generates several hits throughout several sensitive layers. In addition, the response of the detector electronics to these hits are simulated.

3.2.3 Generating FCNC top-Z interactions

The FCNC processes are generated by interfacing the Lagrangian in Equation 1.26 with MadGraph5_aMC@NLO by means of the FeynRules package and its Universal Feynrules Output format. The complex chiral parameters are arbitrary chosen to be $f^{L}_{Xq} = 0$ and $f^{R}_{Xq} = 1$. The processes are generated with the MadGraph5_aMC@NLO (version 2.2.2) and showered with Pythia. The signal consists of two components: events describing the top quark pair production followed by a FCNC decay of one top quark ($t \rightarrow Zq$), and events with the FCNC single top quark production ($Zq \rightarrow t$) for which the top quark decays according to the SM. The leading order generation of the single top quark FCNC process tZ+0,1 jet including a merging technique can not be done since tZ+1 jet also contains contributions from top quark pair FCNC where one quark is decaying in tZ. Therefore, single top quark and top quark pair processes are generated independently, where the single top quark process is generated without the extra hard jet, and the top quark pair FCNC process is generated with up to two extra jets.

The signal rates are estimated by use of the MadGraph5_aMC@NLO program for estimating the partial widths. The anomalous couplings are left free to float for this estimation, and only one coupling is allowed to be non-vanishing at a time. The results are presented in Table 3.1.

The anomalous single top quark cross sections are calculated by convolution of the hard scattering matrix elements with the LO order set of NN23LO1 [152] partons densities. The NLO effects are modelled by multiplying each LO cross section by a global k-factor. The LO single top quark production cross section and the global k-factors for the top-Z production are shown in Table 3.2. The hard scattering events are then matched to parton showers using Pythia to account for the simulation of the QCD environment relevant for hadronic collisions.

Table 3.1: Leading order partial widths related to the anomalous decay modes of the top quark, where the new physics scale Λ is given in GeV.

Anomalous coupling	vertex	Partial decay width (GeV)	
κ_{tZq}/Λ	tZu	1.64×10^4	$\times \left(\kappa_{tZu}/\Lambda\right)^2$
	tZc	1.64×10^4	$\times \left(\kappa_{tZc}/\Lambda\right)^2$
ζ_{tZq}	tZu	1.69×10^{-1}	$\times \left(\zeta_{tZu}\right)^2$
	tZc	1.68×10^{-1}	$\times \left(\zeta_{tZc}\right)^2$

Table 3.2: Leading order single top quark production cross section at a centre-of-mass energy of 13 TeV for $pp \to tZ$ or $\bar{t}Z$, where the new physics scale is given in GeV. The NLO *k*—factors [153] are given in the last column.

Anomalous coupling	vertex	Cross section (pb) $pp \to t + pp \to \bar{t}$		$\sigma_{pp\to\bar{t}}/\sigma_{pp\to t}$	NLO *k*—factor
κ_{tZq}/Λ	tZu	1.92×10^7	$\times \left(\kappa_{tZu}/\Lambda\right)^2$	0.12	1.40
	tZc	2.65×10^6	$\times \left(\kappa_{tZc}/\Lambda\right)^2$	0.50	1.40
ζ_{tZq}	tZu	8.24×10	$\times \left(\zeta_{tZu}\right)^2$	0.14	1.40
	tZc	1.29×10	$\times \left(\zeta_{tZc}\right)^2$	0.50	1.40

The top quark pair production cross sections are derived from the SM $t\bar{t}$ cross section, calculated with `MadGraph5_aMC@NLO` at NLO at a centre-of-mass energy of 13 TeV ($\sigma_{t\bar{t}}^{SM,NLO} = 6.741 \times 10^2$ pb), and considering the decay $t\bar{t} \to (bW^\pm)(Xqt)$. The branching fraction $\mathcal{B}(t \to bW^\pm)$ is assumed to be equal to one and the FCNC branching fraction is calculated as

$$\mathcal{B}(t \to qX) = \frac{\Gamma_{t\to qX}}{\Gamma_t^{SM} + \Gamma_t^{FCNC}} \approx \frac{\Gamma_{t\to qX}}{\Gamma_t^{SM}}, \tag{3.5}$$

where $\Gamma_{t\to qX}$ is given in Table 3.1, $\Gamma_t^{SM} = 1.32$ GeV [66], and the assumption $\Gamma_t^{FCNC} \ll \Gamma_t^{SM}$ is made. In Table 3.3 the resulting NLO cross sections for the top-Z FCNC interactions are given.

Table 3.3: Next to leading order top quark pair cross section for the top-Z FCNC interactions $t\bar{t} \rightarrow (bW^{\pm})(Xqt)$ with a full leptonic decay at a centre-of-mass energy of 13 TeV, where $\sigma^{SM,NLO}_{pp\rightarrow t\bar{t}} = 6.741 \times 10^2$ pb, $\mathscr{B}(Z \rightarrow \ell\bar{\ell}) = 3.36 \times 3 \times 10^{-2}$, and $\mathscr{B}(W \rightarrow \ell\nu) = 10.80 \times 3 \times 10^{-2}$.

Anomalous coupling	vertex	Process	Cross section (pb)	
κ_{tZq}/Λ	tZu	$t\bar{t} \rightarrow (b\ell^+\nu)(\bar{u}\ell^+\ell^-)$	2.727×10^5	$\times\left(\kappa_{tZu}/\Lambda\right)^2$
		$t\bar{t} \rightarrow (\bar{b}\ell^-\bar{\nu})(u\ell^+\ell^-)$	2.727×10^5	$\times\left(\kappa_{tZu}/\Lambda\right)^2$
	tZc	$t\bar{t} \rightarrow (b\ell^+\nu)(\bar{c}\ell^+\ell^-)$	2.726×10^5	$\times\left(\kappa_{tZc}/\Lambda\right)^2$
		$t\bar{t} \rightarrow (\bar{b}\ell^-\bar{\nu})(c\ell^+\ell^-)$	2.726×10^5	$\times\left(\kappa_{tZc}/\Lambda\right)^2$
ζ_{tZq}	tZu	$t\bar{t} \rightarrow (b\ell^+\nu)(\bar{u}\ell^+\ell^-)$	2.807	$\times\left(\zeta_{tZu}\right)^2$
		$t\bar{t} \rightarrow (\bar{b}\ell^-\bar{\nu})(u\ell^+\ell^-)$	2.807	$\times\left(\zeta_{tZu}\right)^2$
	tZc	$t\bar{t} \rightarrow (b\ell^+\nu)(\bar{c}\ell^+\ell^-)$	2.807	$\times\left(\zeta_{tZc}\right)^2$
		$t\bar{t} \rightarrow (\bar{b}\ell^-\bar{\nu})(c\ell^+\ell^-)$	2.807	$\times\left(\zeta_{tZc}\right)^2$

3.2.4 Generating SM background events

The SM tZq sample is generated using the `MadGraph5_aMC@NLO` generator at leading order accuracy. The $t\bar{t}Z$ and triboson samples were generated using the `MadGraph5_aMC@NLO` generator, interfaced through the dedicated MC@NLO matching scheme. The WZ+jets and $t\bar{t}W$ samples are produced with up to one additional parton at next-to-leading order accuracy using `MadGraph5_aMC@NLO` and using FxFx approach for matching and merging. The samples of $t\bar{t}H$, WW, ZZ, and single top quark production channels are generated with the `POWHEG` box. The `JHU` generator is used for the tqH sample, while the tWZ sample is generated using `MadGraph5_aMC@NLO` at leading order. All events are interfaced to `Pythia` to simulate parton shower, hadronisation, and underlying event. Additionally, `MadSpin` is used for the tZq, WZ+jets, $t\bar{t}Z$, $t\bar{t}W$, tWZ, and triboson samples.

The complete list of SM samples is given in Table 3.4, along with their cross sections at a centre-of-mass energy of 13 TeV. The cross sections originate from the generator with which the sample has been made. For some of the cross sections, the uncertainties are provided by the Generator Group [154]. For each MC sample, the integrated luminosity that the sample represents is estimated as the number of simulated events divided by the cross section of the generated process. This luminosity is then matched to integrated luminosity of 35.9 fb^{-1} represented by the data used for analysis. For processes generated with `MadGraph5_aMC@NLO`, the effective number of simulated events is used, taking into account positive and negative event weights. In Figure 3.4, a summary is given of the SM cross section measurements performed by the CMS collaboration. These cross sections are all in agreement with their SM predictions.

Table 3.4: SM MC samples used in this analysis with their corresponding cross section at a centre-of-mass energy of 13 TeV and `MadGraph5_aMC@NLO` correction C for negative event weights when applicable. The generators used for each sample are indicated and the simulation of the parton shower, hadronisation, and underlying event is done by `Pythia` version 8.22 [136] for all samples.

Process	Generator	Cross section (pb)	C	Ref.
$\mathrm{WZ} \rightarrow 3\ell\nu$	MadGraph5_aMC@NLO+MadSpin	5.26	1.61	[154]
tZq with $\mathrm{Z} \rightarrow \ell^+\ell^-$	MadGraph5_aMC@NLO+MadSpin	0.0758	3.77	[154]
tqH with $\mathrm{H} \rightarrow \mathrm{ZZ} \rightarrow \ell^+\ell^-\ell^+\ell^-$	JHU	8.80×10^{-6}	-	[154]
$\mathrm{t\bar{t}W}$+jets with $\mathrm{W} \rightarrow \ell\nu$	MadGraph5_aMC@NLO+MadSpin	0.2043 ± 0.0020	1.94	[154]
$\mathrm{t\bar{t}Z} \rightarrow 2\ell + 2\nu +$ other, with $m_{\ell\ell} > 10$ GeV	MadGraph5_aMC@NLO+MadSpin	0.2529 ± 0.0004	2.15	[154]
$\mathrm{t\bar{t}H}$,no $\mathrm{b\bar{b}}$ decays	POWHEG	0.2151	-	[154]
$\mathrm{t\bar{t}H}$, $\mathrm{b\bar{b}}$ decays	POWHEG	0.2934	-	[154]
$\mathrm{WW} \rightarrow 2\ell 2\nu$	POWHEG	12.178	-	[155]
$\mathrm{ZZ} \rightarrow 4\ell$	POWHEG	0.3366	-	[154]
WZZ	MadGraph5_aMC@NLO+ MadSpin	0.05565	1.14	[154]
ZZZ	MadGraph5_aMC@NLO	0.01398	1.17	[154]
single top quark tWZ, with $\mathrm{Z}_{\mu} \rightarrow \ell^+\ell^-$	MadGraph5_aMC@NLO(LO)+MadSpin	0.001123	-	[154]
single top quark t-channel $\mathrm{\bar{t}}$	POWHEG+MadSpin	$44.33\,^{+1.76}_{-1.49}$	-	[154]
single top quark t-channel t	POWHEG+MadSpin	$26.38\,^{+1.32}_{-1.18}$	-	[154]
single top quark $\mathrm{\bar{t}W}$	POWHEG	35.85 ± 0.90 (scale) ± 1.70 (PDF)	-	[154]
single top quark tW	POWHEG	35.85 ± 0.90 (scale) ± 1.70 (PDF)	-	[154]
$\mathrm{t\bar{t}}$	POWHEG	$831.76\,^{+19.77+35.06}_{-29.20-35.06}$	-	[154]
$\mathrm{Z}/\gamma^* +$jets, with $m_{\ell\ell} >$ 50GeV	MadGraph5_aMC@NLO	$3 \times (1921.8 \pm 0.6 \pm 33.2)$	1.49	[154]
$\mathrm{Z}/\gamma^* +$jets, with 10 GeV $< m_{\ell\ell} <$ 50 GeV	MadGraph	18610	-	[154]

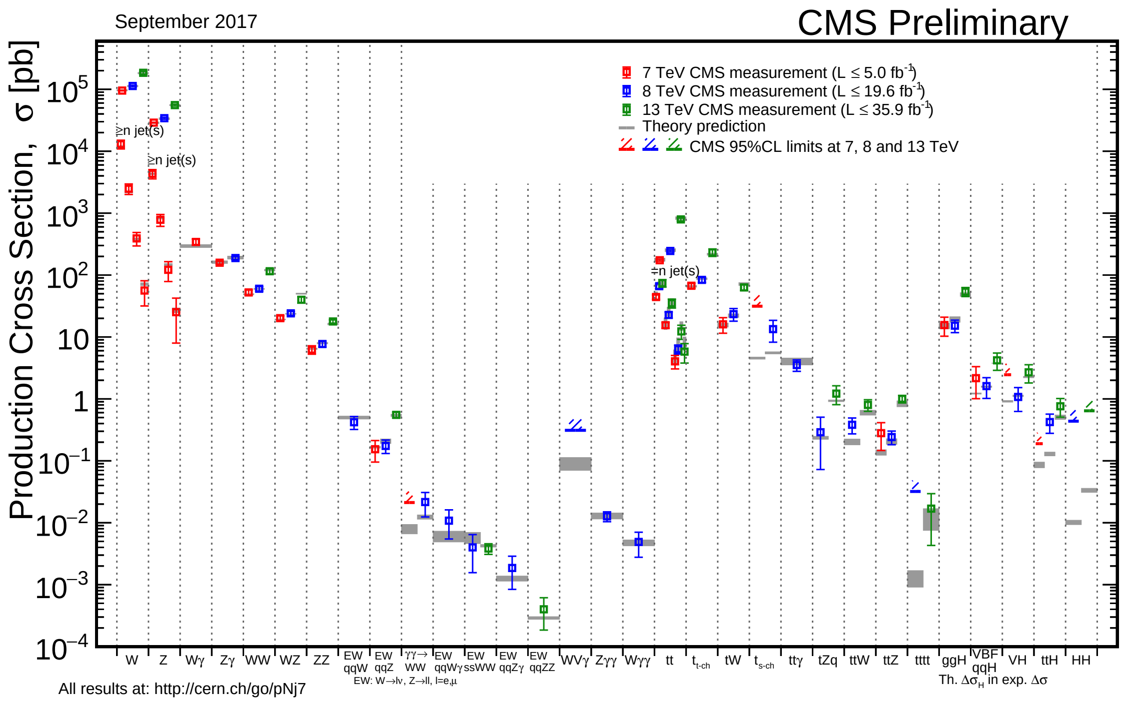

Figure 3.4: Summary of the SM cross section measurements performed by the CMS collaboration. Figure taken from [50].

3.3 Multivariate analysis techniques: Boosted Decision Trees

The need for processing large quantities of data and discriminating between events with largely similar experimental signatures makes multivariate analysis (MVA) a largely used method in the physics community. Multivariate classification methods based on machine learning techniques are a fundamental ingredient to most analyses. The advantage of using a MVA classifier is that it can achieve a better discrimination power with respect to a simpler analysis based on individual selection criteria or poorly discriminating variables. A risk of using MVA classifiers is overtraining. This happens when there are too many model parameters of an algorithm adjusted to too few data points. This leads to an increase in the classification performance over the objectively achievable one.

There are many software tools that exist for MVA. In this thesis, the `Tool for Multivariate Analysis` (TMVA) [156] is used. This software is an open source project included into `ROOT` [157]. By training on events for which the classification is known, a mapping function is determined that describes a classification or an approximation of the underlying behaviour defining the target value (regression). Boosted decision trees (BDT) are employed for the classification of events as implemented in the `TMVA` framework [156]. This multivariate technique is based on a set of decision trees where each tree yields a binary output depending on the fact that an event is signal- or background-like. This has as advantage that several discriminating variables can be combined into a powerful one-dimensional discriminant D.

The decision tree is constructed by training on a dataset for which the outcome is already provided, such as simulation datasets with signal and background processes (supervised learning). Different trees can be combined into a forest where the final output is determined by the majority vote of all trees, so-called boosting. This stabilises the decision trees against statistical fluctuations and makes it possible to keep the decision trees very shallow, making the method more robust against overtraining. Examples of such boosting algorithms are Adaptive Boosting (AdaBoost) and Gradient Boosting [158]. For the search presented in the following chapters, Gradient boost is used with a learning rate of 0.2-0.3 and the depth of the tree is set to three. Additionally, the Gradient boost is used in combination with bagging, so-called stochastic gradient boosting. Bagging smears the statistical fluctuations in the training data and therefore stabilises the response of the classifier and increases the performance by eliminating overtraining. More information about stochastic gradient boosting can be found in Ref. [159].

The discriminating power of a BDT is assessed by analysing the receiver operating characteristic (ROC) curve. This curve represents the background rejection over the signal efficiency of the remaining sample. The area under the curve (AUC) is compared to random guessing in order to identify the best classifier. When the multivariate discriminator has no discriminating power, the resulting AUC will be 0%, while 50% means fully separated event classes. In Figure 3.5 examples of ROC curves are shown.

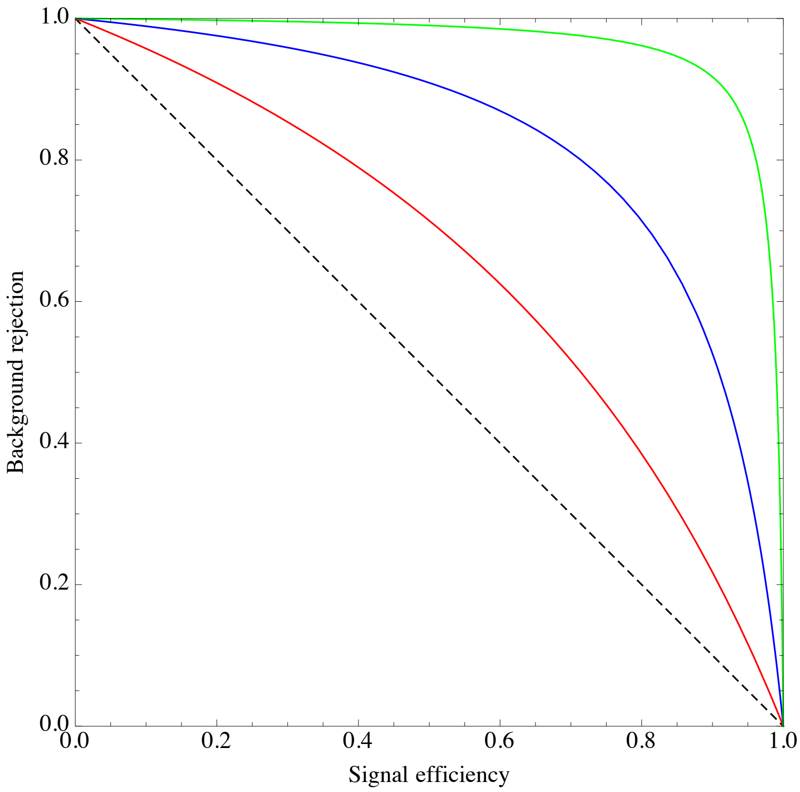

Figure 3.5: Example of ROC curves. In this example, the green method is better than the blue one, which is better than the red one. The dashed line represents a case where there is no separation. Figure taken from [160].

3.4 Statistical methodology

The search performed in the framework of this thesis requires the simultaneous analysis of data from different decay channels. The statistical methodology used for this search is developed by the ATLAS and CMS collaborations in the context of the LHC Higgs Combination group [161–164]. The `Higgs Combine Tool` [165] is a `RooStats` [166] framework which runs different statistical methods. In this section, only the statistical tools necessary for the performed search are described [162].

The event yields of signal and background processes are denoted as s and b respectively. These represent event counts in multiple bins or unbinned probability density functions. By use of simulation, predictions on both signal and background yields are made. The multiple uncertainties on these predictions are accounted for by introducing nuisance parameters θ such that $s = s(\theta)$ and $b = b(\theta)$.

The Bayesian and modified classical frequentist statistical approaches are used in high energy physics to characterise the absence of a signal. The level of incompatibility of data with a signal hypothesis is quantified in terms of confidence levels (CL). The convention is to require a 95% CL for excluding a signal. In general, limits are not set on the signal cross section directly, but are set on the signal strength modifier μ. The signal strength modifier is defined such that it equally changes all the cross sections of all production mechanisms of the signal by the same factor.

In this thesis, the modified frequentist approach [167, 168] for confidence levels, which adopts the classical frequentist method to allow nuisance parameters, is used. It constructs a likelihood $\mathfrak{L}(\text{data}|\,\mu,\theta)$ as

$$\mathfrak{L}(\text{data}|\,\mu,\theta) = \text{Poisson}\left(\text{data}|\,\mu s(\theta) + b(\theta)\right)\, \text{pdf}(\tilde{\theta}|\theta). \tag{3.6}$$

The probability density function $\text{pdf}(\tilde{\theta}|\theta)$ describes all sources of uncertainty. In this thesis, all sources of uncertainties are assumed to be either 100% correlated or uncorrelated. When uncertainties are partially correlated, they are broken down to subcomponents that fit those requirements. This allows to include all constraints in the likelihoods in a clean factorised form.

A systematic uncertainty pdf $\rho(\theta|\tilde{\theta})$ for the nuisance θ with nominal value $\tilde{\theta}$ is used. It reflects the degree of belief of what the true value of the θ is. In this thesis, the approach from the `Higgs Combine Tool` is used where the pdfs $\rho(\theta|\tilde{\theta})$ are re-interpreted as posteriors of real or imaginary measurements $\tilde{\theta}$

$$\rho(\theta|\tilde{\theta}) \sim \text{pdf}(\tilde{\theta}|\theta)\, \pi_\theta(\theta), \tag{3.7}$$

where $\pi_\theta(\theta)$ is the hyper prior for the (imaginary) measurements. The pdfs used by the `Higgs Combine Tool` are described in Ref. [164].

The data in Equation 3.6 represents either the actual observation or pseudo-data to construct sampling distributions. For a binned likelihood, the Poisson probabilities to observe n_i events in bin i is given as

$$\text{Poisson}\left(\text{data}|\,\mu s(\theta) + b(\theta)\right) = \prod_\text{i} \frac{\left(\mu s_\text{i}(\theta) + b_\text{i}(\theta)\right)^{n_\text{i}}}{n_\text{i}!} e^{-\mu s_\text{i}(\theta) - b_\text{i}(\theta)}. \tag{3.8}$$

At the LHC, the test statistic is defined as

$$q_{\mu} = -2\ln\frac{\mathfrak{L}(\text{data}|\,\mu,\hat{\theta}_{\mu})}{\mathfrak{L}(\text{data}|\,\hat{\mu},\hat{\theta}_{\mu})}, \tag{3.9}$$

where the likelihood is maximised in the numerator (maximum likelihood estimator, MLE) for a given μ and (pseudo) data at $\hat{\theta}_{\mu}$, while $\hat{\mu}$ combined with $\hat{\theta}$ defines the point for which the likelihood reaches its global maximum. The estimated signal strength modifier $\hat{\mu}$ can not become negative since a signal rate is positive defined by physics. Furthermore, an upper constraint on the MLE $\hat{\mu} \leq \mu$ is imposed.

The signal is excluded at $1-\alpha$ confidence level when

$$\text{CLs} = \frac{\text{P}\left(q_{\mu} \geq q_{\mu}^{\text{obs}}|\,\mu s+b\right)}{\text{P}\left(q_{\mu} \geq q_{\mu}^{\text{obs}}|\,b\right)} \leq \alpha, \tag{3.10}$$

with $\text{P}\left(q_{\mu} \geq q_{\mu}^{\text{obs}}|\,\mu s+b\right)$ the probability to observe a value of the test statistic at least as large as the one observed in data q_{μ}^{obs}, under the signal plus background $(s+b)$ hypothesis, and $\text{P}\left(q_{\mu} \geq q_{\mu}^{\text{obs}}|\,b\right)$ for the background only (b) hypothesis. These probabilities are defined as

$$\begin{aligned} p_{\mu} &= \text{P}\left(q_{\mu} \geq q_{\mu}^{\text{obs}}|\,\mu s+b\right) = \int_{q_{\mu}^{\text{obs}}}^{\infty} f(q_{\mu}|\,\mu,\hat{\theta}_{\mu}^{\text{obs}})\,dq_{\mu}, \\ 1-p_{b} &= \text{P}\left(q_{\mu} \geq q_{\mu}^{\text{obs}}|\,b\right) = \int_{q_{\mu=0}^{\text{obs}}}^{\infty} f(q_{\mu}|\,\mu=0,\hat{\theta}_{\mu=0}^{\text{obs}})\,dq_{\mu}, \end{aligned} \tag{3.11}$$

where p_{μ} and p_{b} are the p-values associated to the two hypotheses, and $f(q_{\mu}|\,\mu,\hat{\theta}_{\mu}^{\text{obs}})$ and $f(q_{\mu}|\,\mu=0,\hat{\theta}_{\mu=0}^{\text{obs}})$ are the probability density functions of the signal plus background and background only hypothesis constructed from toy Monte Carlo pseudo data. These are generated with nuisance parameters fixed to $\hat{\theta}_{\mu=0}^{\text{obs}}$ (background only) and $\hat{\theta}_{\mu}^{\text{obs}}$ (signal plus backgound). The 95% CL level upper limit on μ is achieved by adjusting μ until CLs= 0.05, this is the so-called observed limit. The expected median upper limit and the $\pm1\sigma$ and $\pm2\sigma$ bands for a hypothesis is generated by a large set of pseudo data and calculating the CLs and the value of μ at 95% CL for each of them. A cumulative probability distribution can be built by starting the integration from the side corresponding to low event yields. The median expected value, so-called expected limit at 95% CL, is where the cumulative distribution function crosses the 50% quantile. The $\pm1\sigma$ (68%) and $\pm2\sigma$ (95%) bands on the expected limit are defined by the crossings of the 16% and 84%, and 2.5% and 97.5% quantiles.

In order to significantly reduce computing time, the Asymptotic CL method is used. This method avoids an ensemble of toy Monte Carlo samples and instead replaces it by one representative dataset, called Asimov dataset. This dataset is constructed such that all observed quantities are set equal to their MLE values ($\hat{\theta}_{\text{Asimov}} = \theta_0$). More information about this procedure can be found in Ref. [162].

4 Event reconstruction and identification

The simulated data after the detector simulation described in Section 3.2, has the exact same format as the real collision data recorded by the CMS experiment. Therefore the same software can be used for the reconstruction of both simulation and real data. In Section 4.1, the object reconstruction is explained. After reconstructing the objects, they are connected to physics objects, which need to be identified (Section 4.2) and corrected for pileup (Section 4.3). The objects used for physics analysis have extra requirements as shown in Section 4.4. A summary of all the corrections applied to data and simulation is given in Section 4.5.

4.1 Object Reconstruction

In Figure 4.1, the particle interaction in a transverse slice of the CMS detector is shown. When a particle is created in the collisions in the detector, it first enters the tracker where charged particle trajectories, so-called tracks, and origins, so-called vertices, are reconstructed from signals or hits in the sensitive layers. The magnetic field bends the charged particles making it able to measure the electric charges and momenta of charged particles. The electrons and photons are absorbed in the ECAL and the corresponding electromagnetic showers are detected as clusters of energy in adjacent cells. From this, the energy and the direction of the particles can be determined. The charged and neutral hadrons initiate a hadronic shower in the ECAL, and their showers are fully absorbed in the HCAL. The clusters from these showers are used to estimate the energy and direction of the hadrons. Muons and neutrinos pass through the calorimeters without little to no energy loss and the neutrinos even escape the CMS detector undetected while muons produce hits in the muon detectors.

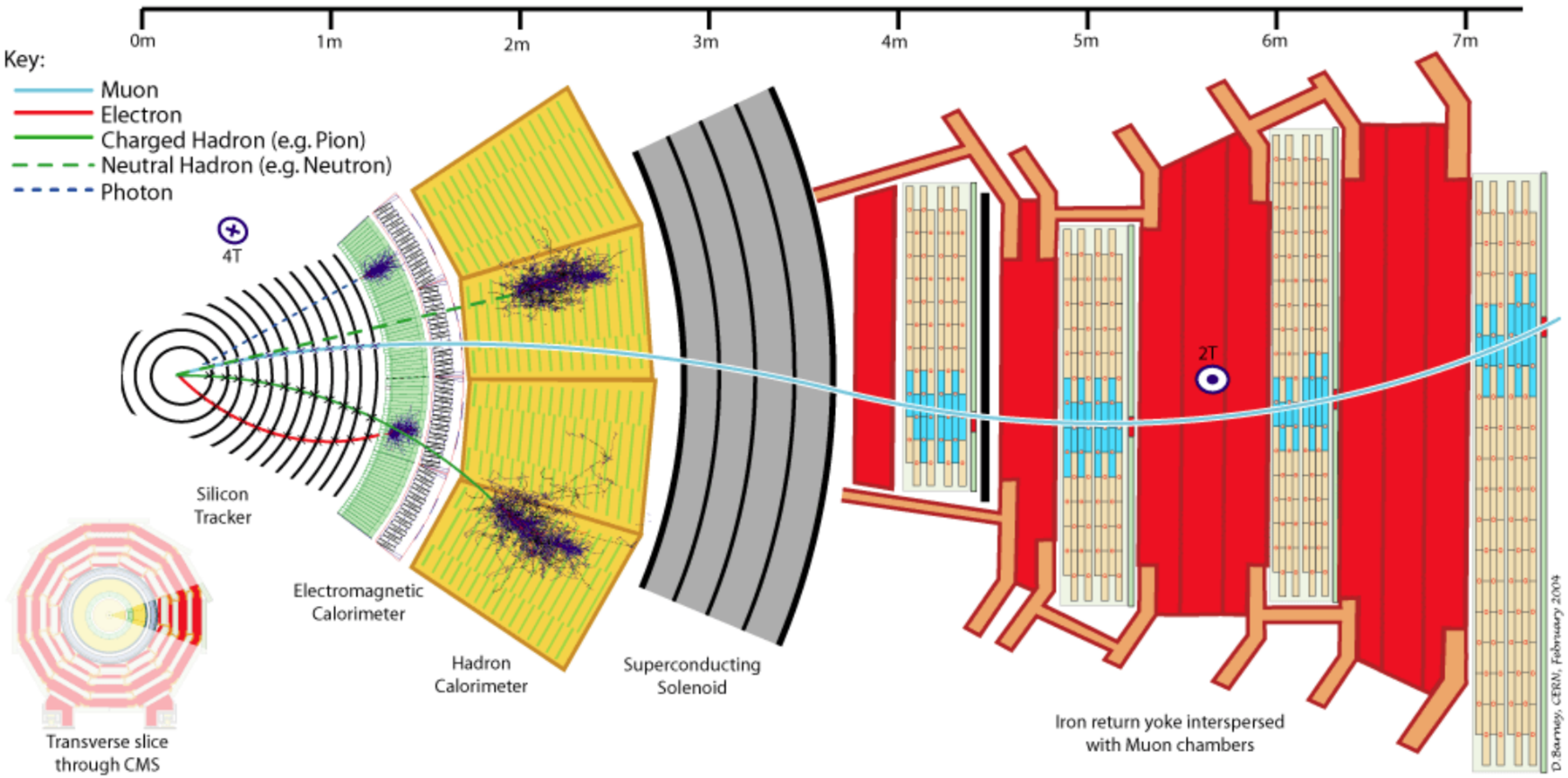

Figure 4.1: Cross-section of the CMS detector with all parts of the detector labelled. This sketch shows the specific particle interactions from a beam interaction reaching the muon detector. The muon and charged pion are positively charged, the electron is negatively charged. Figure taken from [169].

The particle flow (PF) [169] reconstruction algorithm correlates the tracks and clusters from all detector layers with the identification of each final state particle, and combines the corresponding measurements to reconstruct their properties. The muon is identified by a track in the inner tracker, connected to a track in the muon detector as described in Section 4.1.2. The electrons are identified by a track and an ECAL cluster, not connected to an HCAL cluster as described in Section 4.1.3. The ECAL and HCAL clusters without a track link identify the photons and neutral hadrons, while the addition of the tracker determines the energy and direction of a charged hadron (Section 4.1.5).

4.1.1 Charged particle tracks

An iterative tracking algorithm is responsible for the reconstruction of the tracks made by charged particles in the inner tracking system. Each iteration consists of four steps [91]: the track-seed generation, the pattern recognition algorithm, removal of track-hit ambiguities and a final track fit. The pattern recognitions are done by use the Kalman filter method [170, 171] which takes into account the magnetic field and multiple scattering effects. All hits that are unambiguously associated to the final track are removed from the list of available hits. In order to associate the remaining hits, the procedure is repeated with looser track reconstruction criteria. The use of the iterative track reconstruction procedure has a high track finding efficiency, while the fake track reconstruction rate is negligible.

4.1.2 Following the muon's footsteps

The muon reconstruction [172] has three subdivisions: local reconstruction, regional reconstruction and global reconstruction. The local reconstruction is performed on individual detector elements such as strip and pixel hits in the inner tracking system, and muon hits and/or segments in the muon chambers. Independent tracks are reconstructed in the inner tracker, so-called tracker tracks, and in the muon system, so-called standalone muon tracks. Based on these tracks, two reconstructions are considered: Global Muon reconstruction and Tracker Muon reconstruction. The first one is an outside-in approach starting from a standalone muon track while the second one uses an inside-out approach starting from tracker tracks. For low transverse momenta ($p_{\mathrm{T}} \lesssim 5$ GeV), the tracker muon reconstruction is more efficient than the global muon approach. This is due to the fact that tracker muons only require a single muon segment in muon system, while the global muon approach requires typically segments in at least two muon stations. These tracker muons are used for identifying muons from the hadronisation of b or c quarks. The Global Muon approach typically improves the Tracker Muon reconstruction for $p_{\mathrm{T}} \gtrsim 200$ GeV.

4.1.3 The path of the electron

Standard tracking algorithms are based on Kalman filtering which assume that the energy loss is Gaussian distributed. Since the electron tracks are increasingly curved in the magnetic field as a function of its flight distance, these standard tracking algorithms are not suitable to fit the electron tracks. The Gaussian sum filter (GSF) [173] is used instead.

In CMS, the electrons are reconstructed in two ways. The older ECAL based tracking is developed to identify high energetic isolated electrons. This tracking algorithm starts from

ECAL clusters with a transverse energy above 4 GeV and extrapolates from these clusters the position of the hits in the tracker. Another, tracker based algorithm uses all the tracks with a p_{T} higher than 2 GeV found with iterative tracking as seeds. The electron seeds from the ECAL- and tracker-based procedures are merged into a unique collection and are then refitted by using the summed Gaussian distributions as uncertainty per hit in the track fit. The electron efficiency is measured in 8 TeV proton collision data to be better than 93% for electrons with an ECAL supercluster energy of $E_{\mathrm{T}} > 20$ GeV [174]. For electrons with an $E_{\mathrm{T}} > 25$ GeV in 13 TeV proton collision data, the efficiency is about 96% [175].

4.1.4 Primary vertex reconstruction

The primary vertex (PV) reconstruction is able to measure the location of all proton interaction vertices in each event consisting of the signal vertex and all vertices from pileup events. First, tracks are selected to be consistent with being produced promptly in the primary interaction [100]. Then the tracks are grouped according to the z coordinate of their closest approach to the beam line [176] and a vertex fitting algorithm [177] is applied. The primary vertex is found as the vertex corresponding to the highest sum of squared transverse momenta and is taken to be the main interaction point. The resolution on the primary vertex is about 14 μm in $r\phi$ and about 19 μm in the z direction for primary vertices with the sum of the track $p_T > 100$ GeV for the 2016 data taking period. A primary vertex is considered a well reconstructed primary vertex when it has at least five degrees of freedom, the longitudinal distance from the beam spot is maximally 24 cm ($d_z < 24$ cm), and the transversal distance from the beam spot is maximally 2 cm ($d_{xy} < 2$ cm).

4.1.5 Calorimeter clusters

The energy and direction of stable neutral particles such as photons and neutral hadrons are reconstructed using a cluster algorithm. This algorithm also separates neutral particles from charged hadron energy deposits, and reconstructs and identifies electrons and their bremsstrahlung photons. Furthermore, the cluster algorithm is contributing to the energy measurements of charged hadrons that don't have accurate track parameters, e.g. for low quality tracks and high transverse momentum tracks. The clustering is performed separately in each subdetetector: ECAL barrel and endcaps, HCAL barrel and endcaps, and the two preshower layers. The HF has no clustering algorithm since the electromagnetic or hadronic cells give rise to an HF EM or HF HAD cluster.

The clustering algorithm consist of different steps. First seeds are identified when cells have an energy larger than the seeding threshold and larger than their neighbouring cells. Then topological clusters are made by accumulating cells that share at least a corner with a cell already in the cluster and an energy above a cell threshold set to twice the noise level. The third step is an expectation maximization algorithm that reconstructs the cluster [169] and assumes that the energy deposits are Gaussian distributed. The calorimeter clusters are used for reconstructing photons and neutral hadrons. The clusters that are not in the vicinity of the extrapolated charged tracks are identified as neutral hadrons or photons. If the energy deposits are in vicinity of charged tracks, as is the case for charged hadrons, the neutral particle energy deposit is measured as an excess over the charged particle deposit.

4.2 Particle flow identification

The several PF elements from the various CMS subdetectors are connected through a link algorithm. This algorithm tests nearest neighbour pairs of elements in an event. The quality of the link is determined via the distance between the two elements and PF blocks of elements are formed from elements with a direct link or indirect link through common elements. The identification and reconstruction follows a particular order in each PF block. After each identification and reconstruction the corresponding PF elements (tracks and clusters) are removed from the PF block.

The muons are the first to be identified and reconstructed. These are reconstructed if their momenta are compatible with corresponding track only momenta. Then the electrons and their corresponding bremsstrahlung photons, are identified and reconstructed by using the GSF tracking. At the same time, the energetic and isolated photons are identified as well. The remaining elements in the PF block are subjected to a cross identification of charged hadrons, neutral hadrons, and photons that arise from parton fragmentation, hadronisation, and decays in jets. The charged hadron candidate is made from the remaining candidates that have a charged particle track associated with them. Then the charged particle energy fraction is subtracted from the calibrated energy of the linked calorimeter clusters and the remaining energy is assigned to the neutral energy. Depending on the excess of neutral energy in the ECAL and HCAL clusters, a photon or a neutral hadron is assigned respectively. The pseudorapidity range of the inner tracker limits the information on the charged particle trajectories to $|\eta| < 2.4$. Outside this range a simplified identification is done for hadronic and electromagnetic candidates only.

4.3 Pileup mitigation and luminosity measurement

For the 8 TeV dataset, an average of about 21 pileup interactions happens per bunch cross section. For the dataset taken at 13 TeV in 2016, the number of pileup interactions increases to about 27 interactions per bunch crossing. These interactions are spread around the beam axis in the centre of the CMS coordinate system and follow a normal distribution with a standard deviation of about 5 cm [169]. The number of pileup interactions is estimated from the number of interaction vertices reconstructed from charged particle tracks, or from the instantaneous luminosity of the given bunch crossing with dedicated detectors and the inelastic proton-proton crossing. The luminosity of the CMS interaction point is estimated from measuring certain process rates with luminometers such as the pixel detector, HF calorimeter, and the pixel luminosity telescope [178]. The instantaneous luminosity from the recorded process rate R is then determined as

$$\mathrm{L}dt = \frac{Rdt}{\sigma_{\mathrm{fid}}}, \tag{4.1}$$

where $\sigma_{\mathrm{fid}} = \sigma \times A$ corresponds to the fiducial cross section recorded in the luminometer acceptance A which is determined using van der Meer scans [179]. The overall uncertainty on the luminosity measurement is estimated to be 2.5%.

The luminosity is used to infer the number of pileup interactions in data, which can be used to correct the predefined pileup interactions in simulation. Then an event weight can be derived from the ratio of the distributions of pileup interactions in data and simulation. For 13 TeV collisions, the inelastic cross section is measured to be 71.3 ± 3.5 mb [180]. However a better agreement in data and simulation for the pileup sensitive variables, such as the number of primary vertices, is found with a lower cross section of 69.2 mb with an uncertainty of 4.6%.

4.4 Physics object reconstruction and identification

The particle flow objects are used for building physics objects that are used for analysis. Analyses use jets, muons, electrons, photons, taus and missing transverse momentum $\vec{p}\!\!/_{\mathrm{T}}$ with extra, analysis dependent requirements. In the following section, only the physics objects used throughout this thesis are discussed.

4.4.1 Muons

The muon candidates used for analysis in this thesis correspond to the tight and loose working point. Detailed reports on the performance can be found in [181].

The tight working point rejects objects wrongly reconstructed as muons from hadron showers that reach the muon system (punch-throughs), by requiring that the global muon fit includes at least one valid hit in the muon chambers for which at least two muon segments in two muon stations are present. Furthermore, the muon tracks should have a global fit yielding a goodness-of-fit of $\chi^2/\mathrm{ndof} < 10$. Requiring at least one pixel hit in the muon track suppresses the in flight decays to muons. Also a minimum of five hits in the tracker is required. Cosmic muons and muons originating from pileup interactions are rejected by constraining the distance of the muon with respect to the primary vertex to $d_{\mathrm{x,y}} < 2$ mm and $d_{\mathrm{z}} < 5$ mm.

Also muons according to the loose muon working point will be used in the thesis. These are either global muons or tracker muons reconstructed from the particle flow muon object. In Table 4.1, the muon requirements for the muons used throughout this thesis are summarised. In Figure 4.2, the muon efficiencies for data and simulation are presented. These efficiencies are estimated from tag-and-probe methods [181]. Overall, the efficiency is about 40-87%, with two drops due to the space between the wheels of the DT system. The differences between data and simulation are corrected by applying p_{T}- and η-dependent scale factors ($\epsilon_{\mathrm{data}}/\epsilon_{\mathrm{MC}}$) to simulated events.

In addition to the identification criteria, the muons are required to be spatially isolated from electromagnetic and hadronic activity. The relative lepton isolation is defined as estimating the total transverse energy of the particles emitted around the direction of the lepton by defining a cone of radius ΔR in the $\eta\phi$ plane around the lepton direction. Then a summed energy is calculated from the charged hadrons (CH), neutral hadrons (NH), and photons (γ), excluding the lepton itself. This sum is then corrected to remove the energy coming from pileup interactions. The relative isolation for muons $\mathscr{I}_{\mu}$ is defined as [169]:

$$\mathscr{I}_{\mu} = \frac{\sum p_{\mathrm{T}}(\mathrm{CH}) + \max\left(0., \sum E_{\mathrm{T}}(\mathrm{NH}) + \sum E_{\mathrm{T}}(\gamma) - 0.5 \times \sum E_{\mathrm{T}}(\mathrm{CH})\right)}{p_{\mathrm{T}}(\mu)}, \tag{4.2}$$

where a cone of $\Delta R = 0.4$ is adopted and the pileup mitigation is based on the $\Delta\beta$ correction. The $\Delta\beta$ correction estimates the pileup energy as half of the contribution coming from charged

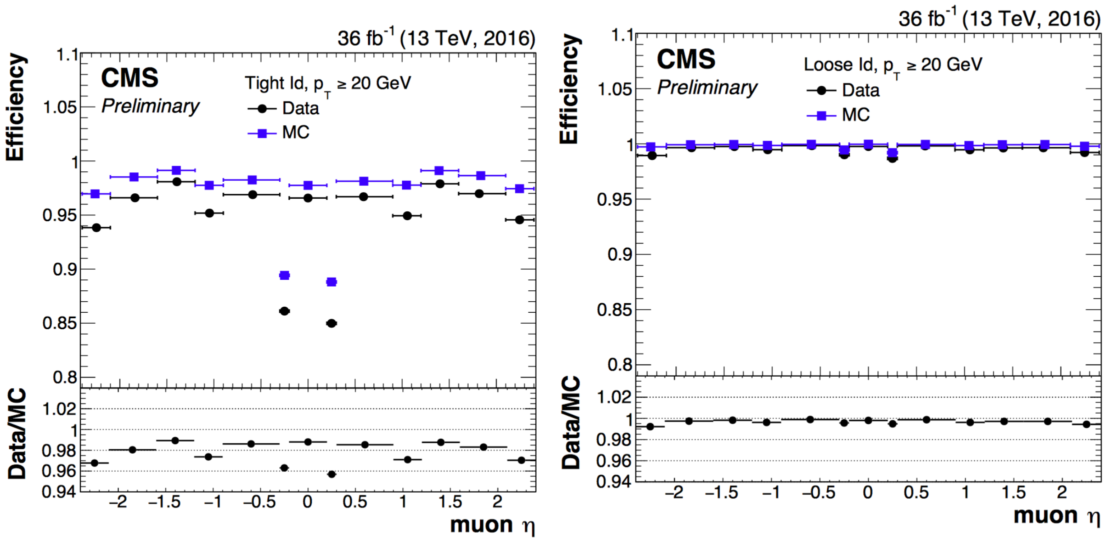

Figure 4.2: Comparison of the muon tight ID (left) and loose ID (right) efficiencies in data and simulation as a function of the pseudorapidity of the muon using the full 2016 dataset. Figure taken from [181].

hadrons. For tight ID muons, this relative isolation should be $\mathscr{I}_\mu < 0.15$, while for loose muons this should be $\mathscr{I}_\mu < 0.25$. In Figure 4.3, the isolation efficiencies as a function of the pseudo rapidities using the tag and probe method are shown for the tight muon working point. The efficiencies are 85-100% and have a decline for low-p_T muons. The differences between data and simulation are accounted for by applying η- and p_T-dependent scale factors on the simulation.

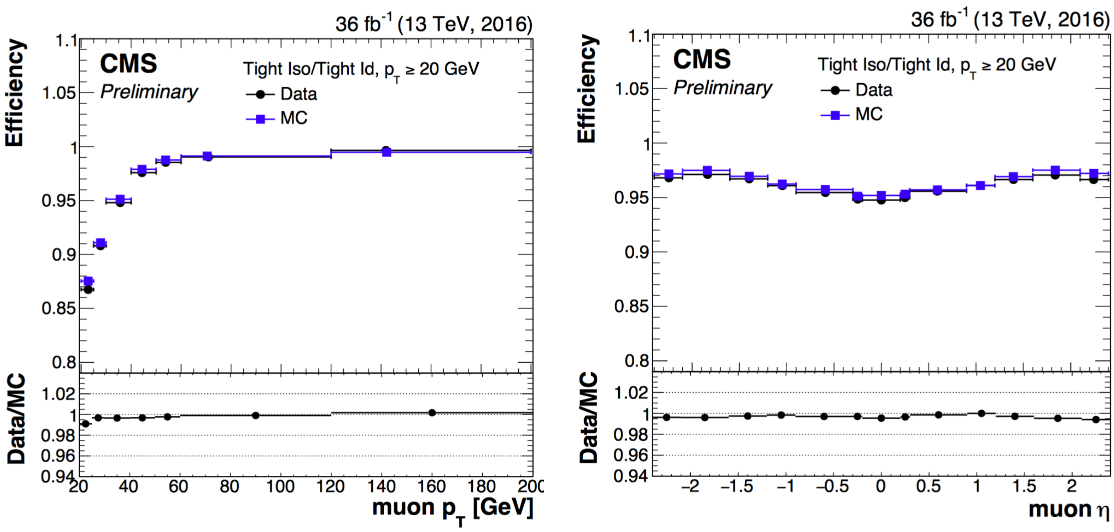

Figure 4.3: Comparison of the muon tight isolation requirement with the muon tight ID efficiencies in data and simulation as a function of the transverse momentum (left) or pseudorapidity (right) of the muon using the full 2016 dataset. Figure taken from [181].

Table 4.1: Muon requirements for the tight and loose working points, used throughout this thesis.

Properties	Loose Muons	Tight Muons
Global muon or Tracker Muon	One or the other	Both
Particle Flow muon	Y	Y
χ^2/ndof of global muon track fit	N/A	< 10
Nb. of hit muon chambers	N/A	> 0
Nb. of muon stations contained in the segment	N/A	> 1
Size of the transverse impact parameter of the track wrt. the PV	N/A	$d_{xy} < 2$ mm
Longitudinal distance wrt. the PV	N/A	$d_z < 5$ mm
Nb. of pixel hits	N/A	> 0
Nb. of tracker layers with hits	N/A	> 5
Relative Isolation	<0.25	<0.15

4.4.2 Electrons

The electron candidates used in this thesis, correspond to the tight and veto working points. The study of the electron reconstruction and identification performance can be found in [175].

Starting from an electron PF candidate with a GSF track that is outside the barrel-endcap transition region ($1.4443 < |\eta| < 1.5660$), several requirements are set. The electron track should not have more than one (two or three) missing hit(s) in the innermost layer for the tight (veto) working point. This dismisses electrons from photon conversions. Additionally, a photon conversion veto is applied by testing if a pair of electron tracks is originating from a common displaced vertex. Furthermore, refined cuts are applied on the shower shape variables such as the difference in η or ϕ between the energy weighted supercluster position in the ECAL and the track direction at the innermost tracker position ($\Delta\eta_{\text{in}}$, $\Delta\phi_{\text{in}}$), and the ECAL crystal based shower covariance in the η direction ($\sigma_{\eta\eta}$). These cuts also include energy related variables such as the absolute difference between the inverse electron energy measured in the ECAL and the inverse momentum measured in the tracker ($|1/E - 1/p|$), and the ratio of the energy measured in the HCAL and ECAL (H/E). Unlike the muon case, the identification criteria also contain requirements on the isolation of the electrons.

Similar to the muons, the electron relative isolation is determined from the sum of the particles in a cone around the electron itself. The cone radius used for electrons is $\Delta R = 0.3$ and a ρ correction for pileup mitigation is applied. For this correction, the expected pileup energy inside the isolation cone is estimated from the median density energy per area of pileup contamination (ρ), computed event by event, and the effective area ($A_{\text{eff.}}$) [169]. This effective area is estimated from simulation and denotes the expected amount of neutral energy from pileup interactions per ρ within the isolation cone as a function of the pseudorapidity of the associated ECAL superclusters. Table 4.2 shows the values used for 13 TeV data. The relative electron isolation $\mathscr{I}_{\text{e}}$ is calculated as

$$\mathscr{I}_{\text{e}} = \frac{\sum p_{\text{T}}(\text{CH}) + \max\left(0., \sum E_{\text{T}}(\text{NH}) + \sum E_{\text{T}}(\gamma) - \rho \times A_{\text{eff.}}\right)}{p_{\text{T}}(\text{e})}. \tag{4.3}$$

Table 4.2: The effective areas $A_{\text{eff.}}$ used for the electron relative isolation [182].

η region	$A_{\text{eff.}}$
$0 < \|\eta\| < 0.1752$	0.1703
$1.0 < \|\eta\| < 0.1479$	0.1715
$1.479 < \|\eta\| < 2.0$	0.1213
$2.0 < \|\eta\| < 2.2$	0.1230
$2.2 < \|\eta\| < 2.3$	0.1635
$2.3 < \|\eta\| < 2.4$	0.1937
$2.4 < \|\eta\| < 2.5$	0.2393

The efficiency of electron identification is estimated from $Z \rightarrow e^{-}e^{+}$ events via the tag-and-probe method and is shown in Figure 4.4 for the tight working point. The efficiencies reach $60-87\%$. The difference between data and simulation is corrected for by dedicated p_{T}- and η dependent scale factors as well.

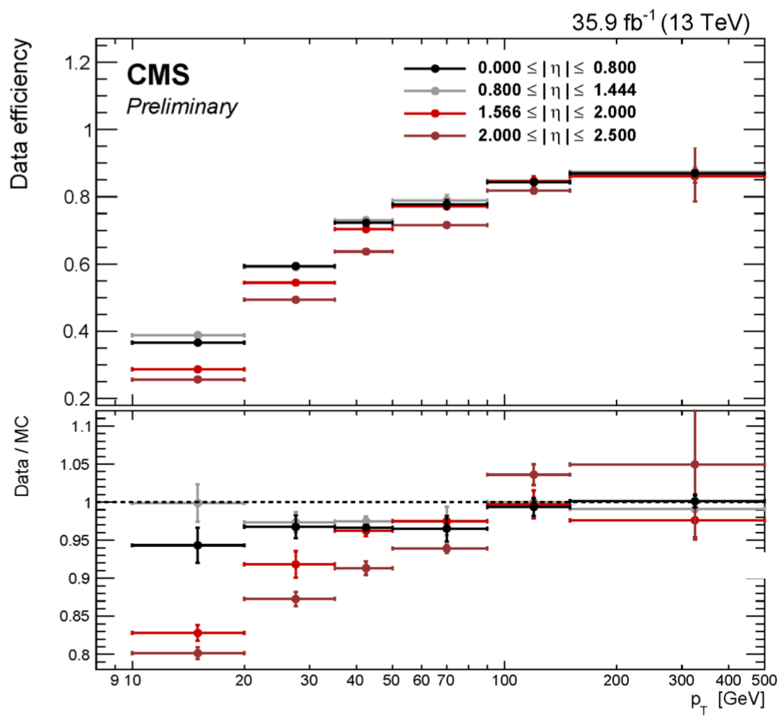

Figure 4.4: Electron identification efficiency as function of the electron transverse momentum from the full 2016 dataset. Figure taken from [175].

Table 4.3: Electron requirements used in this analysis. The requirements are set in the barrel ($|\eta_{supercluster}| \leq 1.479$) and the endcaps ($|\eta_{supercluster}| > 1.479$).

Properties	$\|\eta_{supercluster}\| \leq 1.479$		$\|\eta_{supercluster}\| > 1.479$	
	Veto electron	Tight electron	Veto electron	Tight electron
$\sigma_{\eta\eta}$	< 0.0115	< 0.00998	< 0.037	< 0.0292
$\|\Delta\eta_{\mathrm{in}}\|$	< 0.00749	< 0.00308	< 0.00895	< 0.00605
$\|\Delta\phi_{\mathrm{in}}\|$	< 0.228	< 0.0816	< 0.213	< 0.0394
H/E	< 0.356	< 0.0414	< 0.211	< 0.0641
relative isolation	< 0.175	< 0.0588	< 0.159	< 0.0571
$\|1/E - 1/p\|$ (GeV^{-1})	< 0.299	< 0.0129	< 0.15	< 0.0129
expected missing inner hits	≤ 2	≤ 1	≤ 3	≤ 1
conversion veto	Y	Y	Y	Y

4.4.3 Jets

Jets are reconstructed from all reconstructed particles without the charged hadrons associated to pileup vertices. The clustering is done with the anti$-\mathrm{k_T}$ algorithm [183] with a radius parameter for the cone size of the resulting jet of $R = 0.4$. More information about the jet algorithm performance can be found in Ref. [184].

The jets used for the analysis in this thesis, are identified according to the loose identification working point summarised in Table 4.4. The requirements on the jet constituents are based on the assumption that a proper jet originating from the hadronisation of a quark or gluon consists of multiple PF particles and types. Therefore, the jet should consists of more than one constituent, and the neutral hadron fraction and neutral EM energy fractions should be less than 99%. For the jets within the tracker acceptance ($|\eta| < 2.4$), at least one constituent has to be a charged hadron resulting in a charged hadron energy fraction above 0%. Additionally the charged EM energy fraction should be less than 99%. On top of these requirements, objects that are labelled as jets and found in the vicinity of any isolated lepton, $\Delta R < 0.3$, are removed from the jet collection in that event to avoid duplications of objects.

Table 4.4: Jet criteria used throughout the thesis. The last three requirements are only for jets within the tracker acceptance.

Properties	Loose Jet ID
Neutral hadron fraction	< 0.99
Neutral EM fraction	< 0.99
Number of constituents	> 1
Charged hadron fraction	> 0
Charged multiplicity	> 0
Charged EM fraction	< 0.99

The energy of the reconstructed jets deviates from the energies of the corresponding jets clustered from the hadronisation products of true partons from simulations due to non-linear subdetetector responses and efficiencies. The jet energy corrections (JEC) calibrate the jets in order to have the correct energy scale and resolution. The performance of the jet energy corrections for the 13 TeV dataset can be found in Ref. [185].

Jet energy scale corrections (JES) are determined as a function of pseudorapidity and the transverse momentum from data and simulated events by combining several channels and methods. This is extensively described in Ref. [186]. These corrections account for the effects of pileup, the non uniformity of the detector response, and residual data-simulation jet energy scale differences.

The JES are factorised and subsequently correct for the off-set energy due to pileup, the detector response to hadrons, and residual differences between data and simulation as a function of the jet pseudorapidity and transverse momentum. The consecutive steps of JEC are shown in Figure 4.5. The off-set corrections remove the dependency of the jet energy response of

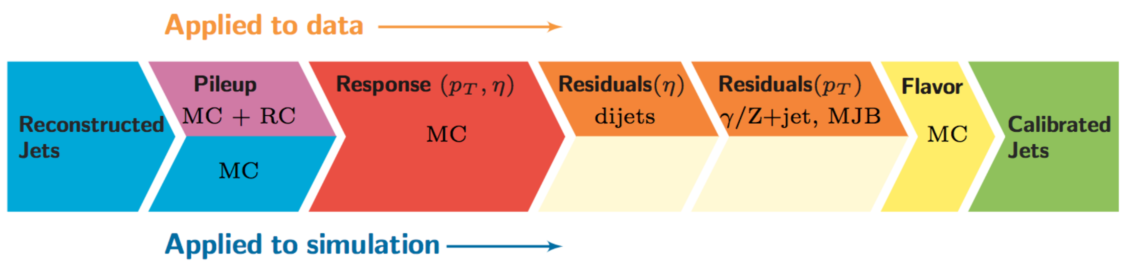

Figure 4.5: The sequence of the JES for data and simulations The corrections marked with MC are derived from simulation studies, while RC stands for random cone, and MJB for the analysis of multi-jet events. Figure taken from [186].

additional pileup activity. It is based on the jet area method, which uses the effective area of the jets multiplied by the average density in the event, to calculate the off-set energy to be subtracted from the jets. The correction factors are derived by comparing the jet response with and without pileup events. The residual differences between data and detector simulation are determined using the random cone method (RC). For this method, many jets are reconstructed in each event by clustering particles through placing random cones. This provides a mapping of the $\eta\phi$ plane and the average p_{T} of those jets gives the average energy off-set due to pileup [186]. The next level of corrections have as goal to have a uniform energy response independent of the transverse momentum or pseudorapidity of the jet. These corrections are determined from simulated events by matching the reconstructed jets to true particle jets and comparing their momenta. The residual corrections between data and simulation are determined by comparing the transverse momentum balance in various types of events (multi-jet, $\mathrm{Z}+$jets, and $\gamma+$jets), using a reference jet in the barrel region. The jet flavour corrections are optional and not used for this thesis. More information on the jet flavour corrections can be found in Ref. [186]. For jets with a transverse momentum above 30 GeV, the uncertainties from the various corrections are 3-5% for the 13 TeV dataset [185].

After applying JES, the transverse momentum resolution of the jet is extracted from data and simulated events. The jet energy resolution (JER) is measured in data and simulation as a function of pileup, jet size and jet flavour. There are two methods used to rescale the reconstructed four momentum based on whether or not the simulated jet can be matched to a true jet in simulation. The factors are defined as

$$\begin{aligned} c_{\mathrm{matched}} &= 1 + \frac{p_{\mathrm{T}}^{\mathrm{reco.}} - p_{\mathrm{T}}^{\mathrm{true}}}{p_{\mathrm{T}}^{\mathrm{reco.}}}\left(s_{\mathrm{JER}} - 1\right), \\ c_{\mathrm{unmatched}} &= 1 + \mathrm{N}(0, \sigma_{\mathrm{JER}})\sqrt{\max\left(s_{\mathrm{JER}}^2 - 1, 0\right)}, \end{aligned} \tag{4.4}$$

where $\mathrm{N}(0, \sigma_{\mathrm{JER}})$ denotes a sample value from a normal distribution centred at zero with as standard deviation the relative resolution in simulation σ_{JER}, and s_{JER} the η-dependent resolution scale factors. These scale factors are derived in data from di-jet or $\gamma + \mathrm{jets}$ events and analysing the p_{T} balance. The resolution scale factors (data/simulation) are found to be 1.1-1.2 [185].

4.4.4 Jets from b quark fragmentation

Jets originating from the hadronisation of bottom quarks can be discriminated from jets from gluons and light-flavour quarks as well as charm quark fragmentation through the use of b-tagging. There are several algorithms developed within CMS to perform b-tagging [187, 188] on jets that fall within the pseudorapidity acceptance of the trackers. These algorithms exploit the properties of the b quark to identify the jet formed by fragmentation. The b hadrons have relative large masses, long lifetimes and daughter particles with hard momentum spectra. Additionally, their semi-leptonic decays can be exploited as well. To use b jet identification in an analysis, one needs to know the efficiency and misidentification probability of the algorithm. In general, these are function of the pseudorapidity and transverse momentum of the considered jet. Their performances are directly measured from data by use of b jet enriched jet samples (multi-jet or top-quark decays).

This thesis uses b jets identified by the Combined Secondary Vertex version 2 (CSVv2) algorithm [187]. This algorithm combines secondary vertices together with track based lifetime information by use of a multivariate technique. The secondary vertex is reconstructed from displaced tracks within a jet, as illustrated in Figure 4.6. The final state b quark provides a B meson (e.g. $\mathrm{B}^{\pm}$, B_0, B_S) after the hadronisation. This B meson has a relatively long lifetime and can travel a measurable distance from the primary vertex before decaying. After reconstruction, the secondary vertices are rejected if not in accordance with the B meson hypothesis based on the amount of shared tracks with the primary vertex, the invariant vertex mass to reject kaon decays, and the direction of the tracks compared to the jet axis.

The b-tagging algorithm performances are evaluated taking into account two cases: discrimination against jets originating from charm quarks, and discrimination against jets coming from gluons or light (u, d, s) quarks. In Figure 4.7, the misidentification probabilities for different b-tagging algorithms within CMS are shown. Different working points are defined based on certain values of the misidentification probability corresponding to the CSVv2 discriminator. These are shown in Table 4.5. The analysis presented in this thesis uses the loose working point which has an average efficiency of 81% and a misidentification probability of 10%.

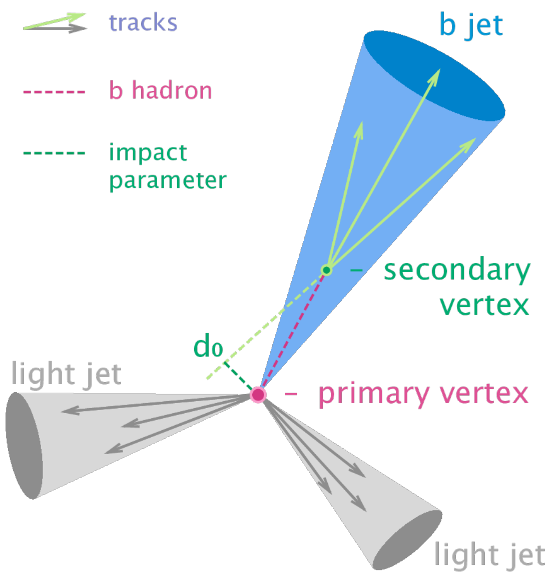

Figure 4.6: Sketch showing the common principle of the identification of b jets. Figure taken from [189].

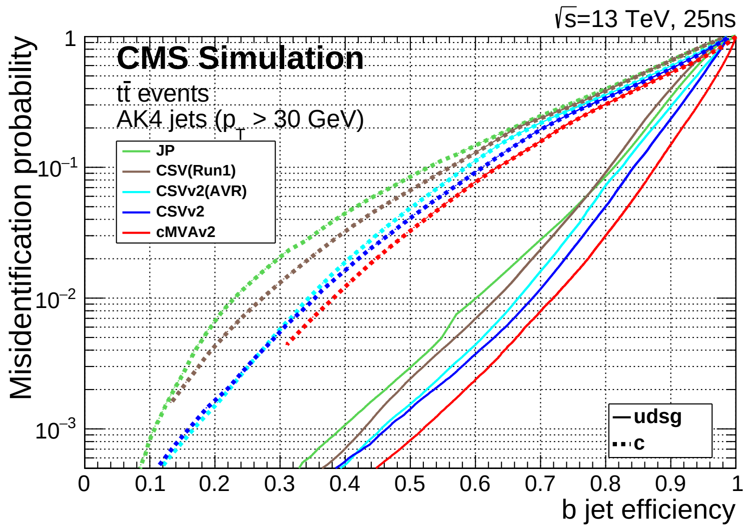

Figure 4.7: Misidentification probabilities of various b-tagging algorithms in simulation. Figure taken from [188].

Table 4.5: Working points used for tagging jets as coming from b quarks for the CSVv2 discriminant.

WP	CSVv2 discr cut	b-tag eff.	misid. prob.
Loose (L)	> 0.5426	$\approx 81\%$	$\approx 10\%$
Medium (M)	> 0.8484	$\approx 66\%$	$\approx 1\%$
Tight (T)	> 0.9535	$\approx 46\%$	$\approx 0.1\%$

The efficiency of tagging a jet as coming from a bottom quark in simulation typically deviates somewhat from data. Efficiency scale factors $\epsilon_b^{data}/\epsilon_b^{MC}$ are derived from data to account for those differences. These scale factors are η-, p_T-, and flavour-dependent, where the flavour of the jet is determined from matched generated hadrons. For cut based analyses these scale factors are applied to the b-tagging efficiencies and mistag probabilities according to the chosen working point [188]. For shape-based analyses however, such as the one presented in this thesis, the scale factors are applied on the distribution of the b-tagging discriminator. This is the so-called IterativeFit method [190].

The uncertainties related to the IterativeFit method cover the possible shape discrepancies between data and simulation. There are two uncertainties coming from the purity of the sample based on the purity of the light flavoured (lf) and heavy flavoured (hf) jet contributions in the sample. Furthermore, the jet energy scale results in jets migrating from one p_T bin to another and has an influence on the bin dependent scale factors. Also the statistical fluctuations of the limited amount of entries in each bin are accounted for and have an influence on the scale factor uncertainties. The statistical fluctuations have four uncorrelated sources: two for heavy flavour and two for light flavour jets. The uncertainty on the scale factors for the jets originating from a charm quark (cf) is determined from the uncertainty on the scale factors from a bottom quark, and results in two independent uncertainties [188].

4.4.5 Missing transverse energy

The missing transverse momentum $\vec{\not{p}}_T$ and energy E_T^{miss} resulting from particles that do not interact with the detector material, are calculated by balancing the vectorial sum of the transverse momenta of all particles:

$$
\begin{aligned}
E_T &= \left|\vec{\not{p}}_T\right|, \\
\vec{\not{p}}_T &= -\sum_{i=1}^{N_{particles}} \vec{p}_{T,i}.
\end{aligned}
\tag{4.5}
$$

The missing transverse energy is influenced by the minimum thresholds in calorimeters, the inefficiencies in the tracker, and the non-linear response of the calorimeter to hadronic particles. The bias is reduced by correcting the transverse momentum of the jets to particle jet p_T via the JEC and propagating it to the missing transverse momentum. The performance of the missing transverse energy reconstruction can be found in [191].

4.5 Summary of corrections

Throughout the chapter several corrections are introduced to improve the agreement between data and simulation. These corrections are sources of systematic uncertainties for the analysis presented in this thesis. Therefore a summary of the corrections and their associated uncertainties is provided.

Lepton scale factors The systematic uncertainty on the lepton scale factors consists of three sources: identification, isolation and tracking. The applied scale factors are varied independently within one standard deviation of their measured uncertainties to account for their systematic impact on the measurements.

Jet energy corrections The momenta of the reconstructed jets are corrected to match on average the expected true energy derived from the hadronisation products of partons in simulation. Furthermore, residual corrections and smearing is applied to match the overall energy scale and resolution for simulation and data. These corrections are also propagated to the missing transverse energy. The systematic uncertainties due to these scale factors are estimated by varying them within their uncertainties and repeating the measurements with recalibrated jets and missing transverse energy.

CSVv2 discriminant shape reweighting There are three sources of uncertainty contributing to the measurement of the scale factors: statistical uncertainties, jet energy scale and the purity of the sample. The jet energy scale uncertainty is 100% correlated to the jet energy uncertainties and is evaluated simultaneously. The uncertainty coming from the purity of the sample is subdivided into two uncorrelated uncertainties based on the purity of the light flavoured (lf) and heavy flavoured (hf) jet contributions in the sample. A one sigma shift in each of the two purity contributions corresponds to a higher/lower contribution in the purity of the considered flavours. The statistical uncertainties have four uncorrelated sources, two for heavy flavour and two for light flavour jets. One of the uncertainties correspond to the shift consistent with the statistical uncertainties of the sample, while the other is propagated in a way that the upper and lower ends of the distribution are affected with respect to the centre of the distribution. The uncertainty on the charm jet scale factors (cf) is obtained from the uncertainty on the heavy flavour scale factors, doubling it in size and constructing two nuisance parameters to control the charm flavour scale factors and treating them as independent uncertainties.

Pileup Varying the minimum bias cross section, used to calculate the pileup distribution by $\pm 4.6\%$, results in a systematic shift in the pileup distribution. The uncertainty is estimated by recalculating the pileup weights to the distributions associated to the minimum bias cross sections.

Luminosity The luminosity is measured with a global uncertainty of 2.5%, affecting the expected number of events.

5 Event selection and categorisation

A basic event selection is made to enhance the signal-like events and is discussed in Section 5.1. The necessary corrections in order to make simulation and data coherent, introduced in Chapter 4, are summarised in Section 4.5 and the resulting data/MC agreement is shown in Section 5.2. The event reconstruction is discussed in Section 5.3.

One of the main background processes entering the analysis are background processes that have prompt leptons contaminated by other leptons. These contaminating leptons originate either from real lepton from decays of tau leptons or from hadronized mesons or baryons (so-called "non-prompt leptons"), or originate from hadrons or jets misidentified as leptons (so-called "fake leptons"). These two classes of contamination together will be referred to as the not prompt-lepton (NPL) background. The NPL background is evaluated with a data-driven method discussed in Section 5.4. The analysis strategy is presented in Section 5.5, where selection criteria are defined to create signal and background regions to constrain the huge SM background compared to the expected signal.

5.1 Baseline event selection and filters

In this analysis a search is performed in a final state made up of a Z boson and a top quark, associated or not with a jet. The leptonic decay of the Z boson and the top quark is considered for which the leading order Feynman diagrams can be seen in Figure 5.1 and Figure 5.2. The signal consists of the single top quark production through a FCNC tZq interaction (tZ in the final state) and the top quark pair production where one of the top quarks decays through the FCNC tZq vertex (tZq with $q = c, u$ in the final state). Their final state signatures consist of three leptons, only considering electrons or muons, and a jet originating from a b quark. For FCNC tZq, there is an additional up or charm jet. Leptons from tau decays are not vetoed and are entering the analysis via their leptonic decays. Four different three-lepton channels based on lepton flavour are considered: 3e, 2e1μ, 1e2μ, and 3μ.

The CMS collaboration recorded in the course of 2016, proton collisions data at a centre-of-mass of 13 TeV with a total recorded integrated luminosity of 35.9 fb^{-1}. The baseline event selection has as goal to substantially reject SM background events, whilst maintaining a high

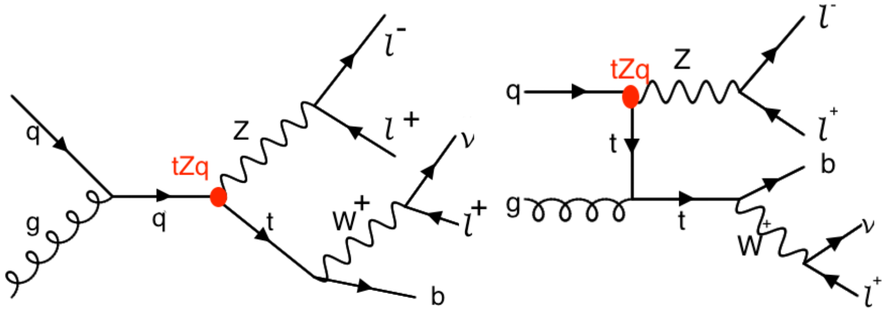

Figure 5.1: Single top quark Feynman diagrams at leading order. The vertex labelled tZq is the sought-for FCNC interaction.

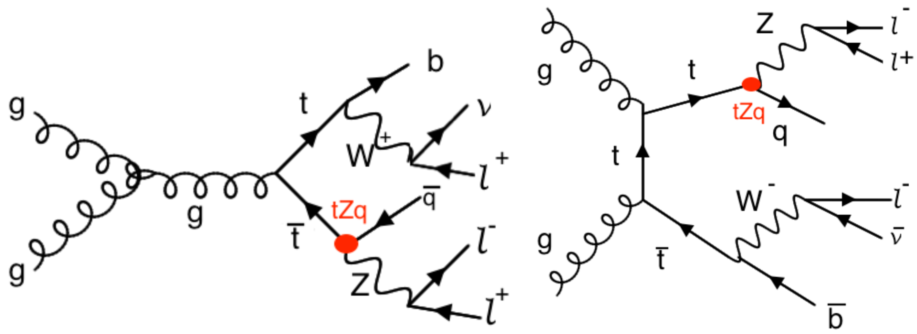

Figure 5.2: Top quark pair Feynman diagrams at leading order. The vertex labelled tZq is the sought-for FCNC interaction.

signal efficiency. The CMS trigger system, described in Section 2.2.3, filters out the main fraction of the collision events from uninteresting processes, and dedicated trigger paths are defined to single out the events with the required detector signature for the search presented in this thesis.

The trigger paths are chosen based on online trigger objects with at least one muon (M), at least one electron (E), at least two muons (MM), at least two electrons (EE), at least one muon and an electron (ME), at least three muons (MMM), at least three electrons (EEE), at least two muons and one electron (MME), or at least two electrons and one muon (EEM). For the MC simulation a simple *or* of all triggers is taken, hence the event is considered when it passes one of the trigger paths. For data however, double counting of the same event has to be taken into account and a procedure to avoid double counting has been put into place. This procedure consists of vetoing in a given dataset the events that are already selected in another, as given in Table 5.1.

For the single lepton triggers, at least one electron (muon) with a transverse momentum p_T higher than 32 (24) GeV is required. The dilepton triggers require the combination of an electron (muon) with $p_T > 23$ GeV and a muon (electron) with $p_T > 8$ GeV, or the combination of an electron (muon) with $p_T > 23\,(17)$ GeV and an electron (muon) with $p_T > 12\,(8)$ GeV. Events collected by the trilepton triggers require a combination of an electron (muon) with

$p_T > 16\,(12)$ GeV, a second electron (muon) of $p_T > 12\,(10)$ GeV, and a third electron (muon) with $p_T > 8\,(5)$ GeV. The mixed trilepton trigger events require a combination of two electrons (muons) with $p_T > 12\,(9)$ GeV and a third muon (electron) with $p_T > 8\,(9)$ GeV. The HLT trigger paths used in data and simulation are summarised in Table 5.2.

Table 5.1: Trigger logic used to select data events in order to avoid double counting.

Dataset	Trigger Logic
1e1μ	EM || EEM || MME
2μ	(MM || MMM) && !(EM || EEM || MME)
2e	(EE || EEE) && !(MM || MMM) && !(EM || EEM || MME)
single μ	M && !(EE || EEE) && !(MM || MMM) && !(EM || EEM || MME)
single e	E && !M && !(EE || EEE) && !(MM || MMM) && !(EM || EEM || MME)

Table 5.2: HLT trigger paths used to select data and simulation events.

Trigger path name	Trigger type
HLT_Mu23_TrkIsoVVL_Ele8_CaloIdL_TrackIdL_IsoVL_v	ME
HLT_Mu23_TrkIsoVVL_Ele8_CaloIdL_TrackIdL_IsoVL_DZ_v	ME
HLT_Mu8_TrkIsoVVL_Ele23_CaloIdL_TrackIdL_IsoVL_v	ME
HLT_Mu8_TrkIsoVVL_Ele23_CaloIdL_TrackIdL_IsoVL_DZ_v	ME
HLT_DiMu9_Ele9_CaloIdL_TrackIdL_v	MME
HLT_Mu8_DiEle12_CaloIdL_TrackIdL_v	EEM
HLT_IsoMu24_v	M
HLT_IsoTkMu24_v	M
HLT_Ele32_eta2p1_WPTight_Gsf_v	E
HLT_Mu17_TrkIsoVVL_Mu8_TrkIsoVVL_v	MM
HLT_Mu17_TrkIsoVVL_TkMu8_TrkIsoVVL_v	MM
HLT_Mu17_TrkIsoVVL_Mu8_TrkIsoVVL_DZ_v	MM
HLT_Mu17_TrkIsoVVL_TkMu8_TrkIsoVVL_DZ_v	MM
HLT_TripleMu_12_10_5_v	MMM
HLT_Ele23_Ele12_CaloIdL_TrackIdL_IsoVL_DZ_v	EE
HLT_Ele16_Ele12_Ele8_CaloIdL_TrackIdL_v	EEE

In order to ensure a full trigger efficiency, the offline p_T thresholds are set higher than the online trigger thresholds. Selected offline electrons (muons) are required to have a $p_T >$ 35 (30) GeV and $|\eta| < 2.1$ (2.4). The electrons and muons corresponding to a tight working point, as discussed in Section 4.4.1 (Table 4.1) and Section 4.4.2 (Table 4.3), are used for analysis. Only events with exactly three leptons are being considered for the analysis. Events with extra leptons according to looser working points, as discussed in Section 4.4.1 (Table 4.1) and Section 4.4.2 (Table 4.3), are vetoed. The trigger efficiency estimation is described in Section 5.1.2 and is approximately 100%. To ensure that all reconstructed particles considered for the analysis are corresponding to a proton interaction and to remove signals from beam halo particles as well as detector noise, several filters are used. These are described in Section 5.1.1. In addition to three leptons, the selected events should at least contain one offline jet with a $p_T > 30$ GeV and $|\eta| < 2.4$. Additionally, at least one of the selected offline jets should be tagged as coming from a b quark (so-called b-tagged jet or b jet).

5.1.1 Event cleaning

Some events arising from instrumental noise and beam backgrounds might end up in the data [191, 192]. In the ECAL, spurious deposits can appear from non-collision origins such as beam halo particles, or from particles hitting the sensors in the ECAL photo-detectors. Conjointly, dead ECAL cells can cause artificial missing transverse energy. The HCAL can also show spurious energy from particle interactions with the light guides and the photomultiplier tubes of the HF, as well as noisy hybrid photo-diodes. In CMS, different algorithms, so-called filters, are developed to identify and suppress these events.

The ECAL electronics noise and spurious signals from particle interactions with photo-detectors are mostly removed via topological and timing-based selections using only the ECAL information. The remaining effects such as anomalously high energy crystals and the lack of information for channels due to inefficiencies in the read-out are removed through dedicated events filters. Five ECAL endcap supercrystals have been identified for giving anomalously high energies due to high amplitude pulses in several channels at once, and are masked. Furthermore, the crystal read-out from a small amount of ECAL towers is not available. Nonetheless, their trigger primitive information is still available making it possible to estimate the magnitude of unmeasured energy and when the value is too large, the event is filtered out.

The machine induced particles via for example beam-gas, or beam-pipe interactions, that are flying with the beam, affect the physics analysis. They leave a calorimeter deposit along a line at constant ϕ in the calorimeter, and interactions in the CSCs will often line up with this deposit. This can be seen in Figure 5.3. Therefore, events containing such beam halo particles are removed from the selection with the CSC Beam Halo Filter. This algorithm uses information related to the geometric quantities, energy deposits, and timing signatures. For 2016 proton collision data, the filter rejects 85% in a halo-enriched sample, whereas the mistag probability determined from simulation is found to be less than 0.01% [191].

Furthermore, there is anomalous high missing transverse energy coming from muons that lead to high-p_T tracks, but are considered not good by the particle flow algorithm. These low quality tracks will be mislabelled as charged hadrons and will therefore be used in the calculation of the missing transverse energy. By investigating the purity of the reconstructed tracks and the relative transverse momentum error of the muons, these events can be filtered out.

5.1.2 Estimation of the trigger efficiency

The trigger efficiency in data is estimated from a data sample collected with unprescaled E_T^{miss} triggers. These allow events with a combination of the missing transverse energy being higher than 110 GeV (120 GeV) and the scalar sum of the transverse momenta of the reconstructed PF jets $H_T^{trig.}$ being at least 300 GeV (120 GeV), or events for which the calorimeter (PF) E_T^{miss}

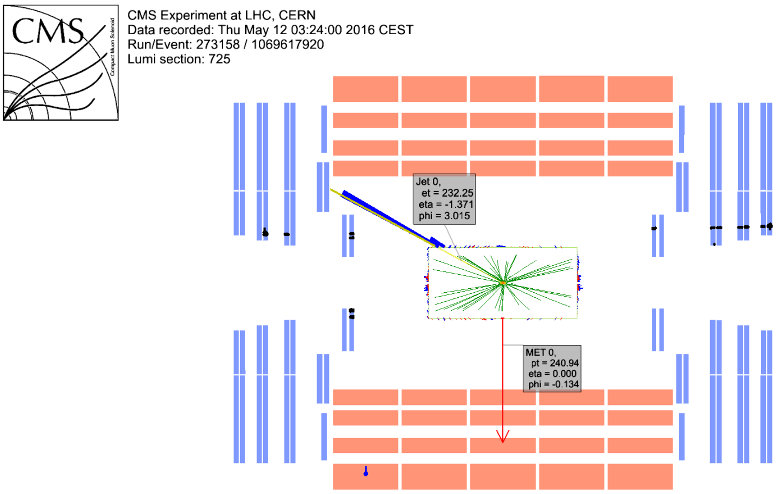

Figure 5.3: Event display of a beam halo event with collinear hits in the CSC (black), missing transverse energy of 240 GeV and a jet of 232 GeV. The hadronic deposit is spread in η, but narrow in ϕ. Figure taken from [191].

is higher than 200 GeV (300 GeV). For an HB-HE cleaned event, the PF missing transverse energy threshold is lowered to 170 GeV. These trigger paths are summarised in Table 5.3 and chosen to be completely uncorrelated with the lepton triggers given in Table 5.2.

Table 5.3: Unprescaled $E_{\mathrm{T}}^{\mathrm{miss}}$ HLT trigger paths for estimating the trigger efficiency. An *or* of the triggers is used to select events.

Trigger path	Requirement
HLT_PFHT300_PFMET110_v*	PF $E_{\mathrm{T}}^{\mathrm{miss}} > 110$ GeV, PF $H_{\mathrm{T}}^{\mathrm{trig.}} > 300$ GeV
HLT_MET200_v*	calorimeter $E_{\mathrm{T}}^{\mathrm{miss}} > 200$ GeV
HLT_PFMET300_v*	PF $E_{\mathrm{T}}^{\mathrm{miss}} > 300$ GeV
HLT_PFMET120_PFHT120_IDTight_v*	PF $E_{\mathrm{T}}^{\mathrm{miss}} > 120$ GeV, and PF $H_{\mathrm{T}}^{\mathrm{trig.,tightWP}} > 120$ GeV
HLT_PFMET170_HBHECleaned_v*	PF $E_{\mathrm{T}}^{\mathrm{miss}} > 170$ GeV, cleaned for HB/HE anomalous signals

The trigger efficiency is studied for the main background, namely WZ+jets, with all corrections applied. For this study, the events passing a three-lepton cut and at least one jet, are being used. The corresponding efficiencies are then calculated as

$$\epsilon_{data} = \frac{\text{Nb. of events passing lepton and MET triggers}}{\text{Nb. of events passing MET triggers}} \tag{5.1}$$

$$\epsilon_{MC} = \frac{\text{Nb. of events passing lepton triggers}}{\text{Nb. of total events}} \tag{5.2}$$

The resulting efficiencies for all lepton channels combined are shown in Table 5.4 and scale factors can be found in Table 5.5, where the scale factors are defined as

$$SF = \frac{\epsilon_{data}}{\epsilon_{MC}}. \tag{5.3}$$

More detailed scale factors and efficiencies can be found in Appendix A.

Table 5.4: Trigger efficiencies on data events selected with $E_{\mathrm{T}}^{\mathrm{miss}}$ triggers and WZ simulation for all three-lepton channels together. For simulation, the unweighted number of events is quoted. Region A contains events after requiring three leptons and at least one jet. Region B has the same requirements as region A, but only events with exactly one jet that is b-tagged are considered. Region C also contains the requirements in region A, where at least one jet should be b-tagged. In region D, no events with a b-tagged jet are allowed. Regions B-D have also a Z mass requirement ($|m_{\mathrm{ll}} - m_{\mathrm{Z}}| < 15$ GeV).

Region	data $\mathrm{N_{selected}/N_{total}}$	WZ simulation $\mathrm{N_{selected}/N_{total}}$
A	117/118	18047/18055
B	6/6	1541/1541
C	26/27	1791/1792
D	69/69	14405/14412

Table 5.5: Trigger scale factors for each three-lepton channel, after requiring three leptons and jets selection criteria, in the Z mass window.

all	3μ	3e	2e1μ	1e2μ
1.00	1.00	0.95	1.00	1.00

The trigger efficiencies are measured to be nearly 100% for both simulation and data. The results are dominated by statistics and assigning a large uncertainty to the trigger efficiency based on the dataset collected by $E_{\mathrm{T}}^{\mathrm{miss}}$ triggers, would be over-conservative. A one percent uncertainty on the trigger selection for the 2e1μ and 3μ final states, and 5% for the 3e and 1e2μ final states is assigned instead, in accordance the SM tZq search [193]. No scale factors will be applied on simulation as they are close to unity.

5.2 Corrections

Mismatches between data and simulation are corrected via the use of scale factors. These are elaborately discussed in Section 4.4. In this section a short overview of the applied corrections on a dilepton dataset is given. Requiring three leptons would enhance the fraction of NPL backgrounds. These backgrounds are however not well simulated and are determined in a data-driven way. For this reason, the study of the agreement between data and simulation is performed with events selected with the trigger logic and trigger paths described in Section 5.1, that contain at least one opposite sign (i.e. not the same electric charge) same flavour lepton pair that has an invariant mass m_{ll} inside a Z boson mass window of $|m_{\mathrm{ll}} - m_{\mathrm{Z}}| < 7.5$ GeV, and with at least one jet present. The main contributing process in this selection is the Z/γ^* +jets process. In the following, the distributions relevant for each correction are shown for all lepton channels. Since events with three leptons are not vetoed from the selection, these will be also entering the collection of the dilepton channels, called "all channels". The effect of each correction is shown by either applying all corrections except the one under investigation ("before"), and applying all corrections ("after").

Pileup reweighting

In data, the number of interactions per bunch crossing (pileup) is calculated with a minimum bias cross section of 69.2 mb. The distribution of the number of simulated pileup events is then reweighted to match the expected number of pileup events in data. Pileup reweighting manifests itself as an altered shape of the number of reconstructed primary vertices as can be seen in Figure 5.4.

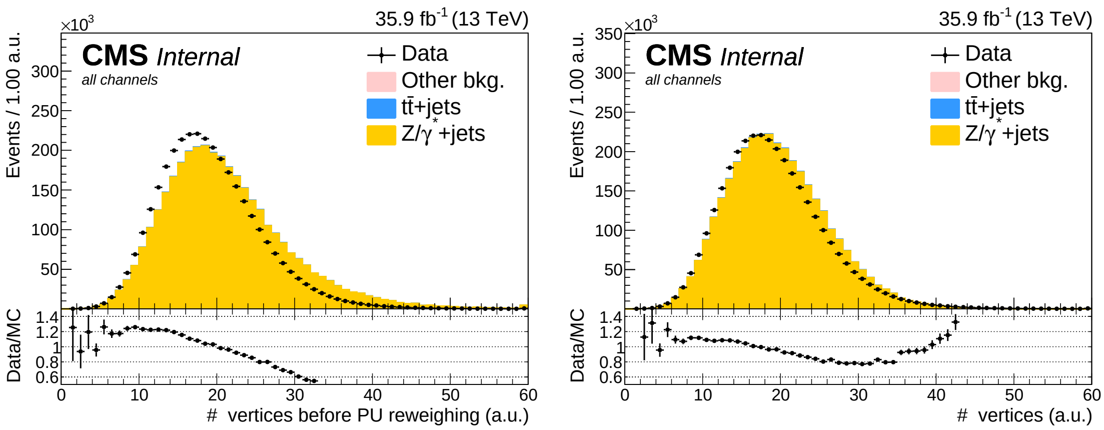

Figure 5.4: Distribution of the number of primary vertices before (left) and after (right) pileup reweighting. Events selected by requiring two leptons in the Z boson mass window and jets.

Note that Figure 5.4 indicates that even after pileup reweighting, the primary vertex multiplicity is not well described by simulation. This is a known effect, and using a minimum bias cross section with a slightly lower value is found to better describe the data. However, the scale factors are only provided for the nominal inelastic cross section, and thus this value is used.

Lepton scale factors

The efficiency to select leptons is different in simulation (ϵ_{MC}) compared to the data (ϵ_{data}). This is corrected for by applying lepton scale factors (SF) to the simulation that are defined as

$$SF = \frac{\epsilon_{\mathrm{data}}}{\epsilon_{\mathrm{MC}}}. \tag{5.4}$$

These scale factors are measured for the identification, isolation, tracking and trigger efficiencies of the objects as a function of p_{T} and η (see Section 4.4.1 and Section 4.4.2). Multiplying these scale factors for each lepton provides an overall efficiency per event:

$$SF^{\mu}_{\text{global}} = \prod_{i}^{\#\mu} SF^{\mu}_{\text{ID}}(p_T, \eta)\, SF^{\mu}_{\text{Iso.}}(p_T, \eta)\, SF^{\mu}_{\text{Trig.}}(p_T, \eta)\, SF^{\mu}_{\text{Track}}(p_T, \eta), \tag{5.5}$$

$$SF^{e}_{\text{global}} = \prod_{i}^{\#e} SF^{e}_{\text{ID}}(p_T, \eta)\, SF^{e}_{\text{Iso.}}(p_T, \eta)\, SF^{e}_{\text{Trig.}}(p_T, \eta)\, SF^{e}_{\text{Track}}(p_T, \eta). \tag{5.6}$$

The effect of the scale factors can be found in Figure 5.5 for the muons and Figure 5.6 for the electrons. The trigger efficiencies are estimated in Section 5.1.2.

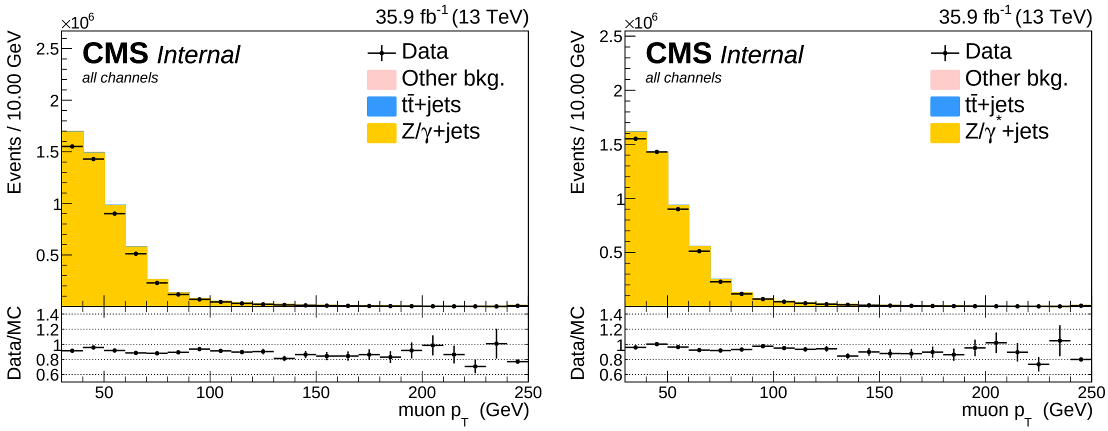

Figure 5.5: Distribution of the p_T of the muons before (left) and after (right) muon scale factors. Events selected by requiring two leptons in the Z boson mass window and jets. All other corrections are applied.

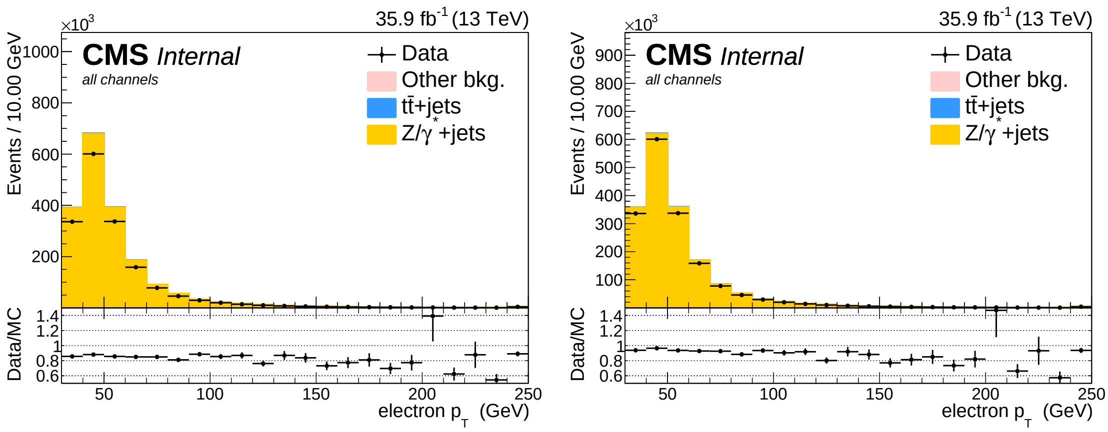

Figure 5.6: Distribution of the p_T of the electrons before (left) and after (right) electron scale factors. Events selected by requiring two leptons in the Z boson mass window and jets. All other corrections are applied.

Additionally, corrections are determined from $\mathrm{Z} \rightarrow \mathrm{ee}$ events for the energy resolution of the leptons. For the electrons, energy smearing and regression is applied [194]. The energy regression uses the detector information to correct the electron energy in order to have the best energy resolution and corrects for material effects in the ECAL, improving the performance. The energy scale and smearing corrects the simulation energies to have identical energy resolution in simulation and data. For the muons, the p_{T} is corrected using the Rochester method [195, 196]. This correction is determined from $\mathrm{Z} \rightarrow \mu\mu$ events and removes the bias of the muon p_{T} from any detector misalignment or any possible error of the magnetic field. The effect of the Rochester correction can be found in Figure 5.7.

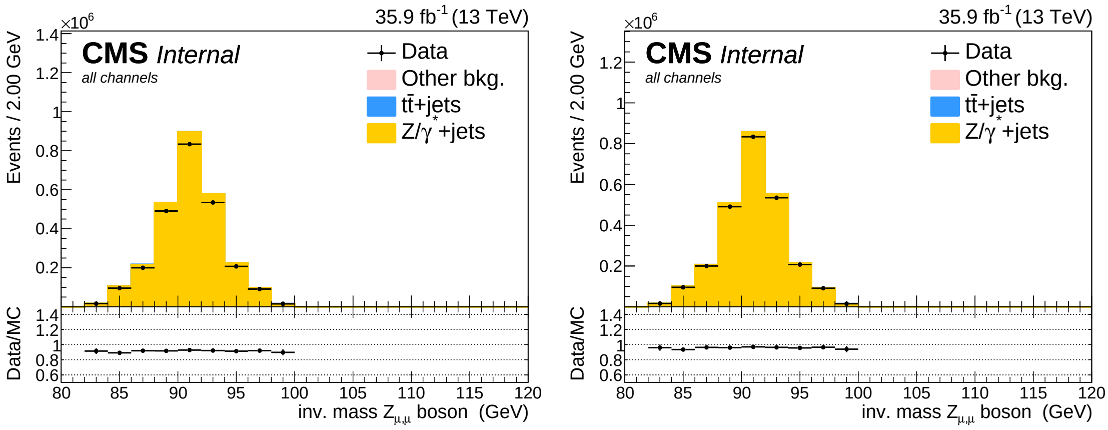

Figure 5.7: Distribution of the mass of the Z boson from muons before (left) and after (right) the Rochester correction. Events selected by requiring two leptons in the Z boson mass window and jets. All other corrections are applied.

CSVv2 shape correction

In order to make the distribution of the CSVv2 b-tagging discriminant in simulation agree with data, jet-by-jet based scale factors are applied. These scale factors are a function of the p_{T} , η and flavour of the jet as discussed in Section 4.4.4. The effect of these scale factors on the distribution of the CSVv2 discriminant of all jets can be found in Figure 5.8.

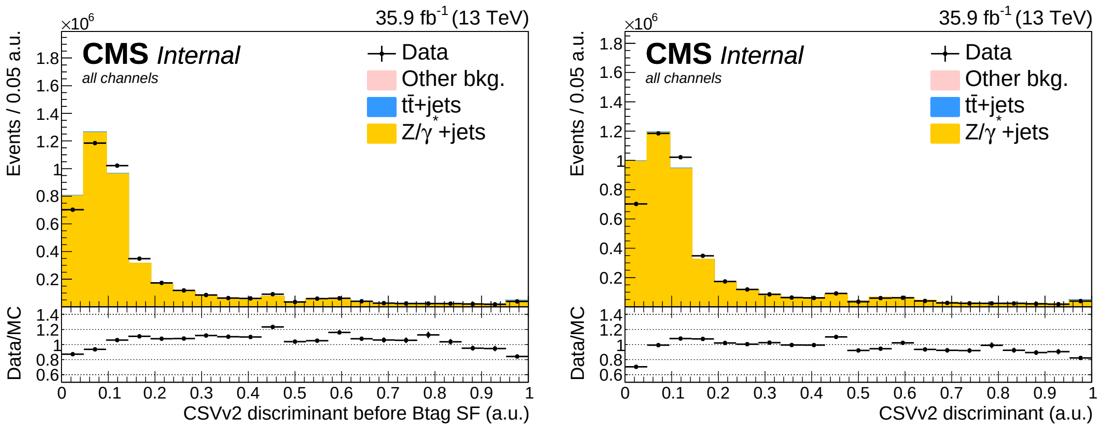

Figure 5.8: Distribution of the CSVv2 discriminant of the jets before (left) and after (right) b-tag scale factors. Events selected by requiring two leptons in the Z boson mass window and jets. All other corrections are applied.

Jet energy

The jet energy in data and simulation is corrected by the measured energy response of the detector. This provides p_T- and η-dependent scale factors and are directly taken from the frontier condition database as discussed in Section 4.4.3. The effect of the jet energy corrections on the distribution of the p_T of all jets can be found in Figure 5.9 and Figure 5.10.

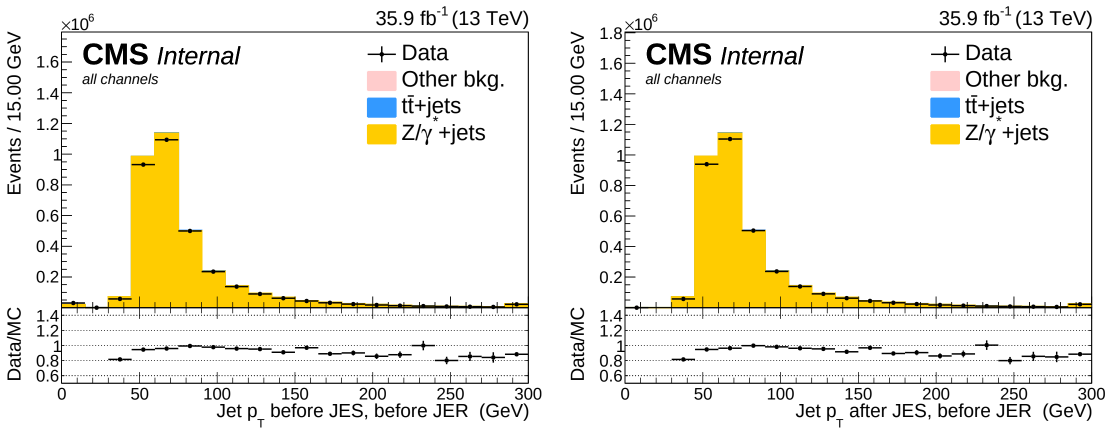

Figure 5.9: Distribution of the p_T of the jets before (left) and after (right) jet energy scale corrections. Events selected by requiring two leptons in the Z boson mass window and jets. All other corrections are applied.

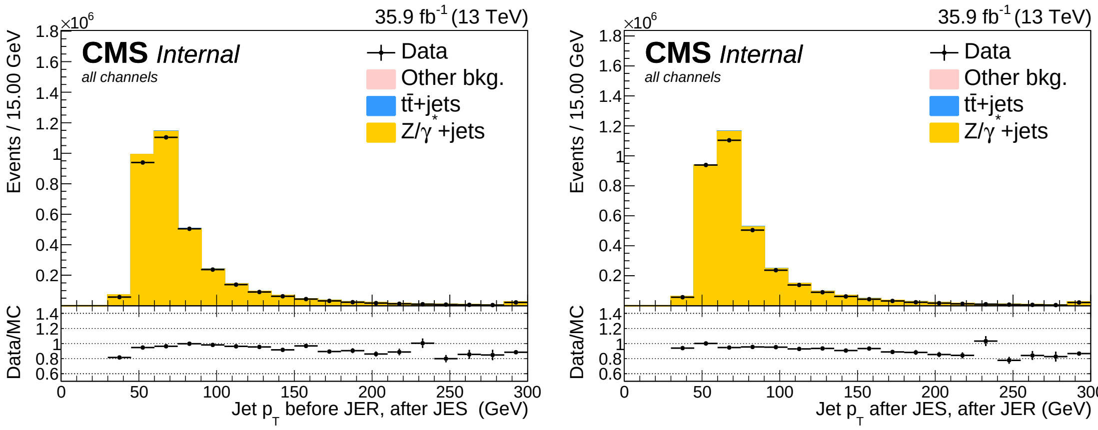

Figure 5.10: Distribution of the p_{T} of the jets before (left) and after (right) jet energy resolution smearing. Events selected by requiring two leptons in the Z boson mass window and jets. All other corrections are applied.

5.3 Event reconstruction

After selecting the events, the objects contained in each event are assigned to physical particles. The Z boson is reconstructed as the sum of the four vectors of the two same flavour leptons of opposite electric charge resulting in an invariant mass that is closest to the value of the known Z boson mass. The third remaining lepton is assigned to the lepton coming from the W boson decay, so-called W lepton. This lepton assignment is validated using simulation by matching the reconstructed objects to their generated counterpart by minimizing the distance in the $\eta\phi$ plane between the true particle and reconstructed one. The efficiencies derived from the simulated signal samples and the SM tZq background process can be found in Table 5.6 for events selected after the three-lepton and jets requirements. The probability that a lepton is assigned to the wrong boson is of the order of a percent for the top quark pair FCNC signal process, and of the order of 2% for the single top quark FCNC signal process. For the SM tZq process, this probability is 3%.

Table 5.6: Efficiencies of assigning the correct leptons in the analysis after requiring three leptons and jets.

Origin	FCNC tZq	FCNC tZ	SM tZq
W boson	99%	98%	97%
Z boson	99%	98%	97%
all leptons in the decay	99%	98%	97%

The jet with the highest CSVv2 discriminant is assigned to the b-flavour jet of the SM decay of the top quark, so-called SM b jet. This jet is then removed from the collection of jets. A loop over the jets is performed and the jet that in combination with the reconstructed Z boson, gives the mass closest to the known top quark mass is assigned as the light-flavour jet coming from the

FCNC decay of the top quark, so-called FCNC jet. The SM top quark candidate is reconstructed by summing the third lepton, the SM b jet and the neutrino ($E_{\mathrm{T}}^{\mathrm{miss}}$).

The longitudinal momentum of the neutrino is calculated from the missing transverse momentum and the lepton momentum. From momentum conservation follows that

$$\vec{p}_{\mathrm{W}} = \vec{p}_{\ell_{\mathrm{W}}} + \vec{p}_{\nu}, \tag{5.7}$$

and energy conservation requires the W boson mass squared,

$$m_{\mathrm{W}}^2 = (80.4\ \mathrm{GeV})^2, \tag{5.8}$$

is equal to the sum of the transverse momenta of the neutrino ν and the lepton ℓ_{W} squared

$$m_{\mathrm{W}}^2 \equiv (p_{\ell_{\mathrm{W}}} + p_{\nu})^2. \tag{5.9}$$

Assuming that the lepton and neutrino are approximately massless, this equation can be solved for the sought-for p_{ν}^{z} by setting $p_{\mathrm{T},\nu}$ equal to the missing transverse energy in the event. This yields a quadratic equation of the form

$$p_{\nu,z} = \frac{-b}{2a} \pm \frac{\sqrt{b^2 - 4ac}}{2a} \tag{5.10}$$

with

$$\begin{aligned} a &= p_{\ell,x}^2 + p_{\ell,y}^2, \\ -b &= m_{\mathrm{W}}^2 p_{\ell,z} + 2p_{\ell,x}p_{\ell,z}p_{\nu,x} + 2p_{\ell,x}p_{\ell,z}p_{\nu,y}, \\ c &= p_{\nu,y}\left(p_{\ell,x}^2 + p_{\ell,z}^2\right) + p_{\nu,x}\left(p_{\ell,x}^2 + p_{\ell,z}^2\right). \end{aligned} \tag{5.11}$$

When the solution of this quadratic equation is complex, only the real part ($-b/2a$) is considered. If there are two real solutions, the solution for p_{ν}^{z} that gives the invariant mass $m_{\mathrm{b}\nu\ell_{\mathrm{W}}}$ closest to the top quark mass (172.9 GeV) is kept.

In Figure 5.11, the normalized distributions of the invariant mass of the W lepton and the SM b jet ($m_{\ell_{\mathrm{W}}b}$), and the invariant mass of the reconstructed Z boson and FCNC jet are shown. The distribution of $m_{\ell_{\mathrm{W}}b}$, peaks around 100 GeV for the FCNC signal and SM $\mathrm{t\bar{t}}$+jets process. The distribution invariant mass of the Z boson and FCNC jet peaks at the known top mass for the FCNC top quark pair signal. For the single top quark FCNC signal, no extra top is expected and this distribution is smeared out.

The normalised distributions of the reconstructed top quark mass and W boson mass are shown in Figure 5.12. For the FCNC signal, the distribution peaks around the known mass of the top quark and has a tail towards higher values. The distribution of the reconstructed W boson mass peaks at 80 GeV for the FCNC signal.

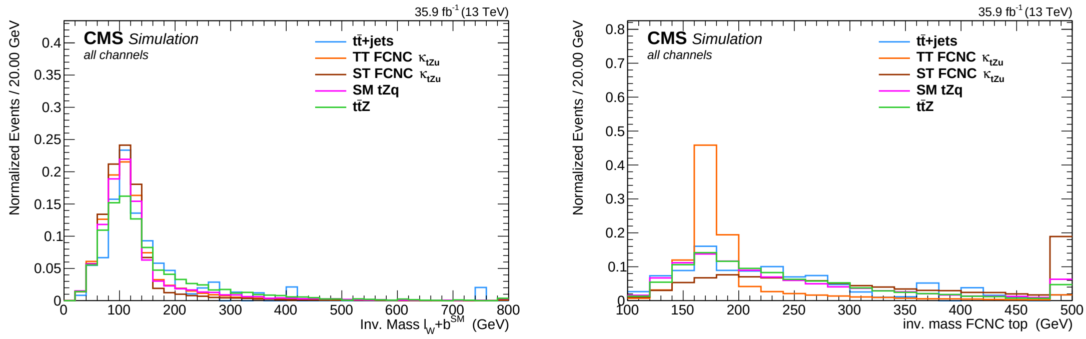

Figure 5.11: Normalised distribution of the invariant mass of the W lepton and the SM b jet (left), and the invariant mass of the reconstructed Z boson and FCNC jet (right). After requiring three leptons and jets, in the Z boson mass window.

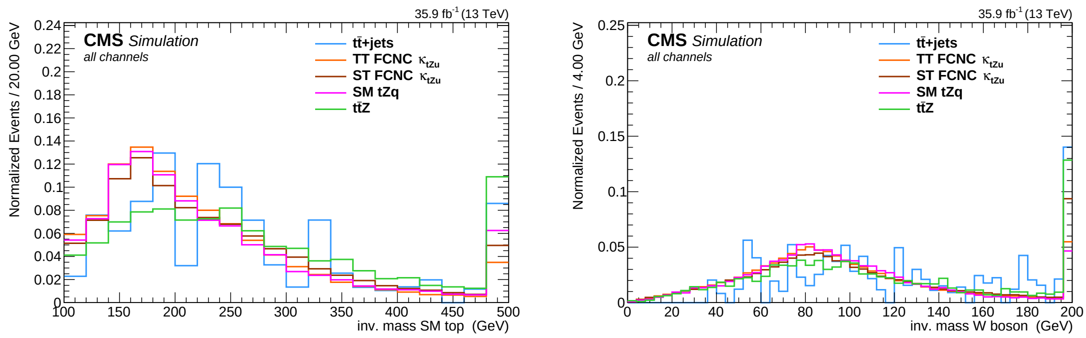

Figure 5.12: Normalised distribution of the invariant mass of the top quark decaying via the SM Wtb vertex (left) and the invariant mass of the W boson. After requiring three leptons and jets, in the Z boson mass window.

5.4 Data driven NPL background

One of the most important backgrounds consists of events with not prompt-leptons (NPL). These originate mostly from instrumental effects and are therefore very difficult to model. The rate and differential distribution of the NPL background is estimated from data.

The NPL background originates from hadronic objects wrongly reconstructed as leptons (so-called fake leptons), or from real leptons coming from the semi-leptonic decay of a b or c hadron and from the conversion of photons that pass the identification and isolation requirements (so-called non-prompt leptons). The dominant source of events contained in this NPL background depends on the flavour of the leptons. Therefore the events with a not prompt-muon (NPμ) are treated independently from those with a not prompt-electron (NPe). For muons, the dominant source is the semi-leptonic decay of heavy flavour hadrons, while for electrons, the dominant sources are hadrons and photon conversions.

The backgrounds causing events that are contained within the NPL background are mostly arising from $Z/\gamma^* +$jets (Drell–Yan) and $t\bar{t}$+jets dilepton processes, and in a smaller amount from WW processes. All of these processes contain two real leptons and one NPL. Due to the fact that the probability for a lepton to be a NPL is small, backgrounds containing two or more not prompt-leptons are neglected in this search. The assumption is made that for the $Z/\gamma^* +$jets process, the two leptons compatible with a Z boson decay are the real leptons, and the additional lepton is coming from a NPL source. For the $t\bar{t}$+jets process, the NPL is assumed to be associated with the Z boson. These two assumptions have been validated using Monte Carlo simulations of the $Z/\gamma^* +$jets process and $t\bar{t}$+jets process by matching the reconstructed leptons to their true initial generated particles, after requiring exactly three leptons in the Z boson mass window, and at least one jet. For the $Z/\gamma^* +$jets process this assumption is true in 80% of the events, increasing to 100% of the events after requiring one b-tagged jet. For the $t\bar{t}$+jets process this is true for 60% of the selected events, and this increases to 90% after requiring one b-tagged jet.

The NPL sample is constructed by selecting events from data by requiring exactly two leptons that are identified as real isolated leptons according to the tight working point given in Table 4.1 and Table 4.3. A third lepton, the so-called not prompt-lepton, is added by taking a lepton for which the identification criteria are loosened and the isolation citeria are inverted. The full requirements on the not prompt-leptons are given in Table 5.7 and Table 5.8. For not prompt-electrons, a large fraction is coming from misidentified photons. These are removed by applying a tighter cut on the $1/E - 1/p$ variable, and by limiting the isolation values to be smaller than one, in coherence with the SM tZq search from CMS [193].

The normalisation of the distributions from the NPL background sample is estimated from data through the use of control regions that are fitted simultaneously with the signal regions. These regions are defined in Section 5.5.

Table 5.7: Not prompt-electron requirements used in this analysis. The requirements for electrons are set in the barrel ($|\eta_{supercluster}| \leq 1.479$) and the end caps ($|\eta_{supercluster}| > 1.479$).

Properties	$\|\eta_{supercluster}\| \leq 1.479$	$\|\eta_{supercluster}\| > 1.479$
$\sigma_{\eta\eta}$	< 0.011	< 0.0314
$\|\Delta\eta_{\text{in}}\|$	< 0.00477	< 0.00868
$\|\Delta\phi_{\text{in}}\|$	< 0.222	< 0.212
H/E	< 0.298	< 0.101
relative isolation	$[0.0588, 1[$	$[0.0571, 1[$
$\|1/E - 1/p\|$ (GeV^{-1})	< 0.0129	< 0.0129
expected missing inner hits	≤ 1	≤ 1
conversion veto	Y	Y
p_{T} (GeV)	> 35	> 35

Table 5.8: Not prompt-muon requirements used in the analysis.

Properties	modified Loose Muon WP
Global muon or Tracker Muon	Both
Particle Flow muon	Y
χ^2/ndof of global muon track fit	N/A
Nb. of hit muon chambers	N/A
Nb. of muon stations contained in the segment	N/A
Size of the transverse impact parameter of the track wrt. PV	N/A
Longitudinal distance wrt. PV	N/A
Nb. of pixel hits	N/A
Nb. of tracker layers with hits	N/A
Relative Isolation	≤ 0.15
p_{T} (GeV)	> 30

5.5 Analysis Strategy

The baseline selection of this analysis selects events where jets and three leptons are present. Additional leptons with a looser identification are vetoed in order to reduce the contamination of backgrounds with four or more leptons in the final state, e.g. ZZ, $t\bar{t}Z$, and $t\bar{t}H$. This makes that the most important backgrounds in this search consist of backgrounds that contain three prompt leptons in the final state. These are mainly WZ+jets, $t\bar{t}Z$ and SM tZq. For these backgrounds, the three lepton topology is identical to the FCNC signal: two opposite sign leptons of the same flavour decaying from the Z boson, and a third additional, high p_{T} lepton coming from the W boson decay.

For the single top quark FCNC final state, one b jet coming from the SM top quark decay is expected. For the top quark pair FCNC signal, an additional light-flavour jet is expected. In the $t\bar{t}Z$ final state, two b jets are present in the final state. However, due to inefficiencies of the b-tagging algorithm, one of the two b jets may be identified as a light-flavour jet, giving the same final state as the top quark pair FCNC final state. For the WZ+jets final states, one of the b jets produced by gluon splitting, can be b-tagged or light-flavour jets coming from the WZ+jets production can be mis-tagged as b jets. The SM tZq final state expects the same signal as the top quark pair FCNC process. Furthermore, the NPL background is responsible for a significant amount of background events.

In Figure 5.13, the number of events per leptonic decay are shown. In the dilepton channels, the data and simulation agrees. For the three lepton decays, there is poor agreement due to the fact that the NPL background is not well simulated. For this reason, the NPL background will be estimated in a data-driven way and the simulated samples of $Z/\gamma^* +$jets, $t\bar{t}$+jets and WW will not be used as explained in Section 5.4. One can also see that in the three lepton channels, the other backgrounds become more important, these are mainly WZ+jets, SM tZq, $t\bar{t}$Z and ZZ processes.

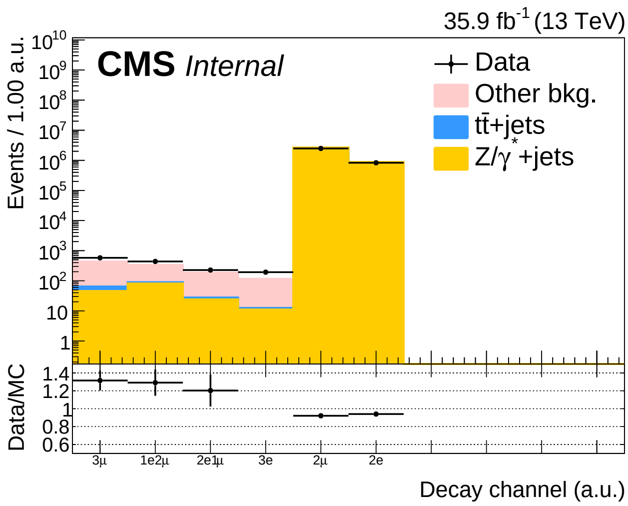

Figure 5.13: Number of events per leptonic-decay after requiring at least two or exactly three leptons and jets, in the Z boson mass window. The different decays are not exclusive.

The analysis strategy is shown in Figure 5.14. Based on the jet multiplicity, the b-tag information and the reconstructed Z boson mass, five statistically independent regions are defined after a common selection of exactly three leptons containing one opposite sign same flavour pair that is assigned to the Z boson, at least one jet and at the most three jets, and the transverse mass of the W boson to be maximal 300 GeV. The requirements for each region are shown in Table 5.9. Two signal regions are considered, targeting the final state of either the single top quark or top quark pair signal. The STSR targets the final state of the single top quark FCNC signal, while the TTSR targets the top quark pair FCNC signal. In each signal region, a multivariate discriminant based on Boosted Decision Trees (BDT) (see Section 3.3) is used to respectively discriminate single top quark FCNC and top quark pair FCNC signal from backgrounds. The rate of WZ+jet events as well as that of the NPL background, mainly originating from the $Z/\gamma^* +$jets process, is estimated in the WZCR. Here, the transverse mass of the W boson $m_{\mathrm{T}}(\mathrm{W})$ that is defined as function of the lepton l_{W} assigned to the W boson and the neutrino ν_{W} coming from the missing transverse energy in the event,

$$m_T(W) = \sqrt{\left(p_T(l_W) + p_T(\nu_W)\right)^2 - \left(p_x(l_W) + p_x(\nu_W)\right)^2 - \left(p_y(l_W) + p_y(\nu_W)\right)^2}, \tag{5.12}$$

is used as discriminating variable between the two background processes, WZ+jets and NPL. The normalisation of the backgrounds is then used in the signal regions via the b-tagging information (Section 5.5.1). The NPL background coming from a $t\bar{t}$+jets process is constrained by two control regions, TTCR and STCR, one for each signal region (respectively TTSR and STSR). The normalisation of the $t\bar{t}$+jets process is estimated by subtracting all other background predictions from the data rate (Section 5.5.3). A simultaneous global fit using the `Higgs Combine Tool` (Section 3.4) is performed taking into account each region (STSR, TTSR, WZCR, TTCR and STCR) for the four different three-lepton channels. The BDTs in the signal regions, as well as the transverse mass of the W boson are discussed in Chapter 6. The number of events for each region is shown in Section 5.5.4.

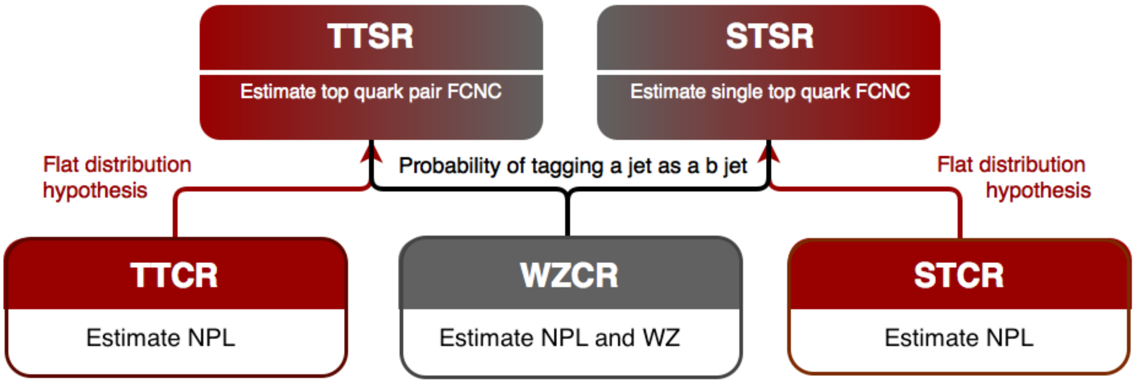

Figure 5.14: The strategy used for the search presented in this thesis. The WZCR region is used to estimate the WZ+jets background process as well as the NPL background coming from the Z/γ^*+jets process. The TTCR and STCR regions are used to estimate the contributions of the NPL background coming from the $t\bar{t}$+jets process.

Table 5.9: The statistically independent regions used in the analysis.

	WZCR	STSR	TTSR	STCR	TTCR
Number of jets	$\geqslant 1$	1	$\geqslant 2$	1	$\geqslant 2$
Number of b jets	0	1	$\geqslant 1$	1	$\geqslant 1$
$\lvert m_Z^{reco} - m_Z \rvert < 7.5$ GeV	Yes	Yes	Yes	No	No
$\lvert m_Z^{reco} - m_Z \rvert < 30$ GeV	Yes	Yes	Yes	Yes	Yes
Number of leptons	3	3	3	3	3

5.5.1 WZCR

The WZCR is constructed by vetoing events with jets tagged as being a b jet, making it statistically independent from the signal regions where at least one b-tagged jet is required. In this control region, a fit is performed on the transverse mass of the W boson, in order to estimate the NPL yield coming from $Z/\gamma^* +$ jets and the WZ+jets backgrounds.

A transfer factor is used to project the yield in the region without b-tagged jets to the regions with exactly, or at least, one b-tagged jet. For this, the probability of tagging at least one jet with the CSVv2 algorithm at the loose working point is used to calculate the expected number of events, N_b, after b-tagging:

$$N_\mathrm{b} = \frac{\sum_\mathrm{events} \mathscr{P}_b}{\text{total nb of events}}, \tag{5.13}$$

where $\mathscr{P}_\mathrm{b}$ is the probability that an event survives the b-tagging requirement,

$$\begin{aligned} \mathscr{P}_\mathrm{b} &= 1 - \mathrm{P(event\ does\ not\ survive\ b\ tag)}, \\ &= 1 - \left(\prod_\mathrm{b} \mathrm{P(b\ not\ b\text{-}tagged)} \prod_\mathrm{c} \mathrm{P(c\ not\ b\text{-}tagged)} \prod_\mathrm{udsg} \mathrm{P(light\ not\ b\text{-}tagged)} \right), \end{aligned} \tag{5.14}$$

with the products going over all b-, c-, and light-flavour jets respectively. The jet flavour is determined by means of matching the reconstructed jet to the generated quarks, based on the distance in the $\eta\phi$ plane. In order to estimate the probability for exactly one b-tagged jet, the expected number of events is corrected by the fraction of events with exactly one jet in the WZCR. The resulting transfer factors are given in Appendix B. The yield of WZ+jets events in the signal region estimated using the above described transfer factor, and the yield calculated with simulated events, are in agreement.

5.5.2 TTSR and STSR

The TTSR is defined to target the top quark pair FCNC (tZq) process, while the STSR focuses on the single top quark FCNC (tZ) process. They have NPL contributions coming from $Z/\gamma^* +$ jets and $\mathrm{t\bar{t}}$+jets events. In these regions, the data driven NPL template is split into two templates, based on the presence of the NPL in the Z boson. The NPL associated with W boson is assigned to $Z/\gamma^* +$ jets and its yield is estimated in the WZCR, while the NPL associated with Z boson is assigned to $\mathrm{t\bar{t}}$+jets and its yield is estimated in the TTCR and STCR.

5.5.3 TTCR and STCR

The TTCR and STCR are constructed with the same selection criteria as TTSR and STSR, with exception that in these regions events with a reconstructed Z boson mass outside the Z boson mass window are selected. These side-bands are defined as

$$7.5\ \mathrm{GeV} < |m_\mathrm{Z}^\mathrm{reco} - m_\mathrm{Z}| < 30\ \mathrm{GeV}, \tag{5.15}$$

where $m_\mathrm{Z}^\mathrm{reco}$ is the reconstructed mass of the Z boson in the event, and m_Z the known mass of the Z boson. These regions are dominated by $\mathrm{t\bar{t}}$+jets (see Appendix B) and are used to estimate the NPL background event yield coming from the $t\bar{t}$+jets process in the STSR and TTSR. Since there are few events entering the STCR and TTCR, no shapes are used in the fit, i.e. only the absolute event yield is used. The distribution of the mass of the Z boson is flat for $t\bar{t}$+jets events, as shown in Figure 5.15. Therefore, the number of expected events, N_s, in the signal regions estimated from the number of expected events, N_c, in the control region through the ratio of the Z boson mass windows:

$$N_s = \frac{2 \times 7.5}{(2 \times 30) - (2 \times 7.5)} N_c. \tag{5.16}$$

The resulting transfer factors are given in Appendix B. The expected yield in the signal region estimated from the TTCR (STCR) is in agreement with the yield calculated from simulated events.

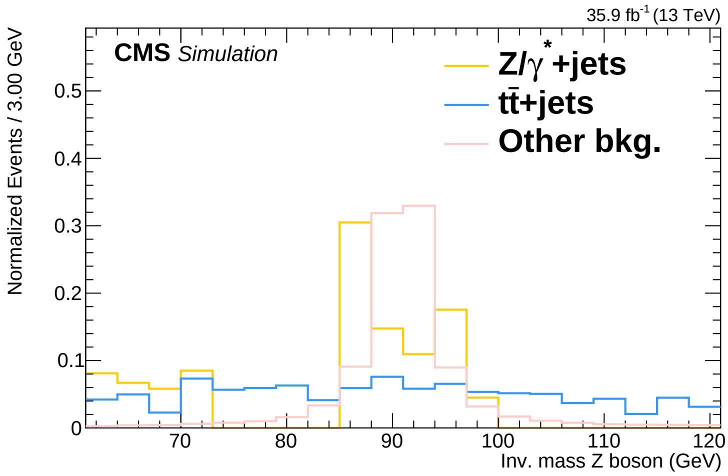

Figure 5.15: The normalized distribution for $Z/\gamma^* +$jets and $t\bar{t}$+jets events before dividing the events into regions, after $|m_Z^{\mathrm{reco}} - m_Z| < 30$ GeV. All three-lepton channels combined.

5.5.4 Event yields

In this section, the event yields for each region are given. In Table 5.10 and Table 5.11 the event yields in the side-band control regions, STCR and TTCR, are given. Table 5.12 contains the event yields for the WZCR. The event yields in the signal regions, STSR and TTSR, are given in Table 5.13 and Table 5.14 respectively. The background yields follow the relative fractions predicted by the simulation. The NPL background is constructed from a dilepton sample with an extra not prompt-lepton. For this reason, the NPL sample is normalised to reach a total background yield equal to the observed data yield. The actual yield will be taken from data during the global fit as explained in the previous section. The signal yield is set to its expected value for branching fraction equal to the expected limits of most stringent upper limit set by CMS [28] at 95% CL, being $\mathcal{B}(t \to uZ) < 2.7 \times 10^{-4}$ and $\mathcal{B}(t \to cZ) < 12 \times 10^{-4}$.

From the tables one can see that for the TTCR and the STCR, the main contribution should come from the NPL background, making this control region well defined for estimating the yield of this background. The WZCR is dominated by the WZ+jets process and also here a large contribution of the NPL background is expected. In the STSR, the main background is the NPL background, followed by the SM tZq, and WZ+jets process. For the TTSR, the main background is also the NPL background, followed by the $t\bar{t}Z$ process, SM tZq process and WZ+jets process.

Table 5.10: Event yields in the STCR. The signal yield is set to its expected value for branching fraction equal to the expected limits of most stringent upper limit set by CMS [28], being $\mathcal{B}(t \to uZ) < 2.7 \times 10^{-4}$ and $\mathcal{B}(t \to cZ) < 12 \times 10^{-4}$. The yield of the NPL background will be taken from the fit.

Process	all channels	3μ channel	1e2μ channel	2e1μ channel	3e channel
NPL $t\bar{t}$	24.02	8.70	14.04	0.83	0.45
$t\bar{t}Z$	0.18 ± 0.21	0.09 ± 0.06	0.03 ± 0.21	0.02 ± 0.03	0.04 ± 0.03
WZ	3.52 ± 0.25	1.53 ± 0.06	1.04 ± 0.15	0.59 ± 0.20	0.35 ± 0.07
ZZ	0.31 ± 0.10	0.15 ± 0.08	0.08 ± 0.02	0.05 ± 0.01	0.03 ± 0.02
Other bkg.	1.66 ± 0.91	0.38 ± 0.76	0.71 ± 0.28	0.47 ± 0.66	0.09 ± 0.05
tZq	0.31 ± 0.06	0.14 ± 0.04	0.09 ± 0.03	0.04 ± 0.01	0.04 ± 0.01
κ_{tZu}/Λ	0.42 ± 0.03	0.16 ± 0.02	0.14 ± 0.02	0.08 ± 0.01	0.04 ± 0.01
κ_{tZc}/Λ	0.32 ± 0.03	0.13 ± 0.01	0.10 ± 0.02	0.06 ± 0.01	0.04 ± 0.01
Data	32 ± 3	11 ± 1	16 ± 1	2 ± 1	1 ± 1

Table 5.11: Event yields in the TTCR. The signal yield is set to its expected value for branching fraction equal to the expected limits of most stringent upper limit set by CMS [28], being $\mathscr{B}(t \rightarrow uZ) < 2.7 \times 10^{-4}$ and $\mathscr{B}(t \rightarrow cZ) < 12 \times 10^{-4}$. The yield of the NPL background will be taken from the fit.

Process	all channels	3μ channel	1e2μ channel	2e1μ channel	3e channel
NPL $t\bar{t}$	30.19	14.40	11.30	4.09	0.41
$t\bar{t}Z$	2.85 ± 0.44	1.11 ± 0.38	0.73 ± 0.19	0.55 ± 0.16	0.46 ± 0.15
WZ	3.98 ± 0.63	1.62 ± 0.53	1.26 ± 0.34	0.48 ± 0.13	0.61 ± 0.07
ZZ	0.32 ± 0.08	0.12 ± 0.06	0.10 ± 0.03	0.05 ± 0.02	0.05 ± 0.02
Other bkg.	3.88 ± 0.66	1.38 ± 0.58	1.38 ± 0.51	0.74 ± 0.24	0.38 ± 0.11
tZq	0.79 ± 0.13	0.36 ± 0.10	0.24 ± 0.07	0.10 ± 0.03	0.09 ± 0.04
κ_{tZu}/Λ	0.61 ± 0.05	0.24 ± 0.04	0.18 ± 0.01	0.11 ± 0.01	0.08 ± 0.01
κ_{tZc}/Λ	0.59 ± 0.05	0.24 ± 0.02	0.20 ± 0.05	0.10 ± 0.01	0.05 ± 0.01
Data	44 ± 3	19 ± 1	15 ± 1	6 ± 1	2 ± 1

Table 5.12: Event yields in the WZCR. The signal yield is set to its expected value for branching fraction equal to the expected limits of most stringent upper limit set by CMS [28], being $\mathscr{B}(\mathrm{t} \rightarrow \mathrm{uZ}) < 2.7 \times 10^{-4}$ and $\mathscr{B}(\mathrm{t} \rightarrow \mathrm{cZ}) < 12 \times 10^{-4}$. The yield of the NPL background will be taken from the fit.

Process	all channels	3μ channel	1e2μ channel	2e1μ channel	3e channel
NPL $Z/\gamma^* + \mathrm{jets}$	431.56	158.98	155.42	54.96	62.20
$\mathrm{t\bar{t}Z}$	9.57 ± 0.69	3.86 ± 0.50	2.42 ± 0.41	1.97 ± 0.22	1.33 ± 0.22
WZ	551.63 ± 29.26	227.59 ± 20.87	155.36 ± 14.20	101.63 ± 9.34	67.05 ± 6.21
ZZ	46.19 ± 2.40	18.34 ± 1.73	14.75 ± 1.49	7.19 ± 0.60	5.90 ± 0.53
Other bkg.	6.75 ± 0.99	3.20 ± 0.79	2.01 ± 0.74	0.96 ± 0.14	0.58 ± 0.14
tZq	7.30 ± 0.45	3.03 ± 0.33	2.04 ± 0.24	1.30 ± 0.14	0.93 ± 0.11
$\kappa_{\mathrm{tZu}}/\Lambda$	14.12 ± 0.23	5.64 ± 0.15	3.86 ± 0.15	2.75 ± 0.07	1.88 ± 0.08
$\kappa_{\mathrm{tZc}}/\Lambda$	26.34 ± 0.51	10.79 ± 0.35	7.13 ± 0.30	5.01 ± 0.12	3.41 ± 0.17
Data	1053 ± 34	415 ± 21	332 ± 19	168 ± 14	138 ± 13

Table 5.13: Event yields in the STSR. The signal yield is set to its expected value for branching fraction equal to the expected limits of most stringent upper limit set by CMS [28], being $\mathscr{B}(\mathrm{t} \rightarrow \mathrm{uZ}) < 2.7 \times 10^{-4}$ and $\mathscr{B}(\mathrm{t} \rightarrow \mathrm{cZ}) < 12 \times 10^{-4}$. The yield of the NPL background will be taken from the fit.

Process	all channels	3μ channel	1e2μ channel	2e1μ channel	3e channel
NPL $\mathrm{Z}/\gamma^* + \mathrm{jets}$	46.61	16.47	15.90	8.80	5.44
$\mathrm{t\bar{t}Z}$	3.51 ± 0.34	1.45 ± 0.22	0.88 ± 0.16	0.72 ± 0.22	0.47 ± 0.11
WZ	6.10 ± 0.66	2.67 ± 0.47	1.68 ± 0.48	1.07 ± 0.17	0.70 ± 0.15
ZZ	4.60 ± 0.53	1.80 ± 0.38	1.64 ± 0.44	0.61 ± 0.12	0.56 ± 0.09
Other bkg.	1.25 ± 0.25	0.63 ± 0.29	0.30 ± 0.05	0.20 ± 0.05	0.12 ± 0.04
tZq	8.03 ± 0.47	3.51 ± 0.36	2.06 ± 0.21	1.46 ± 0.14	0.99 ± 0.09
NPL $\mathrm{t\bar{t}}$	67.87	28.47	24.54	8.14	6.72
$\kappa_{\mathrm{tZu}}/\Lambda$	11.25 ± 0.17	4.48 ± 0.12	2.95 ± 0.09	2.27 ± 0.06	1.54 ± 0.06
$\kappa_{\mathrm{tZc}}/\Lambda$	18.52 ± 0.30	7.70 ± 0.20	4.85 ± 0.15	3.61 ± 0.12	2.36 ± 0.10
Data	138 ± 15	55 ± 8	47 ± 7	21 ± 5	15 ± 5

Table 5.14: Event yields in the TTSR. The signal yield is set to its expected value for branching fraction equal to the expected limits of most stringent upper limit set by CMS [28], being $\mathscr{B}(\mathrm{t} \to \mathrm{uZ}) < 2.7 \times 10^{-4}$ and $\mathscr{B}(\mathrm{t} \to \mathrm{cZ}) < 12 \times 10^{-4}$. The yield of the NPL background will be taken from the fit.

Process	all channels	3μ channel	1e2μ channel	2e1μ channel	3e channel
NPL $Z/\gamma^* + \mathrm{jets}$	86.76	37.56	17.79	12.84	18.57
$\mathrm{t\bar{t}Z}$	42.55 ± 2.28	16.64 ± 1.73	10.97 ± 1.07	8.85 ± 0.86	6.10 ± 0.67
WZ	12.46 ± 1.12	4.98 ± 0.80	3.39 ± 0.51	2.50 ± 0.40	1.57 ± 0.23
ZZ	4.84 ± 0.35	1.78 ± 0.27	1.66 ± 0.23	0.76 ± 0.09	0.64 ± 0.11
Other bkg.	5.62 ± 0.82	2.18 ± 0.29	1.51 ± 0.18	1.19 ± 0.92	0.74 ± 0.10
tZq	16.93 ± 0.89	7.35 ± 0.72	4.57 ± 0.38	2.93 ± 0.24	2.07 ± 0.19
NPL $\mathrm{t\bar{t}}$	73.87	36.51	18.12	8.92	10.32
$\kappa_{\mathrm{tZu}}/\Lambda$	21.76 ± 0.25	8.64 ± 0.19	5.85 ± 0.12	4.27 ± 0.06	3.01 ± 0.09
$\kappa_{\mathrm{tZc}}/\Lambda$	56.85 ± 0.57	23.08 ± 0.37	15.56 ± 0.32	10.96 ± 0.18	7.25 ± 0.22
Data	243 ± 19	107 ± 11	58 ± 10	38 ± 8	40 ± 8

The search for FCNC involving a top quark and a Z boson 6

After imposing the selection requirements to enhance the signal fraction in the selected sample, the events are further classified into five statistically independent regions: STSR, TTSR, WZCR, STCR, and TTCR, shown in Table 5.9. In both signal regions (STSR and TTSR), no clear individual background discriminating variables were found and therefore a multivariate technique was chosen. In this search, it was opted to use Boosted Decision Trees. BDTs and neural networks are the two TMVA methods achieving the best separation power for analyses were the signal and background distributions overlap. Using a BDT has the computational advantage that it is a relatively fast method, it is easy to understand the features, and has an excellent efficiency. In particle physics, using a BDT is the most common approach.

In Section 6.1, the construction of the BDTs in the STSR and TTSR is explained. In each region, a set of discriminating variables is defined for each FCNC coupling, and BDTs are trained in each three-lepton channel separately. In the WZCR, a discriminating variable between the WZ+jets and NPL background is found, and this variable is presented in Section 6.2. The influence of systematic uncertainties on the distributions is investigated and the results are discussed in Section 6.3. The analysis strategy and the global fit is validated on pseudo-data to avoid any bias. This validation is explained in Section 6.4. After the validation, the fit is performed on the actual data and the results are shown in Section 6.5. Lastly, one-dimensional and two-dimensional limits are extracted and presented in Section 6.6.

6.1 Construction of the BDT template distributions

There were no selection criteria found using merely individual variables to make a clear rejection of the background events without sacrificing a significant amount of signal. For this reason, a multivariate approach using Boosted Decision Trees that combines several discriminating variables in the TMVA framework is used. For the training, the BDTs are trained against all backgrounds. The NPL background is not taken into account for the training since it is limited in statistics and would cause overtraining. The BDT settings are chosen to avoid overtraining and to maintain a good discriminating power against the backgrounds (see Section 3.3). The background and signal yields follow the relative fractions predicted by the simulation.

Starting from a large set of possible discriminating variables, a minimal set of variables is chosen for each signal region based on the ROC curves. Since for the tZu and tZc coupling, for example, the expected b-tag information will behave differently, as well as the fact that the charm coupling will have more similarities with the SM tZq process, different trainings with different input variables are performed for each coupling. The input variables do not depend on lepton flavour and are therefore kept the same over all three-lepton channels. However, keeping the NPL background in mind and to account for possible discrepancies between the muon and the electron, the training is done separately for each three-lepton channel. In Section 6.1.1, the construction of the multivariate discriminating variable in the STSR, for the tZu interaction, is shown. The construction of the multivariate discriminating variable in the TTSR for this interaction is shown in Section 6.1.2. For the tZc interaction, these are shown in Section 6.1.3 and Section 6.1.4 respectively.

The main backgrounds estimated from simulation in this search are WZ+jets, SM tZq, $t\bar{t}Z$, and ZZ processes. Their leading order Feynmann diagrams are shown in Figure 6.1, Figure 6.2, Figure 6.3 and Figure 6.4 respectively. The FCNC signal leading order Feynmann diagrams are shown in Figure 5.1 and Figure 5.2.

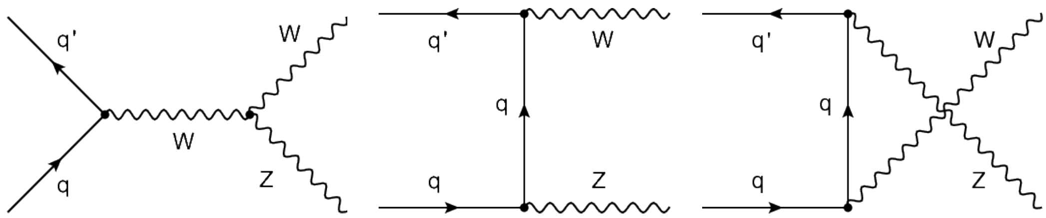

Figure 6.1: Leading order Feynmann diagrams for the WZ production in proton collisions. Left: s-channel, middle: t-channel, right: u-channel. Figure taken from [197].

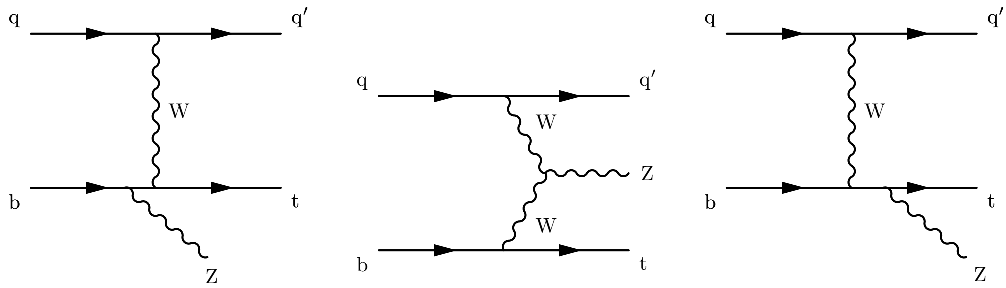

Figure 6.2: Some of the leading order Feynmann diagrams for the SM tZq production in proton collisions. Figure taken from [193].

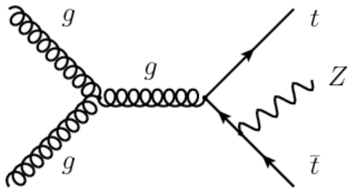

Figure 6.3: Dominant leading order Feynmann diagram for the $t\bar{t}Z$ production in proton collisions. Figure taken from [198].

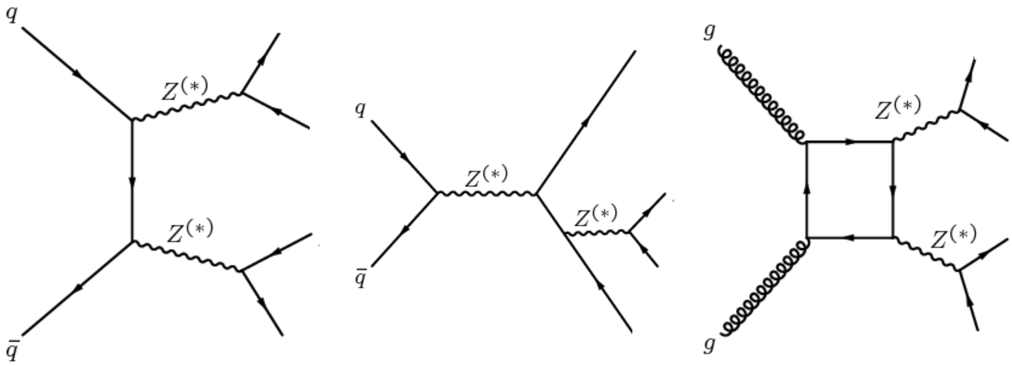

Figure 6.4: Leading order Feynmann diagram for the ZZ production in proton collisions. Left: t-channel production, middle: s-channel production, right: non-resonant production. The $Z^{(*)}$ notation is used to denote the production of on- and off-shell Z bosons and production of off-shell photons ($\gamma*$). Figure taken from [199].

6.1.1 BDT training in the STSR for the tZu interaction

Since in the STSR, the single top quark FCNC signal is expected to have an enhanced discrimination against the background processes compared to the top quark pair FCNC signal, the BDT is trained solely to enhance the single top quark FCNC signal. The single top quark FCNC signal expects one b jet (SM b jet), one lepton (W lepton) and missing transverse energy coming from the SM top quark decay (SM top quark). Furthermore, two leptons from the Z boson decay are expected.

The variables used to reconstruct the multivariate discriminator are chosen based on the differences between signal and background processes. For the STSR, the main background events are coming from the SM tZq, WZ+jets, and ZZ processes. The events originating from the WZ+jet process, are entering the STSR due to a b jet produced by gluon splitting or due to light-flavour jets that are mis-tagged as b jets. The SM tZq process has events entering the STSR when one jets is missing from the reconstruction. The events from the ZZ process enter the analysis when one jet is missing from the reconstruction and the other is (mis-)tagged as a b jet, or when one of the four leptons is missing from the reconstruction.

The WZ+jets and ZZ processes do not contain a top quark, while for the SM tZq the reconstructed SM top quark can lose energy via the radiated Z boson. Therefore variables related to the properties of the top decay through the Wtb vertex are studied for their discriminating power. The pseudorapidity of the SM top quark, η(SM top), as well as the invariant mass of the lepton arising from the W boson, l_W, and the SM b jet, are used as discriminating variables. The distribution of the pseudorapidity of the SM top quark peaks at zero for the single top quark FCNC signal, while the distribution is broader for the background contributions. The distribution of the invariant mass of the lepton arising from the W boson and the SM b jet peaks at around 100 GeV for signal and background, where the distribution of the background processes has a longer tail. Additionally, the difference in ϕ between the W lepton and the SM b jet, $\Delta\phi(\ell_W, b)$, peaks around $|\Delta\phi| = 1$ for signal, while for background this is around $|\Delta\phi| = \pi$. This indicates that for background, the W lepton and the SM b jet are not necessarily coming from the same object, while for signal these objects are closer together. This is also visible in the distribution of the difference in distance in the $\eta\phi$ plane, $\Delta R(\ell_W, b)$, between the W lepton and the SM b jet, where signal is peaking at lower values.

For signal, the lepton assigned to the W boson should be back-to-back to the Z boson. This feature is used by looking at the difference in ΔR between the W lepton and the Z boson, $\Delta R(Z, \ell_W)$, which peaks at π for the single top quark FCNC signal distribution. For the background processes the peak in the distribution is broader. For the signal, the jet with the highest transverse momentum is expected to be the b jet. For this reason, the CSVv2 discriminant of the jet with the highest p_T , CSVv2 jet p_T^{max}, is used as discriminating variable. Its distribution peaks at one for the single top quark FCNC signal process and resembles a flat distribution for the backgrounds. The distribution of the scalar sum of the p_T of the leptons, H_T^{lep}, is peaking at higher values for the single top quark FCNC signal. Hence, the single top quark FCNC signal is more transverse than its backgrounds.

Since the up quark is a valence quark for the proton, while the anti-up quark is a sea quark, one expects a charge asymmetry for the production of top and anti-top quarks. This effect is exploited by using the charge of the W lepton times the absolute pseudorapidity of the W lepton, $|\eta(\ell_W)| \times Q(\ell_W)$, and the p_T of the W lepton times its charge, $p_T(\ell_W) \times Q(\ell_W)$, as discriminating variables. Where the fact that the single top quark FCNC signal is more transverse than it backgrounds is used for the combination $|\eta(\ell_W)| \times Q(\ell_W)$. In the combination $p_T(\ell_W) \times Q(\ell_W)$, the fact that the single top quark FCNC signal is expecting a high-p_T prompt lepton is used.

The distributions of the variables are shown in Figure 6.5 for the 3μ lepton channel, the distributions for the other three-lepton channels can be found in Appendix C.1. The correlation between the different variables are shown in Figure 6.6.

The correlation between the variables is mostly small, but reaches up to $\sim$ 60%. The most discriminating variable is the distance in the $\eta\phi$ plane between the W lepton and the SM b jet, followed by the CSVv2 discriminator of the jet with the highest p_T . On the third place is the invariant mass of the W lepton and SM b jet system.

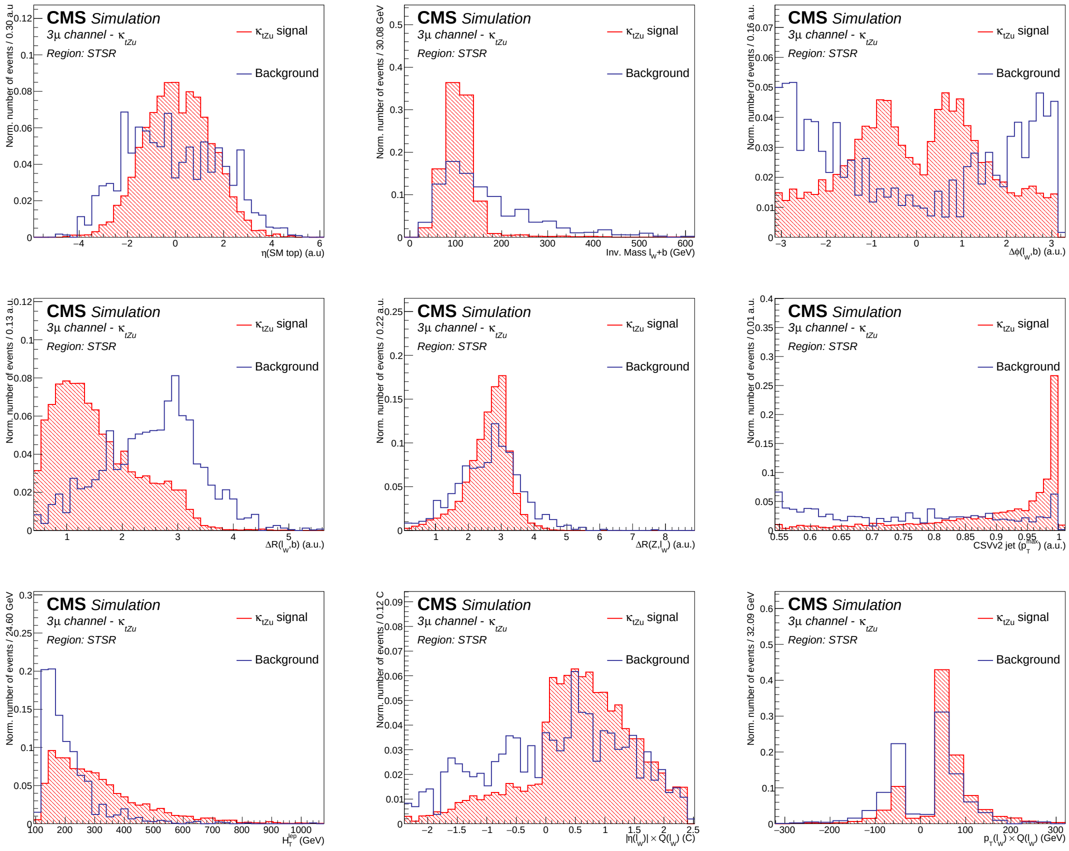

Figure 6.5: The normalised distributions of the input variables for reconstructing the multivariate discriminator in the STSR for the tZu vertex for the 3μ channel. The contribution of the NPL background is not included.

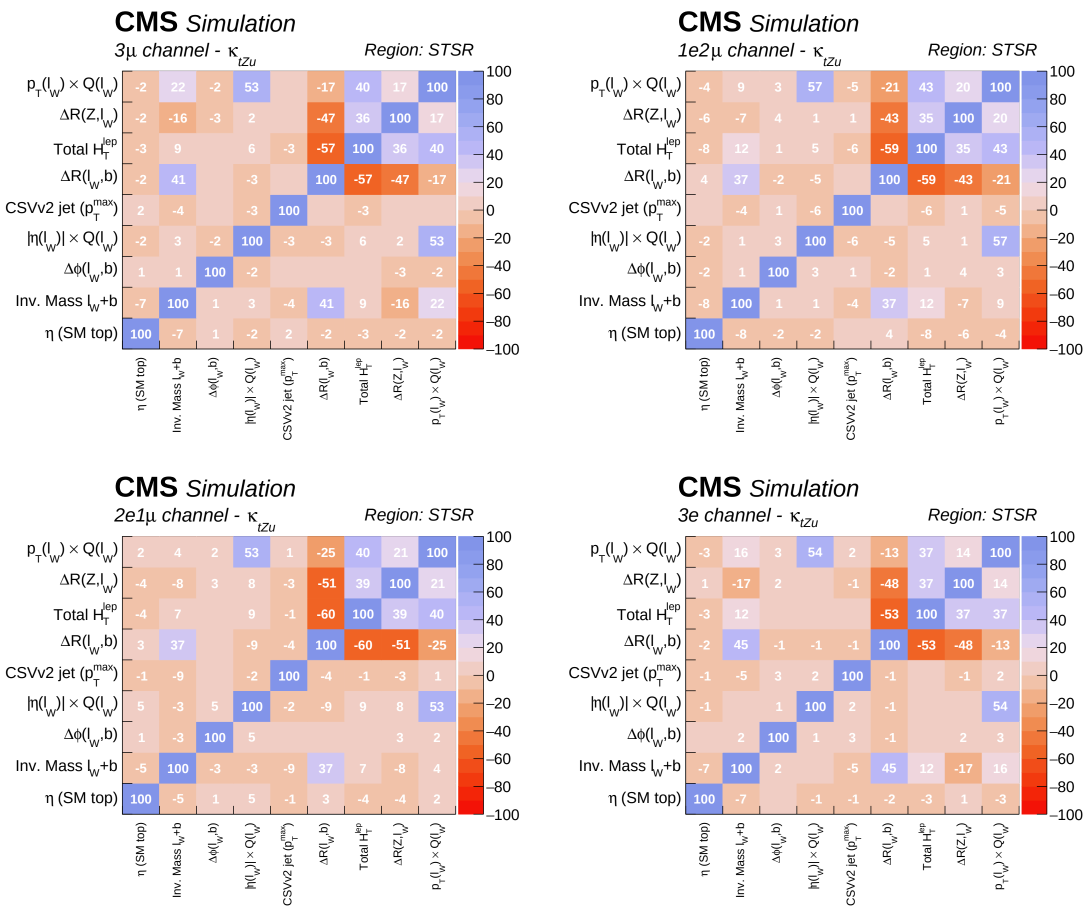

Figure 6.6: The correlations between the input variables used to create the multivariate discriminant in the STSR, for the tZu signal. For the 3μ (left,top), 1e2μ (right,top), 2e1μ (left, bottom) and 3e (right,bottom) three-lepton channel.

The resulting multivariate discriminator D is shown in Figure 6.7 for all three-lepton channels. In these plots one can observe that there is a clear discrimination between the FCNC single top quark signal and the backgrounds. Furthermore, one can investigate the procedure by cross checking the distribution from the training sample with an independent testing sample. As can be seen in the distributions, these samples agree with each other. Hence there is no overtraining for the BDT method and the testing and training sample show the same separation power.

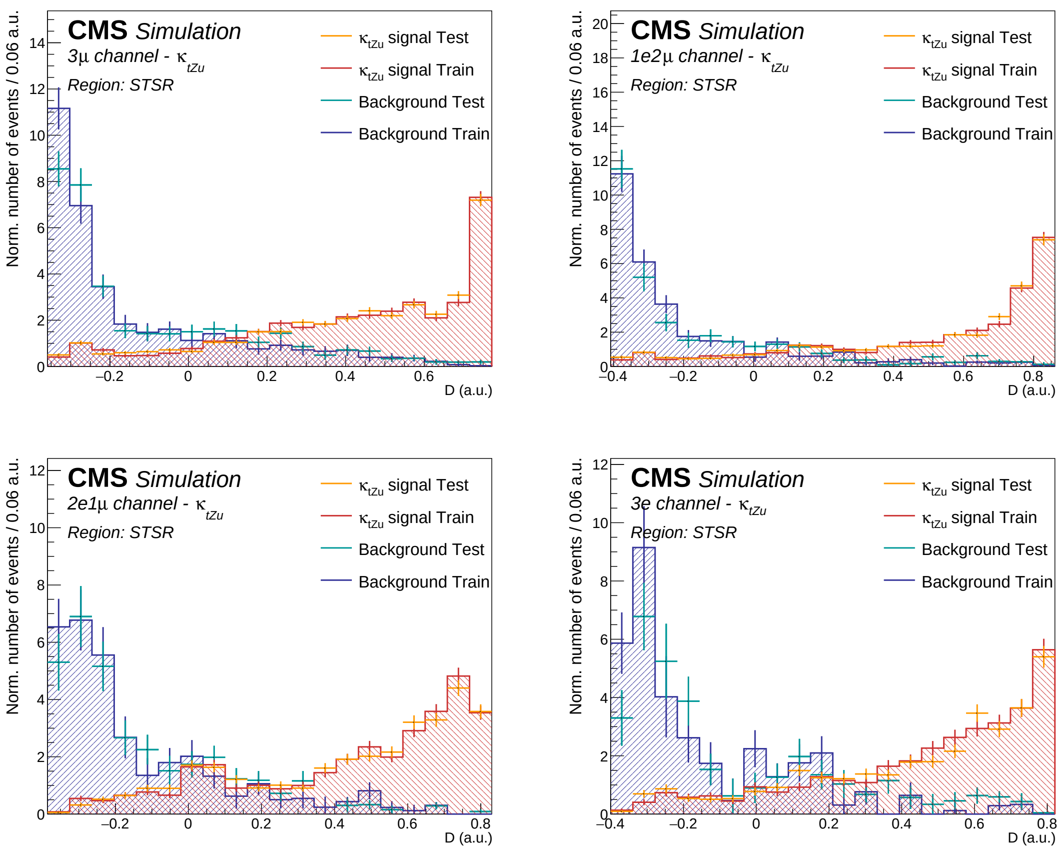

Figure 6.7: The normalised distributions of the resulting multivariate discriminators D in the STSR, for the tZu signal. For the 3μ (left,top), 1e2μ (right,top), 2e1μ (left, bottom) and 3e (right,bottom) three-lepton channel.

Additionally, the Receiving Operator Characteristic (ROC) curves for the testing and training samples are shown in Figure 6.8. One can observe that for all channels there is a clear separating power and that the ROC curve of the testing sample is a bit below the one for the training sample, resulting in slightly worse performance when testing the method. This is the most present in the 3e channel, where there is a lack of statistics. However, the distinction between signal- and background-like events is clearly still present.

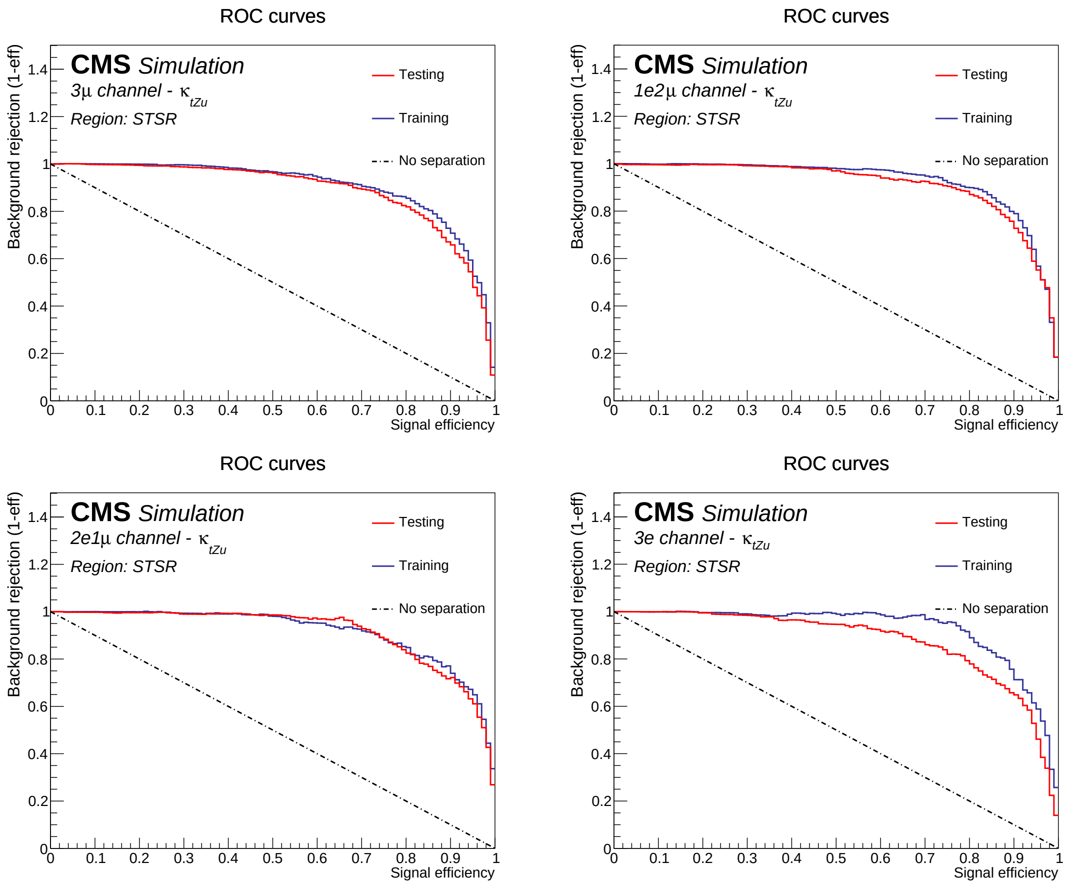

Figure 6.8: ROC curves of the resulting multivariate discriminators D in the STSR, for the tZu signal. For the 3μ (left,top), 1e2μ (right,top), 2e1μ (left, bottom) and 3e (right,bottom) three-lepton channel. The dashed line represents the case of no separation power.

6.1.2 BDT training in the TTSR for the tZu interaction

In this region, the BDT is trained to enhance the top quark pair and the single top quark FCNC signals at the same time. The contribution of the NPL background is again not considered during training. The top quark pair FCNC signal has the largest contribution in this region. Its SM decay side expects one b jet (SM b jet), one lepton (W lepton) and missing transverse energy coming from the SM top quark decay (SM top quark). The other top quark decays through the FCNC vertex and creates two leptons from the Z boson decay and a light-flavour quark (up or charm).

In this region, the main backgrounds are the $t\bar{t}Z$, SM tZq, and WZ+jets processes. Again, the events originating from the WZ+jet process, are entering the STSR due to a b jet produced by gluon splitting or due to light-flavour jets that are mis-tagged as b jets. The SM tZq process has exactly the same signature as the top quark pair FCNC signal. The events from the $t\bar{t}Z$ process are entering the analysis when both tops are decaying leptonically and one b jet is missing from the reconstruction, or in association with not prompt-leptons.

In Figure 6.9, the input variables used to create the multivariate discriminant are shown for the 3μ channel. The distributions for the other three-lepton channels are given in Appendix C.2. For the $t\bar{t}Z$ process, a Z boson is radiated of one of the top quarks of a top quark pair production process. Hence, no top quark is expected to be reconstructed from a light-flavour jet and Z boson. For the SM tZq process this also the case. Therefore, the invariant mass of the reconstructed FCNC top quark, as well as the distances in the $\eta\phi$ plane between the Z boson and the FCNC light-flavour jet are used as discriminating variables for this search. For background, the distribution invariant mass of the FCNC top quark has a broader peak than the FCNC signal which is peaking at the known top quark mass. The distribution of the distance between the FCNC jet and the reconstructed Z boson is peaking at higher values for the backgrounds compared to signal. Also the invariant mass of the Z boson is used as discriminating variable since the peak in the distribution is narrower for the FCNC signal compared to the background.

For the same reasons as in the previous section, the pseudorapidity of the SM top quark, the invariant mass of the W lepton and the SM b jet, as well as their distances in the $\eta\phi$ plane are considered. For the backgrounds, the invariant mass of the W lepton and SM jet system has a longer tail. Furthermore, the difference in distance between the W lepton and SM b jet peaks at lower values for the FCNC signal. The distribution of the difference in the azimuthal angle peaks around $|\Delta\phi| = 1$ for signal, and around $|\Delta\phi| = \pi$ for the background processes. Furthermore, the distribution of the minimal distance in the $\eta\phi$ plane between the W lepton and all the jets in the event is peaking at lower values for the FCNC signal than for backgrounds. This is due to the fact that for the FCNC signal events, this distance will be most likely the distance from the SM b jet, while for the $t\bar{t}Z$ and SM tZq processes this could be biased due to radiation, and for WZ+jets events this distance will come from a final state radiated jet. Also the number of b-tagged jets according to the CSVv2 medium working point is used in the multivariate discriminator. For FCNC signal, this distribution peaks at one, while for background this peaks at zero.

For the FCNC signal, one expects that the decay products coming from the FCNC interaction in the event is opposite in direction compared the decay products of the SM interaction. This is exploited by looking at the distribution of difference in azimuthal angle between the Z boson and W lepton. For the FCNC signal, this distribution peaks around $|\Delta\phi| = \pi$, while it is relatively flat for the background. Furthermore the difference in the $\eta\phi$ plane between the SM b jet and FCNC jet is used as discriminating variable. For the FCNC signal, this distribution peaks around three, and is broader for the backgrounds. The most important input variables for this training, are the invariant mass of the W lepton and the SM b jet system, as well as their distance. On the third place is the number of jets tagged as being a b jet according to the CSVv2 algorithm at its medium working point.

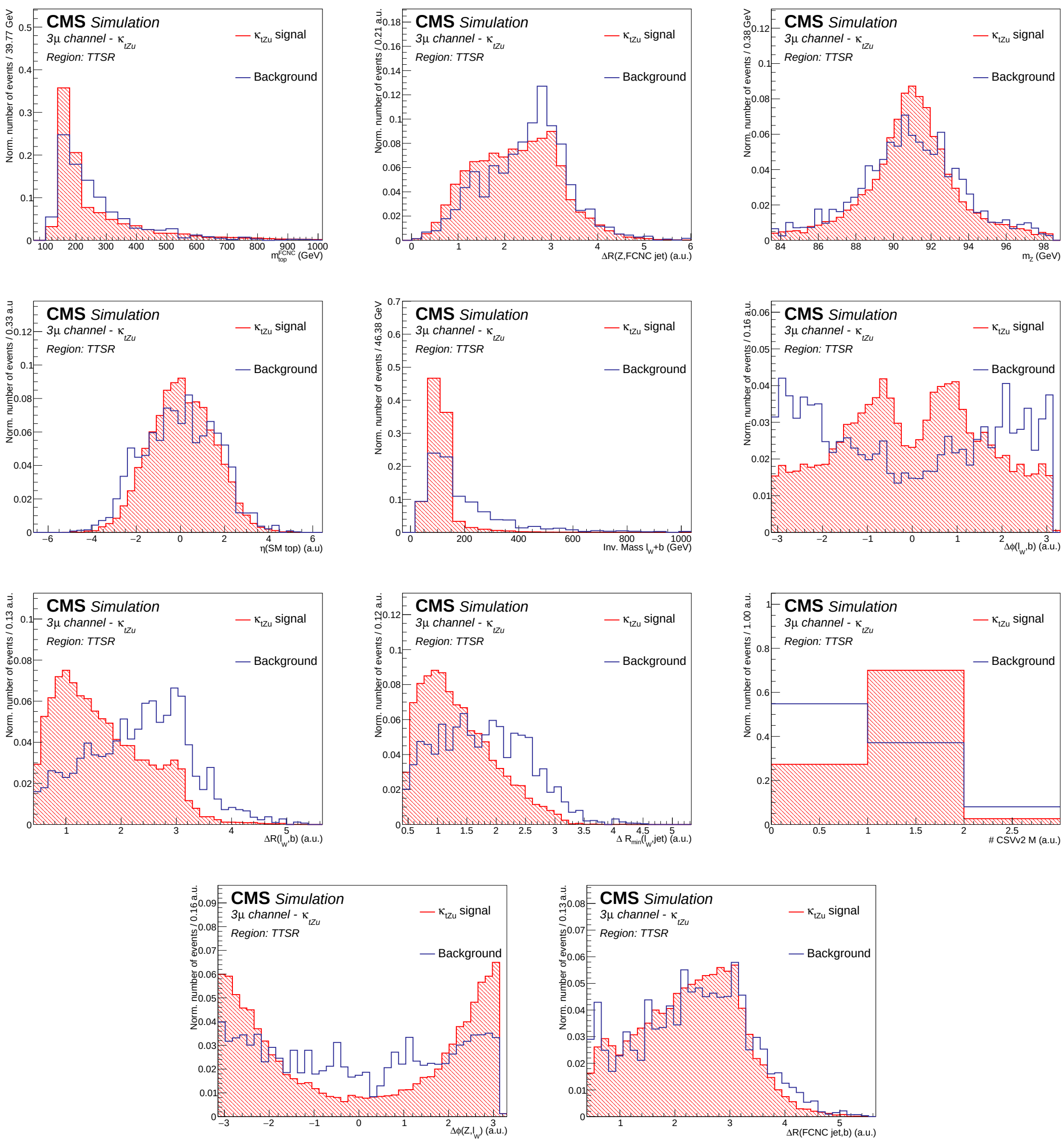

Figure 6.9: The normalised distributions for input variables for reconstructing the multivariate discriminator in the TTSR for the tZu vertex, in the 3μ lepton channel. The contribution of the NPL background is not included.

In Figure 6.10, the correlations between the input variables used for training and creating the multivariate discriminating variable are shown. In general, there is only a small correlation between the variables, with the exception of the distances and mass of the components of the top quarks.

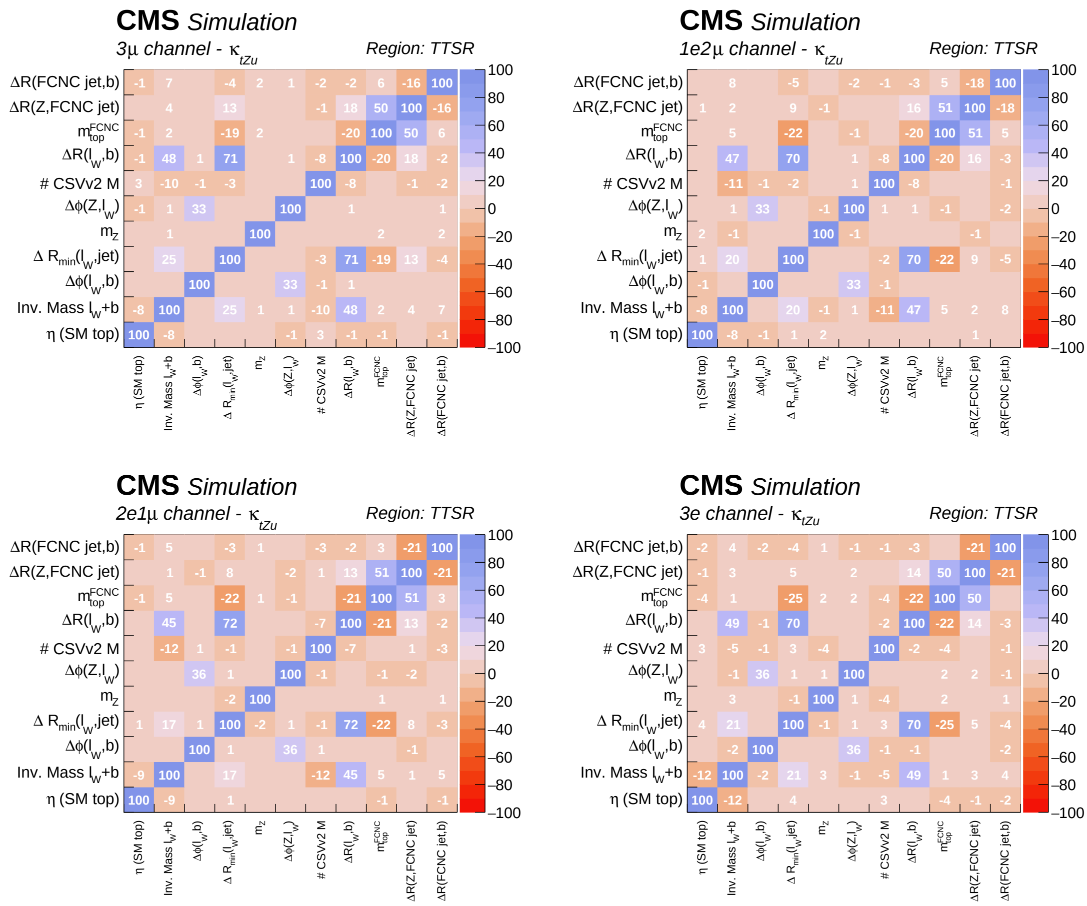

Figure 6.10: The correlations between the input variables used to create the multivariate discriminant in the TTSR, for the tZu signal. For the 3μ (left,top), 1e2μ (right,top), 2e1μ (left, bottom) and 3e (right,bottom) three-lepton channel.

The resulting multivariate discriminator D for this training is shown in Figure 6.11 for all three-lepton channels. Again, there is a clear discrimination between the FCNC signal and the background, and the testing and training samples agree with each other. Hence, there is no overtraining observed. The ROC curves are shown in Figure C.17, where the testing sample has a slightly worse performance compared to the training sample. However, a large separation power is still obtained for signal- and background-like events.

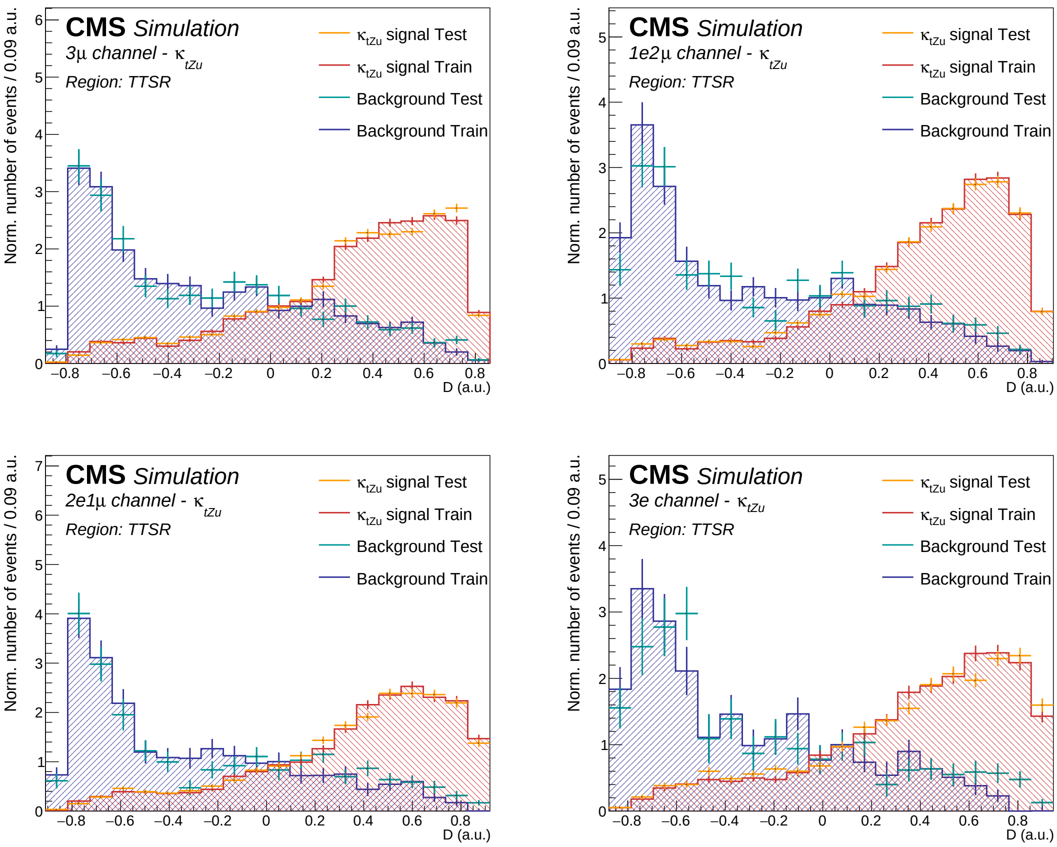

Figure 6.11: The normalised distributions of the resulting multivariate discriminators D in the TTSR, for the tZu signal. For the 3μ (left,top), 1e2μ (right,top), 2e1μ (left, bottom) and 3e (right,bottom) three-lepton channel.

6.1.3 BDT training in the STSR for the tZc interaction

The input variables used to create the multivariate discriminator in the STSR for the tZc interaction are shown in Figure 6.12. In analogy to the training for the tZu vertex in the STSR (Section 6.1.1), the training is performed while enhancing only the single top quark FCNC signal. The single top quark FCNC signal signature is similar to that of the signature expected from the tZu interaction and therefore most of the same variables discussed in Section 6.1.1 are used. For the charm coupling, both quark and anti-quarks responsible for the production of the single top quark FCNC process, are sea quarks. For this reason no charge asymmetry is expected, and the variables related to the charge asymmetry are left out. The most important variables in this training, are the invariant mass of all leptons, followed by the CSVv2 discriminator of the jet with the highest p_T , and the invariant mass of the W lepton and SM b jet system. The distributions for the other three-lepton channels are given in Appendix C.3.

The correlations between the different input variables are given in Figure 6.13. These correlations are in general small, but vary from zero to ∼55%. The resulting multivariate discriminator D is shown in Figure 6.14 for all three-lepton channels. In these plots one can observe that there is a clear discrimination between the FCNC single top quark signal and the backgrounds. Furthermore, the procedure is investigated by cross checking the distribution from the training sample with an independent testing sample. As can be seen in the distributions, these samples agree with each other. The ROC curves for the testing and training samples are shown in Figure C.18, where the testing sample has a slightly worse performance than the training sample. Though a clear discrimination power between signal- and background-like events is observed.

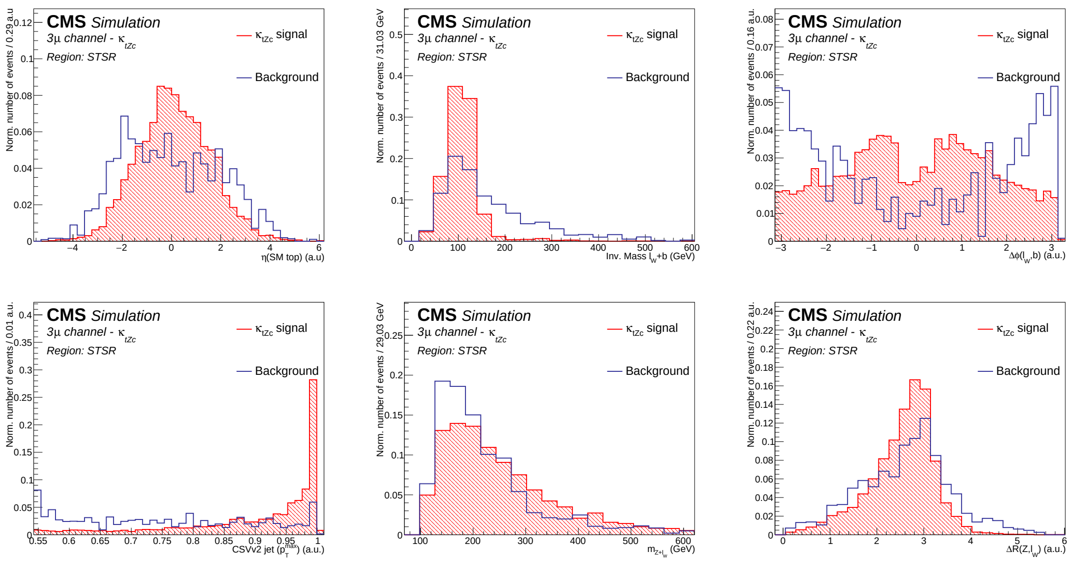

Figure 6.12: The normalised distributions of the input variables for reconstructing the multivariate discriminator in the STSR for the tZc vertex for the 3μ channel. The contribution of the NPL background is not included.

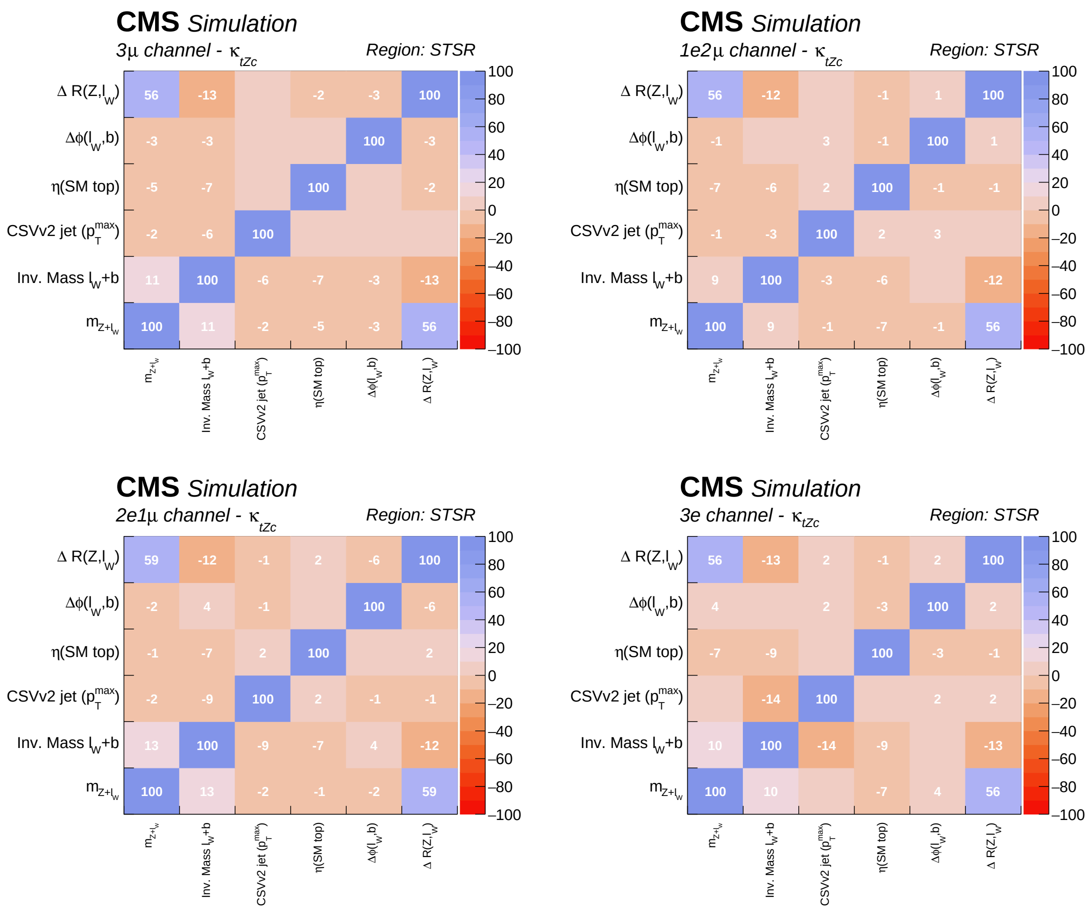

Figure 6.13: The correlations between the input variables used to create the multivariate discriminant in the STSR, for the tZc signal. For the 3μ (left,top), 1e2μ (right,top), 2e1μ (left, bottom) and 3e (right,bottom) three-lepton channel.

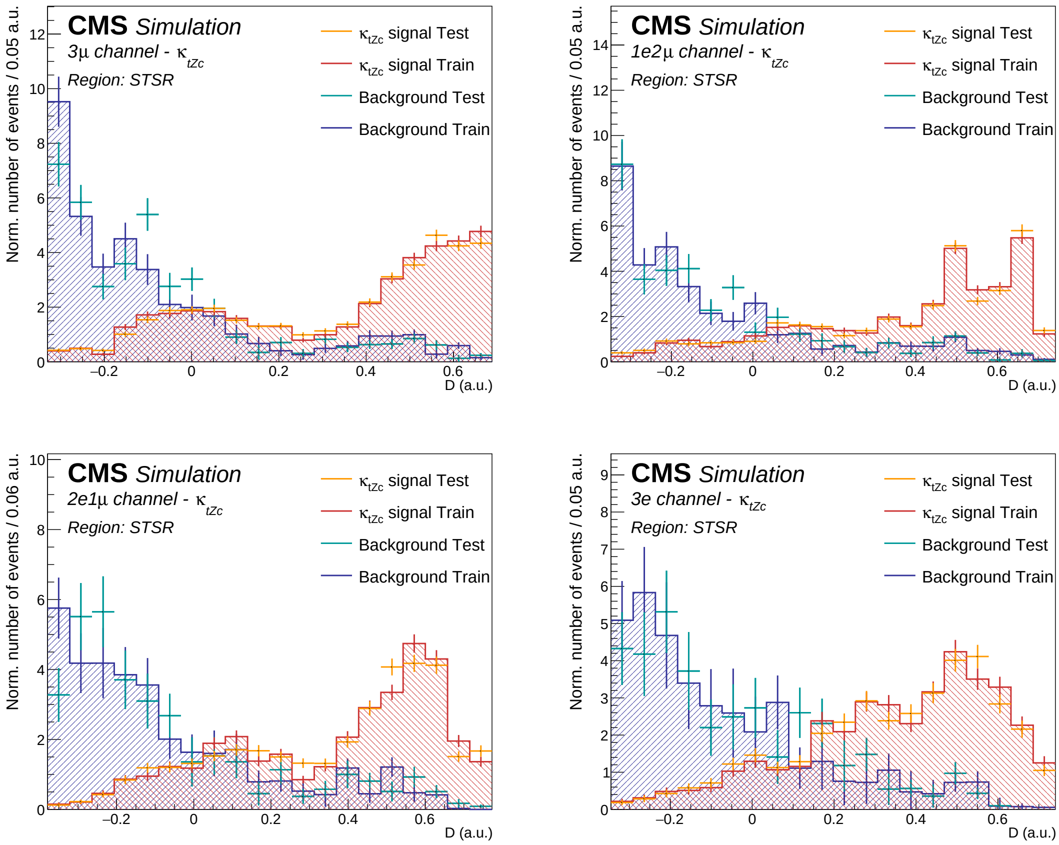

Figure 6.14: The normalised distributions of the resulting multivariate discriminators D in the STSR, for the tZc signal. For the 3μ (left,top), 1e2μ (right,top), 2e1μ (left, bottom) and 3e (right,bottom) three-lepton channel.

6.1.4 BDT training in the TTSR for the tZc interaction

The training in this region for the tZc interaction is performed by looking at both FCNC signal contributions. The discriminating variables used for training are shown in Figure 6.15. Most of the variables are the same as the ones for the tZu interaction, described in Section 6.1.2, since a similar signature is expected. The most important addition is the CSVv2 discriminator value of the FCNC jet. Since here, the FCNC jet is expected to be a charm quark jet, this jet is expected to have a high CSVv2 discriminator value. One can observe that in the FCNC signal distribution, there is a small bump at the value 0.8, whereas the background distribution goes down towards higher discriminator values.

The most important input variables for this region, are the invariant mass of the W lepton and the SM b jet system, the invariant mass of the FCNC top quark and the reconstructed Z boson mass. The distributions for the other three-lepton channels are given in Appendix C.4. The correlations between the input variables are shown in Figure 6.16. These are in general small, but vary from zero to ∼55% correlation.

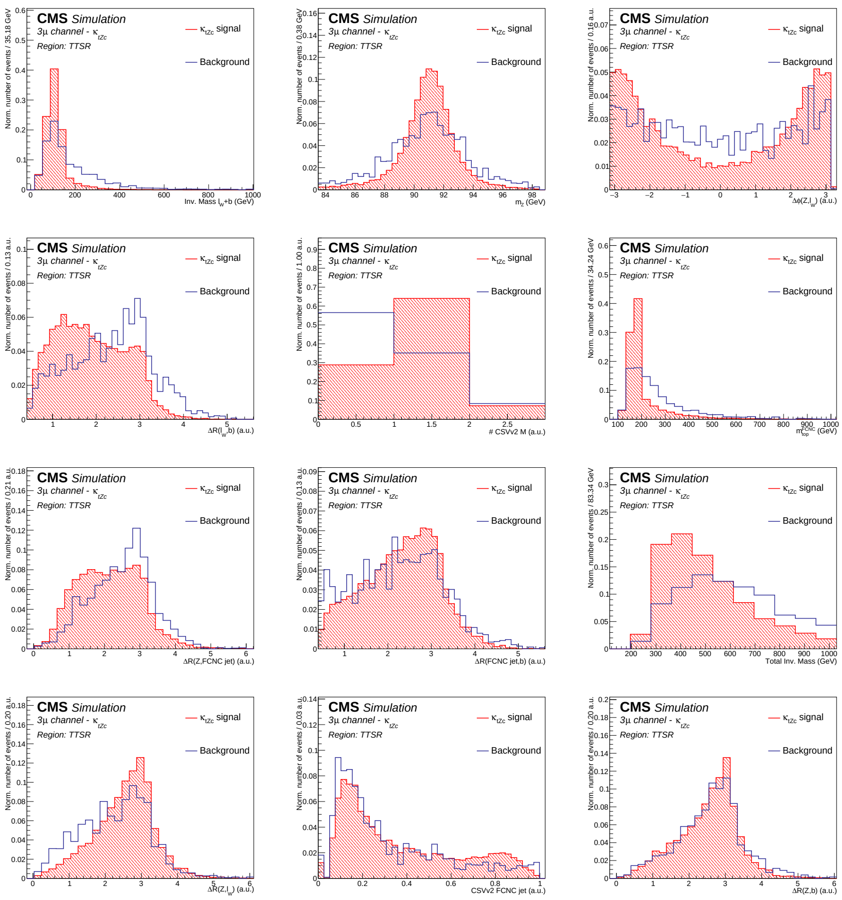

Figure 6.15: The normalised distributions of the input variables for reconstructing the multivariate discriminator in the TTSR for the tZc vertex, in the 3μ channel. The contribution of the NPL background is not included.

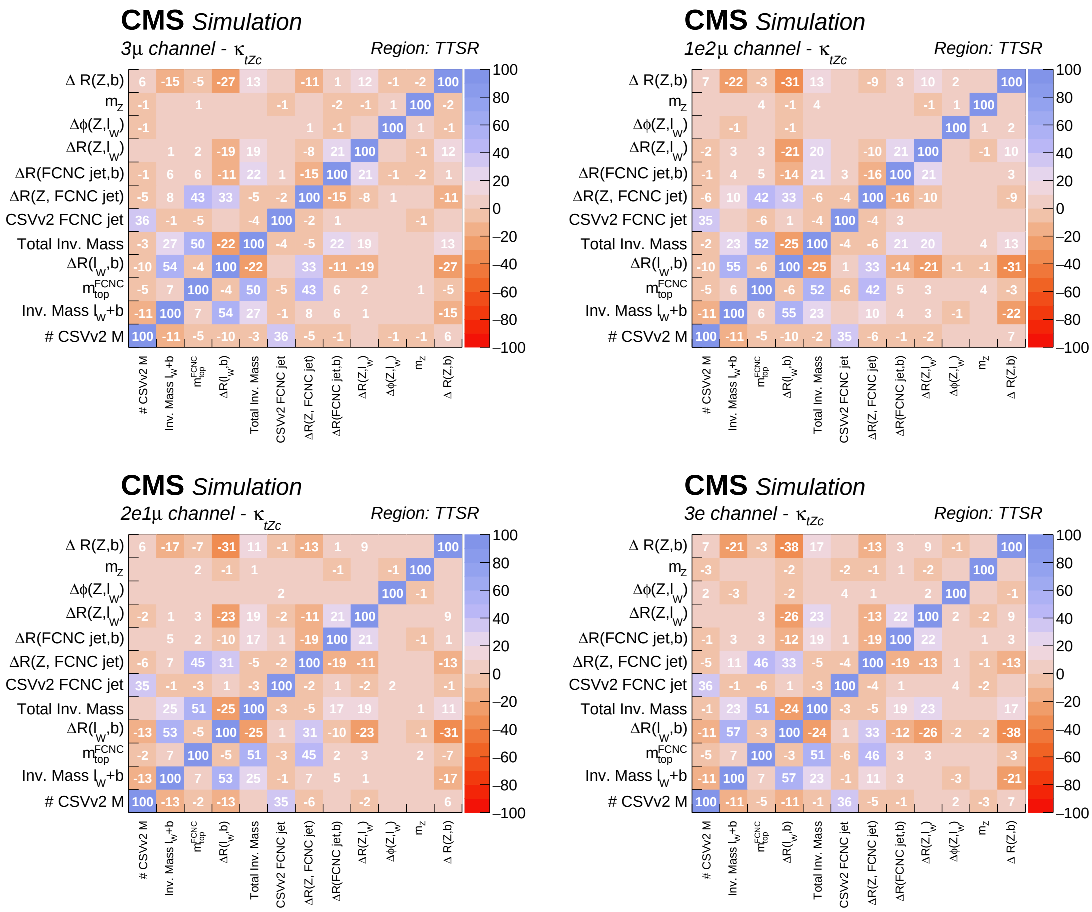

Figure 6.16: The correlations between the input variables used to create the multivariate discriminant in the TTSR, for the tZc signal. For the 3μ (left,top), 1e2μ (right,top), 2e1μ (left, bottom) and 3e (right,bottom) three-lepton channel.

The resulting multivariate discriminator D is shown in Figure 6.17 for all three-lepton channels. In these plots one can see that there is a clear discrimination between the FCNC signal and the backgrounds. Furthermore, the distribution from the training sample is compared with the testing sample, and agree with each other. A small overtraining is observed in the 3e channel due to its low number of events. The ROC curves are shown in Figure C.19 and show a slightly worse performance for the testing sample, while keeping its separation power.

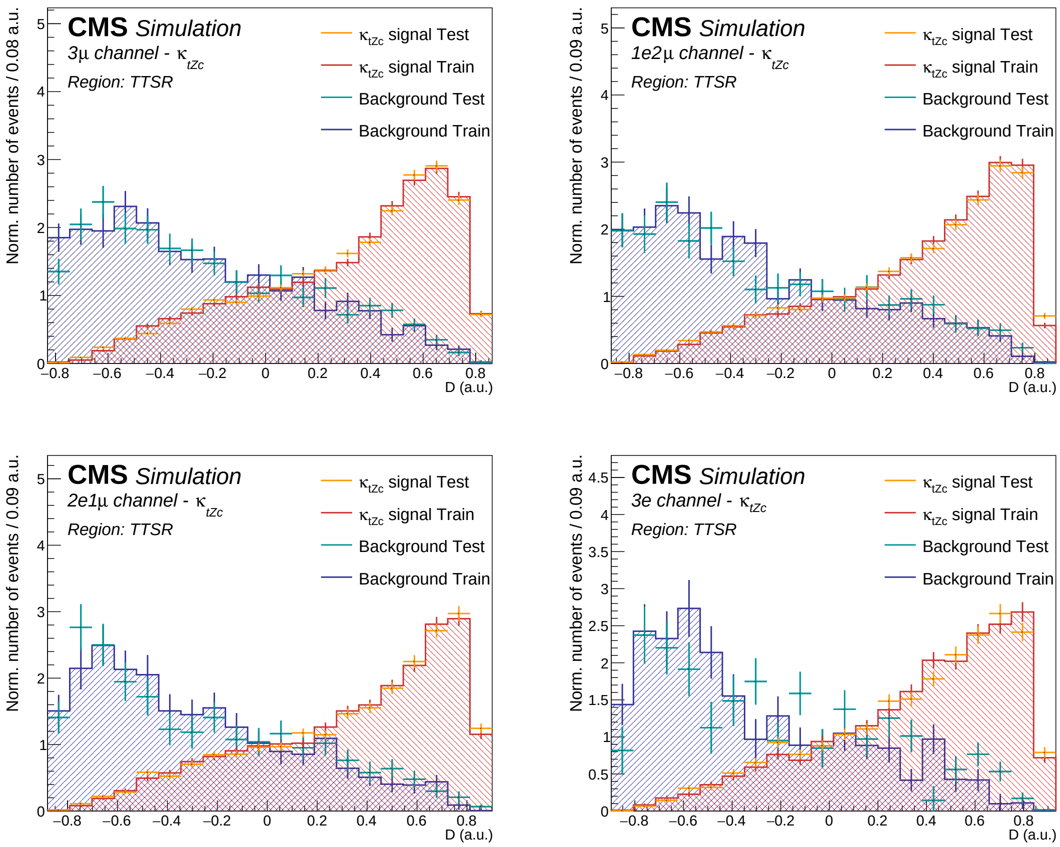

Figure 6.17: The normalised distributions of the resulting multivariate discriminators D in the TTSR, for the tZc signal. For the 3μ (left,top), 1e2μ (right,top), 2e1μ (left, bottom) and 3e (right,bottom) three-lepton channel.

6.2 Transverse mass of the W boson in WZCR

The WZCR is used to estimate the contribution from WZ+jets and NPL backgrounds. This region is constructed such that the contribution of the WZ+jets process is enhanced with respect to the other backgrounds entering the analysis. In this region, a fit is performed on the transverse mass distribution of the W boson. For the WZ+jets background process, a real W boson is expected, and the distribution will peak at the known mass of the W boson. For the NPL background, there is no reason for the distribution to peak at the mass of the W boson. Since the not prompt-leptons in general tend towards lower p_T values, their resulting distribution will peak a zero and decrease towards higher values of $m_T(W)$. The normalised distributions are shown in Figure 6.18 for all three-lepton channels.

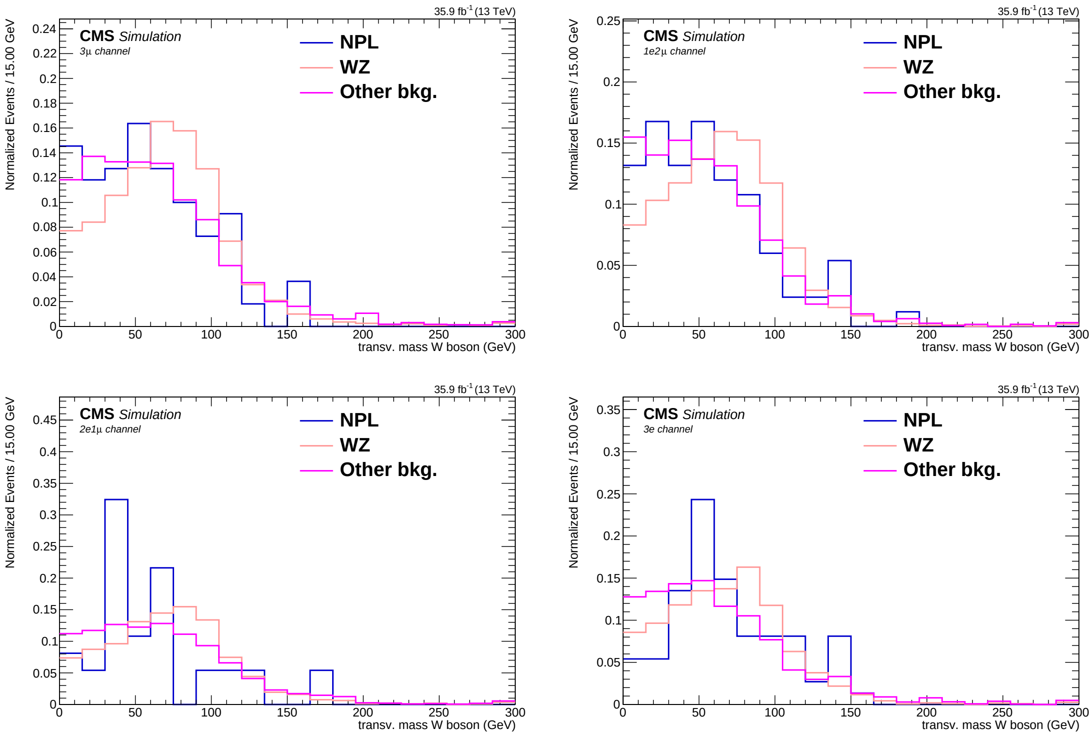

Figure 6.18: The normalised distribution of the transverse mass of the W boson in the WZCR, before the fit. Left: 3μ, left-middle: 1e2μ, right-middle: 2e1μ, and right: 3e lepton channel.

6.3 Systematic uncertainties

The systematic uncertainties entering the analysis are coming from different sources. The experimental uncertainties arise from the reconstruction of the objects and are discussed in Section 4.4. These influence the number of events passing the selection, so-called normalisation uncertainties, and/or the relative occupancies of the distributions, so-called shape uncertainties. The normalisation uncertainties coming from reconstruction include the uncertainty of 2.5% on the measured integrated luminosity and the efficiency of the trigger logic used for the analysis which has a 1% (5%) uncertainty on the 3μ and 1e2μ (2e1μ and 3e) channels. The pileup distribution is calculated via the minimum bias cross section which has a 4.6% uncertainty. This uncertainty results in a systematic shift in the pileup distribution and its shape effect is estimated by recalculating the pileup distribution for each variation of the minimum bias cross section. The shape uncertainties also include the uncertainties coming from the applied lepton scale factors. Their systematic uncertainty originates from three sources: identification, isolation and tracking. The uncertainties arising from jet energy corrections require a recalculation of all jet related kinematic observables and the effect is propagated to the missing transverse energy. The reweighting of the CSVv2 discriminant also induces a source of uncertainty. There are two sources of uncertainty contributing to the measurement of the b-tag related scale factors: statistical uncertainties and the purity of the sample. These result in eight uncorrelated contributions.

Since the NPL sample is artificially made from data by inverting the isolation of the third lepton, the effect of the inversion has to be estimated. The shape uncertainty for the NPL processes is obtained by varying the isolation inversion with respect to relative isolation value for the tight lepton identification and the relative isolation value for the loose lepton identification for electrons and muons at the same time. Changing the relative isolation requirement has a negligible effect on the shape of the relative distribution occupancies of the NPL background. The uncertainty on the normalisation of the overall NPL yield is taken as 50% in accordance with the SM tZq search [193].

The uncertainty on the expected yield of the simulated backgrounds is taken to be 30% of the yield such that it covers all uncertainties at next to leading order accuracy. Theory uncertainties originating from the modelling of the main backgrounds are estimated to account for the effect on the shape of the distributions from the choice of parton density functions, and renormalisation (μ_R) and factorisation (μ_F) scales. The effect of the renormalisation (μ_R) and factorisation (μ_F) scales is estimated by varying each independently ($\mu_R\uparrow$, $\mu_R\downarrow$, $\mu_F\uparrow$, or $\mu_F\downarrow$) and correlated up and down ($\mu_R\uparrow\mu_F\uparrow$ or $\mu_R\downarrow\mu_F\downarrow$) by a factor of two. The envelope of these variations is used as an uncertainty. The uncertainties coming from the parton density functions used for simulation are estimated using the PDF4LHC recipe [200], which combines the MMHT14, CT14, and NNPDF3.0 PDF sets. The theory uncertainties are considered for the main backgrounds coming from simulation: WZ+jets, ZZ+jets, $t\bar{t}Z$, and tZq. This is found to have a negligible effect.

Table 6.1 summarises the uncertainties, their size and their type. A log-normal probability distribution is used as prior for the normalisation uncertainties while the shape uncertainties are auxiliary measurements modelled by template morphing techniques [162]. The effect of systematic uncertainties that are treated as shape uncertainties is shown in Section 6.3.1 and Section 6.3.2 .

Table 6.1: Uncertainties used in this analysis. The column labelled type represents how the uncertainty is treated for the fit.

Source	Systematic input	Type
not prompt-muon norm.	50%	normalisation
not prompt-electron norm.	50%	normalisation
$t\bar{t}Z$ norm.	30%	normalisation
WZ norm.	30%	normalisation
tZq norm.	30%	normalisation
ZZ norm.	30%	normalisation
other bkg. norm.	30%	normalisation
trigger	1% (5%)	normalisation
lepton identification	$\pm\sigma(p_T, \eta)$	shape
JES	$\pm\sigma(p_T, \eta)$	shape
JER	$\pm\sigma(p_T, \eta)$	shape
b-tagging	$\pm\sigma(p_T, \eta)$	shape
pileup	$\pm\sigma$ of min. bias cross section	shape
PDF	PDF4LHC recipe	shape
luminosity	2.5%	normalisation
renorm. and fact. scales	varying indep. and corr.	shape

6.3.1 Effect of systematic uncertainties in WZCR

The effect of the systematic uncertainties influencing the shape of the distribution of the transverse mass of the W boson in the WZCR is shown in this section for the WZ+jet process by varying each source of uncertainty individually within its uncertainty range. The uncertainties due to pileup and lepton scale factors, shown in Figure 6.19, have the smallest effect on the distribution. The uncertainty on the pileup distribution is clearly influencing the shape of the distribution, while the lepton identification uncertainties are affecting the normalisation of the whole distribution.

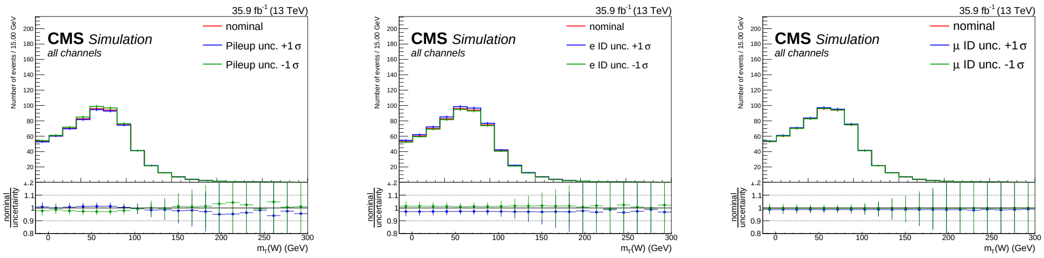

(a) Pileup uncertainty (b) Electron identification uncertainty (c) Muon identification uncertainty

Figure 6.19: Distribution of the nominal values and shift due to the experimental systematic uncertainties originating from pileup (left), electron (middle), and muon (right) scale factors for the transverse mass of the W boson in the WZCR for the WZ+jets process. All three-lepton channels summed.

The effect of the uncertainties arising from the jet energy corrections, shown in Figure 6.20, have the largest effect on the shape of the distribution. The jet energy scale has the most influence on the distribution, affecting both its normalisation and shape. This is due to the fact that the missing transverse energy, which is used for constructing the transverse mass of the W boson, is influenced by the change in jet energy. Still, this effect stays within a 10% margin.

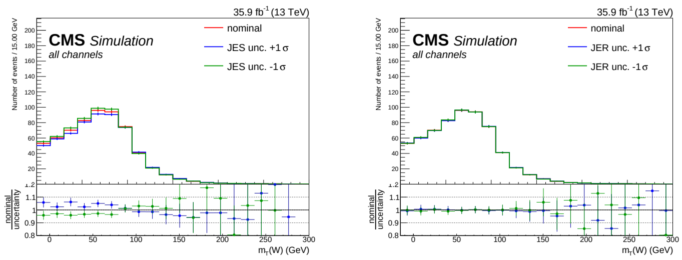

(a) Jet energy scale uncertainty (b) Jet energy resolution uncertainty

Figure 6.20: Distribution of the nominal values and shift due to the experimental systematic uncertainties originating from jet energy scale (left) and jet energy resolution corrections for the transverse mass of the W boson in the WZCR for the WZ+jets process. All three-lepton channels summed.

The uncertainties due to b-tagging are shown in Figure 6.21. The uncertainty due to purity of heavy flavour jets has the largest contribution and stays within 10% of the nominal shape. This is due to the fact that events are migrating in and out of the WZCR, based on the presence of b jets. The other uncertainties due to b-tagging uncertainties have a small impact on the shape of the distribution since no b-tag information is used to construct the transverse mass of the W boson.

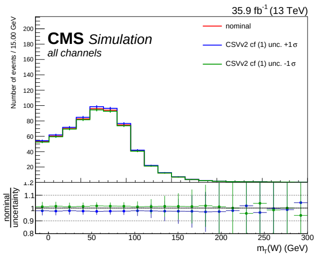

(a) CSVv2: cf uncertainty (1)

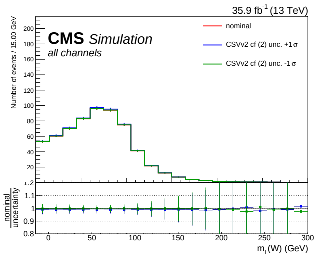

(b) CSVv2: cf uncertainty (2)

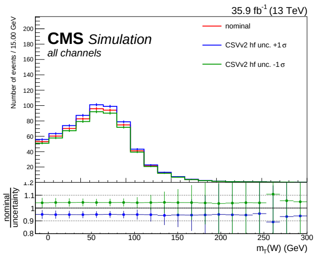

(c) CSVv2: hf uncertainty

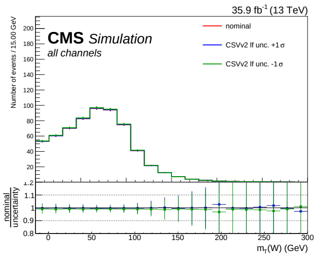

(d) CSVv2: lf uncertainty

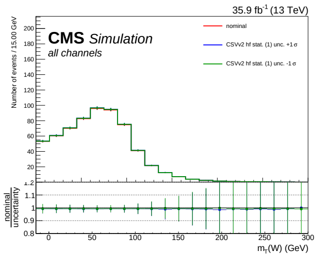

(e) CSVv2: hf statistical uncertainty (1)

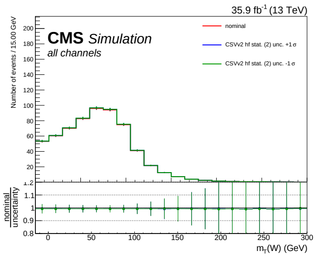

(f) CSVv2: hf statistical uncertainty (2)

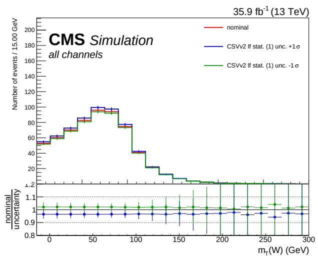

(g) CSVv2: lf statistical uncertainty (1)

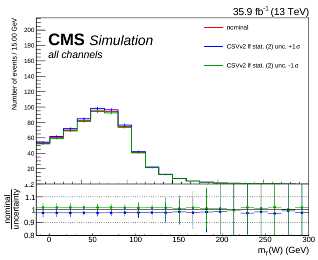

(h) CSVv2: lf statistical uncertainty (2)

Figure 6.21: Distribution of the nominal values and shift due to the experimental systematic uncertainties originating from b-tagging uncertainties for the transverse mass of the W boson in the WZCR for the WZ+jets process. All three-lepton channels summed.

In Figure 6.22, the effect of the theoretical uncertainties uncertainties on the distribution of the WZ+jets process is shown. The effect of the choice of factorisation and renormalisation scale is shown in Figure 6.22 (a), while the effect of the knowledge of the parton density functions is shown in Figure 6.22 (b). These uncertainties have a negligible effect.

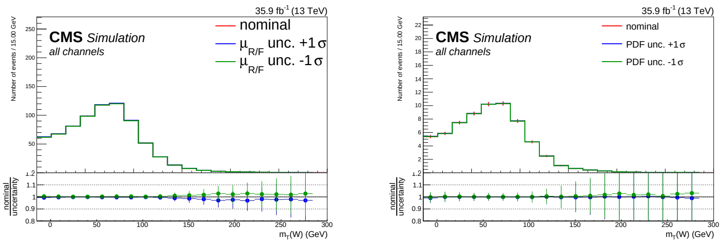

(a) Factorisation and renormalization scale uncertainty

(b) PDF uncertainty

Figure 6.22: Distribution of the nominal values and shift due to theoretical uncertainties for the transverse mass of the W boson in the WZCR for the WZ+jets process. All three-lepton channels summed.

6.3.2 Effect of the systematic uncertainties in the signal regions

The effect of the systematic uncertainties on the multivariate discriminator in the signal regions is also examined. Most systematic uncertainties result in an effect distribution of around 3.5% or less. These include the uncertainties due to pileup, lepton identification, jet energy resolution, the b-tagging, as well as those from theory. The uncertainty arising from the jet energy scale correction, shown in Figure 6.23, has the largest effect on the distributions, and stays within 20%.

6.4 Limit setting procedure validation

The analysis strategy has been established using a blinded methodology, i.e. without looking at the data in the signal regions. This way, one is sure that there is no bias introduced into the analysis. Through the use of a pseudo dataset, the limit setting procedure has been validated. Signal injection tests for which the signal strength from a pseudo dataset with a pre-set signal strength is estimated are performed and shown in Figure 6.24. From these plots, it is clear that for a data set with a signal strength $\mu = 0.1$, 0.2, 0.3, 0.4 or 0.5, the maximum likelihood estimate returns the same values. This validation has been done for both the tZu and tZc interaction.

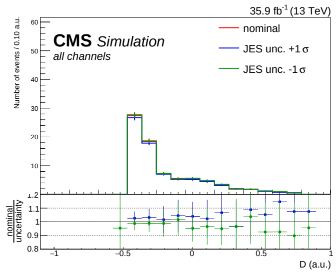

(a) STSR - tZu coupling

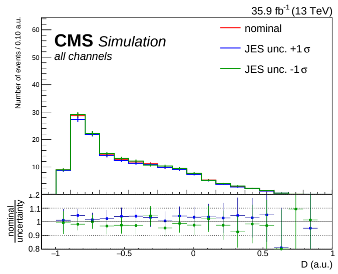

(b) TTSR - tZu coupling

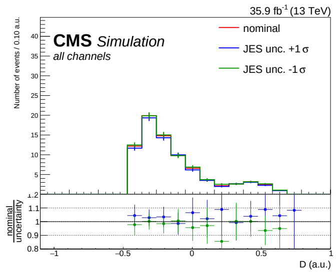

(c) STSR - tZc coupling

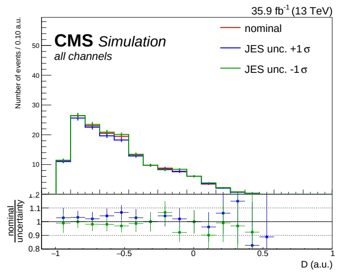

(d) TTSR - tZc coupling

Figure 6.23: Distribution of the nominal values and shift due to the jet energy scale uncertainty for the discriminant in the signal regions for the WZ+jets process. All three-lepton channels summed.

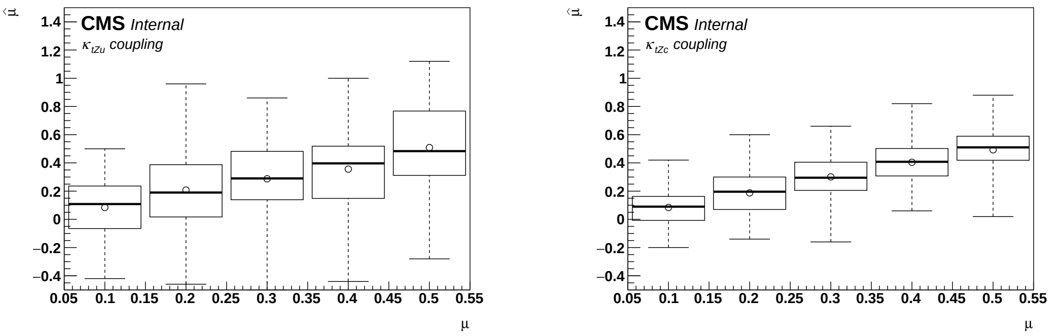

Figure 6.24: The obtained signal strength with the Maximum Likelihood method is in agreement with the signal strength used to generate the pseudo data set for the tZu (left) and tZc (right) couplings. The solid line represents the input signal strength while the open marker is the “measured” signal strength for pseudo data.

Another validation has been done by performing a Maximum Likelihood fit in the WZCR only, considering all three-lepton channels. This validation has been performed to have a confirmation of the method for the data driven estimation of the NPL yield. A simultaneous fit of the "signal" strength of the NPe, NPμ and the WZ+jets backgrounds is done by using the multi-dimensional fit in `Higgs Combine Tool`. The maximum likelihood estimator of the NPμ yield and the one for the NPe are in agreement with each other. The yield of the WZ+jets is estimated to be 20% larger than its initial value, which is within its 30% rate uncertainty. The resulting NPL and WZ+jets signal strengths can then be applied on the distribution of the transverse mass of the W boson to verify data/MC agreement, as can be seen in Figure 6.25.

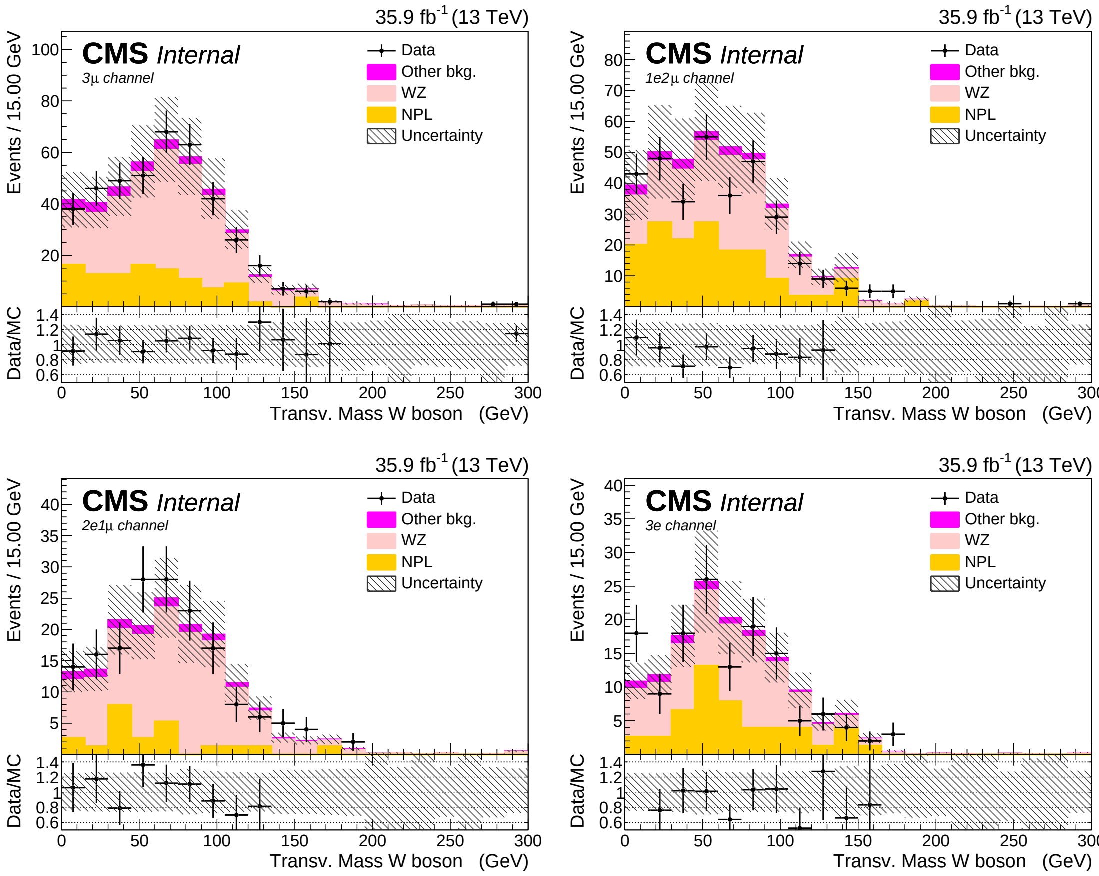

Figure 6.25: Distribution of the transverse mass of the W boson in the WZCR for the 3μ channel (left, upper), 1e2μ channel (right, upper), 2e1μ channel (left, lower), and 3 electrons channel (right, lower). The uncertainty band does not include theoretical uncertainties.

6.5 Results and discussion

The limit setting procedure explained in Section 3.4 is applied and results are obtained for each three-lepton channel separately as well as the four three-lepton channels combined. For both the tZu and tZc coupling, the maximum likelihood estimator of their signal strengths $\hat{\mu}$ is compatible with zero as is shown Figure 6.26. One can see that the 3e lepton channel has the largest uncertainty. This is due to the fact that this channel is the most influenced by the lack of statistics for this search.

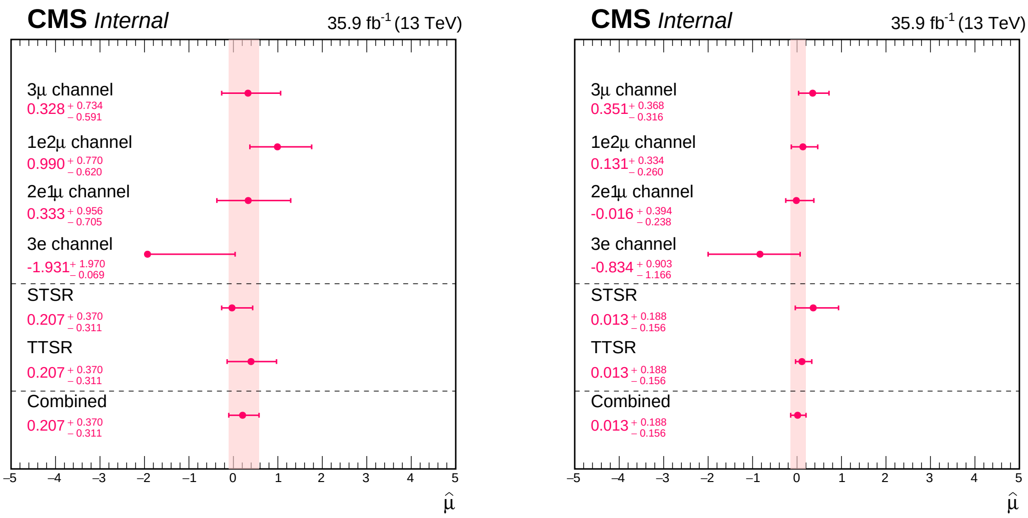

Figure 6.26: The maximum likelihood estimators for the signal strengths for the tZu vertex (left) and tZc vertex (right) per lepton channel as well as the combination in the STSR, TTSR, and all regions combined.

The maximum likelihood estimators for the nuisance parameters $\hat{\theta}$ are shown in Figure 6.27 for the tZc and the tZu interactions. Their values obtained from the signal plus background or background only fits are in agreement with each other. The transfer factors used to project the event rates from the control regions to the signal regions, have an initial value different than one and have small uncertainties. The normalisation uncertainties on the yields of the simulated backgrounds get constrained by the fit. The nuisance parameters related to the NPL backgrounds get pulled by the fit since their initial normalisation was arbitrary chosen. These have the same tendencies for the fit performed for the tZu and tZc interaction.

In Figure 6.28 and Figure 6.29, one can see again that the nuisance parameters related to the NPL normalisations are shifted with respect to their initial values. This is to be expected since their initial normalisation is arbitrary. Furthermore, the effect of the uncertainties on the maximum likelihood estimate of the signal strength is shown. The search is limited by lack of data, as can be seen from Figure 6.36 and Figure 6.37. There one can see that the result where only the statistical uncertainty are taken into account gives similar results as taking all uncertainties into account. The most important systematic uncertainty are the $t\bar{t}Z$ normalisation, JES uncertainty and the NPL normalisation uncertainty.

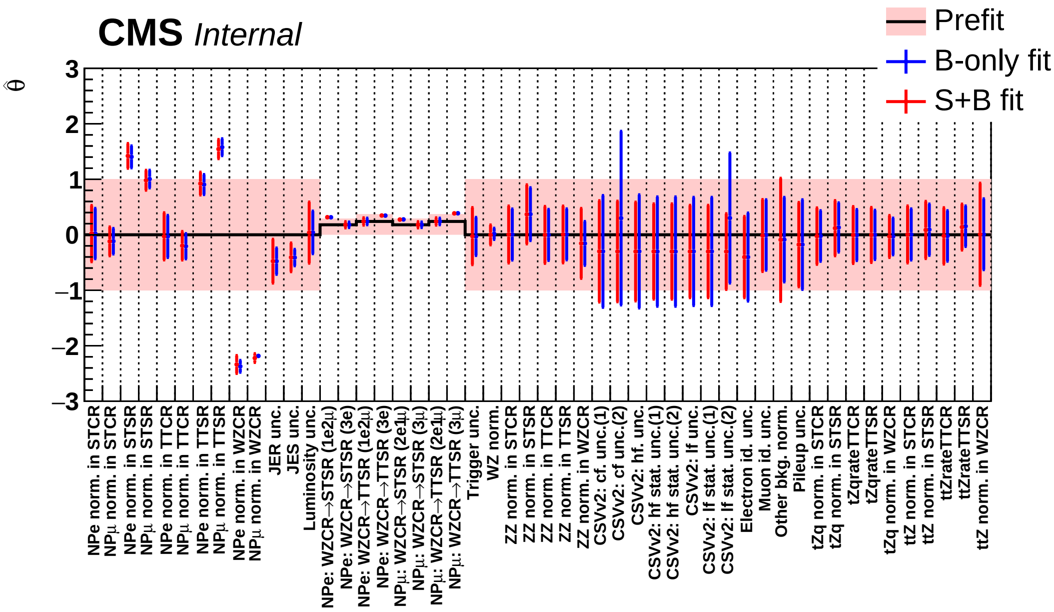

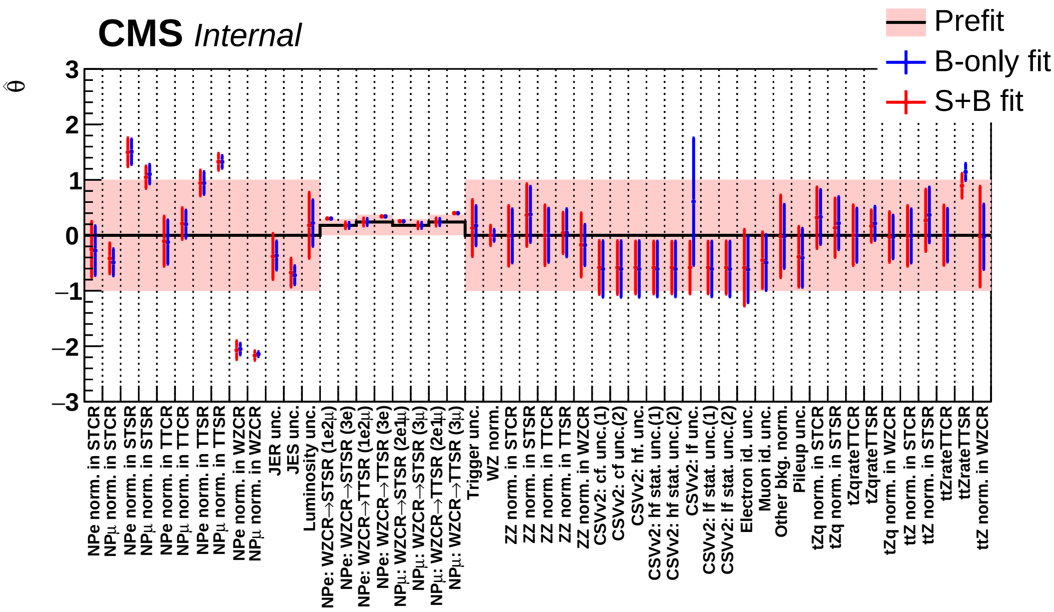

Figure 6.27: Maximum likelihood estimators for the tZc vertex (up) and tZu vertex (down).

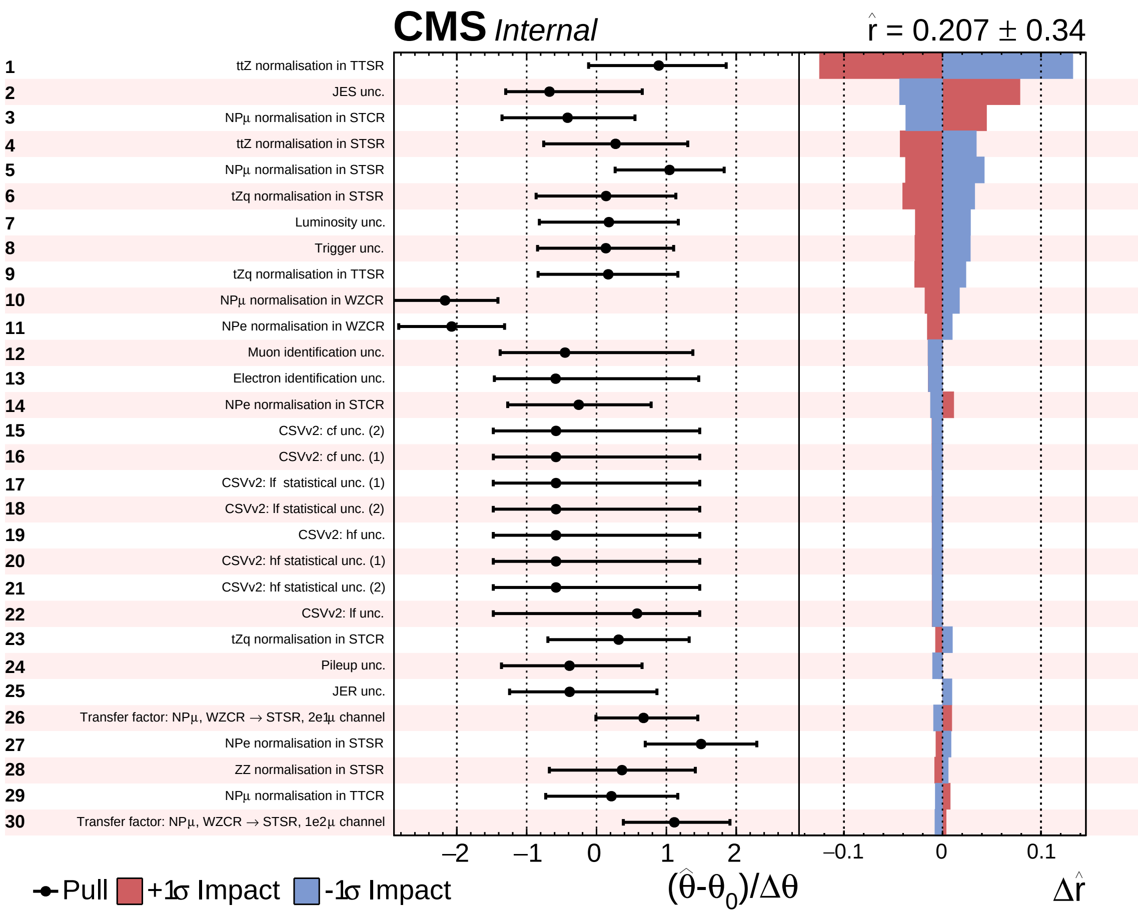

Figure 6.28: The pulls of the most influential nuisance parameters and the influence of their uncertainty on the maximum likelihood estimation of the signal strength $\hat{r}$ for the tZu vertex.

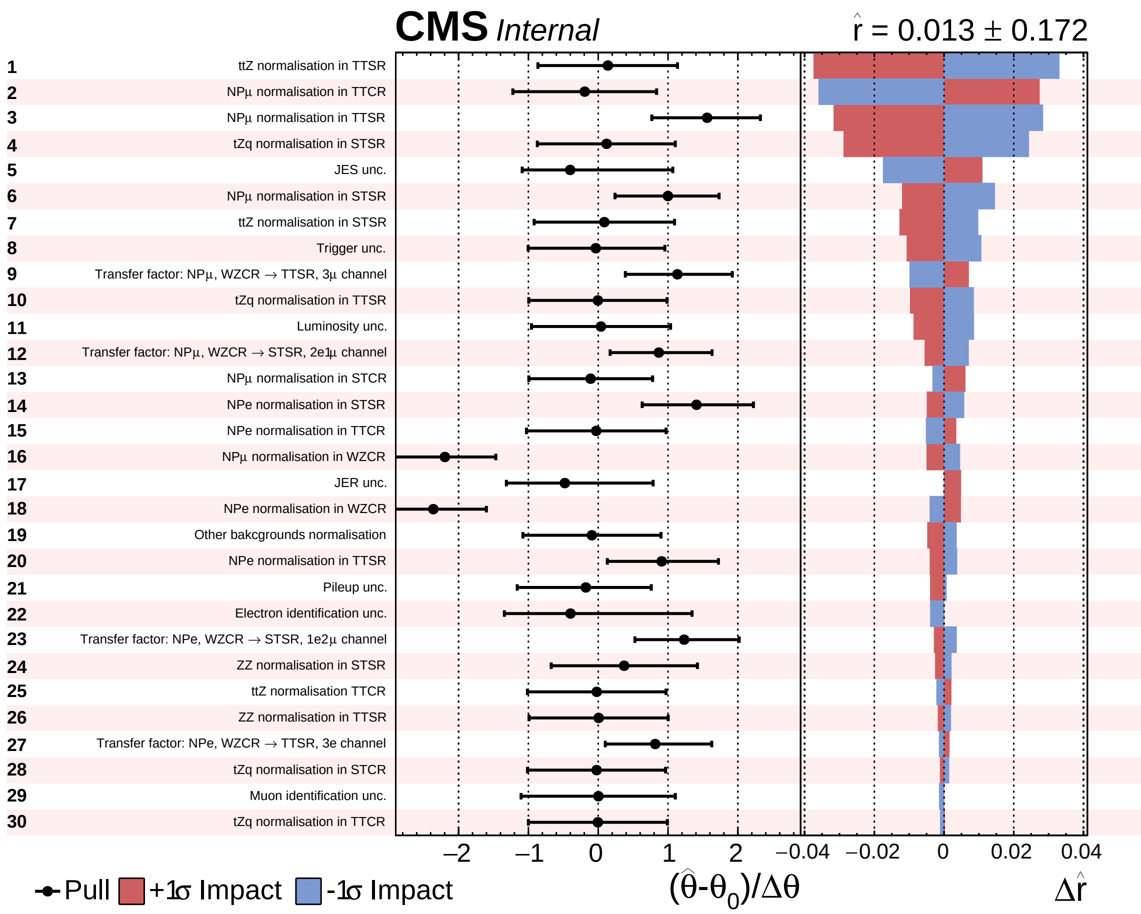

Figure 6.29: The pulls of the most influential nuisance parameters and the influence of their uncertainty on the maximum likelihood estimation of the signal strength $\hat{r}$ for the tZc vertex.

6.5.1 Postfit distributions

The distributions of multivariate discriminating variables as well as the distribution of the transverse mass of the W boson are recreated with the maximum likelihood estimations of the nuisance parameters. The resulting distributions are shown in Figure 6.30, Figure 6.31, Figure 6.32, Figure 6.33, and Figure 6.34. In the WZCR and TTSR, the regions where the most events are entering, there is a clear agreement between data and simulation for all three-lepton channels. In the STSR, there are some jumps due to the fact that the NPL background is made from a limited data sample and does not have a smooth template to fit. The distribution of the transverse mass of the W boson in the WZCR should contain the same event yield for both global fits (tZu and tZc). This behaviour is visible for all three-lepton channels.

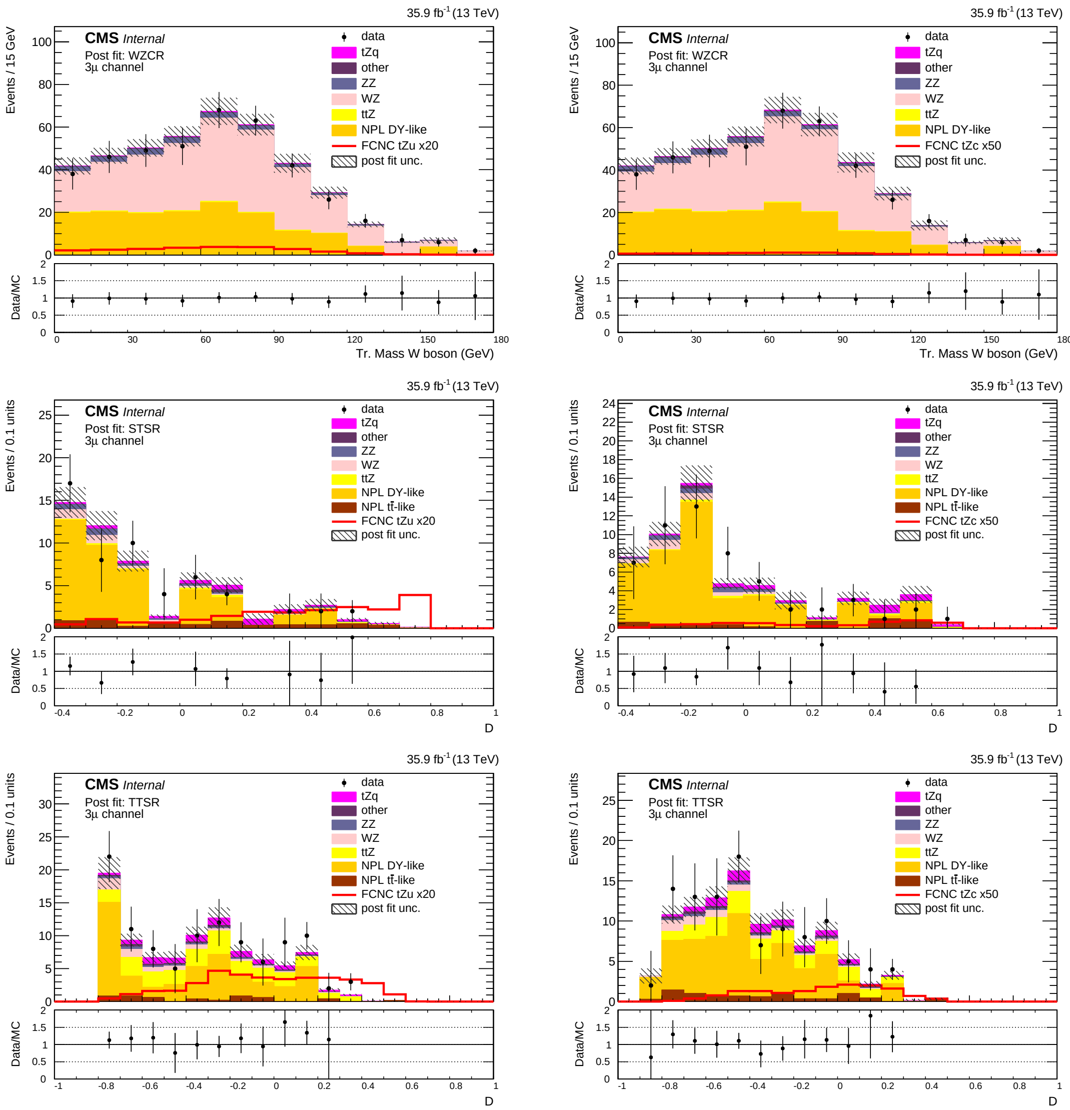

Figure 6.30: Post fit distributions for the 3μ lepton channel of the transverse mass of the W boson in the WZCR (top), the multivariate discriminating variable in the STSR (middle), and the multivariate discriminating variable in the TTSR (bottom) for the tZu (left) and tZc (right) couplings.

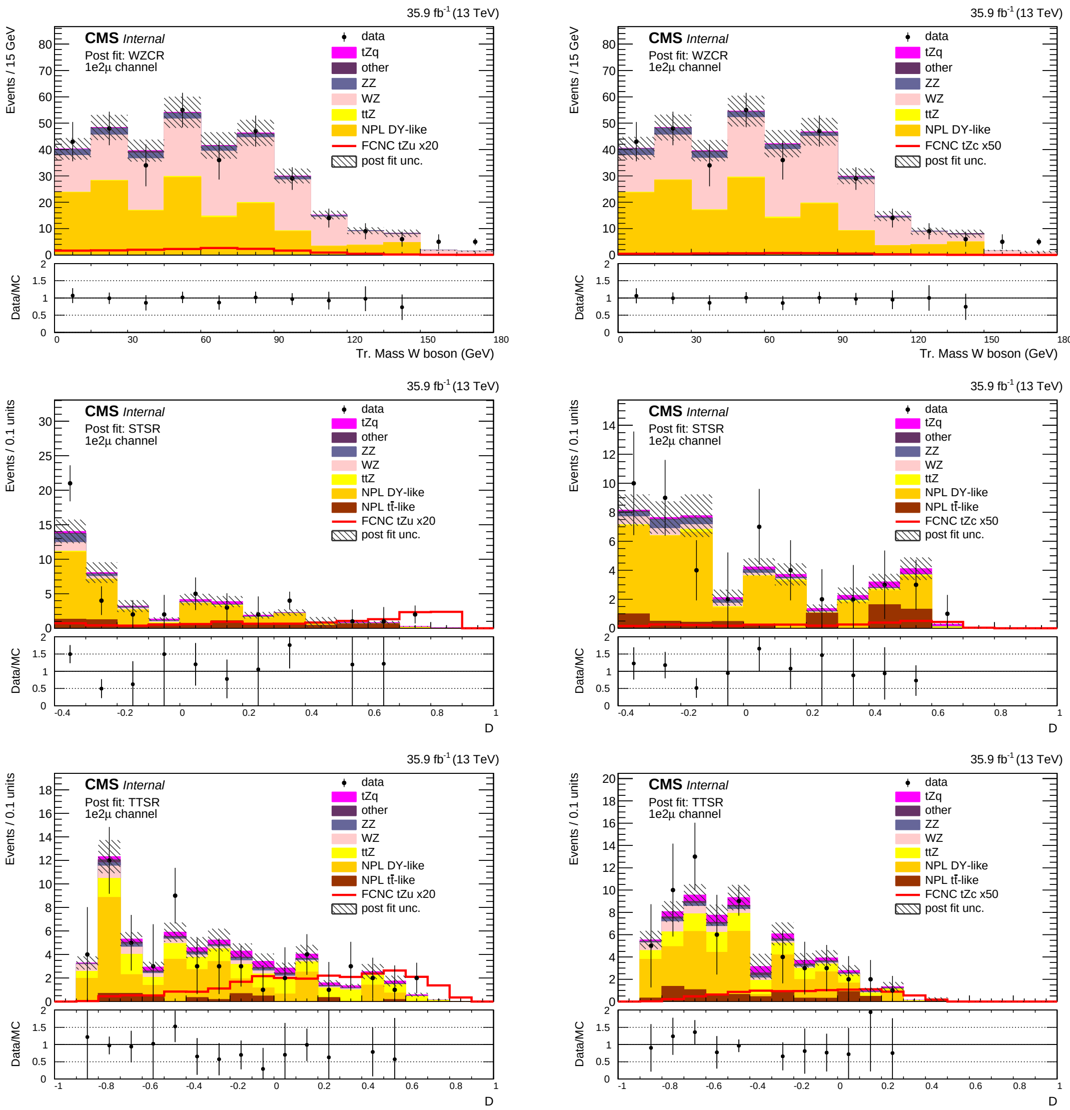

Figure 6.31: Post fit distributions for the 1e2μ lepton channel of the transverse mass of the W boson in the WZCR (top), the multivariate discriminating variable in the STSR (middle), and the multivariate discriminating variable in the TTSR (bottom) for the tZu (left) and tZc (right) couplings.

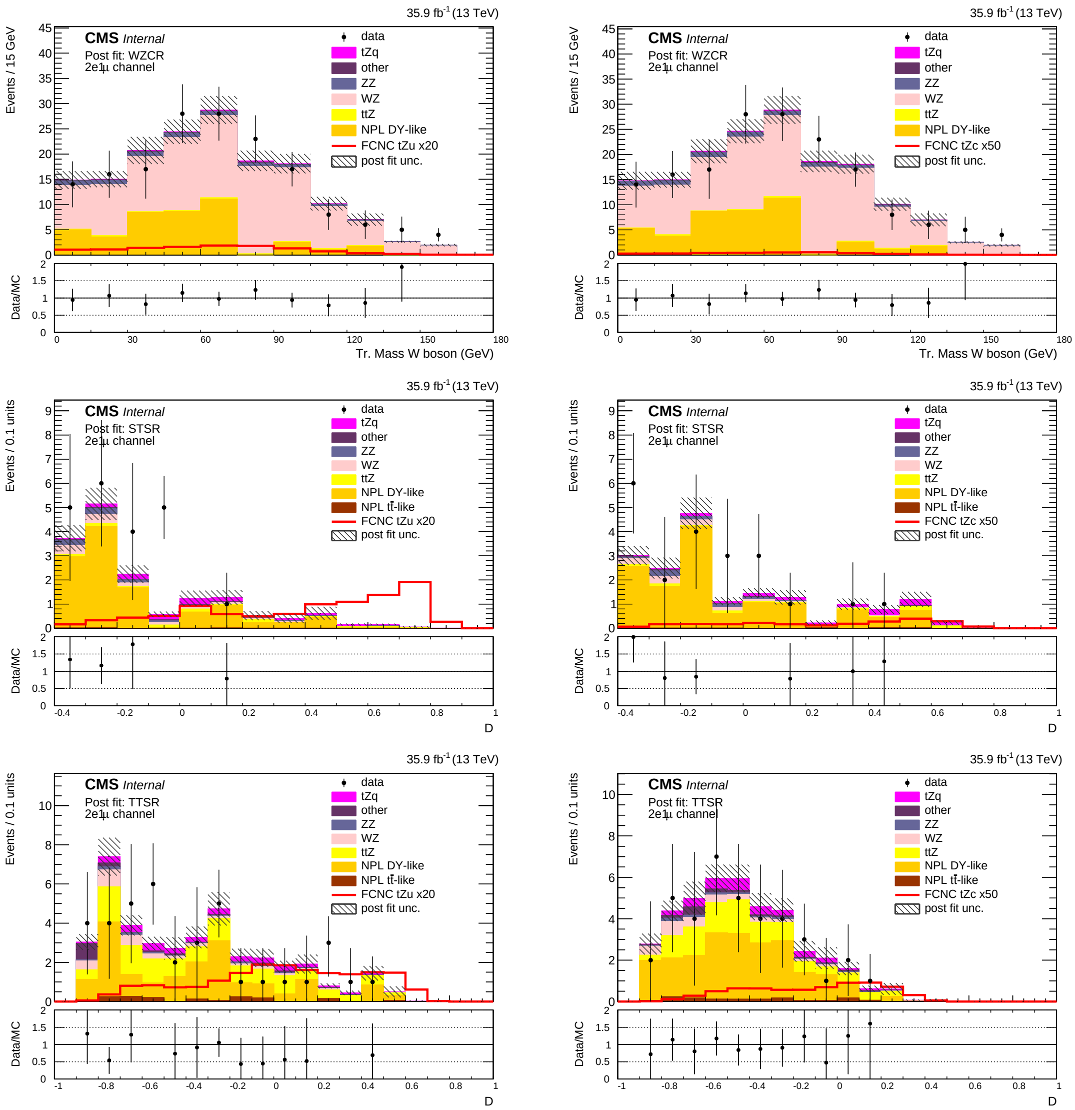

Figure 6.32: Post fit distributions for the 2e1μ lepton channel of the transverse mass of the W boson in the WZCR (top), the multivariate discriminating variable in the STSR (middle), and the multivariate discriminating variable in the TTSR (bottom) for the tZu (left) and tZc (right) couplings.

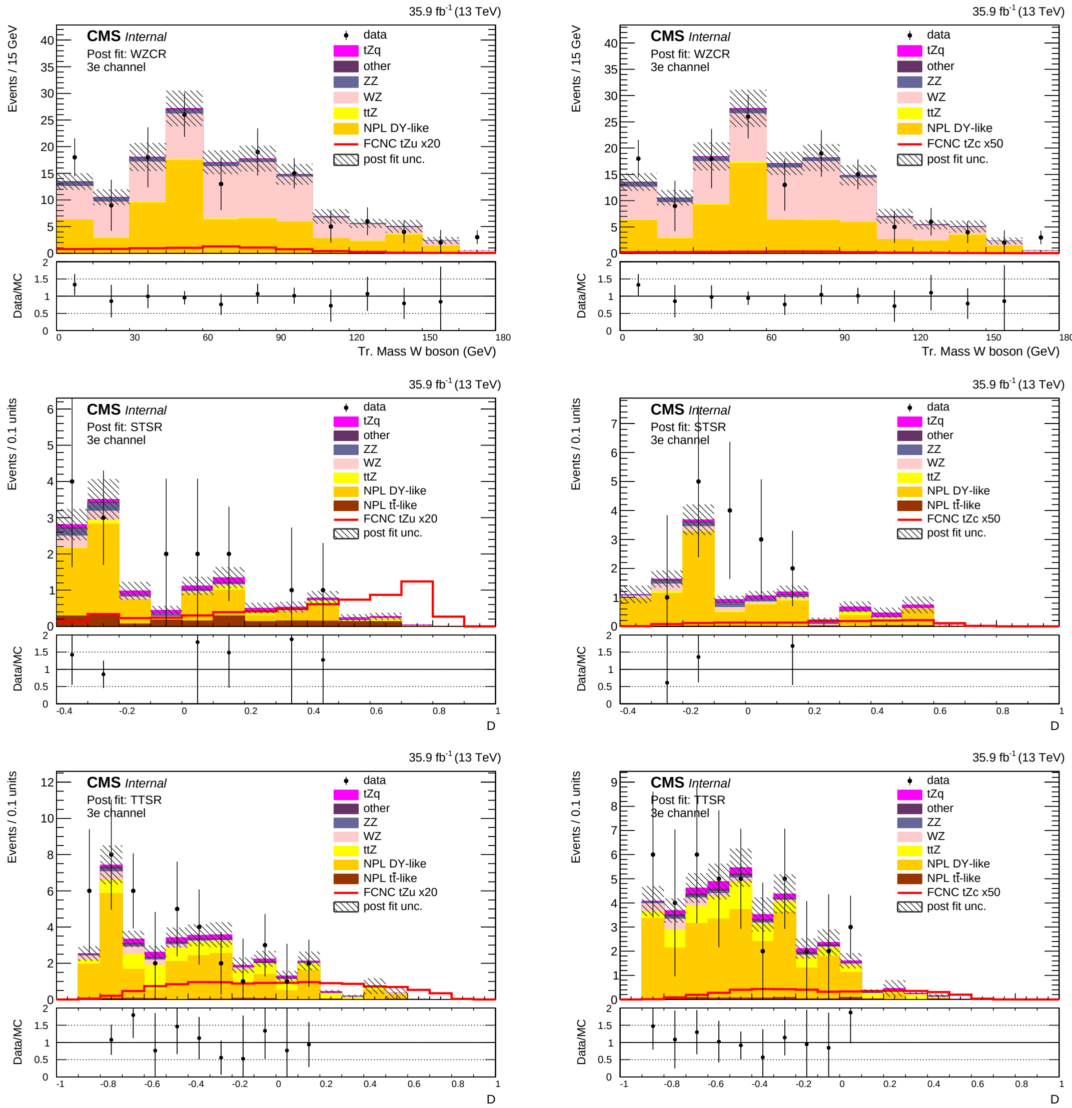

Figure 6.33: Post fit distributions for the 3e lepton channel of the transverse mass of the W boson in the WZCR (top), the multivariate discriminating variable in the STSR (middle), and the multivariate discriminating variable in the TTSR (bottom) for the tZu (left) and tZc (right) couplings.

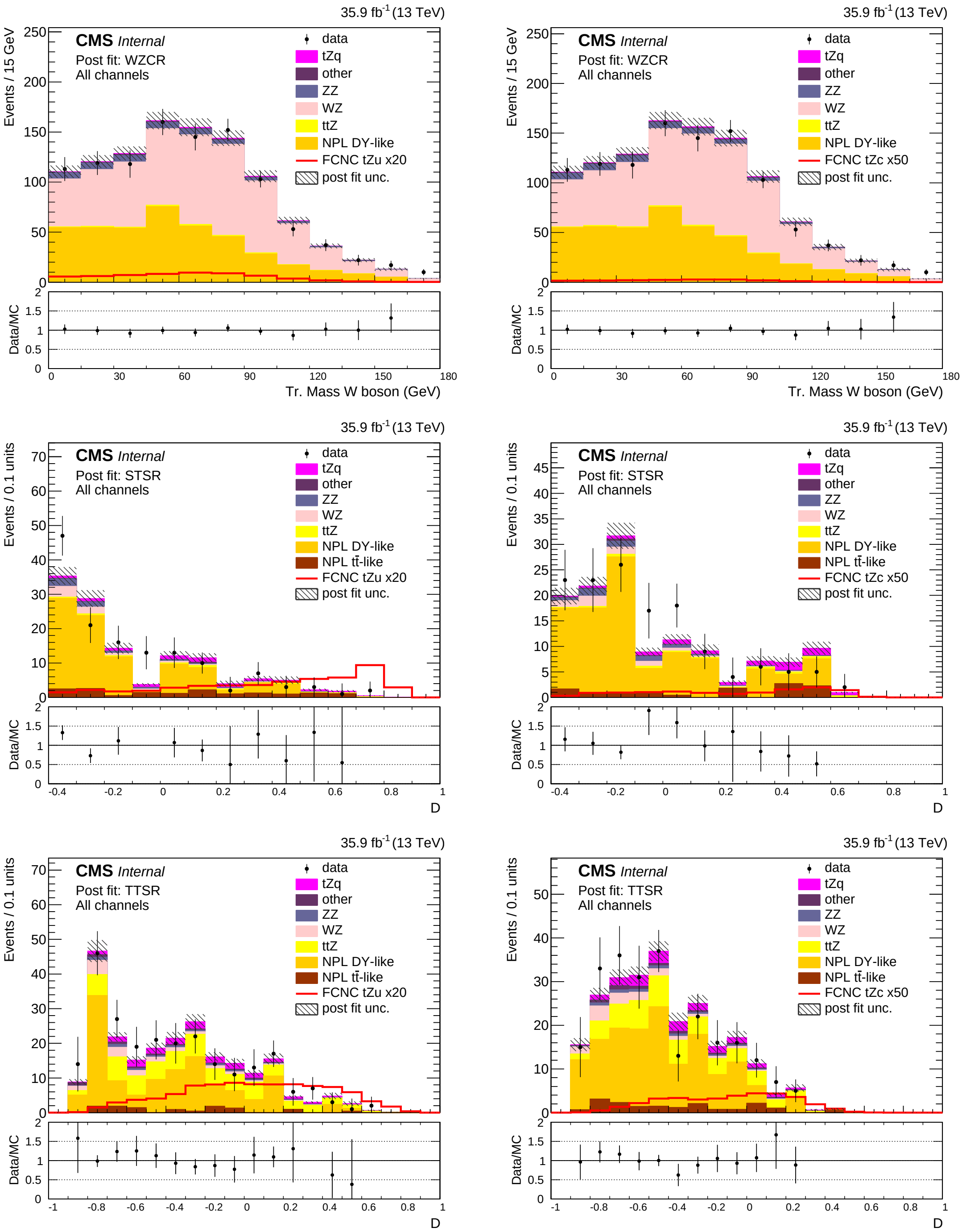

Figure 6.34: Post fit distributions for all three-lepton channels of the transverse mass of the W boson in the WZCR (top), the multivariate discriminating variable in the STSR (middle), and the multivariate discriminating variable in the TTSR (bottom) for the tZu (left) and tZc (right) couplings.

6.5.2 Postfit yields

In Table 6.2 and Table 6.3, the event yields for each process after the global fit for the signal involving a tZu vertex is given for respectively the STCR and TTCR. All background yields are approximately unchanged and the signal is downscaled with factor of 0.2 with respect to its initial yield. In Table 6.4, the postfit yields for the WZCR is given. The postfit signal yield is consistent with that in other control regions. The background contribution of the NPL process has been normalised with respect to data, resulting in an agreement between data and simulation. The event yields in the signal regions, STSR and TTSR, are given in Table 6.5 and Table 6.6 respectively. The contributions of the WZ+jets and $t\bar{t}$Z+jets backgrounds have risen within their uncertainties, and the contribution of the NPL background has increased with almost a factor two. A good agreement between data and simulation is obtained for all regions.

Table 6.2: Event yields in the STCR, after the global fit for the tZu signal.

Process	all channels	3μ channel	1e2μ channel	2e1μ channel	3e channel
NPL $t\bar{t}$	25.33 ± 3.66	9.05 ± 2.12	14.49 ± 2.72	0.40 ± 0.91	1.39 ± 0.82
$t\bar{t}$Z	0.38 ± 0.59	0.13 ± 0.04	0.15 ± 0.59	0.04 ± 0.02	0.05 ± 0.02
WZ	3.82 ± 0.20	1.54 ± 0.03	1.18 ± 0.11	0.78 ± 0.15	0.32 ± 0.03
ZZ	0.38 ± 0.05	0.20 ± 0.05	0.09 ± 0.01	0.05 ± 0.01	0.04 ± 0.02
Other bkg.	2.50 ± 0.42	0.81 ± 0.33	0.78 ± 0.09	0.81 ± 0.25	0.11 ± 0.01
tZq	0.29 ± 0.04	0.13 ± 0.03	0.08 ± 0.02	0.04 ± 0.01	0.04 ± 0.01
κ_{tZu}/Λ	0.09 ± 0.01	0.04 ± 0.01	0.03 ± 0.01	0.02 ± 0.01	<0.01 ± <0.01
Data	32 ± 3	11 ± 1	16 ± 1	2 ± 1	1 ± 1
Total bkg.	33 ± 4	12 ± 2	17 ± 3	2 ± 1	2 ± 1

Table 6.3: Event yields in the TTCR, after the global fit for the tZu signal.

Process	all channels	3μ channel	1e2μ channel	2e1μ channel	3e channel
NPL $t\bar{t}$	28.92 ± 3.47	14.28 ± 2.00	9.79 ± 2.32	4.45 ± 1.49	0.39 ± 0.67
$t\bar{t}$Z	2.93 ± 0.25	1.23 ± 0.20	0.66 ± 0.10	0.56 ± 0.08	0.48 ± 0.08
WZ	4.71 ± 0.43	2.01 ± 0.34	1.55 ± 0.25	0.57 ± 0.08	0.58 ± 0.06
ZZ	0.36 ± 0.04	0.15 ± 0.03	0.10 ± 0.02	0.05 ± 0.01	0.06 ± 0.01
Other bkg.	4.05 ± 0.31	1.60 ± 0.15	1.36 ± 0.22	0.74 ± 0.13	0.35 ± 0.08
tZq	0.79 ± 0.07	0.38 ± 0.06	0.25 ± 0.04	0.10 ± 0.01	0.06 ± 0.02
κ_{tZu}/Λ	0.13 ± 0.01	0.06 ± 0.01	0.04 ± 0.01	0.02 ± 0.01	0.02 ± <0.01
Data	44 ± 3	19 ± 1	15 ± 1	6 ± 1	2 ± 1
Total bkg.	42 ± 3	20 ± 2	14 ± 2	6 ± 2	2 ± 1

Table 6.4: Event yields in the WZCR, after the global fit for the tZu signal.

Process	all channels	3μ channel	$1e2\mu$ channel	$2e1\mu$ channel	3e channel
NPL $Z/\gamma^* + \text{jets}$	408.84 ± 13.11	152.48 ± 8.12	151.47 ± 7.97	40.80 ± 4.57	64.09 ± 4.62
$t\bar{t}Z$	10.22 ± 0.36	4.18 ± 0.25	2.63 ± 0.18	2.03 ± 0.14	1.39 ± 0.12
WZ	591.52 ± 11.22	247.73 ± 8.19	164.23 ± 6.18	112.03 ± 3.28	67.53 ± 3.15
ZZ	44.46 ± 1.25	17.93 ± 0.87	14.36 ± 0.77	6.80 ± 0.33	5.38 ± 0.32
Other bkg.	7.40 ± 0.47	3.54 ± 0.36	2.13 ± 0.29	1.02 ± 0.06	0.70 ± 0.06
tZq	7.47 ± 0.20	3.10 ± 0.15	2.14 ± 0.10	1.36 ± 0.05	0.86 ± 0.05
κ_{tZu}/Λ	2.97 ± 0.13	1.21 ± 0.10	0.80 ± 0.07	0.58 ± 0.05	0.38 ± 0.03
Data	1053 ± 345	415 ± 21	332 ± 19	168 ± 14	138 ± 13
Total bkg.	1070 ± 20	429 ± 13	337 ± 13	164 ± 6	140 ± 7

Table 6.5: Event yields in the STSR, after the global fit for the tZu FCNC signal.

Process	all channels	3μ channel	1e2μ channel	2e1μ channel	3e channel
NPL $Z/\gamma^* + \text{jets}$	80.64 ± 4.44	36.55 ± 3.20	25.49 ± 2.78	11.27 ± 1.09	7.33 ± 0.76
$t\bar{t}Z$	3.91 ± 0.23	1.44 ± 0.12	0.96 ± 0.10	0.94 ± 0.15	0.57 ± 0.06
WZ	7.79 ± 0.15	3.28 ± 0.07	2.32 ± 0.11	1.31 ± 0.05	0.88 ± 0.04
ZZ	6.21 ± 0.40	2.42 ± 0.25	2.31 ± 0.30	0.78 ± 0.07	0.70 ± 0.06
Other bkg.	1.31 ± 0.08	0.71 ± 0.06	0.29 ± 0.03	0.19 ± 0.03	0.11 ± 0.02
tZq	8.92 ± 0.27	4.05 ± 0.21	2.31 ± 0.13	1.55 ± 0.09	1.01 ± 0.05
NPL $t\bar{t}$	16.13 ± 0.88	6.00 ± 0.51	8.04 ± 0.59	0.09 ± 0.07	2.00 ± 0.41
κ_{tZu}/Λ	2.43 ± 0.09	0.99 ± 0.22	0.64 ± 0.05	0.48 ± 0.04	0.31 ± 0.03
Data	138 ± 15	55 ± 8	47 ± 7	21 ± 5	15 ± 5
Total bkg.	125 ± 5	54 ± 3	42 ± 3	16 ± 1	13 ± 1

Table 6.6: Event yields in the TTSR, after the global fit for the tZu FCNC signal.

Process	all channels	3μ channel	$1e2\mu$ channel	$2e1\mu$ channel	3e channel
NPL $Z/\gamma^* +$ jets	113.23 ± 5.31	45.59 ± 3.83	28.77 ± 2.63	17.08 ± 1.76	21.80 ± 1.89
$t\bar{t}Z$	62.23 ± 1.23	25.11 ± 0.89	16.65 ± 0.58	12.17 ± 0.48	8.30 ± 0.39
WZ	15.70 ± 0.27	6.40 ± 0.20	4.39 ± 0.11	3.03 ± 0.12	1.87 ± 0.07
ZZ	5.49 ± 0.12	2.09 ± 0.08	1.87 ± 0.08	0.80 ± 0.03	0.73 ± 0.04
Other bkg.	5.89 ± 0.44	2.21 ± 0.15	1.45 ± 0.10	1.60 ± 0.40	0.62 ± 0.06
tZq	18.54 ± 0.24	8.27 ± 0.15	4.95 ± 0.10	3.21 ± 0.14	2.11 ± 0.07
NPL $t\bar{t}$	10.93 ± 0.54	4.94 ± 0.26	4.05 ± 0.34	1.55 ± 0.20	0.40 ± 0.25
κ_{tZu}/Λ	4.66 ± 0.15	1.00 ± 0.12	1.26 ± 0.07	0.89 ± 0.06	0.60 ± 0.04
Data	243 ± 19	107 ± 11	58 ± 10	38 ± 8	40 ± 8
Total bkg.	232 ± 4	95 ± 4	62 ± 3	39 ± 2	36 ± 2

6.6 Limits at 95% CL

6.6.1 One-dimensional limits

The limit setting procedure used in this search returns limits on the signal strength modifier which can be translated to limits on signal cross sections. These limits are translated to a limit on the branching fraction using Equation 1.29. Additionally, the limit on the couplings are extracted using the fact that the cross sections are quadratically dependent on the couplings. In Figure 6.35, the resulting limits at 95% CL on the branching fraction and couplings related to the tZu vertex are shown. The observed (expected) limit at 95% CL amounts to $\mathscr{B} < 2.4 \times 10^{-4}$ (1.5×10^{-4}) when $\kappa_{tZu}/\Lambda \neq 0$ and $\kappa_{tZc}/\Lambda = 0$. This corresponds to an observed (expected) limit at 95% CL of $\kappa_{tZu}/\Lambda < 1.4 \times 10^{-4}$ (1.1×10^{-4}) GeV^{-1} on the coupling. The expected limit surpasses the expected limit on the branching fraction of $2.7{\times}10^{-4}$ of the previous CMS search at a centre-of-mass energy of 8 TeV [28]. However, the observed limit of 2.4×10^{-4} for the tZu interaction does not surpass the previously observed limit on the branching fraction of 2.2×10^{-4} [28]. The ATLAS collaboration has also set limits on the branching fraction at 95% CL at a centre-of-mass energy of 13 TeV [58] with observed (expected) limits of $1.7{\times}10^{-4}$ ($2.4{\times}10^{-4}$) for the tZu coupling. The expected limit presented in this analysis surpasses as well the expected limit set by ATLAS for the tZu interaction.

In Figure 6.36 and Table 6.7, the limits for each three-lepton channel as well as the combined limit are shown for the tZu vertex. The lepton channels are in agreement with each other, where the presence of a muon helps pushing the limit further. The STSR is the most sensitive region because of the higher presence of the targeted single top quark signal. Further, one can see that by combining single top quark and top quark pair signals the expected limit improves by a factor of 1.33.

Table 6.7: Expected limits on the branching fractions at 95% CL for the tZu coupling [28, 58].

	expected $\times 10^{-4}$	$+2\sigma$ $\times 10^{-4}$	$+1\sigma$ $\times 10^{-4}$	-1σ $\times 10^{-4}$	-2σ $\times 10^{-4}$	observed $\times 10^{-4}$
3μ	3.2	7.4	5.0	2.1	1.4	5.3
$1e2\mu$	3.2	7.4	5.0	0.021	1.4	6.4
$2e1\mu$	3.6	8.4	5.6	2.3	1.6	5.6
3e	5.0	13	8.2	3.1	2.1	3.8
STSR only	2.0	4.9	3.2	1.3	0.86	2.5
TTSR only	2.5	5.4	3.8	2.5	1.7	3.9
combined	1.5	3.3	2.3	0.97	0.68	2.4
8 TeV CMS (19.7 fb^{-1})	2.7	-	42	1.8	-	2.2
13 TeV ATLAS (36 fb^{-1})	2.4	-	35	1.7	-	1.7

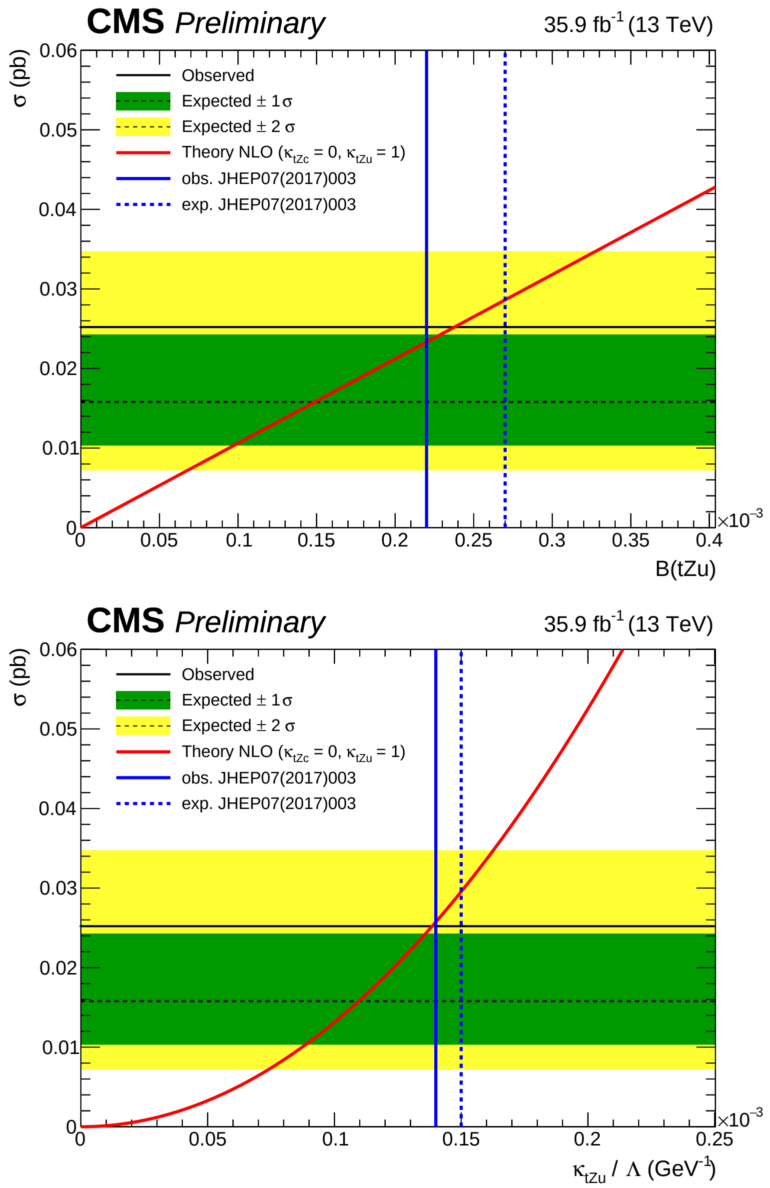

Figure 6.35: Exclusion limits at 95% CL on the FCNC branching fractions (top) and couplings (bottom) as a function of the cross section of the FCNC process, considering only the tZu vertex. The blue (dashed) line indicates the previous observed (expected) limit at 95% CL obtained by CMS at a centre-of-mass energy of 8 TeV [28].

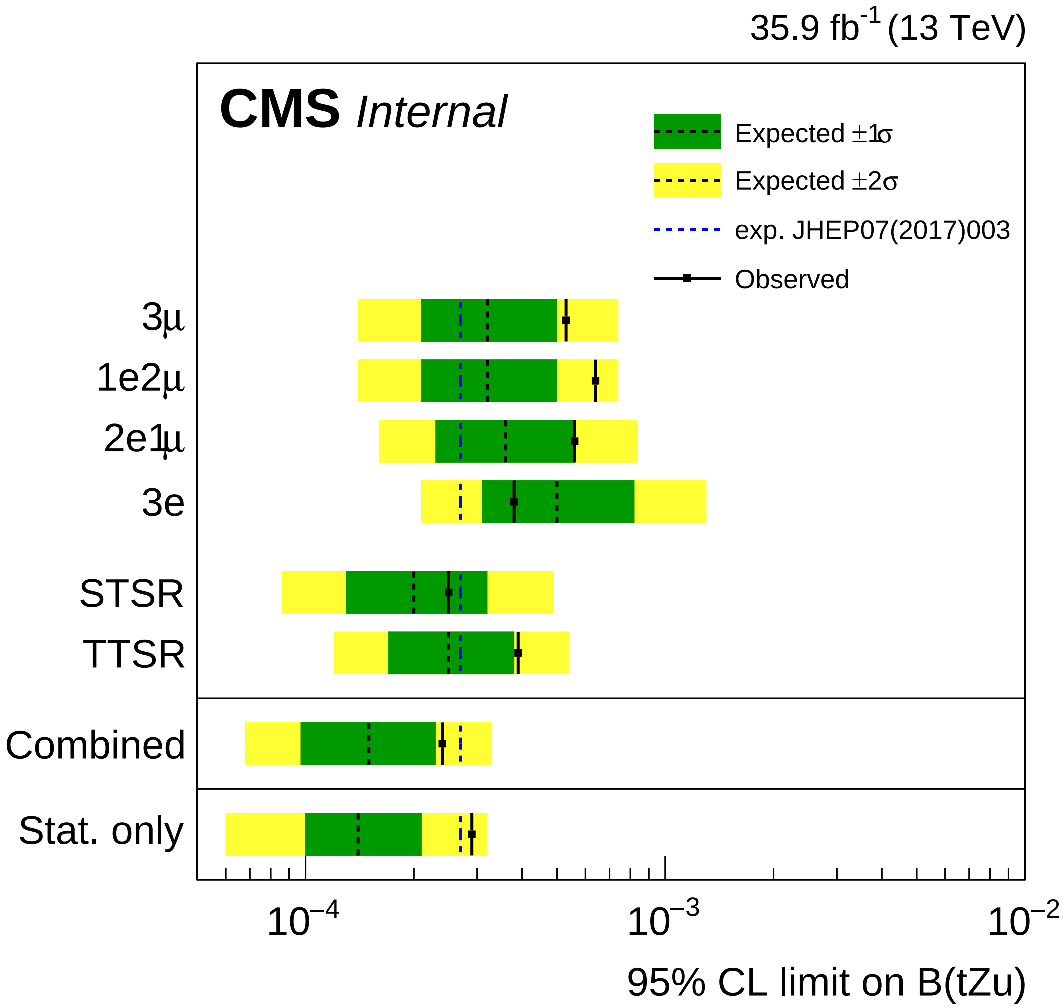

Figure 6.36: Exclusion limits at 95% CL for each three-lepton channel and signal region on the FCNC tZu branching fractions considering one non-vanishing coupling at a time. The blue (dashed) line indicates the previous observed (expected) limit at 95% CL obtained by CMS at a centre-of-mass energy of 8 TeV [28].

In Figure 6.37, the resulting limits at 95% CL on the branching fraction and couplings related to the tZc vertex are shown. For this coupling, the observed (expected) limit at 95% CL is $\mathcal{B} < 4.5\times10^{-4}\,(3.7\times10^{-4})$ when $\kappa_{tZc}/\Lambda \neq 0$ and $\kappa_{tZu}/\Lambda = 0$. This corresponds to an observed (expected) limit at 95% CL of $\kappa_{tZc}/\Lambda < 1.9\times10^{-4}$ (1.7×10^{-4}) GeV^{-1} on the coupling. The expected limit surpasses the expected limit on the branching fraction of 12×10^{-4} set by the previous CMS search at a centre-of-mass energy of 8 TeV [28]. This is also the case for the observed limit, which surpasses the observed limit of 4.9×10^{-4} on the branching fraction set by the previous CMS search [28]. The observed (expected) limiton the branching fraction set by the ATLAS collaboration at a centre-of-mass energy of 13 TeV [58] is 2.3×10^{-2} (3.2×10^{-2}) for the tZc coupling. The expected limit presented in this analysis is in accordance with this limit.

The limits for each three-lepton channel separate as well as their combined limits are shown for the tZc vertex in Figure 6.38 and Table 6.8. The lepton channels are in agreement with each other, and the presence of a muon helps to increase the sensitivity. For the tZc vertex, the TTSR is the most sensitive region and by combining single top quark and top quark pair signals, the sensitivity is improved with a factor of 1.19.

Table 6.8: Expected limits on the branching fractions at 95% CL for the tZc coupling [28, 58].

	expected $\times10^{-4}$	$+2\sigma$ $\times10^{-4}$	$+1\sigma$ $\times10^{-4}$	-1σ $\times10^{-4}$	-2σ $\times10^{-4}$	observed $\times10^{-4}$
3μ	7.0	15	10	4.6	3.2	12
$1e2\mu$	7.9	18	12	5.2	3.6	9.6
$2e1\mu$	8.9	20	14	5.8	4.0	9.9
3e	12	29	19	7.5	5.0	9.5
STSR only	10	20	16	6.6	4.5	17
TTSR only	4.4	9.4	6.6	2.9	2.0	4.3
combined	3.7	8.1	5.6	2.5	1.7	4.5
8 TeV CMS (19.7 fb^{-1})	12	-	22	7.1	-	4.9
13 TeV ATLAS (36 fb^{-1})	3.2	-	4.6	2.2	-	2.3

6.6.2 Two-dimensional limits

One can interpolate the one dimensional limits to a scenario where both couplings are non-vanishing. The interpolation is taken from Ref. [60], where an experimental extrapolation formula

$$\kappa_{tZc}/\Lambda = \kappa_{tZc}/\Lambda^{1D}\sqrt{1-\frac{\kappa_{tZu}/\Lambda}{\kappa_{tZu}/\Lambda^{1D}}}, \tag{6.1}$$

is found from 100 benchmark scenarios. These scenarios are constructed from existing signal samples as

$$\text{Signal yield} = (\kappa_{tZu}/\Lambda)^2(\text{ST tZu yield}+\text{TT tZu yield})+(\kappa_{tZc}/\Lambda)^2(\text{ST tZc yield}+\text{TT tZc yield}).$$

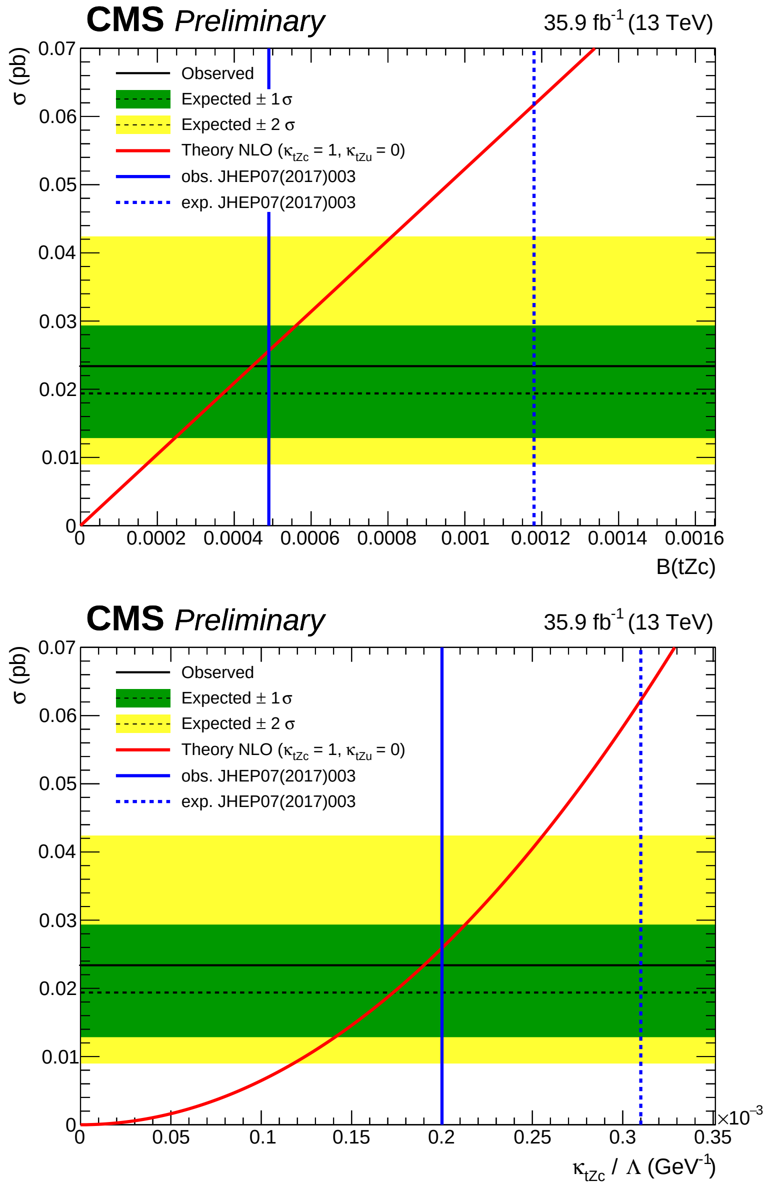

Figure 6.37: Exclusion limits at 95% CL on the FCNC branching fractions (top) and couplings (bottom) as a function of the cross section of the FCNC process, considering only the tZc vertex. The blue (dashed) line indicates the previous observed (expected) limit at 95% CL obtained by CMS at a centre-of-mass energy of 8 TeV [28].

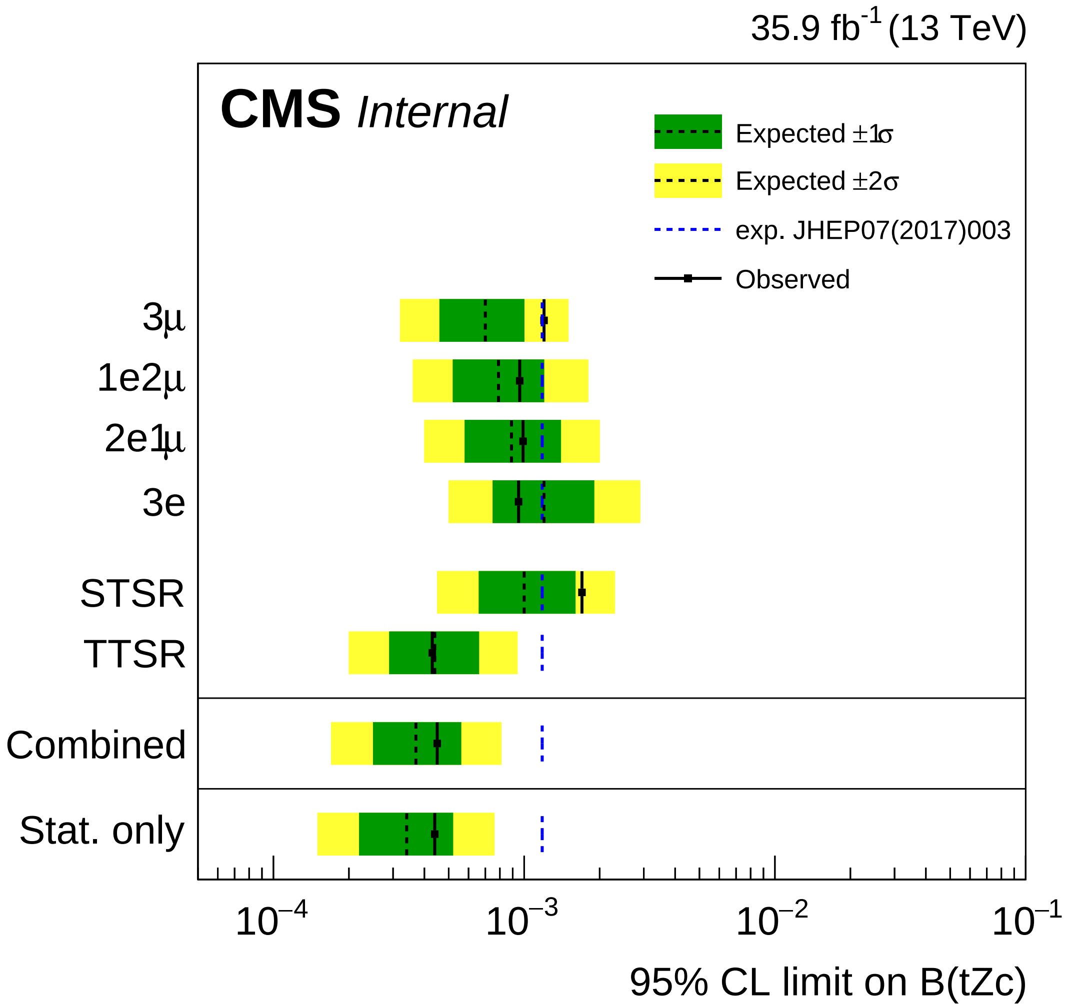

Figure 6.38: Exclusion limits at 95% CL for each three-lepton channel and signal region on the FCNC tZc branching fractions considering one non-vanishing coupling at a time. The blue (dashed) line indicates the previous observed (expected) limit at 95% CL obtained by CMS at a centre-of-mass energy of 8 TeV [28].

The resulting two-dimensional limits are shown in Figure 6.39. One can see that for both couplings, the expected limit of this search is more stringent compared to the search by the CMS collaboration at a centre-of-mass energy of 8 TeV.

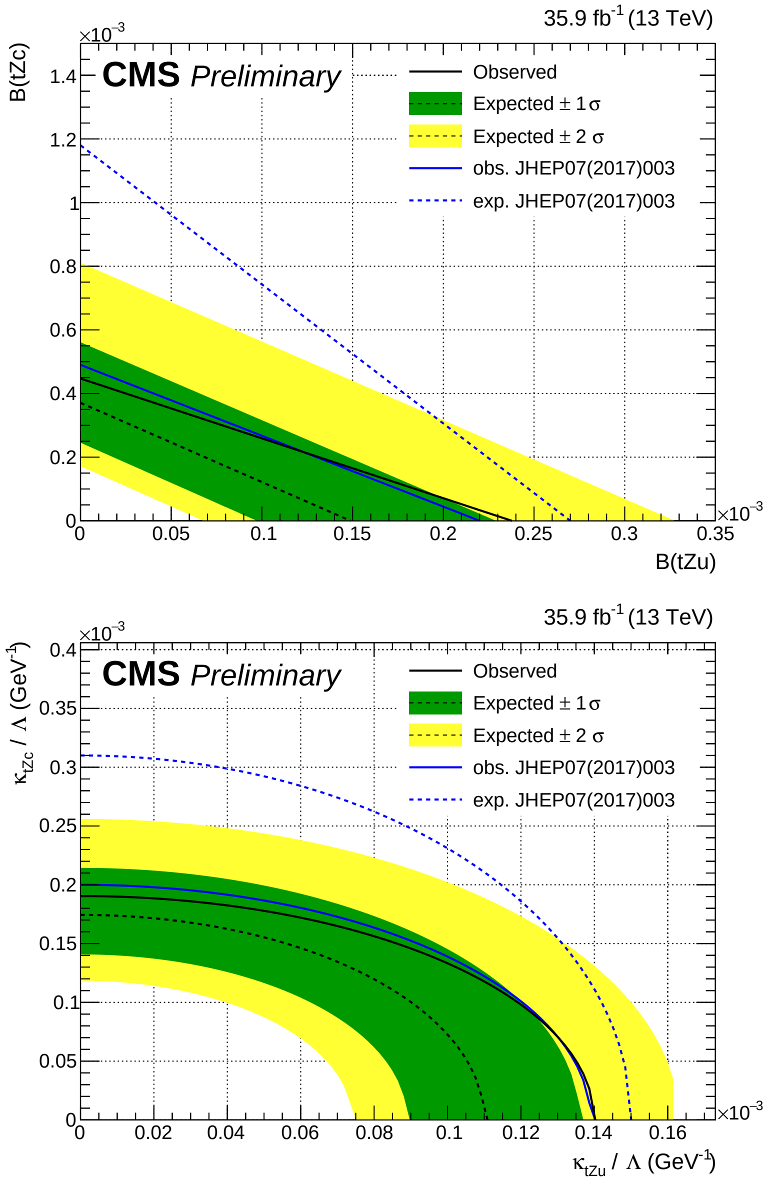

Figure 6.39: Two-dimensional limits on the branching fractions (top) and couplings (bottom) for FCNC interactions involving a tZq vertex. The blue (dashed) line indicates the previous observed (expected) limit at 95% CL obtained by CMS at a centre-of-mass energy of 8 TeV [28].

Conclusion and prospects 7

7.1 Conclusion

The Standard Model of particle physics is the best theoretical framework so far to describe the elementary particles and their interactions. Although severely experimentally tested, this theory has its shortcomings and can not explain phenomena such as neutrino masses, dark matter, or dark energy. The heaviest particle in the Standard Model is the top quark, leading to the belief that it has an enhanced sensitivity to various new particles and interactions suggested by beyond the Standard Model theories. The top quark decays almost exclusively to a W boson and a bottom quark with a very short lifetime, and therefore creates a signature that is clean and easy to distinguish. The top quark is thus an excellent candidate to study new physics phenomena. The Large Hadron Collider is a proton collider, producing a large number of events containing top quarks. At the proton collision points, experiments are placed to study the collisions. The search presented in this thesis is performed on data collected by the Compact Muon Solenoid experiment at a centre-of-mass energy of 13 TeV, resulting in 35.9 fb^{-1} of integrated luminosity.

Flavour changing neutral currents are forbidden at tree level and are highly suppressed at higher orders in the Standard Model. Nonetheless, many beyond the Standard Model theories enhance their probability. In this thesis, a search in three lepton final states is performed for the production of single top quarks via the tZq vertex, with $\mathrm{q} = \mathrm{c}, \mathrm{u}$, or in the top quark pair processes where one of the top quarks decays through this vertex. No significant deviation with respect to the predicted background is observed and upper limits at 95% confidence level are placed. The observed (expected) upper limits at 95% confidence level on the branching fractions of top quark decays are: $\mathscr{B}(\mathrm{t} \rightarrow \mathrm{uZ}) < 2.4 \times 10^{-4}$ (1.5×10^{-4}) and $\mathscr{B}(\mathrm{t} \rightarrow \mathrm{cZ}) < 4.5 \times 10^{-4}$ (3.7×10^{-4}), assuming one non-vanishing coupling at a time. A summary of the observed (expected) limits on the FCNC tZq vertex is shown in Figure 7.1.

Significant improvements are developed with respect to previous searches, namely by using other kinematic variables as input into the BDT as well as a better handle on the not prompt-lepton background. The current most sensitive analysis, with results obtained from proton collision data at a centre-of-mass energy of 13 TeV by the ATLAS collaboration [58], has an observed limit of 1.7×10^{-4} for the FCNC tZu interaction. Its corresponding expected limit is 2.4×10^{-4}. The expected limit obtained in this thesis is more stringent. The observed (expected)

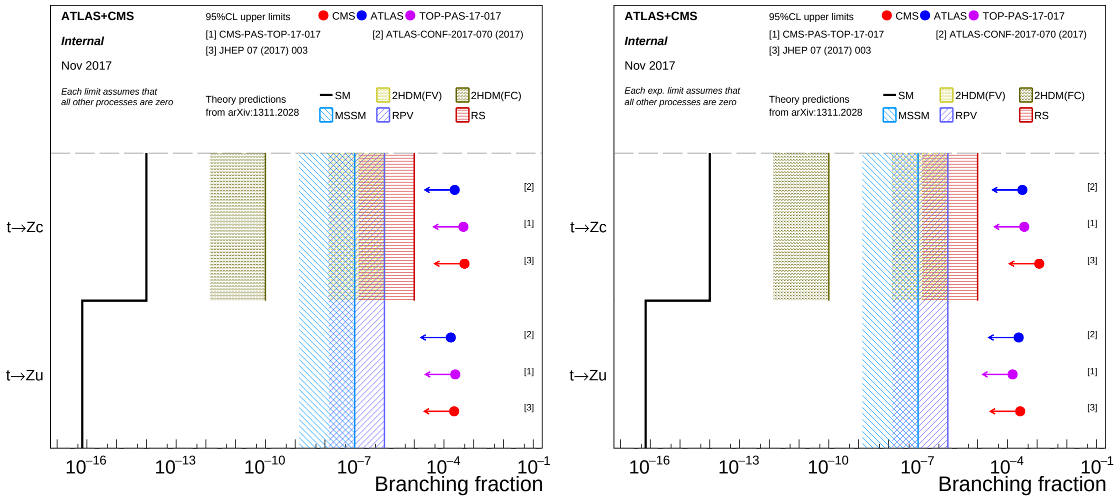

Figure 7.1: Summary of the most stringent observed (left) and expected (right) upper limits on FCNC tZq at 95% CL upper limits from CMS (red) and ATLAS (blue) at a centre-of-mass energy of 8 and 13 TeV. The results from this thesis are shown in purple. A comparison between theory predictions and experimental limits is shown. Figure adapted from [50].

limit on the tZc interaction set by ATLAS is 2.3×10^{-4} (3.2×10^{-4}) and its expected limit is comparable with the expected limit presented in this thesis. For the FCNC interactions with a tZq vertex, the branching fractions predicted within the Standard Model or by typical beyond the Standard Model theories are still out of reach.

7.2 Prospects

This statistically limited search for these FCNC phenomena is expected to have an improved sensitivity when performed on a larger dataset. By extrapolating the current analysis to a dataset of 100 fb^{-1} (full Run 2 dataset), 300 fb^{-1} (Run 2 + Run 3), or 3000 fb^{-1} (HL-LHC), the expected upper limits at 95% CL are extracted. The templates for the systematic uncertainties are unchanged for the extrapolations. The obtained expected limits at 95% CL, with respect to the result obtained in the presented search, are shown in Figure 7.2. The expected limit on the branching fraction is improved with a factor 3 for the tZu vertex, and with a factor 4 for the tZc vertex for 100 fb^{-1}. For 300 fb^{-1} and 3000 fb^{-1}, the sensitivity is further improved and some of the beyond the Standard model theories could be confirmed or excluded. Statistical limitations aside, the largest systematic uncertainty arises from the jet energy scale uncertainty. This uncertainty can be decreased by more precise measurements of the jet energy response with more data as well as using better methodologies.

A new pixel detector was installed in March 2017 and is expected to enhance the performance of heavy-flavour tagging which should help improve the sensitivity of the analysis. Furthermore, the recently developed charm tagging algorithm [190] could help to improve the sensitivity of the analysis. Especially the sensitivity for the top quark pair FCNC signal involving a tZc vertex could benefit from this algorithm. In Figures 7.3-7.5, distributions related to charm tagging are explored for a selection of exactly three leptons among which one lepton pair is

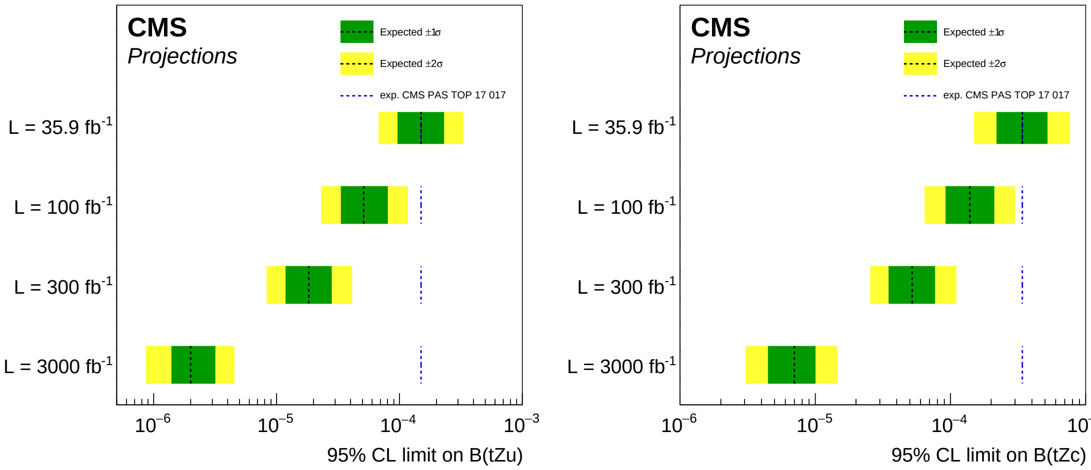

Figure 7.2: The expected limit at 95% CL for the tZu (left) and tZc (right) interaction for an integrated luminosity of 100, 300, and 3000 fb^{-1}, extrapolated from the result obtained in this thesis, which is indicated for reference with the blue (dashed) lines.

compatible with the Z boson, and at least one jet. At CMS, a collection of c-tagged jets can be created in a similar way as is done for b-tagged jets. Dedicated discriminants are created from multivariate analyses aiming for a discrimination of charm quark jets against light-flavour jets (CvsL), and charm quark jets against bottom quark jets (CvsB). By defining thresholds on both discriminators at the same time, the collection of c-tagged jets is created for different working points. The distributions of the c-tagged jet multiplicities according to the different working points are shown in Figure 7.3. The loose working point is defined to keep 90% of the charm quark jets, and only 45% of the bottom quark jets, whilst keeping 99% of the light-flavour jets. The tight working point is defined for discriminating charm quark jets from light-flavour jets and keeps 20% of the charm quark jets, while 0.02% of the light-flavour jets are selected. For this working point, also 24% of the bottom quark jets are surviving. The medium working point creates an intermediate state where 39% of the charm quark jets are kept, with 26% of the bottom quark jets, and 19% of the light-flavour jets. One can see that the distribution of the charm quark jet multiplicity according to the tight working point shows the most promising result. Here, there is one c-tagged jet expected for the top quark pair FCNC signal via the tZc interaction, while less background events are entering the one c-tagged jet region.

The distributions related to the shape of the CvsB and CvsL discriminants are shown in Figure 7.4 and Figure 7.5. The distribution of the CvsB discriminant of the jet with the (second) highest-p_T in the event is dominated at low values by the FCNC signal. A similar behaviour is found when one looks at the CvsB discriminator of all jets in the event. The distribution of the CvsL is peaking at one for the FCNC signal, while the distribution for the background processes declines towards higher discriminant values. This behaviour is visible for the distributions of the CvsL discriminant of the (second) highest-p_T in the event, as well as for the distribution of the CvsL discriminant values of all the jets in the event. One can exploit this behaviour further by considering the distribution for the CvsL discriminator of the jet with the highest

CvsL discriminator value. For the CvsB discriminator, this is done by looking at the jet with the lowest CvsB discriminator value.

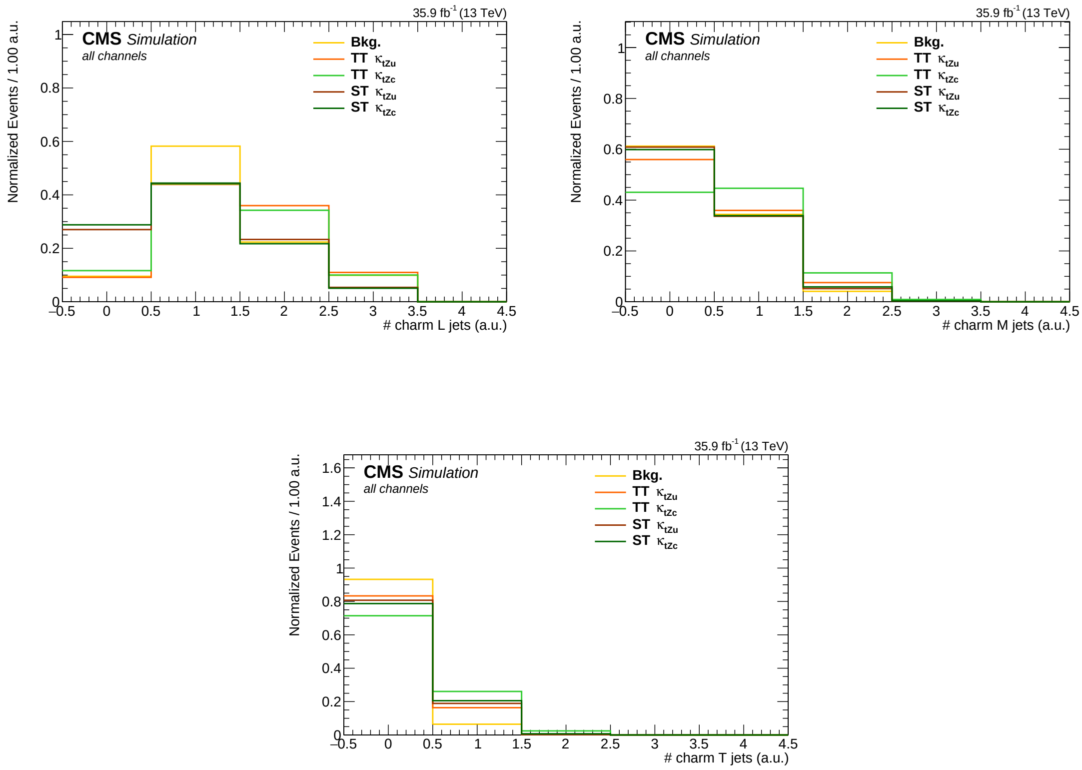

Figure 7.3: Normalised distributions of the c-tagged jet multiplicities according to different working points. Top-left: loose (L), top-right: medium (M), bottom: tight (T) working point. After a three-lepton selection, for which a lepton pair is compatible with the Z boson, and at least one jet .

Furthermore, one could search for background depleted regions based on the charm kinematics. This is shown in Figure 7.6. One can see that for the distributions of the CvsL discriminant versus the CvsB discriminant of all jets in the event, and the distributions of the highest CvsL and CvsB discriminants, the left upper corners are more populated by signal events. The background events are populating the right lower corners of the distribution.

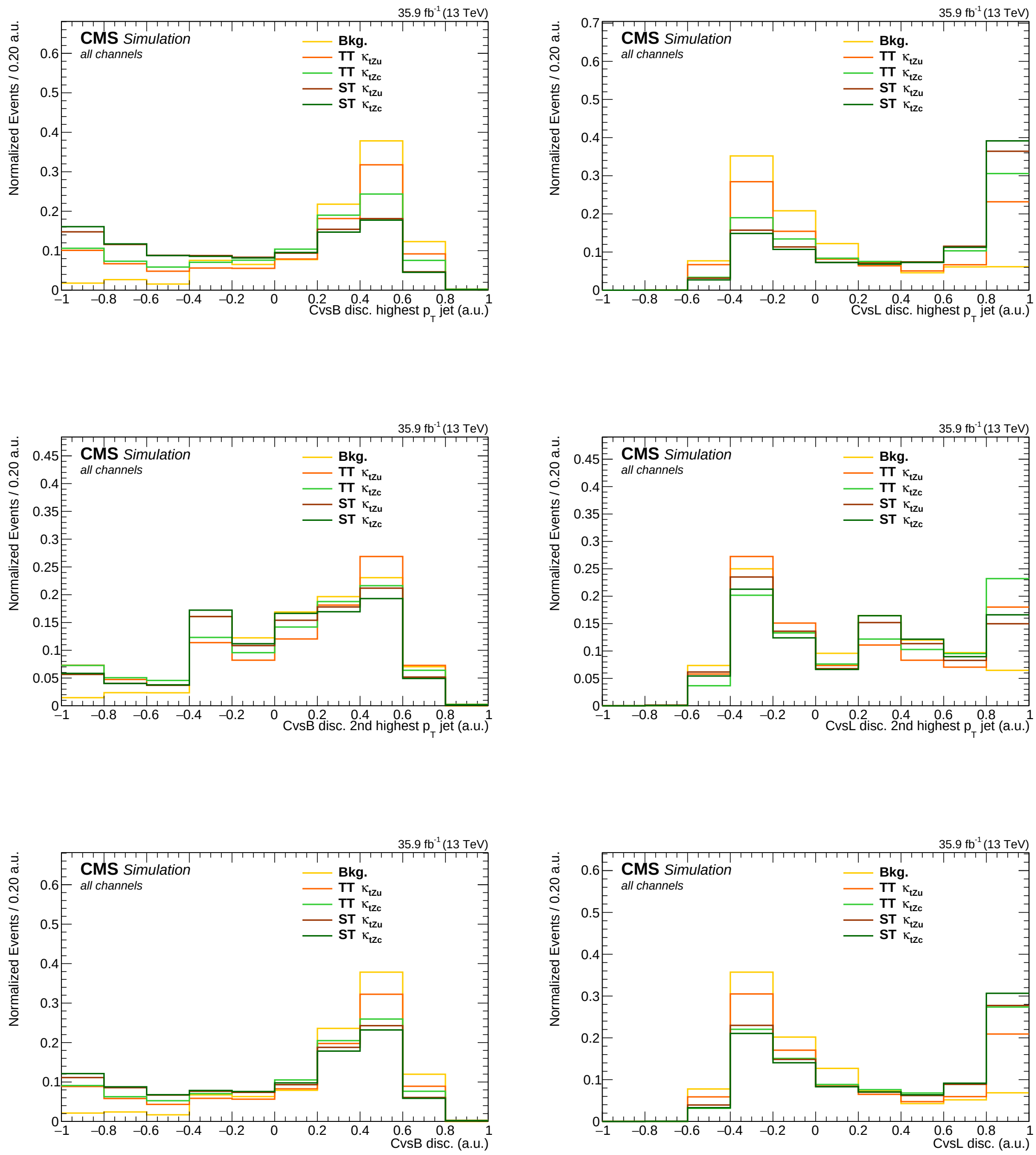

Figure 7.4: Normalised distributions of the CvsB (left) and CvsL (right) discriminants after a three-lepton selection, for which a lepton pair is compatible with the Z boson, and at least one jet . Top: discriminants for the jet with the highest p_T in the event, middle: discriminants for the jet with the second highest p_T in the event, bottom: discriminants for all the jets in the event.

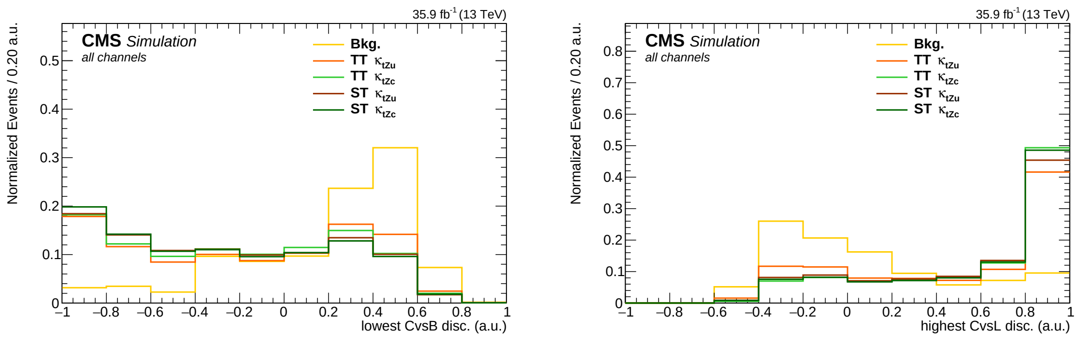

Figure 7.5: Normalised distributions of the lowest CvsB discriminant (left) and highest CvsL discriminant (right) after a three-lepton selection, for which a lepton pair is compatible with the Z boson, and at least one jet .

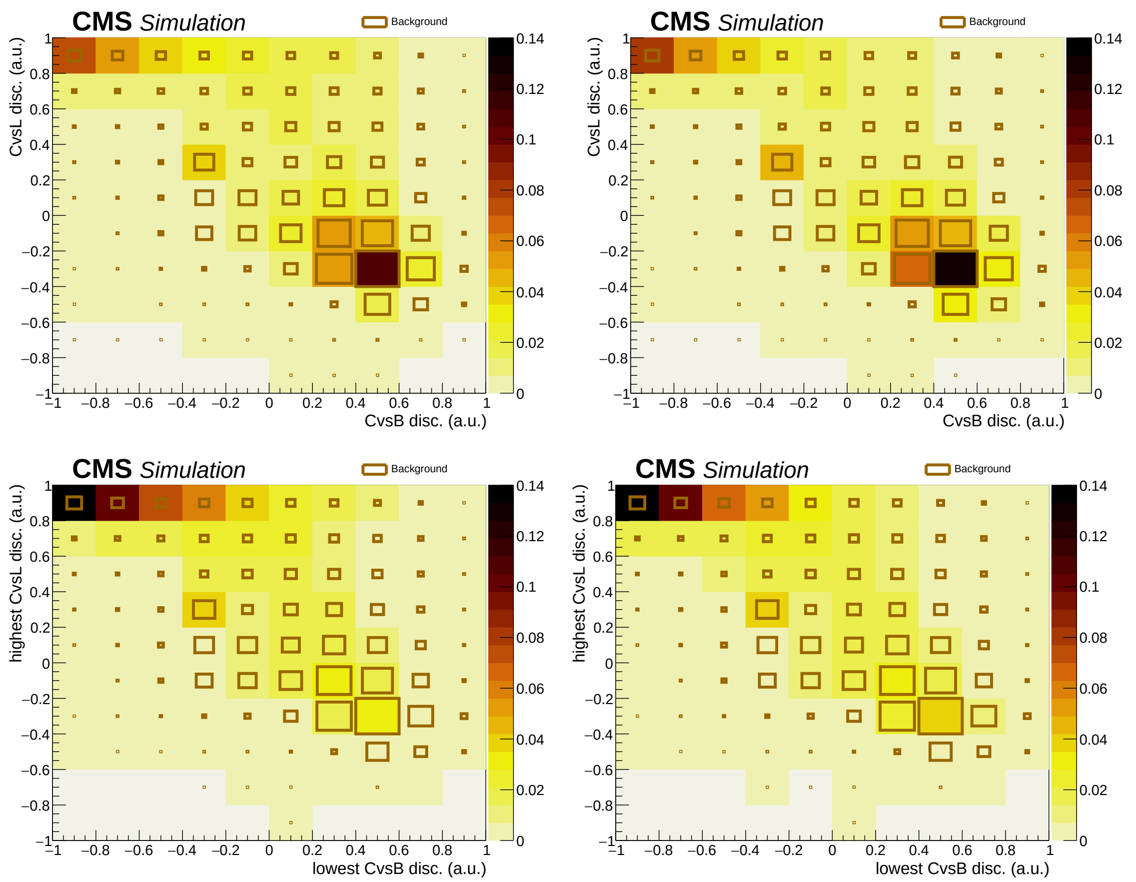

Figure 7.6: Normalised two-dimensional distributions of the CvsB and CvsL discriminants after a three-lepton selection, for which a lepton pair is compatible with the Z boson, and at least one jet for the tZc interaction, right: tZu interaction. The brown boxes represent the background distribution. The signal distribution is shown by the coloured contours. Top: discriminants for all jets in the event, bottom: lowest CvsB discriminant and highest CvsL discriminant.

Future colliders should be able to reach meaningful sensitivity for top-FCNC couplings as well. In Figure 7.7, the sensitivity of the LHC at a centre-of-mass energy of 14 TeV and 3000 fb^{-1} integrated luminosity (HL-LHC) [201], as well as of the ILC/CLIC at a centre-of-mass energy of 500 GeV and 500 fb^{-1} of integrated luminosity [202], the Future Circular hadron Colliders at a centre-of-mass energy of 100 TeV with an integrated luminosity of 10 ab^{-1} (FCC-hh) [201], the Future Circular electron positron Colliders at a centre-of-mass energy of 500 GeV with an integrated luminosity of 10 ab^{-1} (FCC-ee) [203], and the future Large Hadron electron Collider (LHeC) with a centre-of-mass energy of 14 TeV and an integrated luminosity of 200 fb^{-1} [204] are shown. The sensitivities are originating from projections as well as sensitivity studies based on the changes in luminosity, energy, and trigger thresholds.

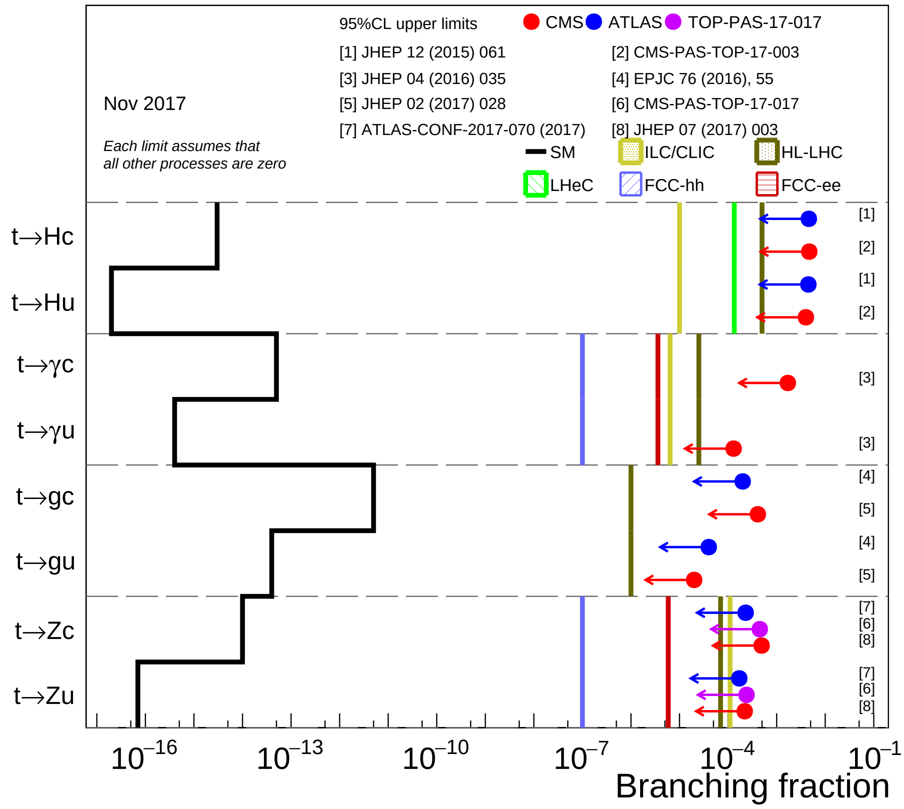

Figure 7.7: Summary of the most stringent upper limits on top-FCNC interactions at 95% CL upper limits from CMS (red) and ATLAS (blue) at a centre-of-mass energy of 8 and 13 TeV. The results from this thesis are shown in purple. A comparison between the projections for future colliders and the current experimental limits is shown. Figure adapted from [50]. The projections are taken from [201–204].

7.3 Reflection on the considered EFT model

There are a few assumptions made in the theoretical model behind this analysis. The Lagrangian presented in Equation 1.21, only considers adding terms of dimension six for beyond the SM physics. Hence there is no interference with the Standard Model which is of dimension four. However, there can be interference amongst the FCNC operators themselves. For the tZq couplings, there is a relation with the tγq through their six-dimensional couplings:

$$\kappa_{t\gamma q} f^{L}_{\gamma q} = \frac{v}{g'\Lambda}\left[\cos\theta_W \bar{c}_{uB} - \sin\theta_W \bar{c}_{uW}\right]^{*}_{i3} , \qquad \kappa_{t\gamma q} f^{R}_{\gamma q} = \frac{v}{g'\Lambda}\left[\sin\theta_W \bar{c}_{uB} - \cos\theta_W \bar{c}_{uW}\right]_{3i} ,$$
$$\kappa_{tZq} f^{L}_{Zq} = -\frac{2\cos\theta_W v}{g\Lambda}\left[\sin\theta_W \bar{c}_{uB} + \cos\theta_W \bar{c}_{uW}\right]^{*}_{i3} , \quad \kappa_{tZq} f^{R}_{Zq} = -\frac{2\cos\theta_W v}{g\Lambda}\left[\cos\theta_W \bar{c}_{uB} + \sin\theta_W \bar{c}_{uW}\right]_{3i} .$$

At leading order, both couplings are independent and can be combined to reconstruct the six-dimensional operators from the single top quark process $pp \to t\ell\bar{\ell}$. The two contributing Feynmann diagrams are shown in Figure 7.8.

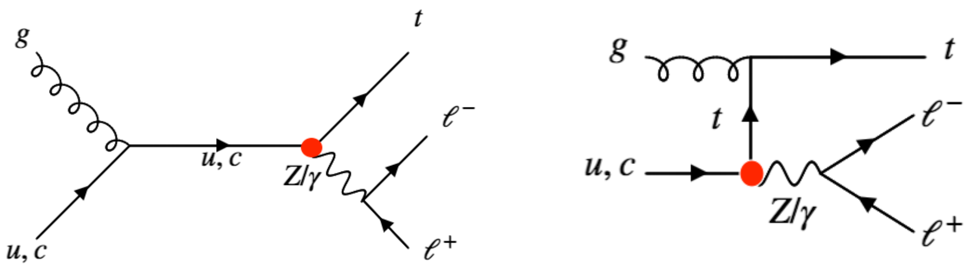

Figure 7.8: Leading order Feynmann diagrams contributing to $pp \to t\ell\bar{\ell}$, for the tZq and tγq anomalous couplings (indicated with a red dot).

Another coupling mixing with the tZq coupling is the tgq coupling, as can be seen in Figure 7.9. This coupling could be contributing to the final state considered in the presented analysis. However, this coupling would be firstly visible in the properties of the single top quark final state, before having a visible effect on the final states where it mixes with the other anomalous couplings, e.g. final states including a Z boson. Hence, if a FCNC signal is observed in a final state, while no deviation is observed in the properties of the single top quark final state, the contribution of the tgq coupling should be negligible.

Furthermore, only the Z boson has been considered in the final state. However, new bosons would also be candidates to give rise to the same final state. When these new bosons are heavy, their interactions can be contracted and give rise to four-fermion operators which are not considered for the search presented in this thesis. These four-fermion operators involve one top-quark field, one light-quark field, and two leptons [205], as illustrated in Figure 7.10. For the single top quark $pp \to t\ell\bar{\ell}$ final state, there is a small contamination of the contributions of four-fermion operators at the Z boson mass peak that becomes dominant outside the Z boson mass peak. This effect is presented in Ref. [205]. For the analysis presented in this thesis, this small contamination is not considered.

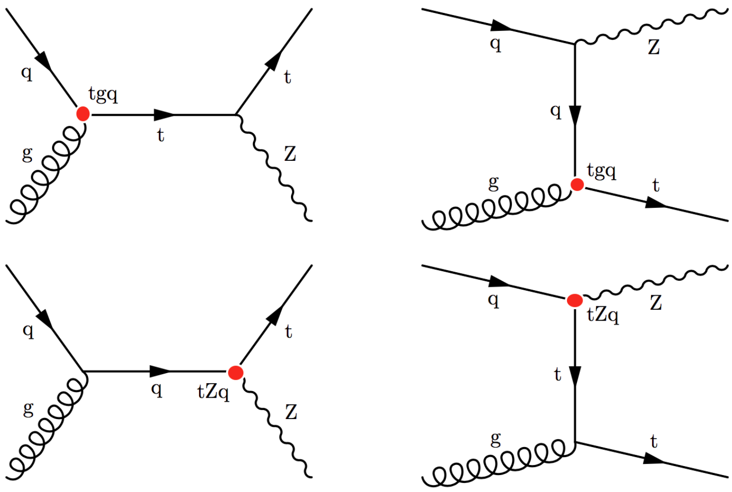

Figure 7.9: Leading order Feynmann diagrams contributing to $\mathrm{pp} \rightarrow \mathrm{tZ}$, for the tZq and tgq anomalous couplings indicated with a red dot. Figure adapted from [28].

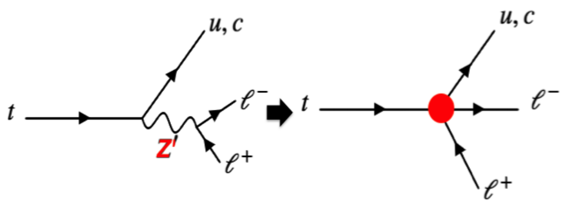

Figure 7.10: Four-fermion operators can contribute to $\mathrm{t} \rightarrow \mathrm{q}\ell\bar{\ell}$, anomalous coupling indicated with a red dot.

All of the previous considerations lead to the belief that the searches for flavour changing neutral currents should evolve towards global analyses for new physics effects. Here, all couplings would be fitted simultaneously in one comprehensive global fit. The phenomenology community has already provided first results [64, 206], but the correlations between the different experimental inputs get lost in translation. Recently at CMS, a new top quark EFT analysis group has been founded. With this group a framework is being built to reinterpret the obtained results, and global assumptions and operators that are used throughout all FCNC searches.

On top of these considerations, it should also be noted that for the search presented in this thesis, the contribution of the ζ_{tZq} coupling is neglected. This coupling arises in the Lagrangian in Equation 1.26 as

$$\frac{\sqrt{2}g}{4\cos\theta_W}\zeta_{tZq}\bar{t}\gamma^{\mu}\left(\tilde{f}_q^{L}P_L+\tilde{f}_q^{R}P_R\right)qZ_{\mu}, \tag{7.1}$$

and is related to the dimension six operators as

$$\begin{aligned}
\zeta_{\mathrm{tZq}}\tilde{f}^{\mathrm{L}}_{\mathrm{Zq}} &= -\frac{2v^2}{\Lambda^2}\left[\left(\bar{c}^{(1)}_{hq}-\bar{c}^{(3)}_{hq}\right)_{i3}+\left(\bar{c}^{(1)}_{hq}-\bar{c}^{(3)}_{hq}\right)^{*}_{3i}\right] , \\
\zeta_{\mathrm{tZq}}\tilde{f}^{\mathrm{R}}_{\mathrm{Zq}} &= -\frac{2v^2}{\Lambda^2}\left[(\bar{c}_{hu})_{i3}+(\bar{c}_{hu})^{*}_{3i}\right] .
\end{aligned} \tag{7.2}$$

In Ref. [207], it is shown that this coupling would yield smaller cross sections compared to the κ_{tZq} coupling. Therefore, if one would observe the FCNC tZq coupling, this would be more likely coming from the κ_{tZq} vertex. Another assumption made from a computational point of view, is the assumption of no interference between the single top quark FCNC signal and the top quark pair FCNC signal. This interference would result in an increase of the expected cross section with respect to the one used in this analysis. Hence, the analysis presented in this thesis is setting a more conservative limit on the FCNC anomalous coupling.

The little girl just could not sleep because her thoughts were way too deep, her mind had gone out for a stroll and fallen down a rabbit hole.

- Lewis Caroll, Alice in Wonderland

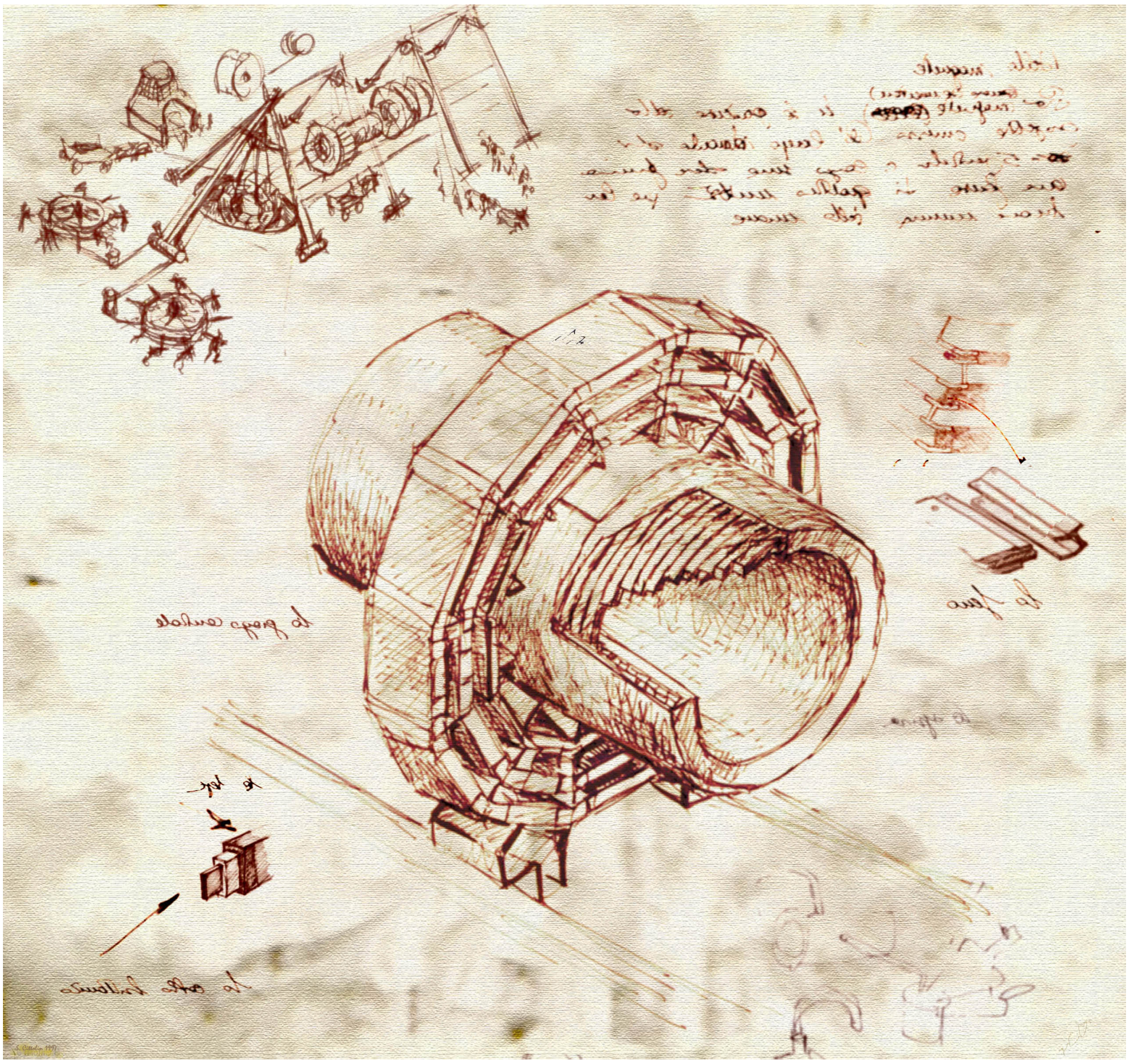

Appendices

A Trigger scale factors

The trigger scale factors using the dataset collected by $E_{\mathrm{T}}^{\mathrm{miss}}$ triggers and WZ simulation, after a 3 lepton and jets selection, in the Z boson mass window.

Table A.1: Trigger efficiencies on data events selected with $E_{\mathrm{T}}^{\mathrm{miss}}$ triggers and WZ simulation for all three-lepton channels together. The unweighed number of events is quoted. When there are no events passing the cuts, it is indicated with N/A.

ALL CHANNEL	data Efficiency	WZ simulation Efficiency
3 lep, at least one jet	117/118 = 99.15 %	18047/18055 = 99.96%
STSR	6/6 = 100.00%	1541/1541 = 100.00%
TTSR	26/27 = 96.30%	1791/1792 = 99.94%
WZCR	69/69 = 100.00 %	14405/14412=99.95%

Table A.2: Trigger efficiencies on data events selected with $E_{\mathrm{T}}^{\mathrm{miss}}$ triggers and WZ simulation for the 3μ lepton channel together. The unweighed number of events is quoted. When there are no events passing the cuts, it is indicated with N/A.

3μ CHANNEL	data Efficiency	WZ simulation Efficiency
3 lep, at least one jet	40/40 = 100.00 %	7814/7814 = 100.00%
STSR	N/A	687/687 = 100%
TTSR	13/13 = 100.00%	763/763 = 100.00%
WZCR	22/22 = 100.00 %	6238/6238=100.00%

Table A.3: Trigger efficiencies on data events selected with $E_{\mathrm{T}}^{\mathrm{miss}}$ triggers and WZ simulation for the 3e lepton channel together. The unweighed number of events is quoted. When there are no events passing the cuts, it is indicated with N/A.

3e CHANNEL	data Efficiency	WZ simulation Efficiency
3 lep, at least one jet	20/21 = 95.24%	2211/2215 = 99.82 %
STSR	4/4 = 100.00%	176/176 = 100.00%
TTSR	2/3 = 66.67%	242/242 = 100.00%
WZCR	14/14 = 100.00 %	1744/1748=99.77%

Table A.4: Trigger efficiencies on data events selected with $E_{\mathrm{T}}^{\mathrm{miss}}$ triggers and WZ simulation for the 2e1μ lepton channel together. The unweighed number of events is quoted. When there are no events passing the cuts, it is indicated with N/A.

2e1μ CHANNEL	data Efficiency	WZ simulation Efficiency
3 lep, at least one jet	32/32 = 100.00 %	3116/3118 = 99.94%
STSR	1/1 = 100.00%	255/255 = 100%
TTSR	9/9 = 100.00%	291/291 = 100.00%
WZCR	14/14 = 100.00 %	2529/2531=99.92%

Table A.5: Trigger efficiencies on data events selected with $E_{\mathrm{T}}^{\mathrm{miss}}$ triggers and WZ simulation for the 1e2μ lepton channel together. The unweighed number of events is quoted. When there are no events passing the cuts, it is indicated with N/A.

1e2μ CHANNEL	data Efficiency	WZ simulation Efficiency
3 lep, at least one jet	25/25 = 100.00%	4906/4908 = 99.96 %
STSR	1/1 = 100.00%	423/423 = 100.00%
TTSR	2/2 = 100.00%	495/496 = 99.80%
WZCR	19/19 = 100.00 %	3894/3895 =99.97%

Transfer factors B

The transfer factors used to project the yields from the control regions to the signal regions are shown in Table B.1. In Table B.2, the yields in the STSR and TTSR expected from simulation and estimated from the sidebands are compared for the $t\bar{t}$+jets process. These are in agreement with each other. In Table B.3, the expected number of events for each process is given together with their expected values from the control regions. The $Z/\gamma^* +$jets process has negative events due to the fact that this sample has negative weights.

Table B.1: Transfer factors for all lepton channels for going fro m WZCR to the signal regions. The transfer factors $Tr_{\text{TTCR}\rightarrow\text{TTSR}}$ and $Tr_{\text{STCR}\rightarrow\text{STSR}}$ are 0.33.

	$Tr_{\text{WZCR}\rightarrow\text{STSR}}$	$Tr_{\text{WZCR}\rightarrow\text{TTSR}}$
κ_{tZu}/Λ	0.22 ± 0.00	0.46 ± 0.00
κ_{tZc}/Λ	0.39 ± 0.01	0.76 ± 0.01
$Z/\gamma^* +$ jets	0.08 ± 0.09	0.10 ± 0.10
$t\bar{t}$	0.54 ± 0.31	0.70 ± 0.31
WZ	0.10 ± 0.00	0.15 ± 0.00
tZq	0.36 ± 0.02	0.67 ± 0.03
$t\bar{t}Z$	0.14 ± 0.02	0.61 ± 0.05
ZZ	0.10 ± 0.00	0.13 ± 0.00
other	0.16 ± 0.03	0.30 ± 0.03

Table B.2: Event yields for the $t\bar{t}$ background in all lepton channels. The yields below the dashed lines shoud be compared with the two first rows.

Region	$t\bar{t}$ event yield
STSR	13.1 ± 2.5
TTSR	9.7 ± 2.1
TTCR	22.3 ± 3.1
STCR	33.7 ± 3.8
STSR (STCR)	11.24 ± 1.28
TTSR (TTCR)	7.44 ± 1.02

Table B.3: Event yields for all lepton channels. The last two columns represent the predicted event yield after applying the transfer factors. The regions between brackets correspond to the region from which the prediction is made.

	STSR	TTSR	WZCR	TTCR	STCR	STSR (WZCR)	TTSR (WZCR)
κ_{tZu}/Λ	3.9 ±0.0	11.2 ±0.0	7.3 ±0.0	0.6 ±0.0	0.3 ±0.0	1.57 ±0.02	3.33 ±0.04
κ_{tZc}/Λ	14.1 ±0.1	30.9 ±0.1	15.5 ±0.1	1.7 ±0.0	1.2 ±0.0	6.12 ±0.08	11.77 ±0.13
$Z/\gamma^* + \text{jets}$	-4.6 ±21.7	22.3 ±14.3	136.9 ±48.5	-14.0 ±22.2	-15.9 ±11.3	10.61 ±11.31	13.69 ±14.68
$t\bar{t}$	13.1 ±2.5	9.7 ±2.1	8.5 ±1.9	22.3 ±3.1	33.7 ±3.8	4.61 ±2.37	5.89 ±2.96
WZ	60.9 ±1.6	83.0 ±1.7	552.7 ±4.6	11.9 ±0.6	8.5 ±0.6	55.86 ±1.57	83.80 ±2.30
tZq	8.0 ±0.2	16.9 ±0.2	7.3 ±0.2	2.2 ±0.1	1.0 ±0.1	2.66 ±0.14	4.86 ±0.25
$t\bar{t}Z$	3.5 ±0.3	42.5 ±0.9	9.6 ±0.5	6.8 ±0.4	0.5 ±0.1	1.37 ±0.18	5.90 ±0.59
ZZ	4.6 ±0.1	4.8 ±0.1	46.2 ±0.3	0.8 ±0.0	0.6 ±0.0	4.48 ±0.16	6.06 ±0.21
other	1.2 ±0.3	5.6 ±0.3	6.8 ±0.5	7.5 ±0.7	2.4 ±0.5	1.09 ±0.18	2.05 ±0.24

Details about the BDTs C

In this appendix, the distributions of the input variables for each multivariate discriminant is given, as well as the resulting receiver operator characteristic curves.

C.1 Variable distributions for the STSR for the tZu coupling

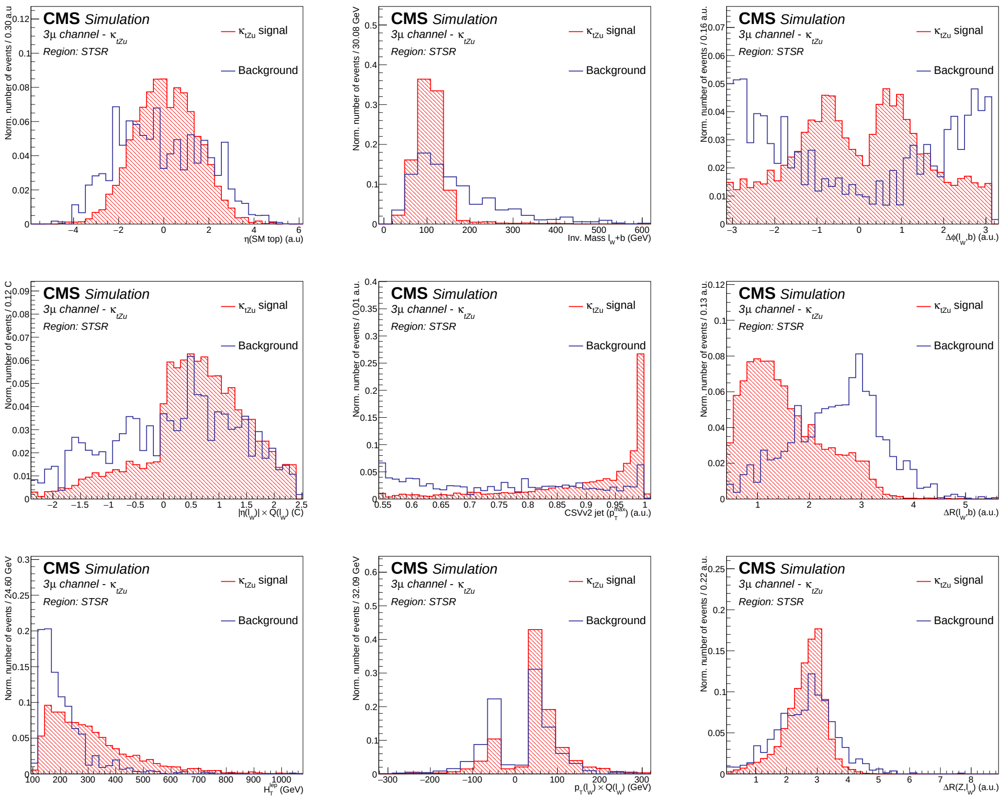

Figure C.1: The normalised distributions of the input variables for reconstructing the multivariate discriminator in the STSR for the tZu vertex for the 3μ channel. The contribution of the NPL background is not included.

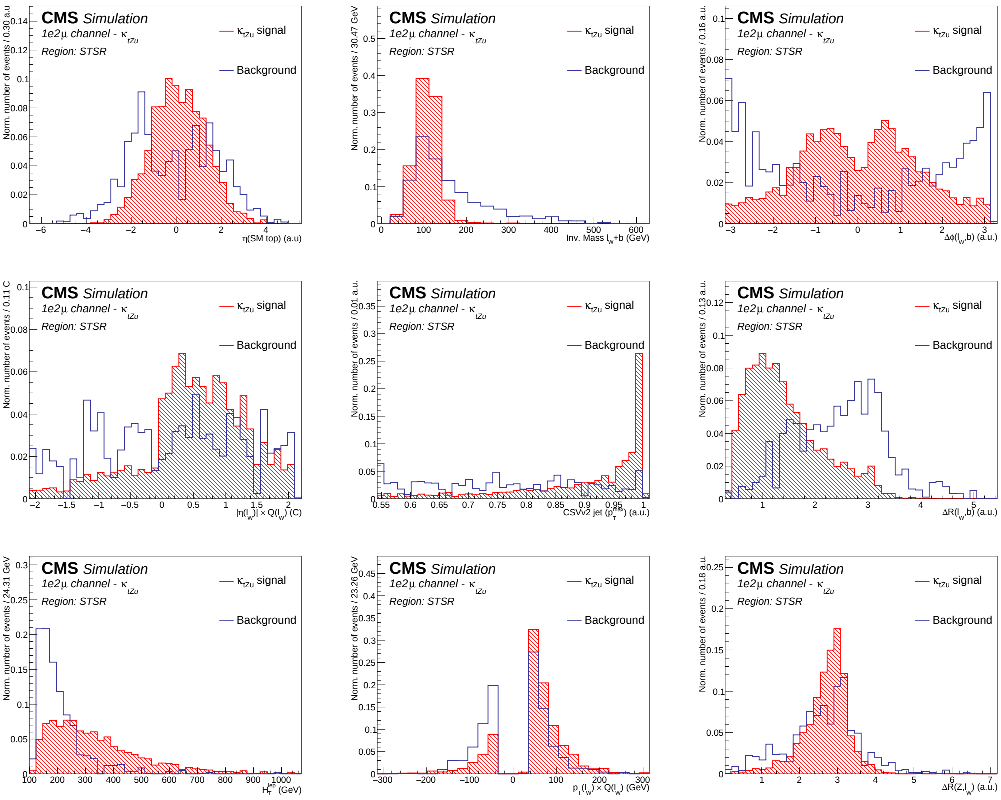

Figure C.2: The normalised distributions of the input variables for reconstructing the multivariate discriminator in the STSR for the tZu vertex for the 1e2μ channel. The contribution of the NPL background is not included.

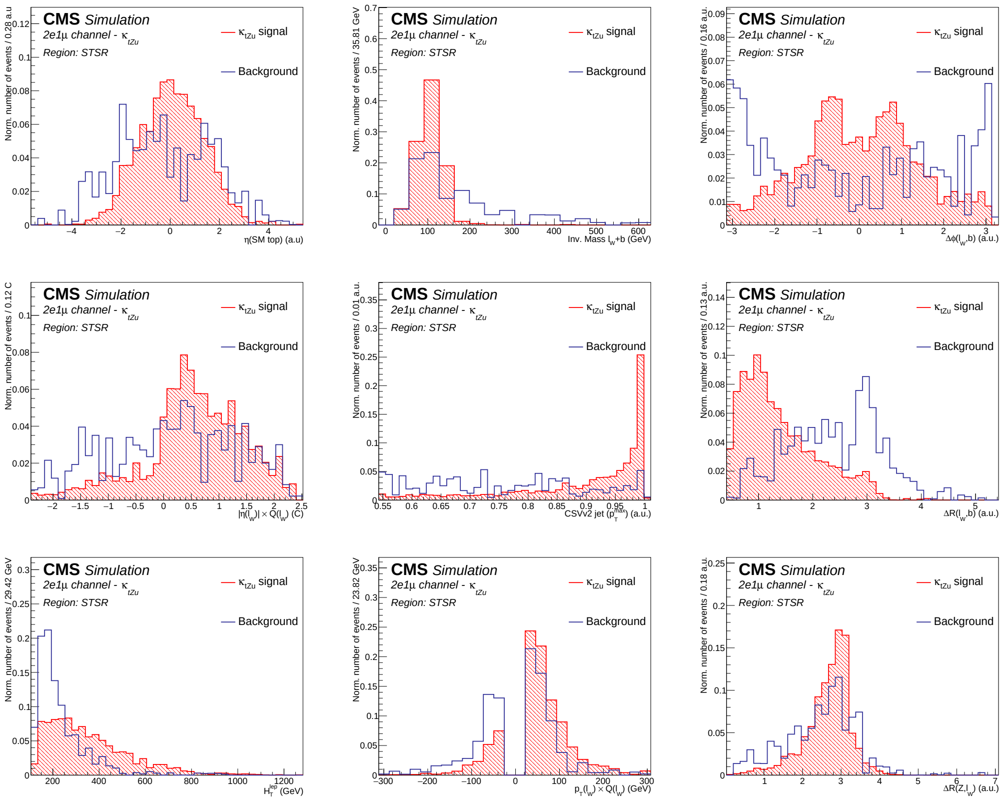

Figure C.3: The normalised distributions of the input variables for reconstructing the multivariate discriminator in the STSR for the tZu vertex for the 2e1μ channel. The contribution of the NPL background is not included.

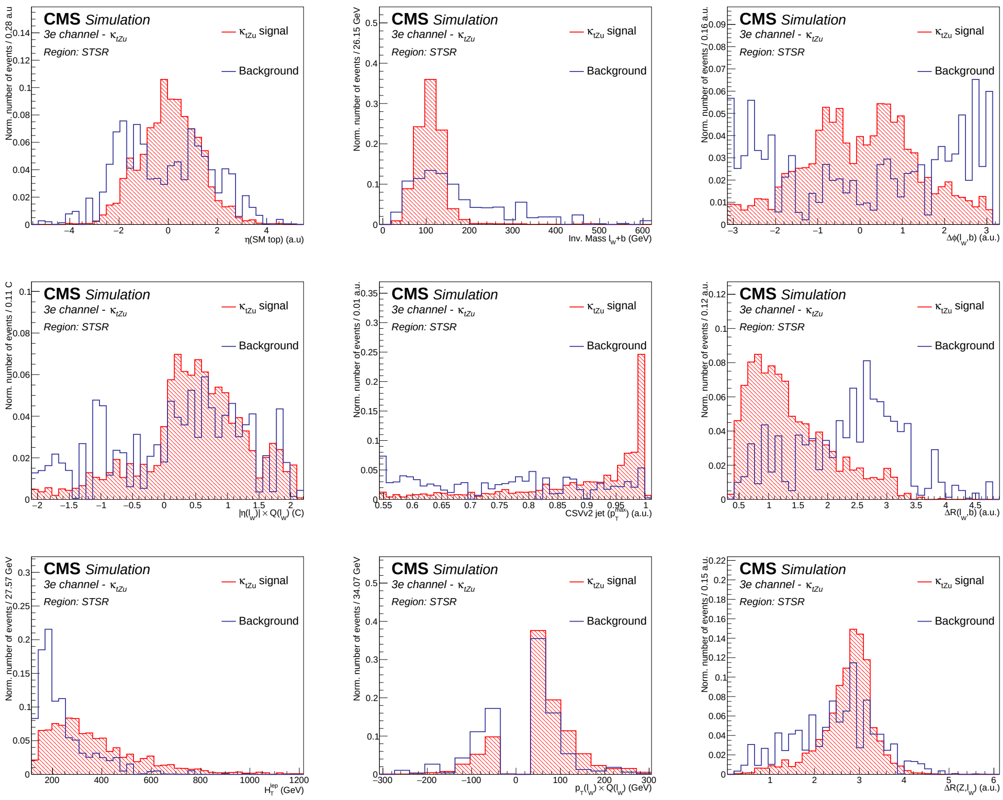

Figure C.4: The normalised distributions of the input variables for reconstructing the multivariate discriminator in the STSR for the tZu vertex for the 3e channel. The contribution of the NPL background is not included.

C.2 Variable distributions for the TTSR for the tZu coupling

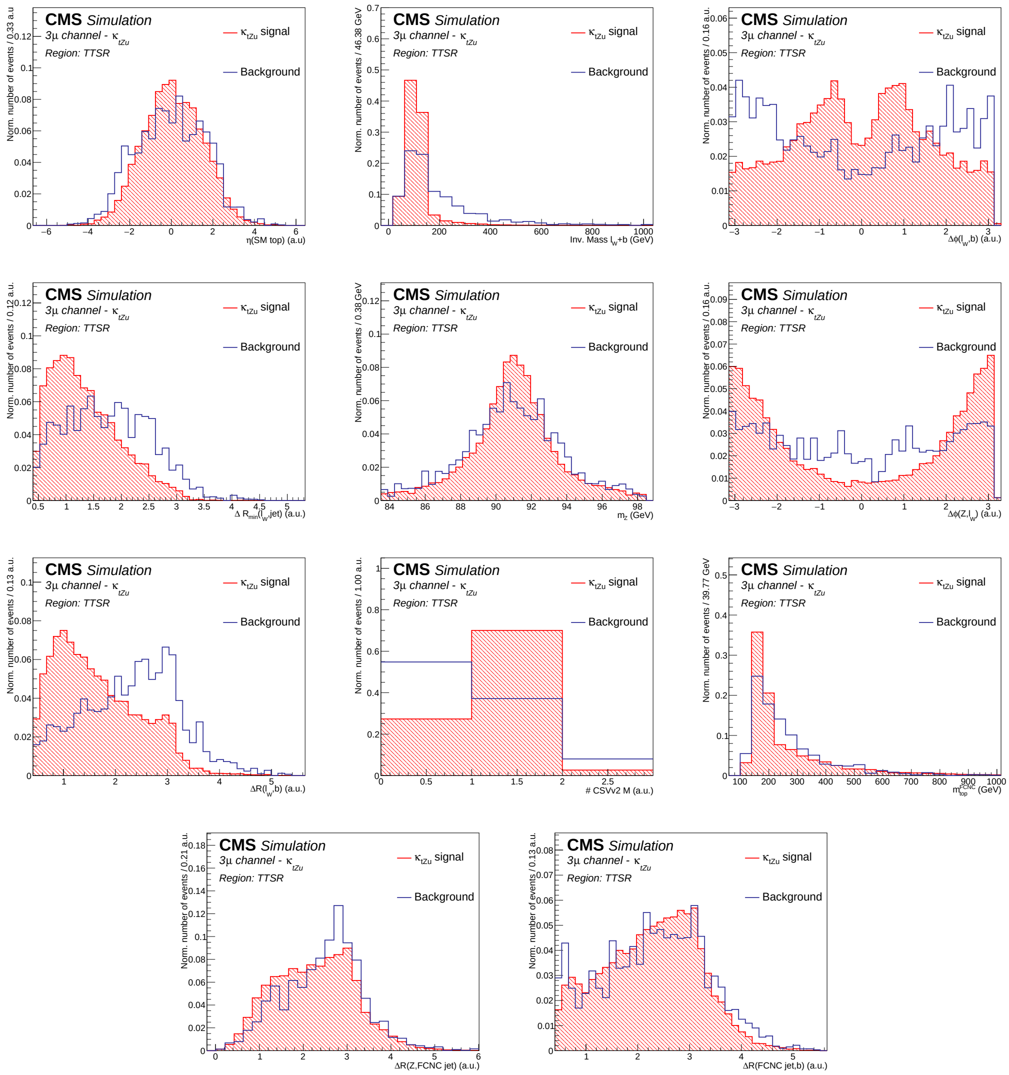

Figure C.5: The normalised distributions for input variables for reconstructing the multivariate discriminator in the TTSR for the tZu vertex, in the 3μ lepton channel. The contribution of the NPL background is not included.

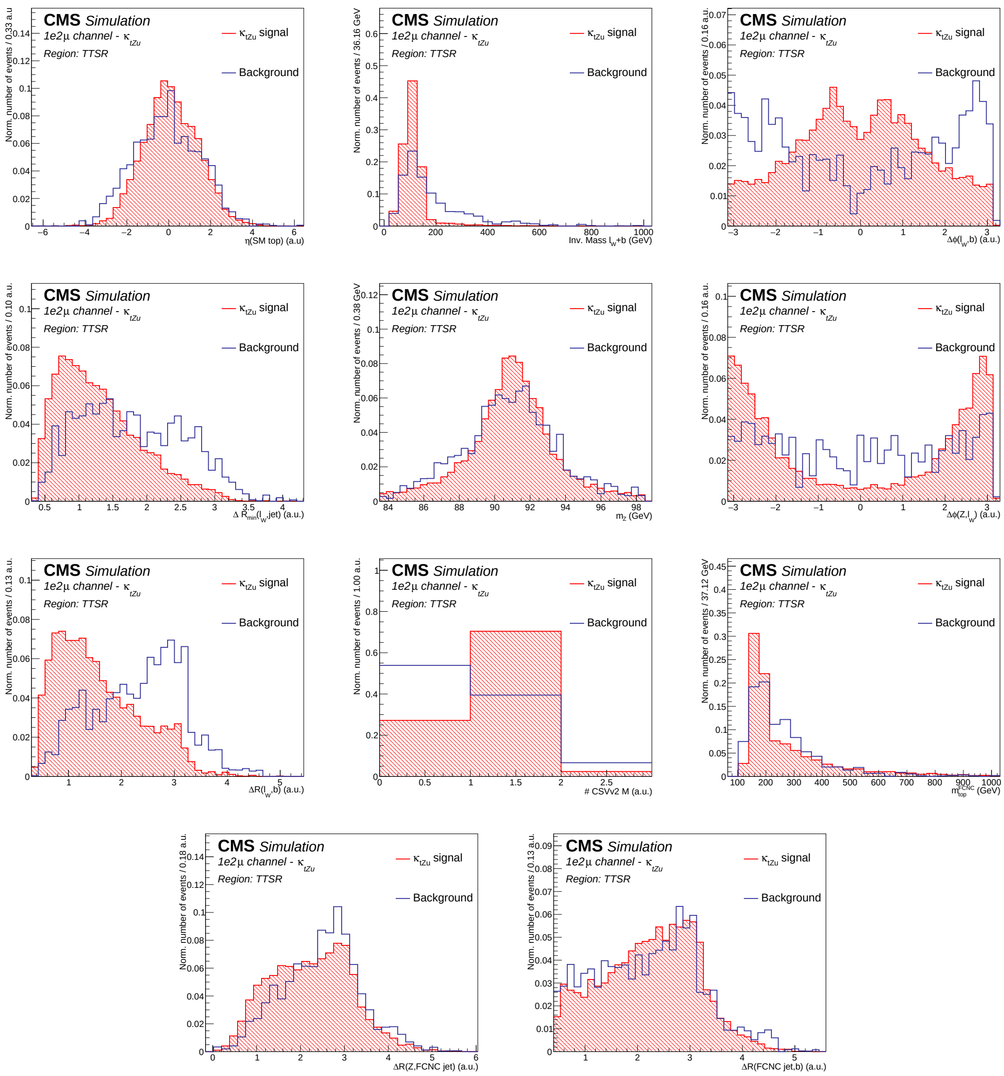

Figure C.6: The normalised distributions for input variables for reconstructing the multivariate discriminator in the TTSR for the tZu vertex, in the 1e2μ lepton channel. The contribution of the NPL background is not included.

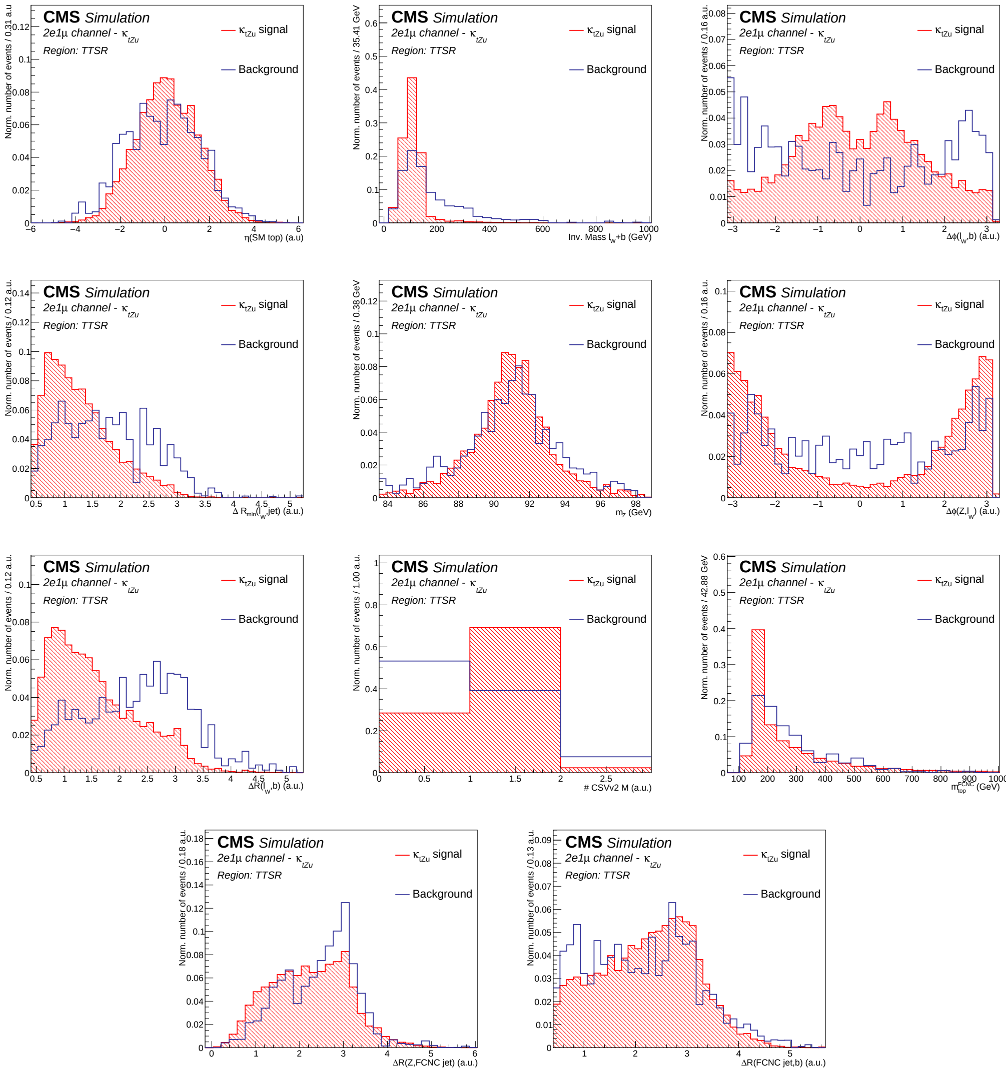

Figure C.7: The normalised distributions for input variables for reconstructing the multivariate discriminator in the TTSR for the tZu vertex, in the 2e1μ lepton channel. The contribution of the NPL background is not included.

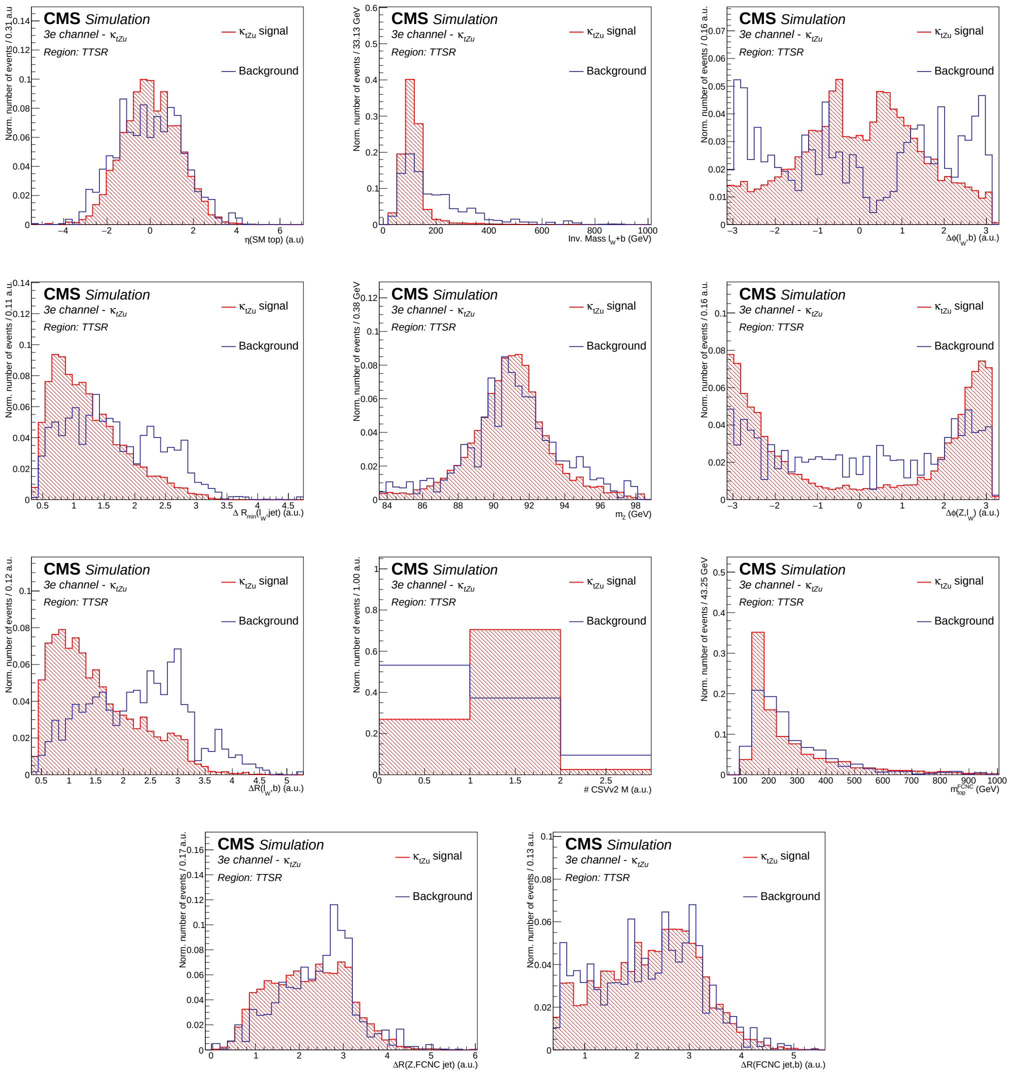

Figure C.8: The normalised distributions for input variables for reconstructing the multivariate discriminator in the TTSR for the tZu vertex, in the 3e lepton channel. The contribution of the NPL background is not included.

C.3 Variable distributions for the STSR for the tZc coupling

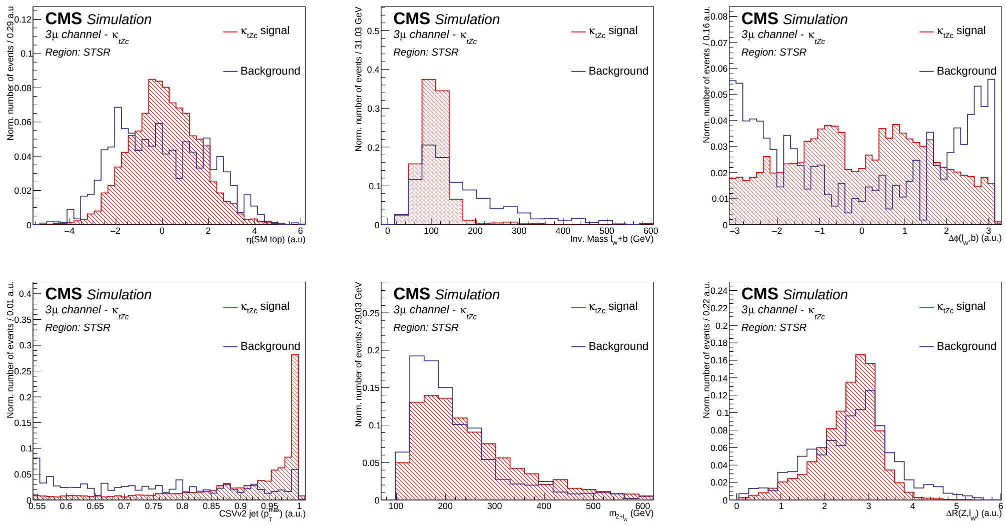

Figure C.9: The normalised distributions of the input variables for reconstructing the multivariate discriminator in the STSR for the tZc vertex for the 3μ channel. The contribution of the NPL background is not included.

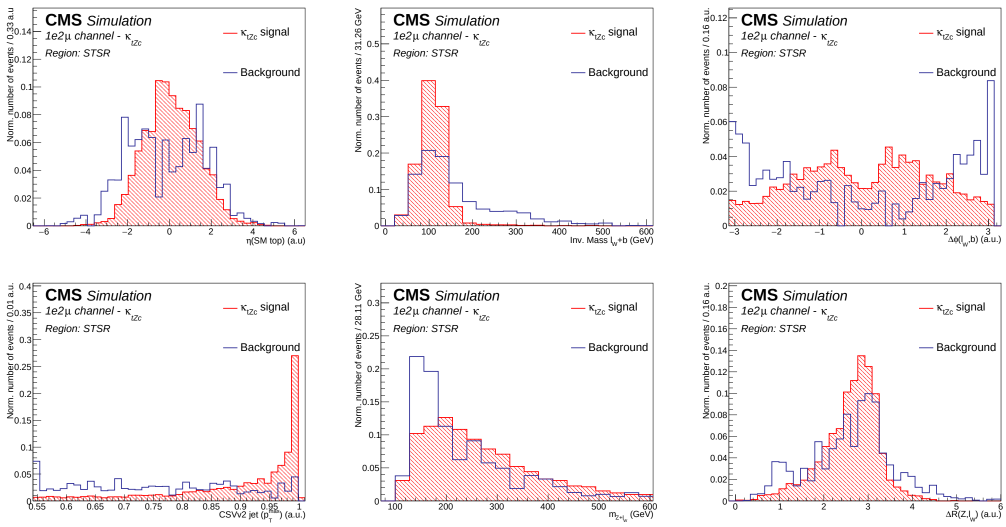

Figure C.10: The normalised distributions of the input variables for reconstructing the multivariate discriminator in the STSR for the tZc vertex for the 1e2μ channel. The contribution of the NPL background is not included.

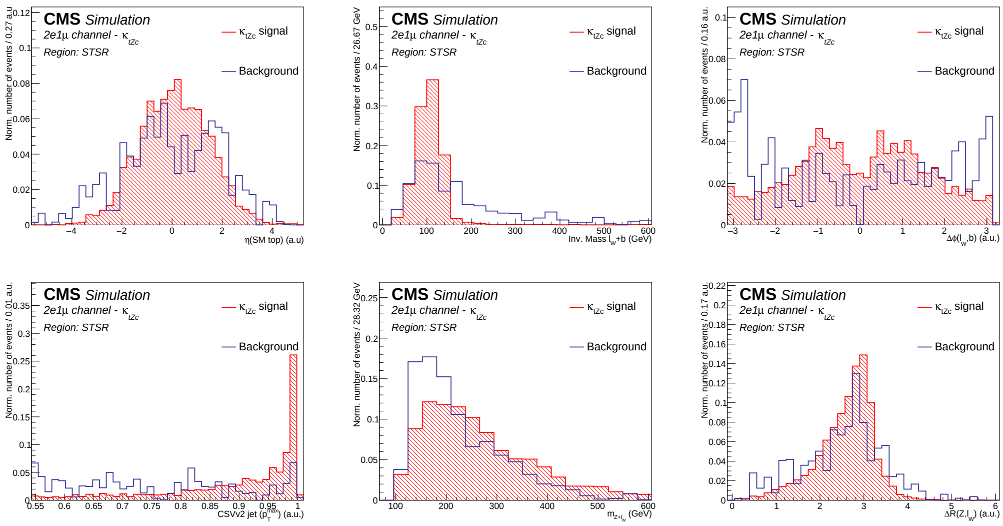

Figure C.11: The normalised distributions of the input variables for reconstructing the multivariate discriminator in the STSR for the tZc vertex for the 2e1μ channel. The contribution of the NPL background is not included.

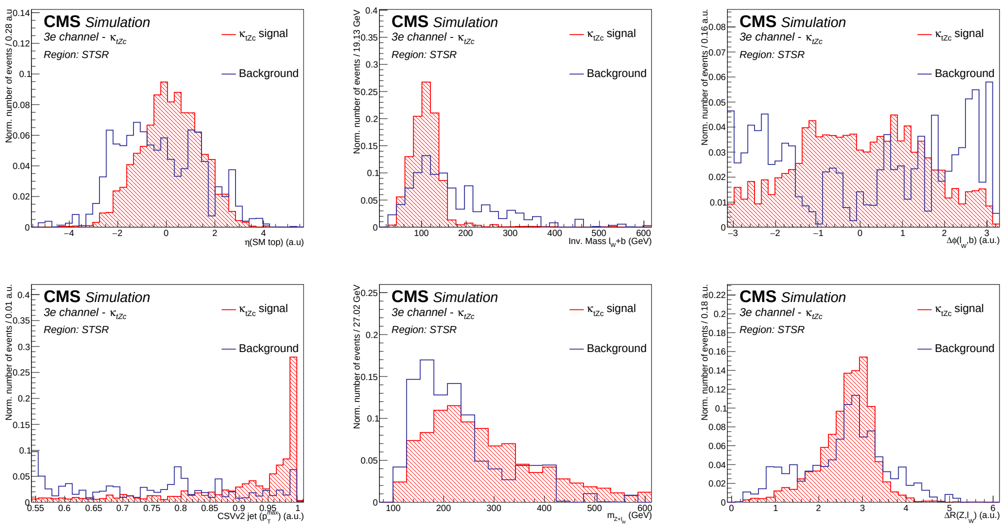

Figure C.12: The normalised distributions of the input variables for reconstructing the multivariate discriminator in the STSR for the tZc vertex for the 3e channel. The contribution of the NPL background is not included.

C.4 Variable distributions for the TTSR for the tZc coupling

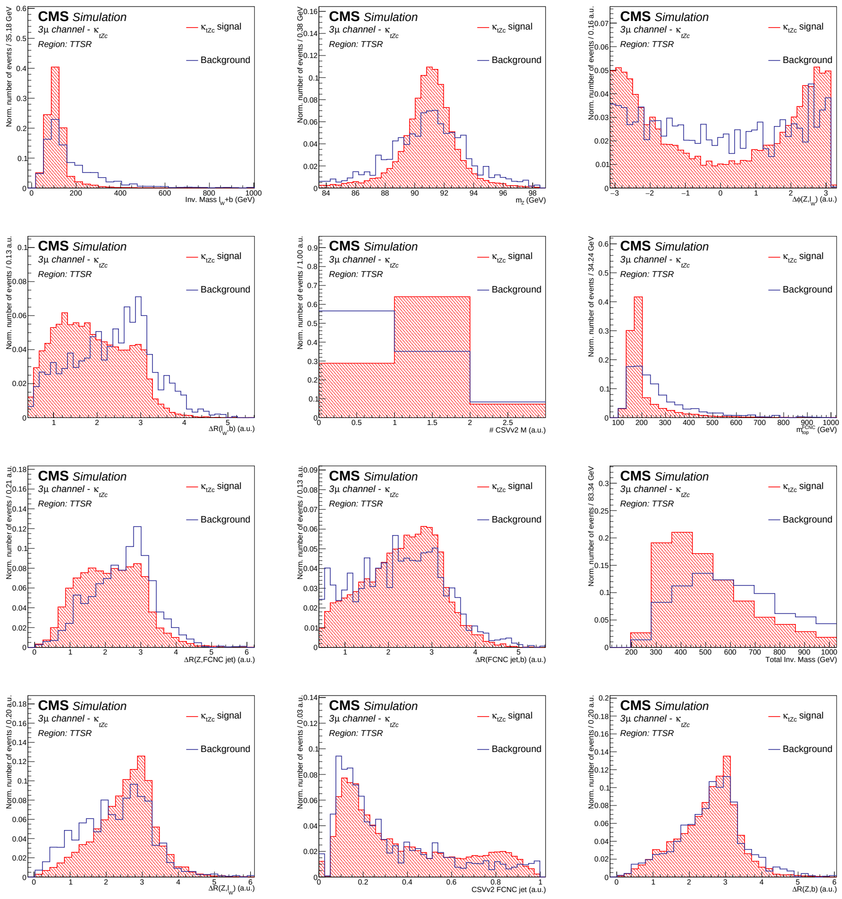

Figure C.13: The normalised distributions of the input variables for reconstructing the multivariate discriminator in the TTSR for the tZc vertex, in the 3μ channel. The contribution of the NPL background is not included.

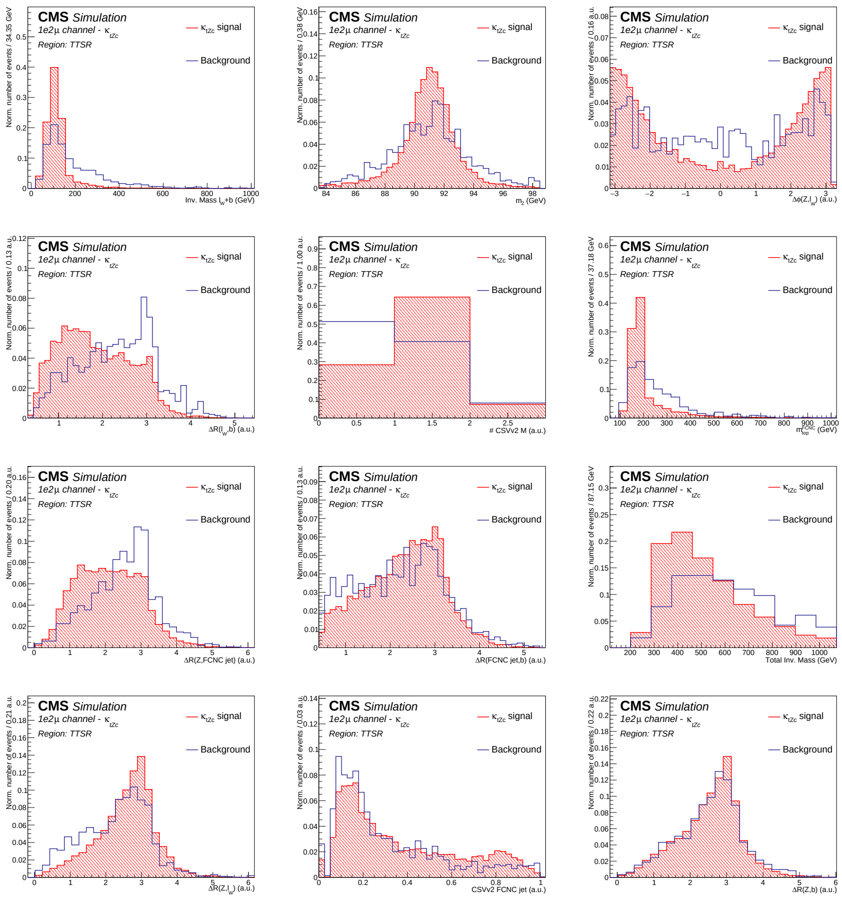

Figure C.14: The normalised distributions of the input variables for reconstructing the multivariate discriminator in the TTSR for the tZc vertex, in the 1e2μ channel. The contribution of the NPL background is not included.

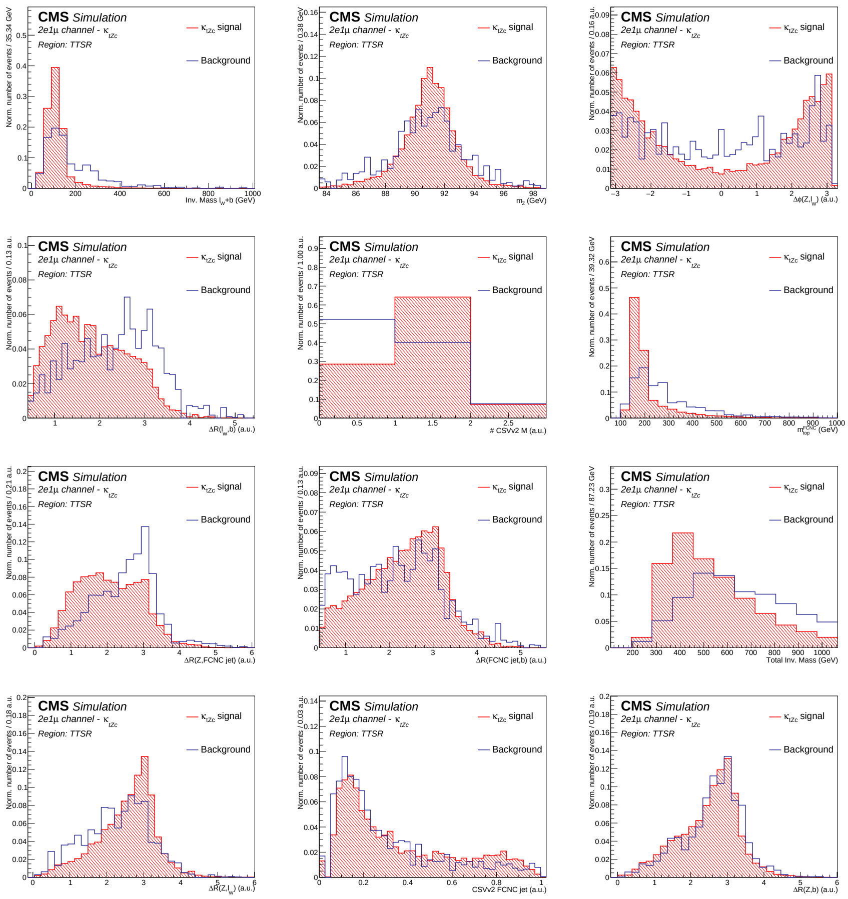

Figure C.15: The normalised distributions of the input variables for reconstructing the multivariate discriminator in the TTSR for the tZc vertex, in the 2e1μ channel. The contribution of the NPL background is not included.

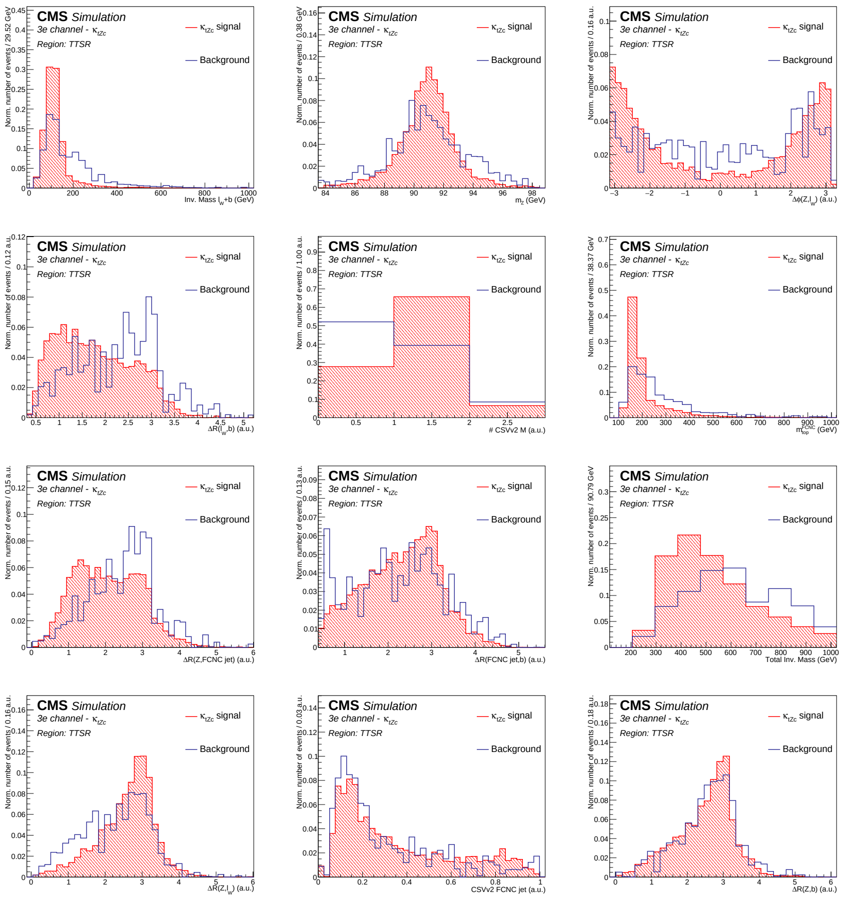

Figure C.16: The normalised distributions of the input variables for reconstructing the multivariate discriminator in the TTSR for the tZc vertex, in the 3e channel. The contribution of the NPL background is not included.

C.5 ROC curves

The receiving operator characteristics are shown in Figure C.17 for the TTSR and tZu interaction. One can see that for all channels there is separating power and that the ROC curve of the testing sample is below the one for the training sample. This is the most present in the 3e channel, where there is a lack of statistics. For the tZc interaction, the ROC curves for the STSR and TTSR are shown in Figure C.18 and Figure C.19 respectively.

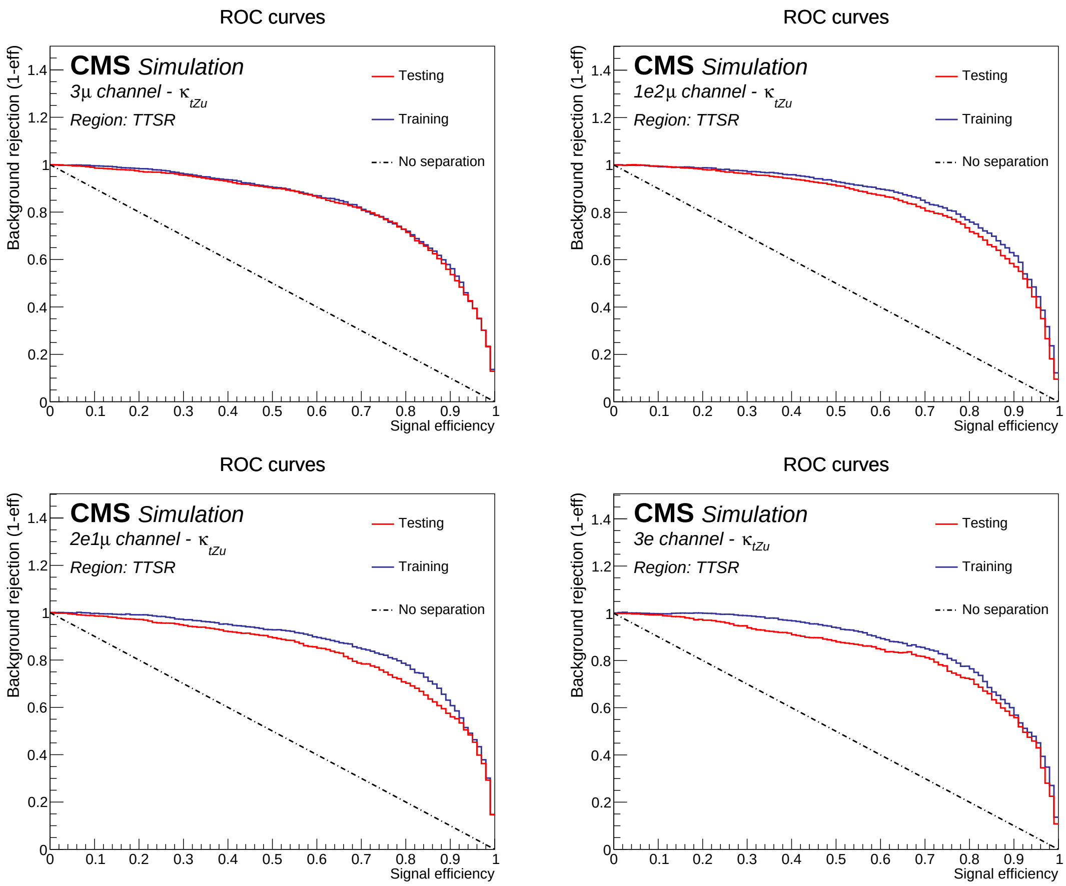

Figure C.17: ROC curves of the resulting multivariate discriminators D in the TTSR, for the tZu signal. For the 3μ (left,top), 1e2μ (right,top), 2e1μ (left, bottom) and 3e (right,bottom) three-lepton channel.

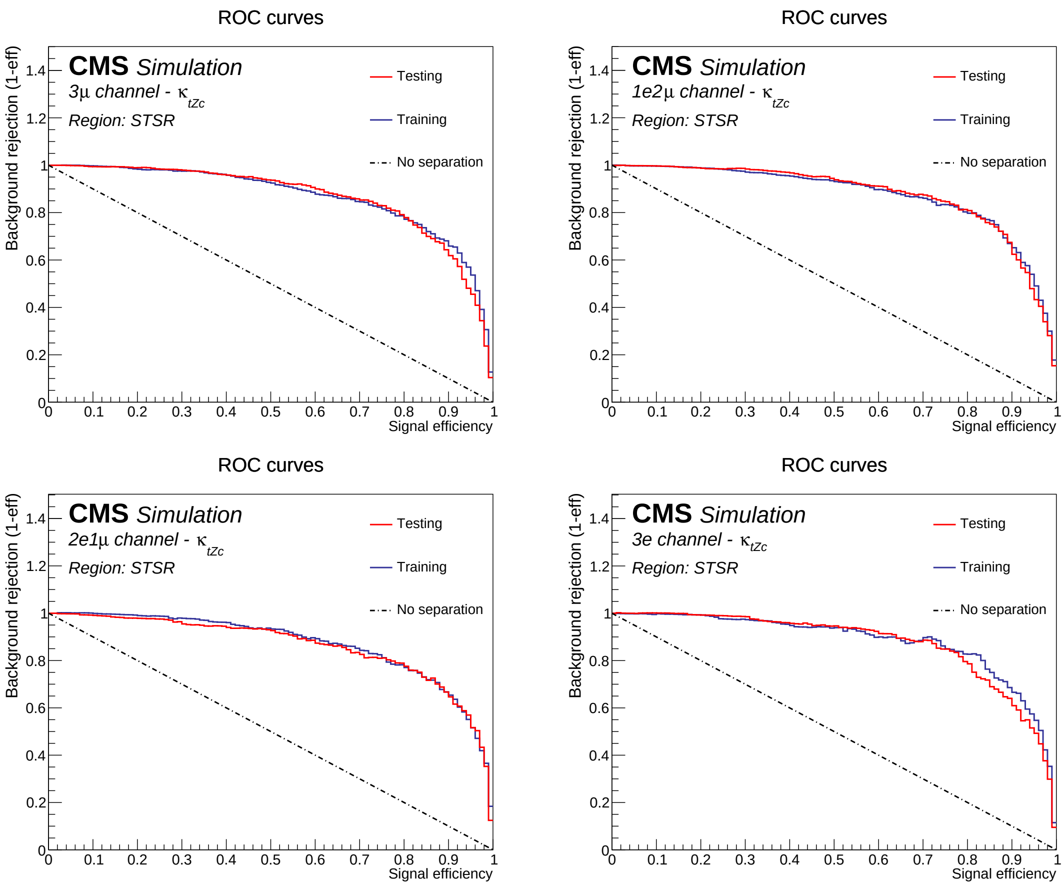

Figure C.18: ROC curves of the resulting multivariate discriminators D in the STSR, for the tZc signal. For the 3μ (left,top), 1e2μ (right,top), 2e1μ (left, bottom) and 3e (right,bottom) three-lepton channel.

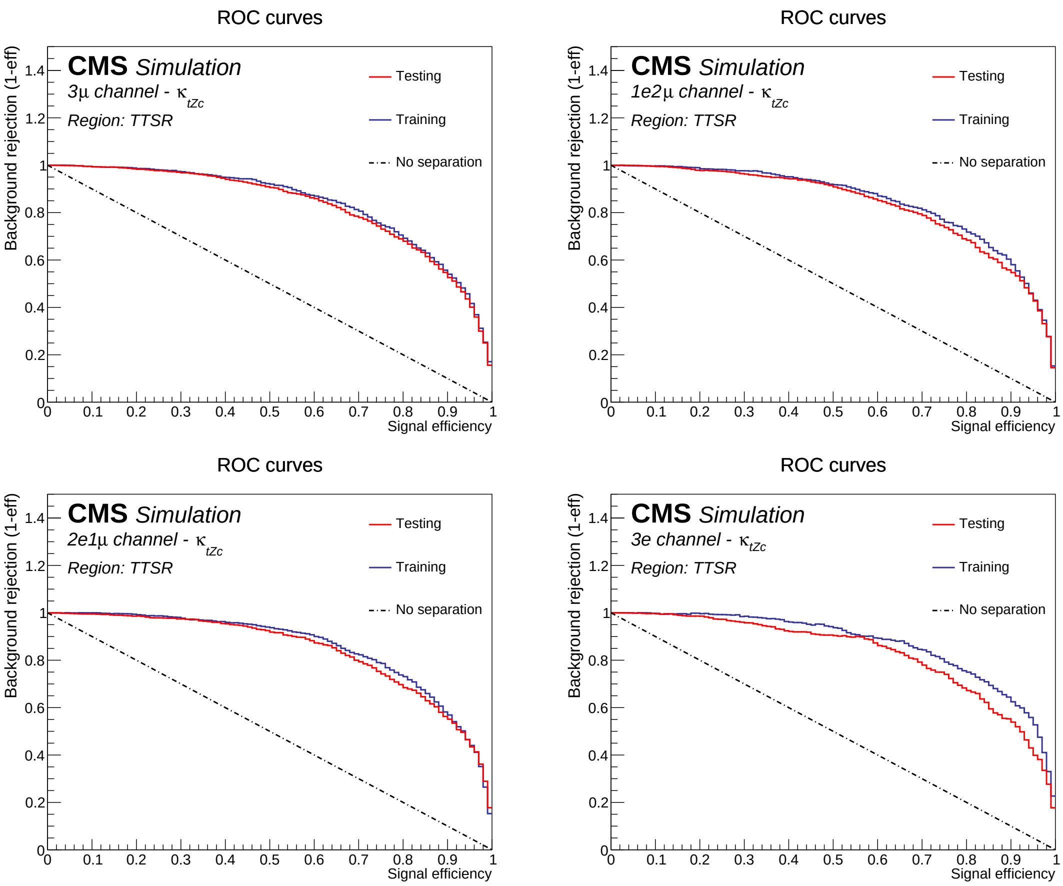

Figure C.19: ROC curves of the resulting multivariate discriminators D in the TTSR, for the tZc signal. For the 3μ (left,top), 1e2μ (right,top), 2e1μ (left, bottom) and 3e (right,bottom) three-lepton channel.

“Who are YOU?" said the Caterpillar. This was not an encouraging opening for a conversation. Alice replied, rather shyly, “I-I hardly know, sir, just at present – at least I know who I was when I got up this morning, but I think I must have been changed several times since then."

- Lewis Caroll, Alice in Wonderland

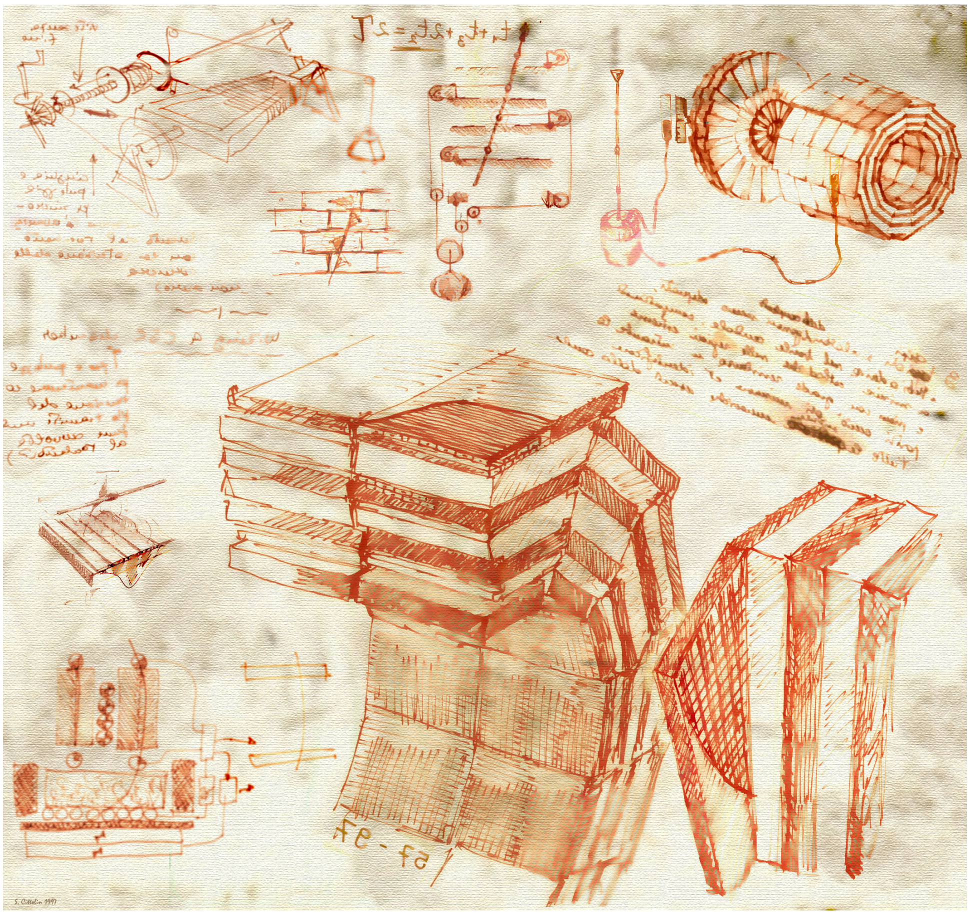

Achievements and contributions

Achievements and contributions

During the course of my doctoral studies, I have been part of the tZ(q) analysis group at the CMS collaboration and have contributed to the paper of the tZq SM and FCNC search at a centre-of-mass energy of 8 TeV by CMS:

> *Search for associated production of a Z boson with a single top quark and for tZ flavour-changing interactions in pp collisions at* $\sqrt{s} = 8$ *TeV, by CMS Collaboration (Albert M Sirunyan et al.), arXiv:1702.01404 [hep-ex], JHEP 1707 (2017) 003.*

Proceeding on this collaboration, I have become one of the convenors of the tZ(q) SM and FCNC reseach group. I coordinated the weekly meetings and the collaborations between the several institutes and universities: the Centro de Investigaciones Energéticas, Medioambientales y Tecnológicas (CIEMAT), Interuniversity Institute of High Energies (IIHE), the Institut Pluridisciplinaire Hubert Curien (IPHC), the National Centre for Physics (NCP) and the Brunel University London. Amongst the research topics in this group are the SM tZq as well as the FCNC tZq search in the three-lepton and the dilepton final states. Both three-lepton searches have been published, where the SM search is published as

> *Evidence for the standard model production of a Z boson with a single top quark in pp collisions at* $\sqrt{s} = 13$ TeV*, by CMS Collaboration (Albert M Sirunyan et al.), CMS-PAS-TOP-16-020, CDS record 2284830,*

and the FCNC search is published as

> *Search for flavour changing neutral currents in top quark production and decays with three-lepton final state using the data collected at sqrt(s) = 13 TeV, by CMS Collaboration (Albert M Sirunyan et al.), CMS-PAS-TOP-17-017, CDS record 2292045.*

The latter comprises the research presented in this thesis and is also where my main contribution lies. A complete list of my 292 peer reviewed publications can be found below[1].

[1] `http://inspirehep.net/search?ln=en&ln=en&p=find+i+van+parijs&of=hb&action_search=Search&sf=earliestdate&so=d&rm=&rg=25&sc=0`

As part of my research I attended many conferences and workshops. I was one of the speakers at the General Scientific Meeting of the Belgian Physical Society in 2016, where I presented

> *Flavor changing neutral currents of top quarks at the LHC, a probe for new physics, by Isis Van Parijs*

Furthermore, I represented the tZ(q) research group at the 3rd Single Top Workshop in 2016 and gave the talk

> *tZq in tri-lepton SM+FCNC, by Isis Van Parijs for the analysis group.*

Additionally, I was chosen by the CMS collaboration to represent the CMS collaboration as one of the speakers at the 9th International Workshop on Top Quark Physics in 2016. Here I presented

> *Multilepton signatures from tZq interactions in the SM and top-FCNC, by CMS Collaboration (Isis Van Parijs for the collaboration)*

for which conference proceedings are published at

> *Three lepton signatures from tZq interactions in the SM and top- FCNC at the CMS experiment at $\sqrt{s}$ = 8 TeV, by CMS Collaboration (Isis Van Parijs for the collaboration), arXiv:1703.00162 [hep-ex].*

At the CMS collaboration, it is common to take on experimental physics responsibility (EPR). I had the opportunity to be part of the Tracker team, where my work was mainly focussed on the Silicon Strip tracker. I have done shifts of detector expert on call, where I was the responsible for the Silicon Strip tracker on site and coordinated the daily activities. During LS1, the tracker has been made ready to operate at lower temperatures. The CMS cooling plant was refurbished, new methods for vapour sealing and insulation were applied, and high-precision sensors to monitor the humidity and temperature were placed. I had the opportunity to be part of the placement of the vapour sealing and sensors. Furthermore, I was involved in hardware testing such as pressure testing of the new dry gas system. Additionally, I have been involved in the calibration of the detector control units (DCUs). The CMS tracker silicon micro-strip sensors are exposed to high levels of radiation which causes an increases in the detector leakage current as well as a change in the detector depletion voltage. The DCUs measures the temperatures, voltages and leakage currents and makes it able to control the radiation damage. A good calibration is therefore necessary to spot any abnormalities. I was also involved in the Phase 2 upgrades of the tracker. For the HL-LHC, the tracker will be included in the level-1 trigger in order to handle the increase in luminosity. Therefore, the tracker geometry is altered and the maps of the tracker used for Detector Quality Monitoring (DQM) had to be updated. Lastly, I was DQM expert on call, where I represented the first line of expertise for the daily data quality monitoring during Run 2.

As member of the IIHE institute, I was involved in the bachelor student excursion to CERN and did recruiting of new physics students at the open days of the university as well as at high schools. Furthermore, I was part of the scientific jury of 90° South. This is an initiative where middle school and high school students could participate in a scientific competition for the opportunity to take part in a physics experiment at the South pole. Additionally, for my work at CMS, I have taken the first aid as well as the fire extinguisher courses to provide a safer working environment.

Why, sometimes I've believed as many as six
impossible things before breakfast.

-Lewis Caroll, Alice in Wonderland

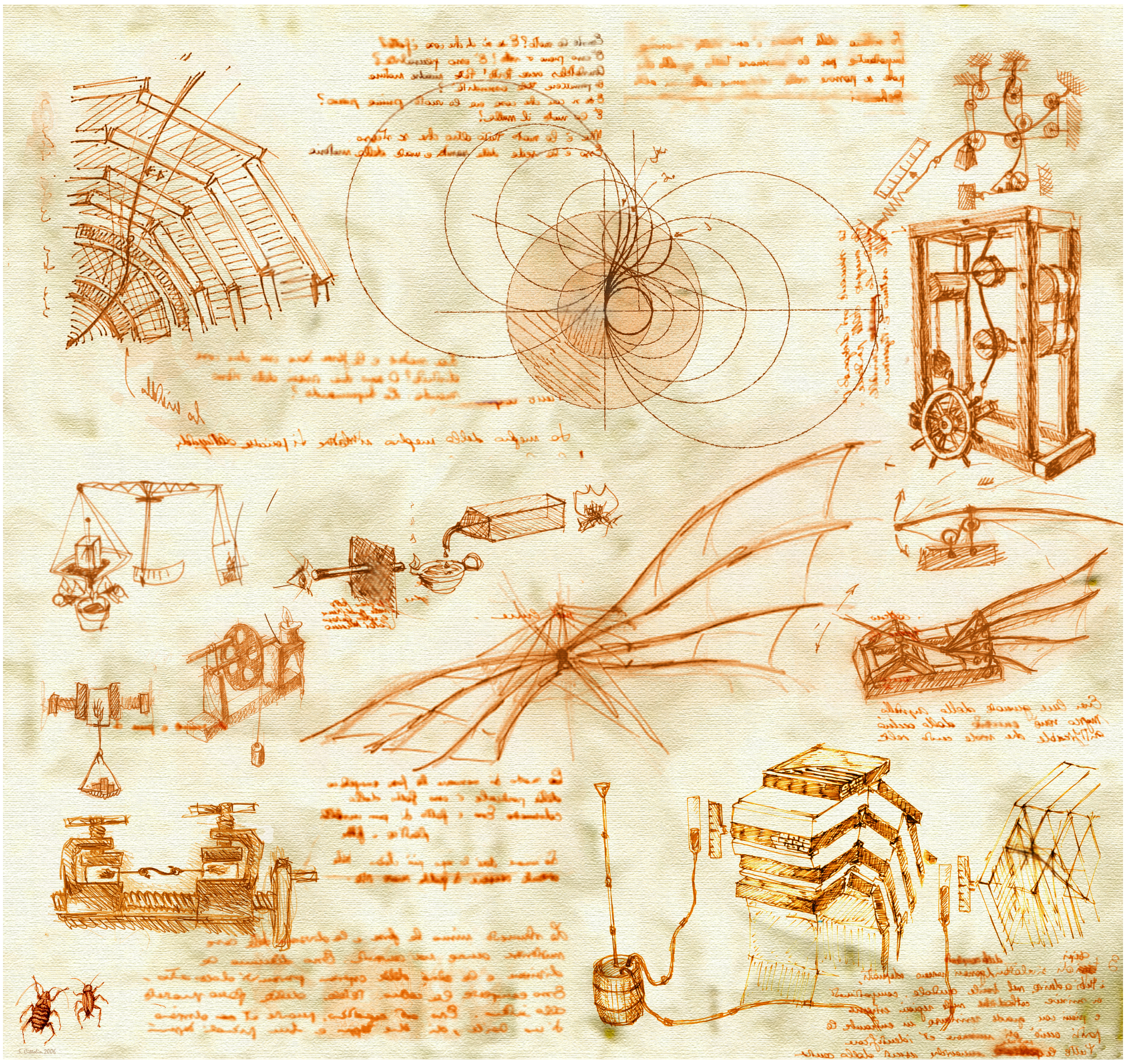

Comprehensive summaries

Summary

The Standard Model of particle physics is a theory of fundamental particles and their interactions. This theory has been experimentally confirmed and all particles predicted by this theory have been found. Nonetheless, this theory has its shortcomings and can not explain phenomena such as neutrino masses or gravity. The heaviest particle of the Standard Model is the top quark and physicists believe that it has an enhanced sensitivity to various new particles and interactions suggested by new physics theories. The top quark has a very short lifetime, hence it does not form bound states and it can be used to study the bare quark. Furthermore, it has a distinct signature since it almost exclusively decays to a W boson and a bottom quark. This makes the top quark an ideal candidate for the study of quark properties. Also, many beyond the Standard Model physics phenomena are studied by measuring the production rate of top quarks for probing the Wtb vertex, and interactions that are heavily suppressed in the Standard Model can be investigated. The Large Hadron Collider (LHC) is a proton collider, producing a large number of events containing top quarks. At the proton collision points, experiments are placed to study the collisions. The search presented in this thesis is performed on data collected by the Compact Muon Solenoid (CMS) experiment at a centre-of-mass energy of 13 TeV, resulting in 35.9 fb^{-1} of integrated luminosity.

Flavour changing neutral currents (FCNC) are highly suppressed in the Standard Model. However, many beyond the Standard Model theories enhance their probability. In this thesis, a search in three lepton final states is performed for the production of single top quarks via the tZq vertex, with q=c or u, for the top quark pair processes where one of the top quarks decays through this vertex. No significant deviation with respect to the predicted background is observed and upper limits at 95% confidence level are obtained. The observed (expected) upper limits at 95% confidence level on the branching fractions are: $\mathcal{B}(t \to uZ) < 2.4 \times 10^{-4}$ (1.5×10^{-4}) and $\mathcal{B}(t \to cZ) < 4.5 \times 10^{-4}$ (3.7×10^{-4}), assuming one non-vanishing FCNC coupling at a time.

Significant improvements are developed with respect to previous searches, namely by using other kinematic variables as input into the BDT as well as a better handle on the non prompt lepton background. The sensitivity of this search exceeds that of previous analysis at the CMS experiment, and is comparable with the sensitivity obtained at the ATLAS experiment. Although the limits on the FCNC interactions with a tZq vertex start to probe physics beyond the Standard Model, the branching fractions predicted within the Standard Model remain out of reach.

Samenvatting

"Een zoektocht naar smaakveranderende neutrale stromen gerelateerd met een top quark en een Z boson, gebruik makend van de data gecollecteerd door het CMS experiment met een massamiddelpuntsenergie van 13 TeV."

Het Standaard Model van de deeltjesfysica is een theorie over fundamentele deeltjes en hun interacties. Deze theorie werd door diverse experimenten geconfirmeerd en al de deeltjes die deze theorie voorspelt zijn ook daadwerkelijk ontdekt. Ondanks zijn vele successen heeft deze theorie echter ook zijn tekortkomingen. Fenomenen zoals neutrino massa's of zwaartekracht blijven onverklaard. De top quark is het zwaarste deeltje in het Standaard Model en doet fysici geloven dat het een verhoogde gevoeligheid heeft voor nieuwe deeltjes en interacties voorspeld door nieuwe theorieën. De top quark heeft zo een korte levensduur, dat het onstnapt aan de vorming van gebonden toestanden en het mogelijk is om rechtstreeks de top quark eigenschappen te onderzoeken. Veel nieuwe fysica theorieën worden onderzocht via de studie van de productie van top quarks en nemen zo het Wtb interactiepunt onder de loep. De "Large Hadron Collider" (LHC) is een proton versneller en produceert een zeer groot aantal proton botsingen die resulteren in top quarks. Dit maakt de LHC een ideale plek om top quark fenomenen te onderzoeken. Op elk proton botsingspunt zijn experimenten geplaatst om de botsingen te onderzoeken. Het onderzoek gepresenteerd in deze thesis omvat de data verzameld door het "Compact Muon Solenoid" (CMS) experiment aan een massamiddelpuntsenergie van 13 TeV, resulterend in een geïntegreerde luminositeit van 35.9 fb^{-1}.

Smaakveranderende neutrale stromen zijn erg beperkt in het Standaard Model, tot op de hoogte dat deze niet waarneembaar zijn. Vele nieuwe fysica theorieën verhogen echter hun waarschijnlijkheid en maken de observatie mogelijk. Het onderzoek gepresenteerd in de thesis kijkt naar interacties resulterend in een eindtoestand met drie leptonen veroorzaakt door de productie van enkelvoudige top quarks door middel van een tZq interactiepunt, of door het verval via een tZq interactiepunt van een top quark in een top quark paar gebeurtenis. De additionele quark kan ofwel een charm quark, ofwel een up quark zijn. Er is geen significante afwijking gevonden ten op zichte van de achtergronden en bovenlimieten met 95% betrouwbaarheid zijn bepaald. De geobserveerde (verwachte) bovenlimieten met een 95% betrouwbaarheid op de vertakkingsfractie zijn: $\mathcal{B}(t \to uZ) < 2.4 \times 10^{-4}$ (1.5×10^{-4}) en $\mathcal{B}(t \to cZ) < 4.5 \times 10^{-4}$ (3.7×10^{-4}), waarbij verondersteld wordt dat er enkel één niet nulle smaakveranderende koppeling aanwezig is.

De vooruitgang ten opzichte van vroeger onderzoek komt door het gebruik van andere kinematische variabelen alsook een beter begrip van de achtergrond gevormd door niet prompte leptonen. Dit onderzoek heeft een hogere gevoeligheid ten op zichte van eerder onderzoek aan het CMS experiment en is vergelijkbaar met de gevoeligheid verkregen met het ATLAS experiment. Ondanks dat de limieten op de smaakveranderende interacties via een tZq vertex nieuwe fysica beginnen te naderen, blijven de vertakkingsfracties voorspeld door het Standaard Model buiten bereik.

Bibliography

[1] Sergio Cittolin: **Drawings of the elements of CMS detector, in the style of Leonardo da Vinci. Dessins des éléments de CMS détecteur, dans le style de Leonardo da Vinci**. Oct. 2014. URL: https://cds.cern.ch/record/1157741 (see p. ii).

[2] Michael Hoch and Maximilien Brice: **CMS experiment**. CMS Collection. Aug. 2008. URL: https://cds.cern.ch/record/1474902 (see p. ii).

[3] S. L. Glashow, J. Iliopoulos, and L. Maiani: **Weak Interactions with Lepton-Hadron Symmetry**. In: *Phys. Rev. D*, **2**: (7 1970). DOI: 10.1103/PhysRevD.2.1285 (see pp. vii–viii, 5).

[4] Luciano Maiani: **The GIM Mechanism: origin, predictions and recent uses**. 2013. arXiv: 1303.6154 [hep-ph] (see pp. vii, 5).

[5] J. J. Aubert et al.: **Experimental Observation of a Heavy Particle J**. In: *Phys. Rev. Lett.*, **33**: (1974). DOI: 10.1103/PhysRevLett.33.1404 (see p. vii).

[6] CDF COLLABORATION, D. Acosta et al.: **First evidence for $B_s^0 \to \phi\phi$ decay and measurements of branching ratio and A_{CP} for $B^+ \to \phi K^+$**. In: *Phys. Rev. Lett.*, **95**: (2005). DOI: 10.1103/PhysRevLett.95.031801. arXiv: hep-ex/0502044 [hep-ex] (see p. vii).

[7] LHCb and CMS COLLABORATION, Vardan Khachatryan et al.: **Observation of the rare $B_s^0 \to \mu^+\mu^-$ decay from the combined analysis of CMS and LHCb data**. In: *Nature*, **522**: (2015). DOI: 10.1038/nature14474. arXiv: 1411.4413 [hep-ex] (see p. vii).

[8] Bernat Capdevila, Andreas Crivellin, Sébastien Descotes-Genon, Joaquim Matias, and Javier Virto: **Patterns of New Physics in $b \to s\ell^+\ell^-$ transitions in the light of recent data**. 2017. arXiv: 1704.05340 [hep-ph] (see p. viii).

[9] Sebastien Descotes-Genon, Tobias Hurth, Joaquim Matias, and Javier Virto: **Optimizing the basis of $B \to K^*ll$ observables in the full kinematic range**. In: *JHEP*, **05**: (2013). DOI: 10.1007/JHEP05(2013)137. arXiv: 1303.5794 [hep-ph] (see p. viii).

[10] LHCb COLLABORATION, R Aaij et al.: **Measurement of Form-Factor-Independent Observables in the Decay $B^0 \to K^{*0}\mu^+\mu^-$**. In: *Phys. Rev. Lett.*, **111**: (2013). DOI: 10.1103/PhysRevLett.111.191801. arXiv: 1308.1707 [hep-ex] (see p. viii).

[11] Sebastien Descotes-Genon, Joaquim Matias, and Javier Virto: **Understanding the $B \rightarrow K^*\mu^+\mu^-$ Anomaly**. In: *Phys. Rev. D*, **88**: (2013). doi: 10.1103/PhysRevD.88.074002. arXiv: 1307.5683 [hep-ph] (see p. viii).

[12] Sebastien Descotes-Genon, Joaquim Matias, Marc Ramon, and Javier Virto: **Implications from clean observables for the binned analysis of $B->K^*\mu^+\mu^-$ at large recoil**. In: *JHEP*, **01**: (2013). doi: 10.1007/JHEP01(2013)048. arXiv: 1207.2753 [hep-ph] (see p. viii).

[13] LHCb COLLABORATION, Roel Aaij et al.: **Angular analysis of the $B^0 \rightarrow K^{*0}\mu^+\mu^-$ decay using 3 fb^{-1} of integrated luminosity**. In: *JHEP*, **02**: (2016). doi: 10.1007/JHEP02(2016)104. arXiv: 1512.04442 [hep-ex] (see p. viii).

[14] LHCb COLLABORATION, R Aaij et al.: **Differential branching fraction and angular analysis of the decay $B_s^0 \rightarrow \phi\mu^+\mu^-$.** In: *JHEP*, **07**: (2013). doi: 10.1007/JHEP07(2013)084. arXiv: 1305.2168 [hep-ex] (see p. viii).

[15] LHCb COLLABORATION, Roel Aaij et al.: **Angular analysis and differential branching fraction of the decay $B_s^0 \rightarrow \phi\mu^+\mu^-$.** In: *JHEP*, **09**: (2015). doi: 10.1007/JHEP09(2015)179. arXiv: 1506.08777 [hep-ex] (see p. viii).

[16] Belle COLLABORATION, A. Abdesselam et al.: **Angular analysis of $B^0 \rightarrow K^*(892)^0\ell^+\ell^-$.** 2016. arXiv: 1604.04042 [hep-ex] (see p. viii).

[17] Belle COLLABORATION, S. Wehle et al.: **Lepton-Flavor-Dependent Angular Analysis of $B \rightarrow K^*\ell^+\ell^-$.** In: *Phys. Rev. Lett.*, **118**:11 (2017). doi: 10.1103/PhysRevLett.118.111801. arXiv: 1612.05014 [hep-ex] (see p. viii).

[18] LHCb COLLABORATION, Roel Aaij et al.: **Test of lepton universality using $B^+ \rightarrow K^+\ell^+\ell^-$ decays**. In: *Phys. Rev. Lett.*, **113**: (2014). doi: 10.1103/PhysRevLett.113.151601. arXiv: 1406.6482 [hep-ex] (see p. viii).

[19] Sbastien Descotes-Genon, Lars Hofer, Joaquim Matias, and Javier Virto: **Global analysis of $b \rightarrow s\ell\ell$ anomalies**. In: *JHEP*, **06**: (2016). doi: 10.1007/JHEP06(2016)092. arXiv: 1510.04239 [hep-ph] (see p. viii).

[20] LHCb COLLABORATION, Roel Aaij et al.: **Measurements of the S-wave fraction in $B^0 \rightarrow K^+\pi^-\mu^+\mu^-$ decays and the $B^0 \rightarrow K^*(892)^0\mu^+\mu^-$ differential branching fraction**. In: *JHEP*, **11**: (2016). doi: 10.1007/JHEP11(2016)047,10.1007/JHEP04(2017)142,10.1007/JHEP11(2016)047,10.1007/JHEP04(2017)142. arXiv: 1606.04731 [hep-ex] (see p. viii).

[21] ATLAS COLLABORATION, **Angular analysis of $B_d^0 \rightarrow K^*\mu^+\mu^-$ decays in pp collisions at $\sqrt{s} = 8$ TeV with the ATLAS detector**. Tech. rep. *CERN*, 2017. url: https://cds.cern.ch/record/2258146 (see p. viii).

[22] CMS COLLABORATION, Albert M Sirunyan, Armen Tumasyan, et al.: **Measurement of angular parameters from the decay $B^0 \rightarrow K^{*0}\mu^+\mu^-$ in proton-proton collisions at $\sqrt{s} = 8$ TeV. Measurement of angular parameters from the decay $B^0 \rightarrow K^{*0}\mu^+\mu^-$ in proton-proton collisions at $\sqrt{s} = 8$ TeV.** Tech. rep. Submitted to Phys. Lett. B. *CERN*, 2017. url: https://cds.cern.ch/record/2287571 (see p. viii).

[23] J. A. Aguilar-Saavedra: **Top flavor-changing neutral interactions: Theoretical expectations and experimental detection**. In: *Acta Phys. Polon. B*, **35**: (2004). arXiv: hep-ph/0409342 [hep-ph] (see pp. viii, 7, 13, 16).

[24] CDF COLLABORATION, T. ET AL. AALTONEN: **Search for the Flavor-Changing Neutral-Current Decay $t \to Zq$ in $p\overline{p}$ Collisions at $\sqrt{s} = 1.96$ TeV**. In: *Phys. Rev. Lett.*, **101**: (19 2008). DOI: 10.1103/PhysRevLett.101.192002 (see pp. viii, 13).

[25] D0 COLLABORATION, VICTOR MUKHAMEDOVICH ABAZOV et al.: **Search for flavour changing neutral currents via quark-gluon couplings in single top quark production using 2.3 fb^{-1} of $p\bar{p}$ collisions**. In: *Phys. Lett. B*, **693**: (2010). DOI: 10.1016/j.physletb.2010.08.011. arXiv: 1006.3575 [hep-ex] (see pp. viii, 13).

[26] ATLAS COLLABORATION, GEORGES AAD et al.: **Search for flavour-changing neutral current top-quark decays to qZ in pp collision data collected with the ATLAS detector at $\sqrt{s} = 8$ TeV**. In: *Eur. Phys. J. C*, **76**:1 (2016). DOI: 10.1140/epjc/s10052-015-3851-5. arXiv: 1508.05796 [hep-ex] (see pp. viii, 13).

[27] ATLAS COLLABORATION, GEORGES AAD et al.: **Search for single top-quark production via flavour-changing neutral currents at 8 TeV with the ATLAS detector**. In: *Eur. Phys. J. C*, **76**:2 (2016). DOI: 10.1140/epjc/s10052-016-3876-4. arXiv: 1509.00294 [hep-ex] (see pp. viii, 13, 18).

[28] CMS COLLABORATION, ALBERT M SIRUNYAN et al.: **Search for associated production of a Z boson with a single top quark and for tZ flavour-changing interactions in pp collisions at $\sqrt{s} = 8$ TeV**. In: (2017). arXiv: 1702.01404 [hep-ex] (see pp. viii, 13, 17, 90–94, 135–141, 152).

[29] CMS COLLABORATION, SERGUEI CHATRCHYAN et al.: **Search for Flavor-Changing Neutral Currents in Top-Quark Decays $t \to Zq$ in pp Collisions at $\sqrt{s} =$ 8TeV**. In: *Phys. Rev. Lett.*, **112**:17 (2014). DOI: 10.1103/PhysRevLett.112.171802. arXiv: 1312.4194 [hep-ex] (see pp. viii, 13).

[30] CMS COLLABORATION, VARDAN KHACHATRYAN et al.: **Search for anomalous single top quark production in association with a photon in pp collisions at $\sqrt{s} = 8$ TeV**. In: *JHEP*, **04**: (2016). DOI: 10.1007/JHEP04(2016)035. arXiv: 1511.03951 [hep-ex] (see pp. viii, 13, 18).

[31] MICHAEL E PESKIN and DANIEL V SCHROEDER: **An introduction to quantum field theory; 1995 ed.** Boulder, CO: Westview, 1995. URL: https://cds.cern.ch/record/257493 (see pp. 1, 5–6, 16).

[32] C. P. BURGESS: **Introduction to Effective Field Theory**. In: *Ann. Rev. Nucl. Part. Sci.*, **57**: (2007). DOI: 10.1146/annurev.nucl.56.080805.140508. arXiv: hep-th/0701053 [hep-th] (see p. 1).

[33] NADIA ROBOTTI: **The discovery of the electron: I**. In: *European Journal of Physics*, **18**:3 (1997). URL: http://stacks.iop.org/0143-0807/18/i=3/a=002 (see p. 2).

[34] Super-Kamiokande COLLABORATION, Y. FUKUDA et al.: **Evidence for oscillation of atmospheric neutrinos**. In: *Phys. Rev. Lett.*, **81**: (1998). DOI: 10.1103/PhysRevLett.81.1562. arXiv: hep-ex/9807003 [hep-ex] (see pp. 2, 11).

[35] Double Chooz COLLABORATION, Y. ABE et al.: **Indication of Reactor $\overline{\nu}_e$ Disappearance in the Double Chooz Experiment**. In: *Phys. Rev. Lett.*, **108**: (13 2012). DOI: 10.1103/PhysRevLett.108.131801 (see pp. 2, 11).

[36] Particle Data Group, C. Patrignani et al.: **Review of Particle Physics**. In: *Chin. Phys. C*, **40**:10 (2016). doi: 10.1088/1674-1137/40/10/100001 (see pp. 2–3, 5–8, 10, 42–43).

[37] D0 COLLABORATION, S. Abachi et al.: **Observation of the top quark**. In: *Phys. Rev. Lett.*, **74**: (1995). doi: 10.1103/PhysRevLett.74.2632. arXiv: hep-ex/9503003 [hep-ex] (see p. 2).

[38] CDF COLLABORATION, F. Abe et al.: **Observation of top quark production in $\bar{p}p$ collisions**. In: *Phys. Rev. Lett.*, **74**: (1995). doi: 10.1103/PhysRevLett.74.2626. arXiv: hep-ex/9503002 [hep-ex] (see p. 2).

[39] ATLAS, CDF, CMS, and D0 COLLABORATION, **First combination of Tevatron and LHC measurements of the top-quark mass**. Tech. rep. 2014. arXiv: 1403.4427 [hep-ex]. url: https://cds.cern.ch/record/1669819 (see p. 2).

[40] CMS COLLABORATION, Serguei Chatrchyan et al.: **Observation of a new boson at a mass of 125 GeV with the CMS experiment at the LHC**. In: *Phys. Lett. B*, **716**: (2012). doi: 10.1016/j.physletb.2012.08.021. arXiv: 1207.7235 [hep-ex] (see pp. 2, 23).

[41] ATLAS COLLABORATION, Georges Aad et al.: **Observation of a new particle in the search for the Standard Model Higgs boson with the ATLAS detector at the LHC**. In: *Phys. Lett. B*, **716**: (2012). doi: 10.1016/j.physletb.2012.08.020. arXiv: 1207.7214 [hep-ex] (see pp. 2, 23).

[42] Nicola Cabibbo: **Unitary Symmetry and Leptonic Decays**. In: *Phys. Rev. Lett.*, **10**: (12 1963). doi: 10.1103/PhysRevLett.10.531 (see p. 5).

[43] B.J. Bjørken and S.L. Glashow: **Elementary particles and SU(4)**. In: *Physics Letters*, **11**:3 (1964). doi: 10.1016/0031-9163(64)90433-0 (see p. 5).

[44] Sébastien Descotes-Genon and Patrick Koppenburg: **The CKM Parameters**. In: *Ann. Rev. Nucl. Part. Sci.*, **67**: (2017). doi: 10.1146/annurev-nucl-101916-123109. arXiv: 1702.08834 [hep-ex] (see p. 6).

[45] D0 COLLABORATION, S. Abachi et al.: **Observation of the top quark**. In: *Phys. Rev. Lett.*, **74**: (1995). doi: 10.1103/PhysRevLett.74.2632. arXiv: hep-ex/9503003 [hep-ex] (see p. 7).

[46] CDF COLLABORATION, F. Abe et al.: **Observation of top quark production in $\bar{p}p$ collisions**. In: *Phys. Rev. Lett.*, **74**: (1995). doi: 10.1103/PhysRevLett.74.2626. arXiv: hep-ex/9503002 [hep-ex] (see p. 7).

[47] LHCTop working group: **LHCTopWG Summary plots**. 2017. url: https://twiki.cern.ch/twiki/bin/view/LHCPhysics/LHCTopWGSummaryPlots (see pp. 9, 21).

[48] CMS COLLABORATION, Andrea Giammanco and Jeannine Wagner-Kuhr: **Measurement of the t-channel single Top-quark production rates in pp collisions at 7 TeV**. 2011. url: http://cms.web.cern.ch/news/measurement-t-channel-single-top-quark-production-rates-pp-collisions-7-tev (see p. 9).

[49] LHCTop working group: **ATLAS-CMS recommended predictions for single top cross sections using the Hathor v2.1 program.** 2017. url: https://twiki.cern.ch/twiki/bin/view/LHCPhysics/SingleTopRefXsec#Predictions_at_7_8_13_and_14_TeV (see p. 10).

[50] CMS COLLABORATION: **Summaries of CMS cross section measurements**. 2017. URL: https://twiki.cern.ch/twiki/bin/view/CMSPublic/PhysicsResultsCombined (see pp. 11, 19–20, 50, 144, 150).

[51] YORIKIYO NAGASHIMA: **Beyond the standard model of elementary particle physics**. Weinheim, Germany: Wiley-VCH Verlag, 2014. URL: http://www-spires.fnal.gov/spires/find/books/www?cl=QC793.2.N34::2014 (see p. 10).

[52] Planck COLLABORATION, P. A. R. ADE et al.: **Planck 2015 results. XIII. Cosmological parameters**. In: *Astron. Astrophys.*, **594**: (2016). DOI: 10.1051/0004-6361/201525830. arXiv: 1502.01589 [astro-ph.CO] (see p. 11).

[53] P. J. E. PEEBLES and BHARAT RATRA: **The Cosmological constant and dark energy**. In: *Rev. Mod. Phys.*, **75**: (2003). DOI: 10.1103/RevModPhys.75.559. arXiv: astro-ph/0207347 [astro-ph] (see p. 11).

[54] A. D. SAKHAROV: **Violation of CP Invariance, c Asymmetry, and Baryon Asymmetry of the Universe**. In: *Pisma Zh. Eksp. Teor. Fiz.*, **5**: (1967). DOI: 10.1070/PU1991v034n05ABEH002497 (see p. 11).

[55] GUSTAVO BURDMAN: **New solutions to the hierarchy problem**. In: *Braz. J. Phys.*, **37**: (2007). DOI: 10.1590/S0103-97332007000400006. arXiv: hep-ph/0703194 [hep-ph] (see p. 12).

[56] ATLAS COLLABORATION, GEORGES AAD et al.: **Search for flavour-changing neutral current top quark decays $t \to Hq$ in pp collisions at $\sqrt{s} = 8$ TeV with the ATLAS detector**. In: *JHEP*, **12**: (2015). DOI: 10.1007/JHEP12(2015)061. arXiv: 1509.06047 [hep-ex] (see p. 13).

[57] ATLAS COLLABORATION, MORAD AABOUD et al.: **Search for top quark decays $t \to qH$, with $H \to \gamma\gamma$, in $\sqrt{s} = 13$ TeV pp collisions using the ATLAS detector**. In: *JHEP*, **10**:CERN-EP-2017-118 (2017). arXiv: 1707.01404 [hep-ex]. URL: https://cds.cern.ch/record/2273256 (see pp. 13, 18).

[58] ATLAS COLLABORATION, **Search for flavour-changing neutral current top quark decays $t \to qZ$ in proton-proton collisions at $\sqrt{s} = 13$ TeV with the ATLAS Detector**. Tech. rep. ATLAS-CONF-2017-070. *CERN*, 2017. URL: https://cds.cern.ch/record/2285808 (see pp. 13, 17–18, 135, 138, 143).

[59] CMS COLLABORATION, VARDAN KHACHATRYAN et al.: **Search for top quark decays via Higgs-boson-mediated flavor-changing neutral currents in pp collisions at $\sqrt{s} = 8$ TeV**. In: *JHEP*, **02**: (2017). DOI: 10.1007/JHEP02(2017)079. arXiv: 1610.04857 [hep-ex] (see p. 13).

[60] CMS COLLABORATION, **Search for the flavor-changing interactions of the top quark with the Higgs boson in $H \to b\bar{b}$ channel at $\sqrt{s} = 13$ TeV**. Tech. rep. CMS-PAS-TOP-17-003. 2017. URL: https://cds.cern.ch/record/2284743 (see pp. 13, 138).

[61] CÉLINE DEGRANDE: **Effective field theories in the Standard Model and beyond**. Thesis. Université Catholique de Louvain, 2011. URL: https://cp3.irmp.ucl.ac.be/upload/theses/phd/degrande.pdf (see p. 13).

[62] B. Grzadkowski, M. Iskrzynski, M. Misiak, and J. Rosiek: **Dimension-Six Terms in the Standard Model Lagrangian**. In: *JHEP*, **1010**: (2010). doi: 10.1007/JHEP10(2010)085. arXiv: 1008.4884 [hep-ph] (see pp. 14–15).

[63] J.A. Aguilar Savvedra, C. Degrande, G. Durieux, et al.: **Constraining the MSMEFT in the top sector at the LHC**. 2017. url: http://www.desy.de/~durieux/topbasis/basis_note.pdf (see p. 14).

[64] Andy Buckley, Christoph Englert, James Ferrando, et al.: **Constraining top quark effective theory in the LHC Run II era**. In: *JHEP*, **04**: (2016). doi: 10.1007/JHEP04(2016)015. arXiv: 1512.03360 [hep-ph] (see pp. 15, 152).

[65] M. Beneke et al.: **Top quark physics**. 2000. arXiv: hep-ph/0003033 [hep-ph]. url: http://weblib.cern.ch/abstract?CERN-TH-2000-100 (see p. 16).

[66] Jun Gao, Chong Sheng Li, and Hua Xing Zhu: **Top Quark Decay at Next-to-Next-to Leading Order in QCD**. In: *Phys. Rev. Lett.*, **110**:4 (2013). doi: 10.1103/PhysRevLett.110.042001. arXiv: 1210.2808 [hep-ph] (see pp. 17, 47).

[67] CMS COLLABORATION, Vardan Khachatryan et al.: **Search for anomalous Wtb couplings and flavour-changing neutral currents in t-channel single top quark production in pp collisions at $\sqrt{s} = 7$ and 8 TeV**. In: *JHEP*, **02**: (2017). doi: 10.1007/JHEP02(2017)028. arXiv: 1610.03545 [hep-ex] (see p. 18).

[68] Stephen Myers: **The LEP Collider, from design to approval and commissioning**. John Adams' Lecture. CERN, 1991. url: http://cds.cern.ch/record/226776 (see p. 23).

[69] Stephen Holmes, Ronald S Moore, and Vladimir Shiltsev: **Overview of the Tevatron collider complex: goals, operations and performance**. In: *JINST*, **6**:08 (2011). url: http://stacks.iop.org/1748-0221/6/i=08/a=T08001 (see p. 23).

[70] OPAL, DELPHI, LEP Working Group for Higgs boson searches, ALEPH, L3 COLLABORATION, R. Barate et al.: **Search for the standard model Higgs boson at LEP**. In: *Phys. Lett. B*, **565**: (2003). doi: 10.1016/S0370-2693(03)00614-2. arXiv: hep-ex/0306033 [hep-ex] (see p. 23).

[71] CDF and D0 COLLABORATION, Kenneth Herner: **Higgs Boson Studies at the Tevatron**. In: *Nucl. Part. Phys. Proc.*, **273-275**: (2016). doi: 10.1016/j.nuclphysbps.2015.09.131 (see p. 23).

[72] Abdelhak Djouadi: **The Anatomy of electro-weak symmetry breaking. I: The Higgs boson in the standard model**. In: *Phys. Rept.*, **457**: (2008). doi: 10.1016/j.physrep.2007.10.004. arXiv: hep-ph/0503172 [hep-ph] (see p. 23).

[73] Lyndon Evans and Philip Bryant: **LHC Machine**. In: *JINST*, **3**:08 (2008). url: http://stacks.iop.org/1748-0221/3/i=08/a=S08001 (see p. 23).

[74] LHC Study Group, Thomas Sven Pettersson and P Lefèvre: **The Large Hadron Collider: conceptual design**. Tech. rep. CERN-AC-95-05-LHC. 1995. url: https://cds.cern.ch/record/291782 (see p. 23).

[75] Jorg Wenninger and Ezio Todesco: **Large Hadron Collider momentum calibration and accuracy**. Tech. rep. CERN-ACC-2017-0007. *CERN*, 2017. url: https://cds.cern.ch/record/2254678 (see p. 24).

[76] Cinzia De Melis: **The CERN accelerator complex. Complexe des accélérateurs du CERN**. 2016. URL: https://cds.cern.ch/record/2197559 (see p. 24).

[77] CMS COLLABORATION, J. A. Murillo Quijada: **Recent upgrades and results from the CMS experiment**. In: *J. Phys. Conf. Ser.*, **912**:1 (2017). DOI: 10.1088/1742-6596/912/1/012005 (see p. 24).

[78] Antonella Del Rosso: **HL-LHC updates in Japan. Projet HL-LHC : une réunion fait le point au Japon**. In: BUL-NA-2014-272. 51/2014 (2014). URL: https://cds.cern.ch/record/1975962 (see p. 25).

[79] Oliver Sim Brüning, Paul Collier, P Lebrun, et al.: **LHC Design Report**. CERN Yellow Reports: Monographs. CERN, 2004. URL: https://cds.cern.ch/record/782076 (see p. 25).

[80] ATLAS COLLABORATION, G. Aad et al.: **The ATLAS Experiment at the CERN Large Hadron Collider**. In: *JINST*, **3**: (2008). DOI: 10.1088/1748-0221/3/08/S08003 (see p. 25).

[81] CMS COLLABORATION, S. Chatrchyan et al.: **The CMS Experiment at the CERN LHC**. In: *JINST*, **3**: (2008). DOI: 10.1088/1748-0221/3/08/S08004 (see pp. 25, 33–36).

[82] ALICE COLLABORATION, K. Aamodt et al.: **The ALICE experiment at the CERN LHC**. In: *JINST*, **3**: (2008). DOI: 10.1088/1748-0221/3/08/S08002 (see p. 25).

[83] LHCb COLLABORATION, A. Augusto Alves Jr. et al.: **The LHCb Detector at the LHC**. In: *JINST*, **3**: (2008). DOI: 10.1088/1748-0221/3/08/S08005 (see p. 25).

[84] M. Bongi et al.: **Astroparticle physics at LHC: The LHCf experiment ready for data taking**. In: *Nucl. Instrum. Meth. A*, **612**: (2010). DOI: 10.1016/j.nima.2009.08.039 (see p. 26).

[85] TOTEM COLLABORATION, G. Anelli et al.: **The TOTEM experiment at the CERN Large Hadron Collider**. In: *JINST*, **3**: (2008). DOI: 10.1088/1748-0221/3/08/S08007 (see p. 26).

[86] MoEDAL COLLABORATION, B. Acharya et al.: **The Physics Programme Of The MoEDAL Experiment At The LHC**. In: *Int. J. Mod. Phys. A*, **29**: (2014). DOI: 10.1142/S0217751X14300506. arXiv: 1405.7662 [hep-ph] (see p. 26).

[87] James Gillies: **Luminosity? Why don't we just say collision rate?** 2011. URL: http://cds.cern.ch/record/1997001 (see p. 26).

[88] Harriet Jarlett and Harriet Kim Jarlett: **LHC pushes limits of performance**. 2016. URL: http://cds.cern.ch/record/2212301 (see p. 26).

[89] CMS COLLABORATION: **Public Luminosity results**. 2017. URL: https://twiki.cern.ch/twiki/bin/view/CMSPublic/LumiPublicResults#Online_Luminosity_AN2 (see p. 27).

[90] **Technical proposal**. LHC Tech. Proposal. CERN, 1994. URL: https://cds.cern.ch/record/290969 (see p. 27).

[91] CMS COLLABORATION, G L Bayatian, S Chatrchyan, G Hmayakyan, et al.: **CMS Physics: Technical Design Report Volume 1: Detector Performance and Software**. Technical Design Report CMS. CERN, 2006. URL: https://cds.cern.ch/record/922757 (see pp. 27, 32, 57).

[92] CMS COLLABORATION: **Detector Drawings**. 2012. URL: https://cds.cern.ch/record/1433717 (see p. 28).

[93] CMS COLLABORATION, S CHATRCHYAN, V KHACHATRYAN, A M SIRUNYAN, et al.: **Performance of the CMS Drift Tube Chambers with Cosmic Rays**. In: *JINST*, **5**:CMS-CFT-09-012 (2009). arXiv: 0911.4855. URL: http://cds.cern.ch/record/1223944 (see pp. 30–31).

[94] CMS COLLABORATION: **News from the CMS experimental site: 22 November 2013.** URL: http://cms.web.cern.ch/news/news-point-5-22-november-2013 (see p. 31).

[95] INSTITUTE OF RESEARCH INTO THE FUNDAMENTAL LAWS THE UNIVERSE: **The CMS detector superconducting solenoid**. 2006. URL: http://irfu.cea.fr/en/Phocea/Vie_des_labos/Ast/ast_visu.php?id_ast=839 (see p. 33).

[96] FERGUS WILSON: **Experimental Particle Physics**. 2012. URL: http://slideplayer.com/slide/794631/ (see p. 33).

[97] LUCAS TAYLOR: **Experimental Particle Physics**. 2011. URL: http://cms.web.cern.ch/news/electromagnetic-calorimeter (see p. 34).

[98] **Proceedings, 34th International Conference on High Energy Physics**. 2008. URL: http://www.slac.stanford.edu/econf/C080730 (see p. 34).

[99] L. BRIANZA: **Precision crystal calorimetry in LHC Run II with the CMS ECAL**. In: *JINST*, **12**:01 (2017). URL: http://stacks.iop.org/1748-0221/12/i=01/a=C01069 (see pp. 35, 38).

[100] CMS COLLABORATION, SERGUEI CHATRCHYAN, KHACHATRYAN, et al.: **Description and performance of track and primary-vertex reconstruction with the CMS tracker**. In: *JINST*, **9**:CERN-PH-EP-2014-070. CMS-TRK-11-001 (2014). arXiv: 1405.6569. URL: http://cds.cern.ch/record/1704291 (see pp. 35, 58).

[101] CMS COLLABORATION: **A beautiful barrel for CMS**. 2014. URL: http://cds.cern.ch/record/1998635 (see p. 36).

[102] CHRISTINE SUTTON: **Chronicles of CMS: the saga of LS1**. 2015. URL: http://cds.cern.ch/record/2024986 (see p. 36).

[103] CMS COLLABORATION, VARDAN KHACHATRYAN et al.: **The CMS trigger system**. In: *JINST*, **12**:01 (2017). DOI: 10.1088/1748-0221/12/01/P01020. arXiv: 1609.02366 [physics.ins-det] (see p. 37).

[104] CORINNE PRALAVORIO and CORINNE PRALAVORIO: **Major work to ready the LHC experiments for Run 2**. 2015. URL: http://cds.cern.ch/record/2024977 (see p. 38).

[105] CMS COLLABORATION: **Cool running for CMS tracker**. 2014. URL: http://cds.cern.ch/record/1998606 (see p. 38).

[106] CMS COLLABORATION, SERGUEI CHATRCHYAN et al.: **Energy Calibration and Resolution of the CMS Electromagnetic Calorimeter in pp Collisions at $\sqrt{s} = 7$ TeV**. In: *JINST*, **8**: (2013). DOI: 10.1088/1748-0221/8/09/P09009. arXiv: 1306.2016 [hep-ex] (see p. 38).

[107] CMS COLLABORATION, LUIGI GUIDUCCI: **CMS muon system towards LHC Run 2 and beyond**. Tech. rep. CMS-CR-2014-333. *CERN*, 2014. URL: https://cds.cern.ch/record/1966038 (see p. 38).

[108] CMS COLLABORATION, CARLO BATTILANA: **The CMS muon system status and upgrades for LHC run-2 and performance of muon reconstruction with 13 TeV data**. Tech. rep. CMS-CR-2016-437. *CERN*, 2016. URL: http://cds.cern.ch/record/2239185 (see p. 38).

[109] L. CADAMURO: **The CMS Level-1 trigger system for LHC Run II**. In: *JINST*, **12**:03 (2017). URL: http://stacks.iop.org/1748-0221/12/i=03/a=C03021 (see p. 39).

[110] CMS COLLABORATION, DAVID AARON MATZNER DOMINGUEZ, D. ABBANEO, K. ARNDT, et al.: **CMS Technical Design Report for the Pixel Detector Upgrade**. 2012 (see p. 39).

[111] CMS COLLABORATION, HANNO CHRISTOPHER PERREY: **Plans and Status of the Phase I Upgrade of the CMS Pixel Tracker**. Tech. rep. CMS-CR-2014-005. *CERN*, 2014. URL: http://cds.cern.ch/record/1644757 (see p. 39).

[112] CMC COLLABORATION, CLAUDIO GRANDI, DAVID STICKLAND, LUCAS TAYLOR, ACHILLE PETRILLI, and ALAIN HERVÉ: **CMS Computing Model: The "CMS Computing Model RTAG"**. Tech. rep. CMS-NOTE-2004-031. CERN-LHCC-2004-035. LHCC-G-083. 2004. URL: http://cds.cern.ch/record/814248 (see p. 39).

[113] CHRISTOPH ECK, J KNOBLOCH, LESLIE ROBERTSON, et al.: **LHC computing Grid: Technical Design Report. Version 1.06 (20 Jun 2005)**. Technical Design Report LCG. CERN, 2005. URL: https://cds.cern.ch/record/840543 (see p. 39).

[114] WORLDWIDE LHC COMPUTING GRID: **WorldWide LHC Computing Grid**. 2017. URL: http://wlcg-public.web.cern.ch (see p. 40).

[115] JOHN C. COLLINS, DAVISON E. SOPER, and GEORGE F. STERMAN: **Factorization of Hard Processes in QCD**. In: *Adv. Ser. Direct. High Energy Phys.*, **5**: (1989). DOI: 10.1142/9789814503266_0001. arXiv: hep-ph/0409313 [hep-ph] (see p. 41).

[116] RINGAILE PLACAKYTE: **Parton Distribution Functions**. In: *Proceedings, 31st International Conference on Physics in collisions (PIC 2011): Vancouver, Canada, August 28-September 1, 2011*. 2011. arXiv: 1111.5452 [hep-ph] (see p. 41).

[117] RICHARD D. BALL, VALERIO BERTONE, STEFANO CARRAZZA, et al.: **Parton distributions for the LHC run II**. In: *JHEP*, **2015**:4 (2015). DOI: 10.1007/JHEP04(2015)040 (see p. 41).

[118] JON BUTTERWORTH et al.: **PDF4LHC recommendations for LHC Run II**. In: *J. Phys. G*, **43**: (2016). DOI: 10.1088/0954-3899/43/2/023001. arXiv: 1510.03865 [hep-ph] (see pp. 41–42).

[119] H. ABRAMOWICZ and A. CALDWELL: **HERA collider physics**. In: *Rev. Mod. Phys.*, **71**: (1999). DOI: 10.1103/RevModPhys.71.1275. arXiv: hep-ex/9903037 [hep-ex] (see p. 42).

[120] STEPHEN HOLMES, RONALD S. MOORE, and VLADIMIR SHILTSEV: **Overview of the Tevatron Collider Complex: Goals, Operations and Performance**. In: *JINST*, **6**: (2011). DOI: 10.1088/1748-0221/6/08/T08001. arXiv: 1106.0909 [physics.acc-ph] (see p. 42).

[121] Juan Rojo et al.: **The PDF4LHC report on PDFs and LHC data: Results from Run I and preparation for Run II**. In: *J. Phys. G*, **42**: (2015). doi: 10.1088/0954-3899/42/10/103103. arXiv: 1507.00556 [hep-ph] (see p. 42).

[122] Alan D. Martin: **Proton structure, Partons, QCD, DGLAP and beyond**. In: *Acta Phys. Polon. B*, **39**: (2008). arXiv: 0802.0161 [hep-ph] (see p. 42).

[123] J. Pumplin, D. Stump, R. Brock, et al.: **Uncertainties of predictions from parton distribution functions. 2. The Hessian method**. In: *Phys. Rev. D*, **65**: (2001). doi: 10.1103/PhysRevD.65.014013. arXiv: hep-ph/0101032 [hep-ph] (see p. 42).

[124] Franz Mandl and Graham G Shaw: **Quantum field theory; 2nd ed.** New York, NY: Wiley, 2010. url: https://cds.cern.ch/record/1236742 (see p. 44).

[125] S Banerjee: **CMS Simulation Software**. In: *Journal of Physics: Conference Series*, **396**:2 (2012). url: http://stacks.iop.org/1742-6596/396/i=2/a=022003 (see p. 44).

[126] M Hildreth, V N Ivanchenko, D J Lange, and M J Kortelainen: **CMS Full Simulation for Run-2**. In: *Journal of Physics: Conference Series*, **664**:7 (2015). url: http://stacks.iop.org/1742-6596/664/i=7/a=072022 (see p. 44).

[127] S. Agostinelli, J. Allison, K. Amako, et al.: **Geant4-a simulation toolkit**. In: *Nuclear Instruments and Methods in Physics Research Section A: Accelerators, Spectrometers, Detectors and Associated Equipment*, **506**:3 (2003). doi: https://doi.org/10.1016/S0168-9002(03)01368-8 (see pp. 44, 46).

[128] Michael H. Seymour and Marilyn Marx: **Monte Carlo Event Generators**. In: *Proceedings, 69th Scottish Universities Summer School in Physics : LHC Phenomenology (SUSSP69): St.Andrews, Scotland, August 19-September 1, 2012*. 2013. doi: 10.1007/978-3-319-05362-2_8. arXiv: 1304.6677 [hep-ph] (see p. 44).

[129] Torbjorn Sjöstrand: **Monte Carlo Tools**. In: *Proceedings, 65th Scottish Universities Summer School in Physics: LHC Physics (SUSSP65): St. Andrews, UK, August 16-29, 2009*. 2009. doi: 10.1201/b11865-14. arXiv: 0911.5286 [hep-ph] (see p. 44).

[130] Stefan Höche: **Introduction to parton-shower event generators**. In: *Proceedings, Theoretical Advanced Study Institute in Elementary Particle Physics: Journeys Through the Precision Frontier: Amplitudes for Colliders (TASI 2014): Boulder, Colorado, June 2-27, 2014*. 2015. doi: 10.1142/9789814678766_0005. arXiv: 1411.4085 [hep-ph] (see pp. 44–45).

[131] Adam Alloul, Neil D. Christensen, Céline Degrande, Claude Duhr, and Benjamin Fuks: **FeynRules 2.0 - A complete toolbox for tree-level phenomenology**. In: *Comput. Phys. Commun.*, **185**: (2014). doi: 10.1016/j.cpc.2014.04.012. arXiv: 1310.1921 [hep-ph] (see p. 44).

[132] Celine Degrande, Claude Duhr, Benjamin Fuks, et al.: **UFO - The Universal FeynRules Output**. In: *Comput. Phys. Commun.*, **183**: (2012). doi: 10.1016/j.cpc.2012.01.022. arXiv: 1108.2040 [hep-ph] (see p. 44).

[133] Johan Alwall, Michel Herquet, Fabio Maltoni, Olivier Mattelaer, and Tim Stelzer: **MadGraph 5 : Going Beyond**. In: *JHEP*, **06**: (2011). doi: 10.1007/JHEP06(2011)128. arXiv: 1106.0522 [hep-ph] (see p. 45).

[134] Michelangelo L. Mangano, Mauro Moretti, Fulvio Piccinini, and Michele Treccani: **Matching matrix elements and shower evolution for top-quark production in hadronic collisions**. In: *JHEP*, **01**: (2007). doi: 10.1088/1126-6708/2007/01/013. arXiv: hep-ph/0611129 [hep-ph] (see p. 45).

[135] Torbjorn Sjostrand, Stephen Mrenna, and Peter Z. Skands: **PYTHIA 6.4 Physics and Manual**. In: *JHEP*, **0605**: (2006). doi: 10.1088/1126-6708/2006/05/026. arXiv: hep-ph/0603175 [hep-ph] (see pp. 45–46).

[136] Torbjorn Sjostrand, Stefan Ask, Jesper R. Christiansen, et al.: **An Introduction to PYTHIA 8.2**. In: *Comput. Phys. Commun.*, **191**: (2015). doi: 10.1016/j.cpc.2015.01.024. arXiv: 1410.3012 [hep-ph] (see pp. 45–46, 49).

[137] Johan Alwall et al.: **Comparative study of various algorithms for the merging of parton showers and matrix elements in hadronic collisions**. In: *Eur. Phys. J. C*, **53**: (2008). doi: 10.1140/epjc/s10052-007-0490-5. arXiv: 0706.2569 [hep-ph] (see p. 45).

[138] J. Alwall, R. Frederix, S. Frixione, et al.: **The automated computation of tree-level and next-to-leading order differential cross sections, and their matching to parton shower simulations**. In: *JHEP*, **07**: (2014). doi: 10.1007/JHEP07(2014)079. arXiv: 1405.0301 [hep-ph] (see p. 45).

[139] Stefano Frixione and Bryan R. Webber: **Matching NLO QCD computations and parton shower simulations**. In: *JHEP*, **06**: (2002). doi: 10.1088/1126-6708/2002/06/029. arXiv: hep-ph/0204244 [hep-ph] (see p. 45).

[140] Simone Alioli, Paolo Nason, Carlo Oleari, and Emanuele Re: **A general framework for implementing NLO calculations in shower Monte Carlo programs: the POWHEG BOX**. In: *JHEP*, **2010**:6 (2010). doi: 10.1007/JHEP06(2010)043 (see p. 45).

[141] Simone Alioli, Paolo Nason, Carlo Oleari, and Emanuele Re: **NLO single-top production matched with shower in POWHEG: s - and t -channel contributions**. In: *JHEP*, **2009**:09 (2009). url: http://stacks.iop.org/1126-6708/2009/i=09/a=111 (see p. 45).

[142] Stefano Frixione, Paolo Nason, and Carlo Oleari: **Matching NLO QCD computations with parton shower simulations: the POWHEG method**. In: *JHEP*, **2007**:11 (2007). url: http://stacks.iop.org/1126-6708/2007/i=11/a=070 (see p. 45).

[143] Simone Alioli, Paolo Nason, Carlo Oleari, and Emanuele Re: **A general framework for implementing NLO calculations in shower Monte Carlo programs: the POWHEG BOX**. In: *JHEP*, **06**: (2010). doi: 10.1007/JHEP06(2010)043. arXiv: 1002.2581 [hep-ph] (see p. 45).

[144] Stefano Frixione, Paolo Nason, and Carlo Oleari: **Matching NLO QCD computations with Parton Shower simulations: the POWHEG method**. In: *JHEP*, **11**: (2007). doi: 10.1088/1126-6708/2007/11/070. arXiv: 0709.2092 [hep-ph] (see p. 45).

[145] Paolo Nason: **A New method for combining NLO QCD with shower Monte Carlo algorithms**. In: *JHEP*, **11**: (2004). doi: 10.1088/1126-6708/2004/11/040. arXiv: hep-ph/0409146 [hep-ph] (see p. 45).

[146] Andrei V. Gritsan, Raoul Röntsch, Markus Schulze, and Meng Xiao: **Constraining anomalous Higgs boson couplings to the heavy flavor fermions using matrix element techniques**. In: *Phys. Rev. D*, **94**:5 (2016). doi: 10.1103/PhysRevD.94.055023. arXiv: 1606.03107 [hep-ph] (see p. 45).

[147] Ian Anderson et al.: **Constraining anomalous HVV interactions at proton and lepton colliders**. In: *Phys. Rev. D*, **89**:3 (2014). doi: 10.1103/PhysRevD.89.035007. arXiv: 1309.4819 [hep-ph] (see p. 45).

[148] Sara Bolognesi, Yanyan Gao, Andrei V. Gritsan, et al.: **On the spin and parity of a single-produced resonance at the LHC**. In: *Phys. Rev. D*, **86**: (2012). doi: 10.1103/PhysRevD.86.095031. arXiv: 1208.4018 [hep-ph] (see p. 45).

[149] Yanyan Gao, Andrei V. Gritsan, Zijin Guo, et al.: **Spin determination of single-produced resonances at hadron colliders**. In: *Phys. Rev. D*, **81**: (2010). doi: 10.1103/PhysRevD.81.075022. arXiv: 1001.3396 [hep-ph] (see p. 45).

[150] Pierre Artoisenet, Rikkert Frederix, Olivier Mattelaer, and Robbert Rietkerk: **Automatic spin-entangled decays of heavy resonances in Monte Carlo simulations**. In: *JHEP*, **03**: (2013). doi: 10.1007/JHEP03(2013)015. arXiv: 1212.3460 [hep-ph] (see p. 46).

[151] V. Khachatryan and etal: **Event generator tunes obtained from underlying event and multiparton scattering measurements**. In: *Eur. Phys. J. C*, **76**:3 (2016). doi: 10.1140/epjc/s10052-016-3988-x (see p. 46).

[152] Richard D. Ball et al.: **Parton distributions with LHC data**. In: *Nucl. Phys. B*, **867**: (2013). doi: 10.1016/j.nuclphysb.2012.10.003. arXiv: 1207.1303 [hep-ph] (see p. 46).

[153] Yue Zhang, Bo Hua Li, Chong Sheng Li, Jun Gao, and Hua Xing Zhu: **Next-to-leading order QCD corrections to the top quark associated with γ production via model-independent flavor-changing neutral-current couplings at hadron colliders**. In: *Phys. Rev. D*, **83**: (2011). doi: 10.1103/PhysRevD.83.094003. arXiv: 1101.5346 [hep-ph] (see p. 47).

[154] **CMS Monte Carlo Generator Group**. url: https://twiki.cern.ch/twiki/bin/view/CMS/GeneratorMain (see pp. 48–49).

[155] T. Gehrmann, M. Grazzini, S. Kallweit, et al.: **W^+W^- Production at Hadron Colliders in Next to Next to Leading Order QCD**. In: *Phys. Rev. Lett.*, **113**:21 (2014). doi: 10.1103/PhysRevLett.113.212001. arXiv: 1408.5243 [hep-ph] (see p. 49).

[156] A. Hoecker, P. Speckmayer, J. Stelzer, et al.: **TMVA - Toolkit for Multivariate Data Analysis**. 2007. eprint: physics/0703039 (see p. 50).

[157] R. Brun and F. Rademakers: **ROOT: An object oriented data analysis framework**. In: *Nucl. Instrum. Meth. A*, **389**: (1997). doi: 10.1016/S0168-9002(97)00048-X (see p. 50).

[158] A. Mayr, H. Binder, O. Gefeller, and M. Schmid: **The Evolution of Boosting Algorithms - From Machine Learning to Statistical Modelling**. In: *ArXiv e-prints*, (2014). doi: 10.3414/ME13-01-0122. arXiv: 1403.1452 [stat.ME] (see p. 51).

[159] Olaf Behnke, Kevin Kroninger, Gregory Schott, and Thomas Schorner-Sadenius: **Data Analysis in High Energy Physics: A Practical Guide to Statistical Methods**. 1st. Wiley-VCH, 2013 (see p. 51).

[160] Lieselotte Moreels: **Example of ROC curves**. Private discussions. 2017 (see p. 51).

[161] CMS COLLABORATION, Serguei Chatrchyan et al.: **Combined results of searches for the standard model Higgs boson in pp collisions at $\sqrt{s} = 7$ TeV**. In: *Phys. Lett. B*, **710**: (2012). DOI: 10.1016/j.physletb.2012.02.064. arXiv: 1202.1488 [hep-ex] (see p. 52).

[162] Glen Cowan, Kyle Cranmer, Eilam Gross, and Ofer Vitells: **Asymptotic formulae for likelihood-based tests of new physics**. In: *Eur. Phys. J. C*, **71**: (2011). DOI: 10.1140/epjc/s10052-011-1554-0,10.1140/epjc/s10052-013-2501-z. arXiv: 1007.1727 [physics.data-an] (see pp. 52–53, 114).

[163] CMS COLLABORATION, **Observation of a new boson with a mass near 125 GeV**. Tech. rep. CMS-PAS-HIG-12-020. *CERN*, 2012. URL: https://cds.cern.ch/record/1460438 (see p. 52).

[164] The ATLAS COLLABORATION, The CMS COLLABORATION, The LHC Higgs Combination Group, **Procedure for the LHC Higgs boson search combination in Summer 2011**. Tech. rep. CMS-NOTE-2011-005. ATL-PHYS-PUB-2011-11. *CERN*, 2011. URL: http://cds.cern.ch/record/1379837 (see p. 52).

[165] Higgs working group: **Documentation of the RooStats based statistics tools for Higgs PAG**. 2017. URL: https://twiki.cern.ch/twiki/bin/viewauth/CMS/SWGuideHiggsAnalysisCombinedLimit (see p. 52).

[166] Lorenzo Moneta, Kevin Belasco, Kyle S. Cranmer, et al.: **The RooStats Project**. In: *PoS*, **ACAT2010**: (2010). arXiv: 1009.1003 [physics.data-an] (see p. 52).

[167] Thomas Junk: **Confidence level computation for combining searches with small statistics**. In: *Nuclear Instruments and Methods in Physics Research Section A: Accelerators, Spectrometers, Detectors and Associated Equipment*, **434**:2 (1999). DOI: 10.1016/S0168-9002(99)00498-2 (see p. 52).

[168] A L Read: **Presentation of search results: the CL s technique**. In: *Journal of Physics G: Nuclear and Particle Physics*, **28**:10 (2002). URL: http://stacks.iop.org/0954-3899/28/i=10/a=313 (see p. 52).

[169] CMS COLLABORATION, A. M. Sirunyan et al.: **Particle-flow reconstruction and global event description with the CMS detector**. In: *JINST*, **12**: (2017). DOI: 10.1088/1748-0221/12/10/P10003. arXiv: 1706.04965 [physics.ins-det] (see pp. 56–60, 62).

[170] R. Frühwirth: **Application of Kalman filtering to track and vertex fitting**. In: *Nuclear Instruments and Methods in Physics Research Section A: Accelerators, Spectrometers, Detectors and Associated Equipment*, **262**:2 (1987). DOI: http://dx.doi.org/10.1016/0168-9002(87)90887-4 (see p. 57).

[171] Pierre Billoir: **Progressive track recognition with a Kalman like fitting procedure**. In: *Comput. Phys. Commun.*, **57**: (1989). DOI: 10.1016/0010-4655(89)90249-X (see p. 57).

[172] CMS COLLABORATION, SERGUEI CHATRCHYAN et al.: **Performance of CMS muon reconstruction in pp collision events at $\sqrt{s} = 7$ TeV**. In: *JINST*, **7**: (2012). DOI: 10.1088/1748-0221/7/10/P10002. arXiv: 1206.4071 [physics.ins-det] (see p. 57).

[173] W ADAM, R FRÜHWIRTH, A STRANDLIE, and T TODOROV: **Reconstruction of electrons with the Gaussian-sum filter in the CMS tracker at the LHC**. In: *Journal of Physics G: Nuclear and Particle Physics*, **31**:9 (2005). URL: http://stacks.iop.org/0954-3899/31/i=9/a=N01 (see p. 57).

[174] **Performance of electron reconstruction and selection with the CMS detector in proton-proton collisions at $\sqrt{s} = 8$TeV**. In: *JINST*, **10**:06 (2015). URL: http://stacks.iop.org/1748-0221/10/i=06/a=P06005 (see p. 58).

[175] CMS COLLABORATION: **Electron and photon performance in CMS with the full 2016 data sample.** 2017. URL: http://cds.cern.ch/record/2255497 (see pp. 58, 62–63).

[176] K. ROSE: **Deterministic annealing for clustering, compression, classification, regression, and related optimization problems**. In: *Proceedings of the IEEE*, **86**:11 (1998). DOI: 10.1109/5.726788 (see p. 58).

[177] CMS COLLABORATION, WOLFGANG WALTENBERGER: **Adaptive Vertex Reconstruction**. Tech. rep. CMS-NOTE-2008-033. *CERN*, 2008. URL: https://cds.cern.ch/record/1166320 (see p. 58).

[178] CMS COLLABORATION, ANDREAS KORNMAYER: **The CMS Pixel Luminosity Telescope**. Tech. rep. CMS-CR-2015-121. *CERN*, 2015. URL: https://cds.cern.ch/record/2039978 (see p. 59).

[179] CMS COLLABORATION, **CMS Luminosity Measurements for the 2016 Data Taking Period**. Tech. rep. CMS-PAS-LUM-17-001. *CERN*, 2017. URL: http://cds.cern.ch/record/2257069 (see p. 59).

[180] CMS COLLABORATION, **Measurement of the inelastic proton-proton cross section at $\sqrt{s} = 13$ TeV**. Tech. rep. CMS-PAS-FSQ-15-005. *CERN*, 2016. URL: https://cds.cern.ch/record/2145896 (see p. 60).

[181] CMS COLLABORATION: **Muon Identification and Isolation efficiency on full 2016 dataset**. 2017. URL: http://cds.cern.ch/record/2257968 (see pp. 60–61).

[182] CMS COLLABORATION: **Effective areas used for Summer16 samples**. 2017. URL: https://indico.cern.ch/event/482673/contributions/2187022/%20attachments/1282446/1905912/talk_electron_ID_spring16.pdf (see p. 63).

[183] MATTEO CACCIARI, GAVIN P. SALAM, and GREGORY SOYEZ: **The Anti-k(t) jet clustering algorithm**. In: *JHEP*, **04**: (2008). DOI: 10.1088/1126-6708/2008/04/063. arXiv: 0802.1189 [hep-ph] (see p. 64).

[184] CMS COLLABORATION, **Jet algorithms performance in 13** TeV **data**. Tech. rep. CMS-PAS-JME-16-003. *CERN*, 2017. URL: http://cds.cern.ch/record/2256875 (see p. 64).

[185] CMS COLLABORATION: **Jet energy scale and resolution performances with 13** TeV **data**. 2016. URL: http://cds.cern.ch/record/2160347 (see pp. 65–66).

[186] V. Khachatryan et al.: **Jet energy scale and resolution in the CMS experiment in pp collisions at 8** TeV. In: *JINST*, **12**:02 (2017). URL: http://stacks.iop.org/1748-0221/12/i=02/a=P02014 (see p. 65).

[187] CMS COLLABORATION: **Identification of b-quark jets with the CMS experiment**. In: *JINST*, **8**:04 (2013). URL: http://stacks.iop.org/1748-0221/8/i=04/a=P04013 (see p. 66).

[188] CMS COLLABORATION, Albert M Sirunyan et al.: **Identification of heavy-flavour jets with the CMS detector in pp collisions at 13 TeV**. Submitted to JINST. 2017 (see pp. 66–68).

[189] Nazar Bartosik: **Diagram showing the common principle of identification of jets initiated by b-hadron decays**. 2016. URL: http://bartosik.pp.ua/hep_sketches/btagging (see p. 67).

[190] CMS COLLABORATION, **Identification of c quark jets at the CMS Experiment in the LHC Run 2**. Tech. rep. CMS-PAS-BTV-16-001. *CERN*, 2017. URL: https://cds.cern.ch/record/2205149 (see pp. 68, 144).

[191] CMS COLLABORATION, **Performance of missing energy reconstruction in 13** TeV **pp collision data using the CMS detector**. Tech. rep. CMS-PAS-JME-16-004. *CERN*, 2016. URL: http://cds.cern.ch/record/2205284 (see pp. 68, 74–75).

[192] Jordan Damgov: **Missing Et Optional Filters Run 2**. 2017. URL: https://twiki.cern.ch/twiki/bin/viewauth/CMS/MissingETOptionalFiltersRun2 (see p. 74).

[193] CMS COLLABORATION, **Evidence for the standard model production of a Z boson with a single top quark in pp collisions at $\sqrt{s} = 13$ TeV**. Tech. rep. CMS-PAS-TOP-16-020. *CERN*, 2017. URL: http://cds.cern.ch/record/2284830 (see pp. 76, 84, 96, 114).

[194] CMS COLLABORATION: **EGM corrections for Moriond17**. 2017. URL: https://indico.cern.ch/event/613162/contributions/2472046/attachments/1410308/2156822/EGMSmearerAndRegression_PPD_022017.pdf (see p. 79).

[195] Arie Bodek, Jiyeon Han, and Willis Sakumoto: **Misalignment and Muon Scale corrections**. 2012. URL: https://www-cdf.fnal.gov/~jyhan/cms_momscl/rochcor_cmsnote.pdf (see p. 79).

[196] CMS COLLABORATION: **Rochestor Correction**. 2017. URL: https://twiki.cern.ch/twiki/bin/viewauth/CMS/RochcorMuon (see p. 79).

[197] CMS COLLABORATION, V. Khachatryan, Albert M Sirunyan, et al.: **Measurement of the WZ production cross section in pp collisions at $\sqrt{s} = 7$ and 8 TeV and search for anomalous triple gauge couplings at $\sqrt{s} = 8$ TeV**. In: *Eur. Phys. J. C*, **77**:CMS-SMP-14-014 (2016). DOI: 10.1140/epjc/s10052-017-4730-z. URL: https://cds.cern.ch/record/2216557 (see p. 96).

[198] CMS COLLABORATION, Vardan Khachatryan, Albert M Sirunyan, et al.: **Measurement of top quark-antiquark pair production in association with a W or Z boson in pp collisions at $\sqrt{s} = 8$ TeV**. In: *Eur. Phys. J. C*, **74**:CMS-TOP-12-036. CERN-PH-EP-2014-136. CMS-TOP-12-036 (2014). URL: https://cds.cern.ch/record/1712680 (see p. 97).

[199] ATLAS COLLABORATION, GEORGES AAD, BRAD ABBOTT, et al.: **Measurements of four-lepton production in pp collisions at $\sqrt{s}$ =8 TeV with the ATLAS detector**. In: *Phys. Lett. B*, **753**: (2015). arXiv: 1509.07844. URL: https://cds.cern.ch/record/2055247 (see p. 97).

[200] NNPDF COLLABORATION, RICHARD D. BALL et al.: **Parton distributions from high-precision collider data**. In: *Eur. Phys. J. C*, **77**: (2017). DOI: 10.1140/epjc/s10052-017-5199-5. arXiv: 1706.00428 [hep-ph] (see p. 114).

[201] Top Quark Working Group, K. AGASHE et al.: **Working Group Report: Top Quark**. In: 2013. arXiv: 1311.2028 [hep-ph] (see p. 150).

[202] M. L. MANGANO et al.: **Physics at a 100 TeV pp collider: Standard Model processes**. In: *CERN Yellow Report*, 3 (2017). DOI: 10.23731/CYRM-2017-003.1. arXiv: 1607.01831 [hep-ph] (see p. 150).

[203] HAMZEH KHANPOUR, SARA KHATIBI, MORTEZA KHATIRI YANEHSARI, and MOJTABA MOHAMMADI NAJAFABADI: **Single top quark production as a probe of anomalous $tq\gamma$ and tqZ couplings at the FCC-ee**. In: *Phys. Lett. B*, **775**: (2017). DOI: 10.1016/j.physletb.2017.10.047. arXiv: 1408.2090 [hep-ph] (see p. 150).

[204] WEI LIU, HAO SUN, XIAOJUAN WANG, and XUAN LUO: **Probing the anomalous FCNC top-Higgs Yukawa couplings at the Large Hadron Electron Collider**. In: *Phys. Rev. D*, **92**:7 (2015). DOI: 10.1103/PhysRevD.92.074015. arXiv: 1507.03264 [hep-ph] (see p. 150).

[205] CEN ZHANG: **Top couplings and new physics: theoretical overview and developments**. 2014. arXiv: 1411.7685 [hep-ph] (see p. 151).

[206] GAUTHIER DURIEUX, FABIO MALTONI, and CEN ZHANG: **Global approach to top-quark flavor-changing interactions**. In: *Phys. Rev. D*, **91**:7 (2015). DOI: 10.1103/PhysRevD.91.074017. arXiv: 1412.7166 [hep-ph] (see p. 152).

[207] JEAN-LAURENT AGRAM, JEREMY ANDREA, ERIC CONTE, et al.: **Probing top anomalous couplings at the LHC with trilepton signatures in the single top mode**. In: *Phys. Lett. B*, **725**: (2013). DOI: 10.1016/j.physletb.2013.06.052. arXiv: 1304.5551 [hep-ph] (see p. 153).

"But I don't want to go among mad people," Alice remarked.
"Oh, you can't help that," said the Cat: "we're all mad here. I'm mad. You're mad."
"How do you know I'm mad?" said Alice.
"You must be," said the Cat, "or you wouldn't have come here."

-Lewis Caroll, Alice in Wonderland

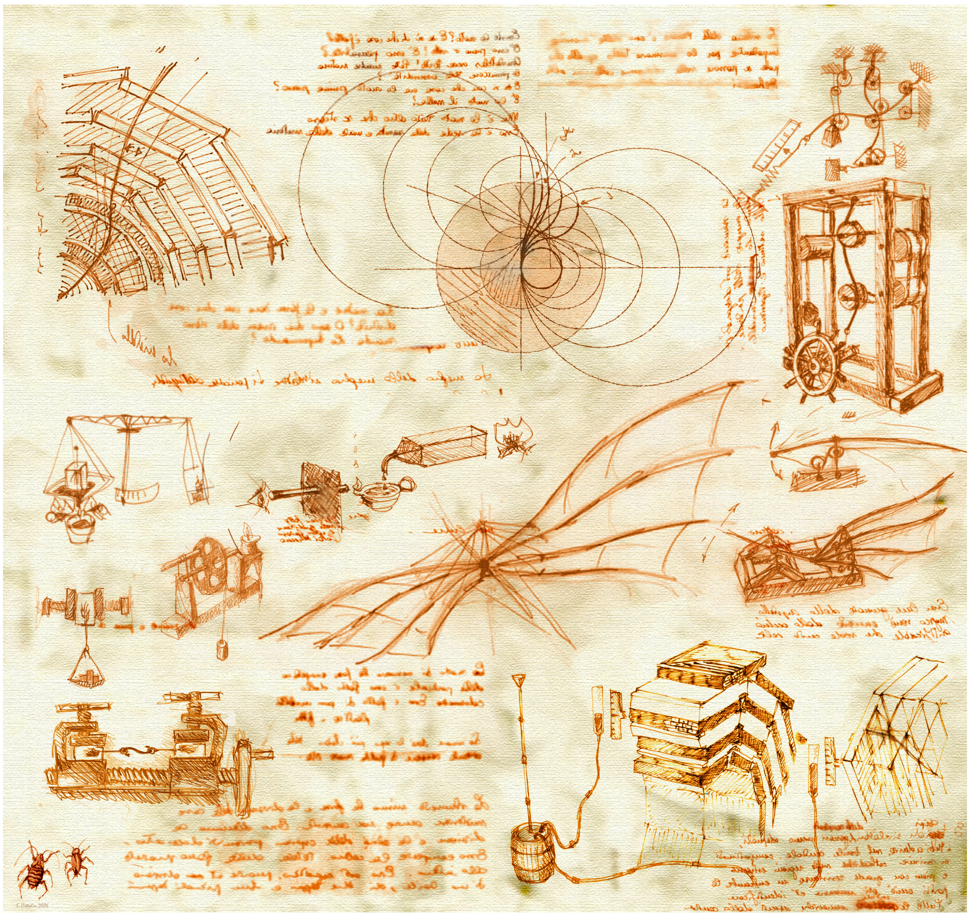

Acknowledgements

Acknowledgements

Today is the day. After an intensive period of four years, writing this note of thanks is the finishing touch to my thesis. It concludes an era of intense growth, not only in the scientific area, but also on a personal level. The work put into this thesis had a big impact on me and I would like to reflect on the people who have supported and helped me throughout this period.

I would first like to thank my promotor Jorgen D'Hondt, who was the first professor I spoke when choosing an education and who introduced me to particle physics. He gave me the opportunity and motivation to conduct my research for which I will always be grateful. Furthermore I would like to acknowledge the people that have helped improve this research and thesis. The feedback from the TOP PAG conveners, Rebeca, Pedro, and Maria, as well as the members of the analysis review committee Bob, Alexander, and Yuan Chao, was highly appreciated. I would also like to thank the members of the jury for reading the thesis and the valuable discussion during the private defence. Their input and comments helped making this work of titans a masterpiece to be proud of. Throughout my research, Rebeca has always supported me and has become a personal friend. Her constant enthusiasm about research and life inspires me still and for this I am thankful.

I was lucky to meet different people with various cultural backgrounds during my journey in particle physics. I feel enriched by all my encounters and am happy for the opportunities the collaborations have brought. At our corner at the IIHE, there was a sanctuary for anyone and I can honestly say that this experience wouldn't have been the same without my office-friends. Thank you to Simon (and Joni) and Doug for making everyone fat from eating cake and biscuits. Quentin, your background musical sounds will never be forgotten. Gerrit, James, Taejong, Nadir, Natalie, Annik, Petra, Shimaa, Giannis, Seth, Jarne, Dom, Emil, and Kirill. You are all wonderful people and I wish you all you could hope for. I want to also especially thank Denys who, though he has joined our office later in time, I could always lean on.

My journey has always been together with two special persons, Kevin and Lieselotte. We have followed the same path for a third of our life. Sharing victories and defeat together, and I look forward to keep on sharing life's journey with you. Isabelle has joined later, and together with Lieselotte we have become the tracker girls. Our journeys to CERN will always be close to my heart. I cherish the moments we shared and will continue to share as we make our way in life.

My gratitude goes also out to my other amazing colleagues at the IIHE. Thank you, Marleen, for your spirit and guiding us through the administrative maze of the VUB. Olivier, remember, we will always be your “kindjes” and if you miss us, I can always come coding next to you. I know you (and I) cherish those quality moments. Romain, Samir, Shkelzen, Abdel (Jr. and Sr.), and Stephane. Your personal en technical support is highly appreciated and was vital for the good outcome of my journey.

Also the Silicon Strip Tracker Group will always have a special place in my heart. Thank you Erik for showing me the other side of experimental physics and taking us to places that most people dream of: the heart of CMS! Ferdinando, Christian, Derek, and Francesco, you are the people that made CERN trips so amazing and wonderful to do. I wish you all the best in your future endeavours and hope our paths will cross again down the line.

I would also like to thank my mother, brothers and sister for their wise counsel and sympathetic ear. You are always there for me. Finally, there are my not-working-in-physics friends. Thank you for always being there though I have not always been available to return the favour. The knowledge of having a supporting team is a treasure that cannot be taken away.

Frank, thank you for the support and dealing with my craziness. You and Balou are the only wolf pack one could need.